

2021

Proton Aurora at Mars: Assessing the Characteristics, Variability, and Driving Mechanisms of a Newly Discovered Phenomenon

Andréa C.G. Hughes
Embry-Riddle Aeronautical University

Follow this and additional works at: <https://commons.erau.edu/edt>



Part of the [Engineering Physics Commons](#), and the [The Sun and the Solar System Commons](#)

Scholarly Commons Citation

Hughes, Andréa C.G., "Proton Aurora at Mars: Assessing the Characteristics, Variability, and Driving Mechanisms of a Newly Discovered Phenomenon" (2021). *Doctoral Dissertations and Master's Theses*. 611.

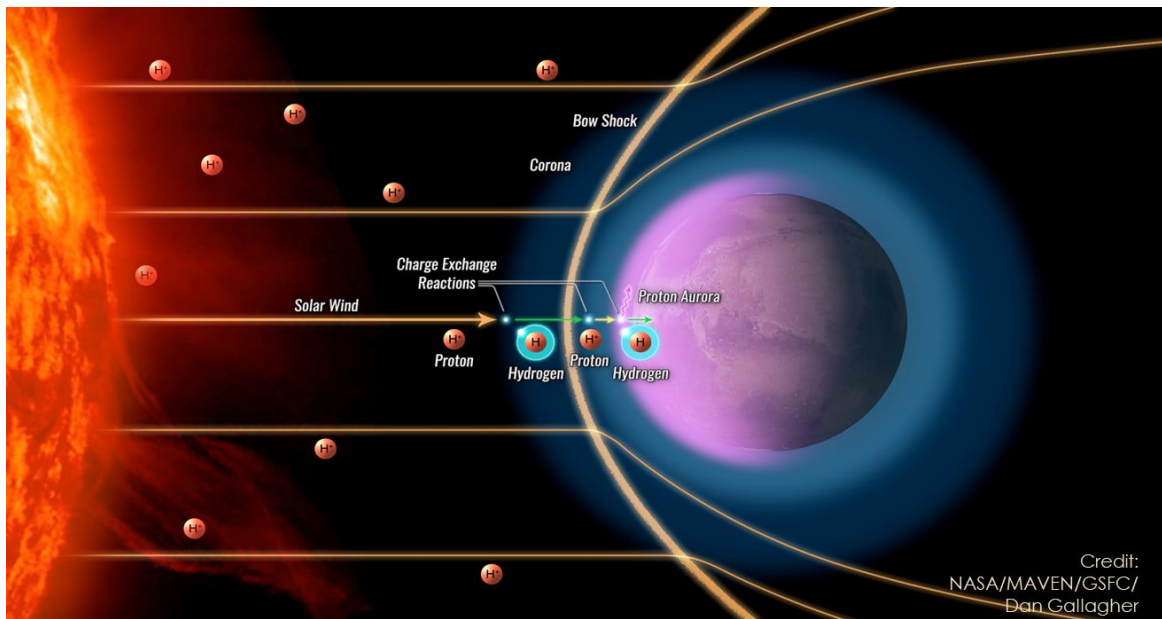
<https://commons.erau.edu/edt/611>

This Dissertation - Open Access is brought to you for free and open access by Scholarly Commons. It has been accepted for inclusion in Doctoral Dissertations and Master's Theses by an authorized administrator of Scholarly Commons. For more information, please contact commons@erau.edu.

Proton Aurora at Mars: Assessing the Characteristics, Variability, and Driving Mechanisms of a Newly Discovered Phenomenon

By

Andréa C.G. Hughes



A doctoral dissertation submitted to the Department of Physical Sciences in partial fulfillment of
the degree requirements for Doctor of Philosophy in Engineering Physics

Embry-Riddle Aeronautical University

Daytona Beach, FL

© Copyright by Andréa Hughes 2021

All Rights Reserved

Proton Aurora at Mars: Assessing the Characteristics, Variability, and Driving Mechanisms of a Newly Discovered Phenomenon

By

Andréa C.G. Hughes

This Dissertation was prepared under the direction of the candidate's Dissertation Committee chairs, Dr. Edwin Mierkiewicz and Dr. Michael Chaffin, and has been approved by the members of the Dissertation Committee. It was submitted to the Department of Physical Sciences in the College of Arts and Sciences and accepted in partial fulfillment of the requirements for the degree of Doctor of Philosophy in Engineering Physics.

Dissertation Committee:

**Edwin
Mierkiewicz**

Digitally signed by Edwin Mierkiewicz
DN: cn=Edwin Mierkiewicz, o, ou,
email=mierkiee@erau.edu, c=US
Date: 2021.08.02 10:50:17 -0600



Dr. Edwin Mierkiewicz
Committee Chair

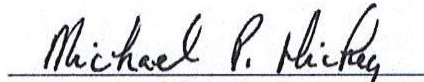


Dr. Lawrence Mathew Haffner
Committee Member

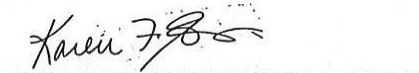
**Matthew
Zettergren**

Digitally signed by Matthew Zettergren
Date: 2021.08.04 10:00:34 -04'00'

Dr. Mathew Zettergren
Committee Member



Dr. Michael Hickey
Committee Member



Dr. Karen Gaines
Dean, College of Arts and Sciences



Provost Lon Moeller, J.D.
Senior Vice President for Academic Affairs and Provost

**Edwin
Mierkiewicz**

Digitally signed by Edwin Mierkiewicz
DN: cn=Edwin Mierkiewicz, o, ou,
email=mierkiee@erau.edu, c=US
Date: 2021.08.02 10:51:05 -0600

Dr. Edwin Mierkiewicz
Graduate Program Chair
Engineering Physics



Dr. John Hughes
Interim Department Chair
Physical Sciences

Abstract

The purpose of this doctoral research dissertation is to develop a deeper understanding of the phenomenology, variability and driving processes of proton aurora at Mars. Proton aurora are the most recently discovered of the three types of Martian aurora. Due to Mars' lack of a global dipole magnetic field, the formation processes of Martian proton aurora are uniquely different than aurora on Earth. Martian proton aurora are expected to form on the planet's dayside via electron stripping/charge exchange processes between solar wind protons and the neutral hydrogen corona. Herein, I present the results of a study of proton aurora at Mars observed using the Imaging UltraViolet Spectrograph (IUVS) onboard the Mars Atmosphere and Volatile EvolutioN (MAVEN) spacecraft. Martian proton aurora are observed in IUVS data as a prominent enhancement in the intensity of the hydrogen Lyman-alpha ($\text{Ly-}\alpha$) emission (121.6 nm) between ~110-150 km altitude.

Using altitude-intensity profiles from IUVS periapsis limb scan data spanning multiple Martian years, I create a comprehensive database of proton aurora detections and characterize their phenomenology. Based on the results of this study, proton aurora are observed in ~15% of dayside periapsis profiles (with notable seasonal variability), making proton aurora the most commonly observed type of aurora at Mars. The primary factors influencing proton aurora occurrence rates are solar zenith angle (SZA) and season. The highest proton aurora occurrence rates are at low SZAs on the Mars dayside, consistent with known formation processes. Proton aurora have highest emission enhancements, peak intensities, peak altitudes, and occurrence rates (nearing 100%) around southern summer solstice. This time period corresponds with the seasonal inflation of the neutral lower atmosphere, the onset of Martian dust storm season, higher

atmospheric temperatures and solar wind flux following perihelion, and seasonally increased coronal hydrogen column densities.

I compare remote sensing and *in situ* observations of Martian proton aurora events. By evaluating concurrent Ly- α emission enhancements and penetrating proton fluxes associated with proton aurora, it is determined that these two parameters generally track with each other, and that discrepancies between the datasets correlate with periods of high dust activity and/or extreme solar events. These discrepancies are caused by a combination of geophysical and observational factors. I also compare proton aurora detections with magnitudes and orientations of the upstream magnetic fields that control the Martian magnetic/plasma environment. I identify a possible preferential influence on Martian proton aurora activity caused by the upstream magnetic field orientations.

Numerous types of “atypical” proton aurora are examined, and the causes and variability of these events are constrained. I identify/characterize variations in proton aurora associated with local spatial and temporal variability. And though rare in the IUVS dataset, detections on the planet’s nightside are found to comprise ~4% of all proton aurora observations. The statistical properties of nightside events are quantified and possible formation mechanisms are explored.

Lastly, I coordinate a multi-model proton aurora comparison campaign: collaborating with a partnership of ~20 different modelers/scientists at nine different research institutes in the United States and around the world. Through this campaign we develop a better understanding of the physics and driving processes of Martian proton aurora, particularly emphasizing inter-model and data-model comparisons. The results of this doctoral dissertation provide a novel and unprecedented understanding of Martian proton aurora, including the short/long-term variability and primary influencing factors of these unique phenomena.

Acknowledgements

I am incredibly thankful for the tremendous support that I have received during my PhD. Any success that I have and will achieve must be rightfully attributed to my “standing on the shoulders of giants”. First, I want to acknowledge and thank my two advisors. Mike and Ed: I am overwhelmingly grateful for your guidance, patience, persistence, and support over the years. I once heard Neil deGrasse Tyson say of his first meeting with Carl Sagan that he (CS) didn’t just show him (NdT) what kind of scientist he wanted to be, but also what kind of person he wanted to be. I genuinely share this sentiment when I think of my interactions with both of you during our years of working together. Thank you for your help during my process of becoming more like the kind of scientist and person that I would like to be.

I am deeply grateful to the MAVEN/IUVS teams for welcoming, supporting, and challenging me to become a better scientist (Nick, Mike, Justin, Sonal, and Bruce, to name a few). I would never have had the opportunity to work on such a cool PhD project if not for Bruce taking time from his busy schedule to meet with me and encouraging me to contact the IUVS team, Nick welcoming me into the IUVS team with open arms, and Mike gladly taking on a graduate student half-way across the country who he’d never met before (and somehow making it work!). I’m thankful for their willingness to say “yes” when I approached each of them! Lastly, I especially want to acknowledge my tremendous appreciation to Nick for providing financial support through a research assistantship, thereby facilitating me to complete my degree.

I would also like to thank my PhD committee for their keen insights and contributions. They provided a well-rounded perspective to this work and many thought-provoking discussions.

I am extremely blessed to have a supportive community of friends who encourage me in my work (some scientists/engineers and some who have no idea what I’m talking about but listen

to me excitedly, nonetheless!). I am grateful for the supportive communities of PhD students/postdocs at ERAU and CU, especially Tomomi, The Kishnus, Marie, Kaydian, Chris, Niloofar (my example of the type of hard working PhD student, and loving friend that I strive to be!), and Eryn (who knew that an “academic half-sister” even existed, but I’m grateful for it!).

None of my accomplishments in life would be possible without the love and support of my family; there isn’t enough space to list all the ways that they’ve helped me succeed. Mom: thanks for being my biggest cheerleader in life and for always encouraging me to pursue my dreams (even though your approach can be frustrating at times), also thanks for sending me food when things got busy! Christian: thank you for lending an ear to listen, a shoulder to cry on, and a voice of encouragement/reason during the difficult times. Micah: thanks for the healthy competition in trying to finish my PhD before you (I won!). Brandy and Gerian: thank you for continually believing in and supporting me both in life and work.

I would be remiss not to mention the great debt of gratitude that I owe to all of those with a passion for social equality, who paved the way for women and minorities like myself to have the opportunity to pursue my dreams and to the support to achieve it.

And most importantly, I thank God for helping me accomplish my goal of attaining my PhD and pursuing a career in Planetary Science; and for instilling in me the passion for studying space and allowing me to help unravel the mysteries of the unfathomably beautiful and intricate universe that He created!

“The fact of the matter is that realistically, the talents that we have are talents that have been given to us, if you will, by God, and that it is our responsibility to utilize these talents for the amelioration of humanity in a creative and constructive manner.” -Shirley Chisholm

Contents

Abstract	iv
Acknowledgements	vi
Contents.....	viii
List of Tables.....	xv
List of Figures	xv
Preface.....	xxv
Aurora: “goddess of the Dawn”	xxv
1. Mars: A Planet of Unique Enigmas and Extremes.....	1
1.1 Introduction.....	2
1.2 The MAVEN Mission.....	3
1.3 The Three types of Martian Aurora	3
1.4 Proton Aurora Formation: Earth versus Mars.....	4
1.5 The Connection between Martian Hydrogen and Proton Aurora	7
1.6 Previous Observational Studies of Martian Proton Aurora	9
1.7 Primary Dataset: MAVEN/IUVS	10
1.8 Doctoral Dissertation Overview: Project Goals and Scientific Novelty.....	13
2. Proton Aurora on Mars: A Dayside Phenomenon Pervasive in Southern Summer	15
Chapter 2 Key Points.....	16

Chapter 2 Abstract	16
2.1 Introduction.....	17
2.2 Data and Methodology.....	20
2.2.1 Data.....	20
2.2.2 Methodology.....	21
2.2.3 Sensitivity to Detection Threshold	24
2.3 Proton Aurora Phenomenology and Variations	28
2.3.1 Proton Aurora Correlations and Occurrence Rates: SZA, Season, Local Time, and Altitude Dependence	28
2.3.2 Variables with No Apparent Correlations: Geographic Location and Spacecraft Observation Parameters	31
2.3.3 Atypical Proton Aurora Detections	32
2.4 Discussion.....	35
2.4.1 Dependence on Local Time, SZA, and Induced Magnetic Field	36
2.4.2 Seasonal and Intermittent Drivers on Proton Aurora	39
2.4.3 Influence of the Bow Shock and Geographic Location on Proton Aurora.....	41
2.4.4 Solar Cycle Variations.....	43
2.5 Summary and Conclusions	44
Chapter 2 Supplementary Figures	46
3. A Combined Remote Sensing and <i>In Situ</i> Evaluation of Martian Proton Aurora.....	51

Chapter 3 Key Points	52
Chapter 3 Abstract	52
3.1 Introduction.....	53
3.2 Data and Databases	55
3.2.1 MAVEN/IUVS proton aurora detections	55
3.2.2 MAVEN/SWIA penetrating proton observations.....	56
3.2.3 MAVEN/MAG observations	57
3.2.4 MAVEN Science Impacting event database	57
3.2.5 Mars Climate Database (Montabone et al. (2015) Dust Optical Depths).....	58
3.2.6 MAVEN/SEP solar activity database	58
3.2.7 Potential caveats of remote sensing-in situ data comparisons.....	59
3.3 Observations and Results	60
3.3.1 Proton aurora correlation with MAVEN science-impacting events	60
3.3.2 Comparison of IUVS Ly- α emission enhancements and SWIA penetrating proton fluxes for proton aurora detections	61
3.3.3 Proton aurora observations compared with dust optical depth and solar activity	63
3.3.4 Comparison of IUVS proton aurora detections with MAG upstream magnetic field observations	67
3.4 Discussion.....	69

3.4.1	Expected results based on previous studies and observations	69
3.4.2	Causes for discrepancies between proton aurora IUVS Ly- α emission enhancement and SWIA penetrating proton flux.....	71
3.4.3	Empirical estimation of proton aurora Ly- α emission enhancement.....	76
3.4.4	Connections between proton aurora and the upstream magnetic field environment	77
3.5	Conclusions.....	78
	Chapter 3 Supplementary Figures	80
4.	Atypical Observations of Martian Proton Aurora	86
	Chapter 4 Key Points.....	87
	Chapter 4 Abstract.....	87
4.1	Introduction and Background	88
4.1.1	Relationship between Penetrating Protons and Proton Aurora on Mars	89
4.1.2	“Typical” vs. “Atypical” Martian Proton Aurora.....	90
4.1.3	“Modulated” H and Penetrating Proton Detections at Mars.....	91
4.2	Data and Methods	92
4.3	Observations of “Atypical” Proton Aurora.....	93
4.3.1	“Variable” proton aurora	93
4.3.2	Nightside proton aurora.....	98
4.4	Discussion.....	100

4.4.1	Variability associated with neutral atmospheric waves/tides	102
4.4.2	Variability associated with “modulated” H and penetrating protons	104
4.4.3	Nighttime proton aurora detections	106
4.5	Conclusions & Future work	109
Chapter 4 Supplementary Figures:		111
5.	Evaluating Martian Proton Aurora through a Coordinated Multi-Model Comparison Campaign	117
Chapter 5 Key Points		118
Chapter 5 Abstract		118
5.1	Introduction and Background	119
5.2	Modeling Campaign Description	121
5.2.1	Description of models/teams involved in study	121
5.2.2	Campaign Outline/Steps	123
5.3	Inputs and Results for Inter-model Comparison (Step 1)	124
5.3.1	Assumptions/Constraints for Step 1	124
5.3.2	Representative inputs for Step 1	125
5.3.3	Results of Step 1A	127
5.3.4	Results of Step 1B	128
5.4	Inputs and Results for Data-Model comparison (Step 2).....	130
5.4.1	Description of MAVEN/IUVS proton aurora observation and input data	130

5.4.2	Assumptions/Constraints for Step 2	132
5.4.3	Results of Step 2A	134
5.4.4	Results of Step 2B	135
5.5	Discussion of parameters affecting model differences and similarities.....	137
5.5.1	Monodirectional vs. Isotropic assumption.....	137
5.5.2	Cross Section Processes and Scattering Angle Distributions	139
5.5.3	Other Assumptions	140
5.5.4	Data Quality and Caveats	142
5.6	Summary, Conclusions, and Future Work.....	142
6.	Summary and Conclusions.....	145
6.1	Doctoral Dissertation Project Summary	146
6.2	Scientific Novelty and Press Coverage.....	147
6.3	Conclusions.....	149
	Bibliography.....	151
	Chapter 1 References.....	151
	Chapter 2 References.....	152
	Chapter 3 References.....	155
	Chapter 4 References.....	157
	Chapter 5 References.....	160
	Appendix A: Proton/Hydrogen Precipitation Model Descriptions	162

I.	Jolitz 3-D Monte Carlo Model (Model Name: “ASPEN”).....	162
II.	Kallio 3-D Monte Carlo Model.....	164
III.	Bisikalo/Shematovich et al. 1-D Monte Carlo Model	168
IV.	Gronoff et al. 1-D Kinetic Model (Model Name: “Aeroplanets”).....	170

List of Tables

Table 5.1: Representative input for the five example cases in the inter-model comparison step

(Step 1). These parameters were varied to assess their relative importance in each model... 126

List of Figures

Figure 1.1: Comparison between magnetic field lines at Earth and Mars, as pertaining to diffuse and discrete aurora (Figure credit: Schneider et al., 2015)..... 4

Figure 1.2: Formation mechanism for Martian proton aurora originating from solar wind charge exchange. Solar wind protons charge exchange with neutral hydrogen in the corona, then penetrate the Mars bow shock and travel unimpeded to the lower atmosphere as energetic neutral atoms (ENA), having the same energy and velocity of the solar wind. These ENAs charge exchange again with other neutral atoms lower in the atmosphere depositing energy in the lower thermosphere. (Figure credit: Deighan et al., 2018)..... 6

Figure 1.3: Observations of annual hydrogen variability at Mars. Center: Ly- α Intensities and SZAs for the first 5000 MAVEN orbits. Top and Bottom: Profiles of maximum, minimum, and median (at 150 km altitude) for select months; color corresponds to SZA & solid lines are altitude binned averages of the data. 9

Figure 1.4: IUVS FUV and MUV example spectral observations and resulting altitude-intensity profile (Figure credit: Schneider et. al., 2012). 11

Figure 1.5: Example of IUVS periapsis limb scan data collection process. Note that the left image is a limb-viewing perspective, and the right image is a top-down perspective. (Figure credit: McClintock et al., 2014)..... 11

Figure 1.6: Example of IUVS raw detector data (using “detector-dark-subtracted” data) (Top) and resulting line spectra (Bottom). 12

Figure 1.7: General data reduction procedure for creating altitude-intensity profiles. Left: IUVS line spectra at multiple altitudes from a single observation (i.e., data from different mirror and slit positions all from different corresponding limb altitudes). Right: Resulting altitude-intensity profile for a single IUVS observation..... 12

Figure 2.1: (Left): Proton aurora formation mechanism (modified from Deighan et al., 2018) showing how solar wind protons charge exchange with coronal H and convert to energetic neutral atoms (ENA) which pass unimpeded through the bow shock and subsequently charge exchange again to convert back into protons and deposit energy in the lower atmosphere as proton aurora. (Right): Example H Lyman- α altitude profile for coronal H (dark grey) and profile with proton aurora detection (blue) including a heuristic estimated coronal background profile for reference (light grey) (note that the background coronal profile is not distinguishable from proton aurora in the data). We detect and characterize proton aurora using the method indicated in the figure, where the second highest intensity in the peak altitude range is subtracted from the high altitude median of a profile; emission enhancement differences above a predetermined threshold (described in Figure 2.2) are considered detections..... 20

Figure 2.2: Detection methodology and threshold selection. (Top Left): Histogram of emission enhancement differences (as defined in Figure 2.1) of all H profiles in dataset. Chosen

detection threshold is $\text{Mean} + 0.5\sigma$ (which also closely coincides with the 90th percentile).

(Bottom Left): Negative histogram values overlain on top of positive; note that positive values become non-symmetric with negative values near detection threshold, suggesting an appropriate threshold choice. (Right): Normalized percentile-binned altitude profiles; each profile represents median intensities from every emission enhancement percentile bin. An enhancement is prominent where proton aurora occur, and profiles become indistinguishable from coronal H profiles near $\sim 90^{\text{th}}$ Percentile. Using two independent criteria we establish a rigorous detection threshold for proton aurora. 24

Figure 2.3: Histograms of all IUVS data (grey) and proton aurora detections using 0.5σ threshold (blue) and 3σ threshold (green) as a function of different observational variables. In each sub-panel we present normalized proton aurora detections showing occurrence rates (pink). Occurrence rates are determined by dividing 0.5σ detection counts by all data counts in each histogram bin. Note that potential data sampling biases affect the local time and geographic latitude histograms, and local time data have been subset to include only low- and mid-latitude data (discussed further in text). Highest proton aurora occurrence rates are observed on the dayside at low SZAs and around L_s 270 (southern summer solstice). 27

Figure 2.4: Normalized 2-D histograms showing proton aurora occurrence rates as a function of different observational variables and MAVEN orbit (occurrence rates determined as in Figure 2.3). Note that local time data have been subset to include only low- and mid-latitude data (discussed further in text). Highest occurrence rates, emission enhancements, peak intensities, and peak altitudes are observed around southern summer solstice ($L_s \sim 270$), and correspond with low SZAs (i.e., daytime occurrences). 33

Figure 2.5: Proton aurora variations with respect to SZA (A&B), local time (C), and season (L_s) (D-F). Color represents emission enhancement percentile bin (as in Figure 2.2, right), and proton aurora detections correspond with percentiles greater than $\sim 90^{\text{th}}$ percentile. Note that local time data have been subset to include only low- and mid-latitude data (discussed further in text). Proton aurora display high intensities, large peak enhancements, and low SZAs (occurring in daytime), and display highest intensities, enhancement, and altitudes near southern summer solstice ($L_s \sim 270$). 34

Figure 2.6: Seasonal and latitudinal variations of SZA for proton aurora. Horizontal bins correspond with latitude (60° bin size) and vertical bins with Mars season (90° bin size, around each major season). Top plots: All IUVS data (grey) and proton aurora detections (blue). Bottom subplots: Proton aurora occurrence rates (pink) (occurrence rates determined as in Figure 2.3). Beige areas on normalized subplots represent bins where the total number of counts is less than or equal to ten. Note that apparent latitudinal dependence is likely due to a data sampling biases (discussed further in text). Occurrence rates reach nearly 100% at low SZAs around southern summer solstice ($L_s \sim 270$). 35

Figure 3.1: Proton aurora detections are shown on the top of the plot with offset and color corresponding to Ly- α emission enhancement. The bottom portion of the plot shows most major MAVEN science impacting events observed in the first few years of the mission. These science events include dust storms, solar winds streams, CME/SEP events, solar flares (including CME and/or SEP events), and discrete and/or diffuse aurora. The season (L_s) and orbit-maximum IUVS limb scan tangent point SZA are overplotted for reference as grey linear and light blue sinusoidal plots, respectively 61

Figure 3.2: Left: comparison of orbit-averaged IUVS Ly- α emission enhancement values and SWIA penetrating proton fluxes for orbits containing proton aurora detections (color corresponds with solar longitude, L_s). We identify a quasi-linear correlation between the two observables, with notable spread in the data (corresponding with orbits near southern summer solstice). Right: for each point in the left panel, y-distance offset from the line of best fit versus MAVEN orbit number. The offsets from the best-fit line correspond to a relative excess (positive offset) or deficit (negative offset) of penetrating proton flux compared with Ly- α emission enhancement (area of each data point corresponds with the orbit-averaged Ly- α emission enhancement). We note that these plots are constrained to only orbits containing proton aurora detections. 63

Figure 3.3: Same as Figure 2 (Right) with annotations showing major dust and solar activity as observed in the Mars Climate Database (MCD) and by the MAVEN/SEP instrument, respectively. The overplotted green line represents globally averaged normalized column dust optical depth (CDOD) from the MCD. By comparing the datasets in this manner, we observe a trend that proton aurora events during orbits with a very large positive offset from the best-fit line appear to correspond with major dust storm activity; conversely, proton aurora events during orbits with a very large negative offset from the best-fit line appear to correspond with major solar events. (Description of data colors and area are provided in the caption of Figure 2.)..... 64

Figure 3.4: A) Perpendicular distance from line of best fit (as described in Figure 2, Right) plotted against globally averaged normalized column dust optical depth (CDOD) values for each orbit. Note that the points on the far right side of the plot correspond with the small number of proton aurora events occurring during the 2018 planet encircling dust event

(PEDE) as the location of the MAVEN periapsis was moving onto the night side (causing unusually high IUVS tangent point SZAs during these orbits). B) Subset of data highlighted in yellow from plot (A); a trend become evident that relatively high CDOD values generally correspond with a positive offset from the line of best fit. C) Comparison between CDOD values and emission enhancement for proton aurora events. D) Same as plot (C) but subset to only the orbits that are positively offset from the best-fit line, revealing an apparent correlation between dust activity and proton aurora enhancement for positively offset orbits. E) Same as (C) but subset to evaluate only orbits with high SWIA penetrating proton flux values. We observe a strong linear correlation between CDOD and proton aurora enhancement during orbits with the highest SWIA fluxes. 66

Figure 3.5: Orbit-mean IUVS proton aurora emission enhancements compared with the magnitude (A) and orientation (i.e., cone angle (B) and clock angle (Figure 3.5C)) of the upstream interplanetary magnetic field (IMF). No clear correlation is observed between proton aurora enhancement and IMF magnitude, but a double peak proton aurora enhancement is apparent in both the cone angle and clock angle plots. 68

Figure 3.6: Proton aurora observations with respect to IMF cone angle (A) and clock angle (C) (Note that blue histograms shows all IUVS observations and orange histograms show only proton aurora observations). Proton aurora occurrence rates are also shown these respective angles (B and D, respectively). 69

Figure 3.7: IUVS Ly- α emission enhancement versus SWIA penetrating proton flux (inverted plot of Figure 3.1, considering Ly- α enhancement as the dependent variable). The trendlines give an estimate of the Ly- α enhancement for proton aurora event assuming a foreknowledge of the penetrating proton flux and the local dust/solar activity conditions. 77

Figure 4.1: (Top) Offset IUVS limb scan altitude-intensity profiles from MAVEN orbit 4107 for A) Ly- α and B) CO₂⁺ UVD emissions. Variations in Ly- α peak altitude between the scans within the orbit (observing a single proton aurora event) track with altitude variations in the CO₂⁺ UVD profiles (note that such variations in the CO₂⁺ UVD are consistent with previous observations of lower atmospheric waves/tides). C) Concurrent observations of IUVS emission enhancement, SWIA penetrating proton flux, and NGIMS CO₂ density during the periapsis portion of MAVEN orbit 4107. We observe similar fluctuations in the different instrument measurements on roughly the same temporal scale during this orbit, consistent with being caused by the same driving mechanisms..... 97

Figure 4.2: Altitude-intensity profiles overlain on top of a synthetic image format of Ly- α intensities for each IUVS limb scan/mirror angle in MAVEN Orbit 6753 (e.g., Figure 2 from Deighan et al. 2018). Examples of “modulated” proton aurora (middle and bottom plots) in comparison with a proton aurora event with minimal variability (top). The middle plot shows altitude variation in a central orbit limb scan (during near-radial IMF conditions) and the bottom plot shows intensity variation in a central orbit limb scan (also during near-radial IMF conditions). Note that the given SZA values given correspond with the median SZA in each IUVS scan; the boxes highlight the variability within each orbit, and the horizontal lines represent the average peak altitude for each orbit..... 98

Figure 4.3: Altitude-intensity profiles overlain on top of a synthetic image format of Ly- α intensities for each IUVS limb scan/mirror angle in MAVEN Orbit 6753 (e.g., Figure 2 from Deighan et al. 2018). This orbit shows an example of a nighttime proton aurora event. Note that the given SZA values given correspond with the median SZA in each IUVS scan..... 99

- Figure 4.4: Statistical comparisons of proton aurora observational parameters for dayside versus nightside events. Nightside events exhibit smaller peak Ly- α intensities (A), emission enhancements (B), and altitudes (C); they do not appear to exhibit a clear seasonal dependence (D), or to be geographically constrained on the planet (E). Note the difference on the scales between the day/night axes. (Note: day and night observations are defined as $\pm 10^\circ$ of SZA=90°, respectively.)..... 100
- Figure 4.5: Sequence of images from IMAGE spacecraft showing “pulsating” proton aurora at Earth on 9 March 2004 (credit: Yahnin+2009)...... 106
- Figure 5.1: Simulation results of proton aurora altitude-VER profiles from each model for the five representative input cases in the inter-model comparison step of the campaign (Step 1-A). The two parameters that have the most significant effect on the results are the input solar wind flux and velocity..... 128
- Figure 5.2: Simulation results from the inter-model comparison after running the results through the Deighan Radiative Transfer (RT) model (Step 1-B). Using the RT “forward-models” the results into observation space (e.g., perform a “line-of-sight” integration comparison). The model results more closely resemble each other after this step, but the dominant influencing factors identified in Step 1-A (Figure 5.1) are still present..... 130
- Figure 5.3: IUVS Ly- α intensity data of proton aurora observation used in the data-model portion of the campaign (Step 2). Left: IUVS altitude-intensity profiles for limb scans used in the study (MAVEN orbit 4235). Right: altitude-intensity profiles overlain on top of a synthetic image format of Ly- α intensities for each IUVS limb scan/mirror angle in this orbit (e.g., Figure 2 from Deighan et al. 2018). Note that only the central nine scans were used in this

study (yellow highlighted scans), and that the given SZA values given correspond with the median SZA in each scan. 132

Figure 5.4: Empirically-derived theoretical CO₂ profile used in models for the data-model comparison step (Step 2). This profile was created by fitting a best-fit exponential to the derived IUVS and measured inbound NGIMS (lower NGIMS curve) data from this MAVEN orbit. 134

Figure 5.5: Simulation results from the data-model comparison step of the campaign (Step 2-A), showing proton aurora altitude-VER profiles from each model for the specified input parameters and SZAs. Most of the model results display similar peak altitudes and VERs (within an order of magnitude)..... 135

Figure 5.6: Simulation results for the data-model comparison after running the results through the Deighan Radiative Transfer (RT) model (Step 2-B). The uncorrected IUVS limb scan profiles for this orbit is shown on the far left plot, and the corrected background-subtracted limb scans (after subtracting out the theoretical “background” coronal H contribution) are shown on the far right plot. The Ly- α intensities of the model results much more closely correlate with those of the background-subtracted data. However, there is still a notable discrepancy between the average peak altitude of the data profiles (solid grey horizontal line) and the average peak altitude of the model profiles (dashed grey horizontal line). Note that the SZA of the observations is decreasing from left to right (i.e., moving toward the subsolar point), as shown in Figure 5.3. 137

Figure 5.7: Example comparison of assuming purely monodirectional movement of the incident particle population versus purely isotropic (results from the Bisikalo/Shematovich et al. model). Left: Comparison proton aurora profiles using each assumption; Middle: Simulated H

energy flux in the downward and upward directions using a monodirectional assumption;

Right: Simulated H energy flux in the downward and upward directions using an isotropic assumption. The simulated proton aurora profile using the isotropic assumption has a higher peak altitude and smaller VER due to the larger upward (e.g., backscattered) H population.

Although the models assume purely monodirectional movement in this study, the reality is likely somewhere between these extreme assumptions, which could in turn lead to some of the observed discrepancies between the data and the models in Step 2 of the campaign. (Figure credit: Bisikalo/Shematovich et al. team)..... 139

Figure 6.1: IUVS apoapsis observations of nominal conditional of the Martian hydrogen corona (left panel) and observations when proton aurora are underway (middle panel). By subtracting out the hydrogen coronal intensities we may see the spatial constraints proton aurora on the sunward facing side of the planet (right panel). (Image credit: NASA/LASP/Univ. of Colorado/ERAU)..... 147

Figure 6.2: Martian proton aurora exhibit significant seasonal variation due to dust-driven lower-atmospheric forcing and hydrogen escape. The peak activity occurs during southern summer, when the Mars atmosphere experiences increased dust activity and higher temperatures. (Figure credit: NASA/LASP /Univ. of Colorado/ERAU)..... 149

Preface

*“As when descends Eos (“Aurora” / “Dawn”) from Olympos’
crest of adamant, Eos, heart-exultant in her radiant steeds amidst
the bright-haired Horai; and o’er them all, how flawless-fair
soever these may be, **her splendor of beauty glows pre-eminent.**”*

*- Quintus Smyrnaeus, Fall of Troy 1. 48 ff (trans. Way)
(Greek epic C4th A.D.)*

Aurora: “goddess of the Dawn” (and Hemera: “goddess of the Day”)

In this doctoral dissertation I evaluate proton aurora on Mars. Throughout the history of human civilization, sky watchers, philosophers, and scientists alike have been mesmerized by aurora on Earth. These Northern/Southern lights (*i.e.*, Aurora Borealis and Aurora Australis, respectively) have been a source of great wonder, awe, and even religious/mythological omens.

It is interesting to note that the word “aurora” is derived from the Latin word for “dawn” and is the name of the Roman mythological goddess of the dawn (also known in Greek mythology as “Eos”). However, as the reader will learn in the following chapters of this dissertation, Martian proton aurora are unique in that they occur almost exclusively on the dayside of the planet. Thus, I propose (for purposes of the reader’s and my own amusement) that a more suitable naming convention, and means of contemplating Martian proton aurora, may instead be in association with the Greek goddess of the day, “Hemera” (or equivalently, the Roman goddess “Dies” - though I personally find the former more aesthetically pleasing). Hemera’s personification as the “brightness of the day” would indeed be an appropriate representation of this unique Martian phenomenon. Perhaps one day human travelers to the Red Planet may have the pleasure of observing firsthand (while wearing ultraviolet goggles, of course) the mesmerizing beauty of Martian “proton hemera” (*aka*, proton aurora)!

1. Mars: A Planet of Unique Enigmas and Extremes

1.1 Introduction

Mars is a planet of many enigmas. Although it is only a third the size of Earth, it is home to the solar system's largest volcano (Olympus Mons), largest canyon system (Valles Marineras), and some of the largest impact craters (*e.g.*, Hellas Basin). In addition to these large scale geologic features, there is also vast morphologic and mineralogic evidence that liquid water once shaped and formed the surface of Mars. This evidence is manifest through features such as long fluvial channels, paleobasins with inlet/outlet valleys, river deltas and alluvial fans, crossbedding and polygonal fractures consistent with desiccation cracks, and vast aqueous mineralogies such as phyllosilicates and carbonates. Yet in spite of Mars' remarkable geologic history, the planet is no longer geologically active and does not possess the pressures and temperatures necessary to sustain liquid water on the surface. This paradox between observations of features on Mars that are consistent with an aqueous history and the current instability of liquid water on the Martian surface may be the planet's most intriguing paradox. This discrepancy may lead the curious reader to ask the crucial question: "What happened to all of the water on Mars?"

Due to Mars' small size, the planet's escape velocity is much less than that of Earth. One important result of this difference is that Mars is not able to hold onto atmospheric constituents and therefore has lost most of its atmosphere over time. Another important factor is that the planet's core cooled much faster than that of Earth, eradicating the planet-wide dynamo magnetic field. We know that Mars once had a global intrinsic field because of the remnant crustal fields that are still present in southern hemisphere. The significance of losing this global intrinsic magnetic field was not trivial and allowed what was left of Mars' atmosphere to be stripped away to space by the solar wind over the course of billions of years.

Of particular relevance to this study is the loss of hydrogen (H) to space, which is driven by the breakdown and subsequent escape of Martian water. Because H comprises the most extended regions of the Martian exosphere, it directly contributes to the formation of proton aurora on Mars (described in detail below). Thus, as we will find in subsequent chapters, by studying proton aurora on Mars we also are evaluating a proxy for H escape, and consequently, the loss of water from Mars.

1.2 The MAVEN Mission

In order to understand Mars' atmospheric loss to space over time, the Mars Atmosphere and Volatile Evolution (MAVEN) spacecraft (Jakosky *et al.*, 2015) was sent to Mars. MAVEN was launched in 2013 and arrived at Mars in late 2014, and was the first mission to be sent to Mars with the primary purpose of studying the planet's upper atmosphere and loss to space. There are eight instruments onboard the MAVEN spacecraft. Most of the MAVEN instruments are *in situ* instruments that study atmospheric and solar wind particles, with the exception of a remote sensing instrument, the Imaging UltraViolet Spectrograph (IUVS), which provided the primary dataset utilized in this study (see Data section of this chapter for more details).

1.3 The Three types of Martian Aurora

Aurora have been observed on almost every planet in our solar system, including Mars. Proton aurora are one of three types of aurora at Mars, in addition to discrete (Bertaux *et al.*, 2005) and diffuse aurora (Schneider *et al.*, 2015). Discrete aurora, first identified by Bertaux *et al.* (2005), are spatially confined aurora that are linked to the topology of the crustal magnetic field. Alternatively, diffuse aurora, which were initially identified by Schneider *et al.* (2015), are not spatially constrained or linked to the crustal magnetic field. Both discrete and diffuse aurora are formed via electrons exciting atoms in the neutral atmosphere and are observed exclusively

on the Martian nightside. The formation processes of Martian aurora are different than those at Earth due to the presence of a Martian induced magnetic field (and lack of an intrinsic global dipole magnetic field). Figure 1.1 (right) shows a schematic of solar wind particles interacting with draped/open magnetic field lines around Mars to create diffuse electron aurora; alternatively, discrete aurora are formed by solar wind particles that are accelerated along diverging magnetic flux tubes above crustal fields (e.g., Lundin *et al.*, 2006).

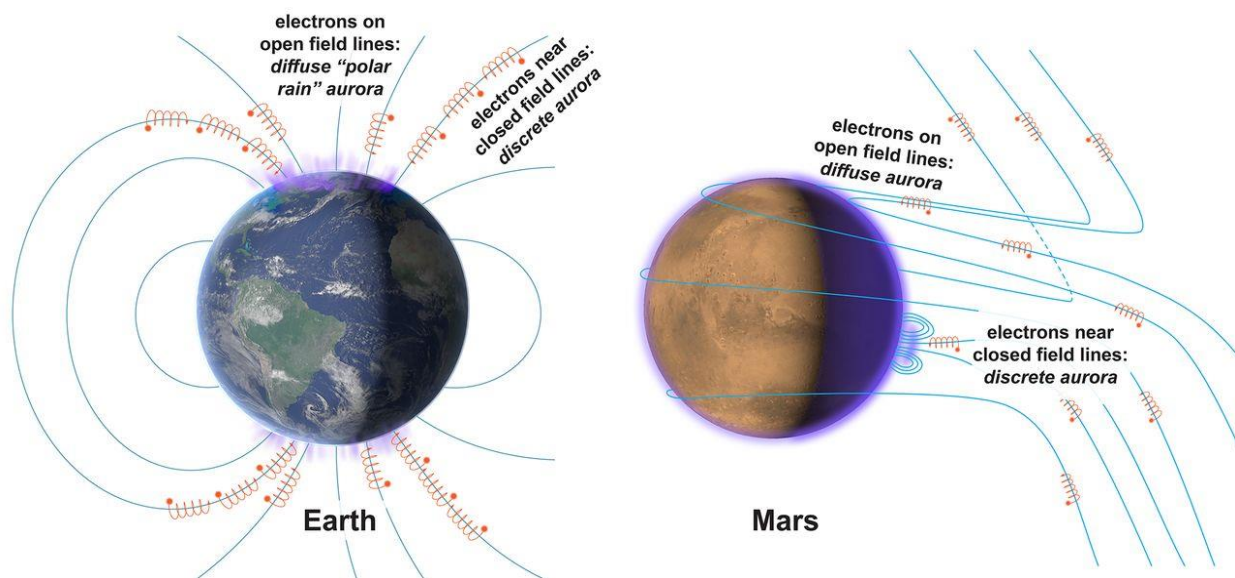


Figure 1.1: Comparison between magnetic field lines at Earth and Mars, as pertaining to diffuse and discrete aurora (Figure credit: Schneider *et al.*, 2015)

1.4 Proton Aurora Formation: Earth versus Mars

Aurora form on Earth by energetic particles (typically solar wind electrons and protons) that are accelerated along the planet's magnetic field lines toward the poles, where they subsequently excite neutral atmospheric constituents (e.g., Figure 1.1, left). Upon deexciting, those neutral particles emit a photon which can be observed in visible (and other) wavelengths as the Northern/Southern Lights (*i.e.*, Aurora Borealis and Aurora Australis, respectively). While

most terrestrial aurora are formed through excitation by solar electrons, aurora formed by solar proton (H^+) excitation also exist at Earth.

Proton aurora were first identified at Earth by Vegard (1939) as doppler shifted hydrogen (H) Balmer-alpha and -beta spectral lines within the emissions of auroral observations. Proton aurora were later thoroughly characterized in a detailed review paper by Eather (1967). At Earth, proton aurora are strongly influenced by the planet's magnetospheric field lines.

Due to the lack of a Martian global intrinsic magnetic field, the formation process of proton aurora at Mars is notably different than at Earth. As H is the lightest constituent of the upper atmosphere, the H corona comprises the most extended portion of the exosphere and dominates initial interactions with the solar wind. The lack of a global dipole magnetic field at Mars allows for solar wind interactions with the Martian H corona on the dayside of the planet before it reaches the bow shock and is diverted around the planet by the Martian induced magnetic field (*i.e.*, the magnetic structure of the near-space environment, *e.g.*, Akalin *et al.*, 2010). Martian proton aurora form via solar wind protons, traveling with the high energies and velocities relative to the Martian corona, interacting with the extended H corona (Figure 1.2). These solar particles can charge exchange with neutral H in the corona, pulling an electron from a neutral H atom and becoming an Energetic Neutral Atom (ENA) (Kallio and Barabash, 2001). The ENAs, having approximately the same velocity and energy as the incident solar wind particles, can then travel unimpeded past the planet's bow shock and magnetic pileup boundary (MPB) into the atmosphere. These particles interact with neutral atmospheric constituents (primarily CO_2) to convert between ENAs and protons through charge exchange and/or electron stripping processes. The H^+ /ENA conversion process can take place hundreds of times before being absorbed or destroyed. During this process, the ENA can be excited and emit H Lyman-

alpha ($\text{Ly-}\alpha$) photons, creating proton aurora (Figure 1.2). These proton aurora events can be observed in ultraviolet (UV) wavelengths as an enhancement (*e.g.*, a brightness peak) in the $\text{Ly-}\alpha$ emission (121.6 nm) at an altitude of $\sim 110\text{km}$ - 150km . Note that unlike typical aurora, where the neutral atmospheric gases emit photons, in this case it is the precipitating particle that emits.

Because of the unique formation mechanisms of Martian proton aurora, they are expected to be confined to the dayside of the planet but are not expected to exhibit any geographic/latitudinal constraints such as Earth aurora. And due to the dependence on charge exchange processes with coronal H, Martian proton aurora can be influenced by variations in either the solar wind flux or the H corona.

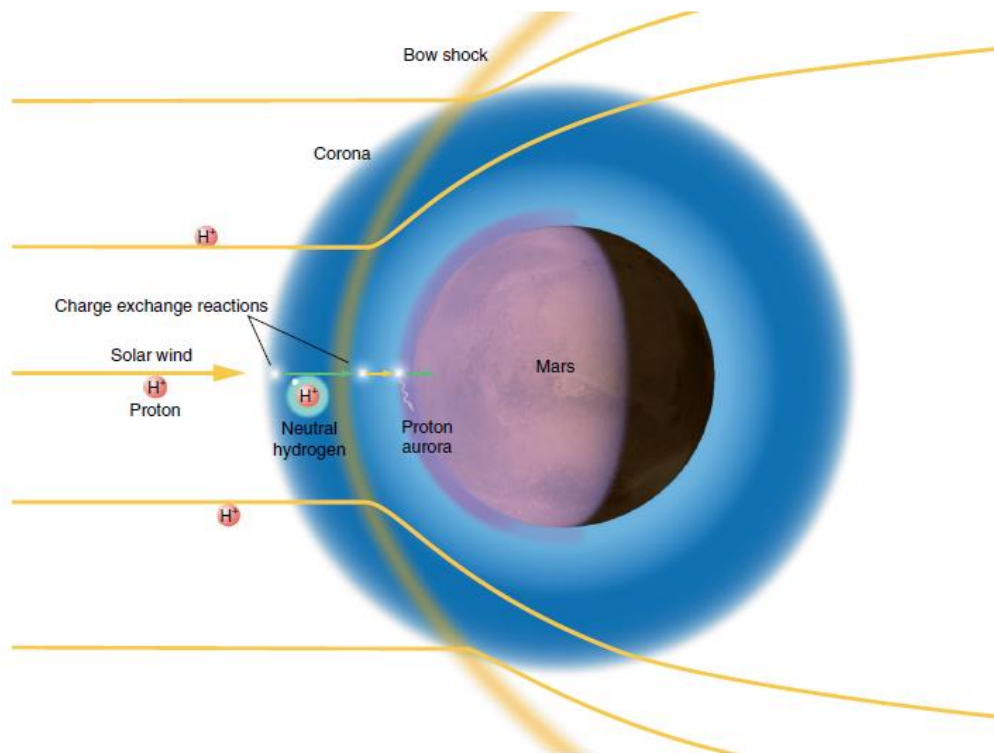


Figure 1.2: Formation mechanism for Martian proton aurora originating from solar wind charge exchange. Solar wind protons charge exchange with neutral hydrogen in the corona, then penetrate the Mars bow shock and travel unimpeded to the lower atmosphere as energetic neutral atoms (ENA), having the same energy and velocity of the solar wind. These ENAs charge exchange again with other neutral atoms lower in the atmosphere depositing energy in the lower thermosphere. (Figure credit: Deighan et al., 2018)

1.5 The Connection between Martian Hydrogen and Proton Aurora

Proton aurora are observed at Mars in the H Ly- α emission as an enhancement on top of a broad, diffuse background emission from thermal H in the extended Mars corona. The typical coronal H Ly- α altitude-intensity profile is relatively flat (*e.g.*, Figure 1.3, low intensity subplots) due to the diffusive separation of H from CO₂ above the homopause, the relatively large scale height of H in the Martian atmosphere, and the optically thick nature of Ly- α . Alternatively, the Ly- α emission associated with proton aurora is optically thin and Doppler shifted out of the thermal H distribution. Thus, proton aurora are identifiable in UV spectral data as an enhancement in brightness between ~110-150 km in the Ly- α profile (*e.g.*, Figure 1.3, high intensity peaked subplots). The emission enhancement (between a few hundred R to a few kR) is sharply peaked at these altitudes due to the energy deposition process. It is interesting to note that the enhancement altitude range is consistent with previously determined predictions of the peak altitude of energy deposition for protons and H in the Mars atmosphere (*e.g.*, Halekas *et al.*, 2015; Deighan *et al.*, 2018).

Because of the important role of the H corona in the proton aurora formation process, variability in the H corona will affect the proton aurora profile as well. Numerous previous studies carried out by different spacecraft/instruments have identified significant seasonal variability in the Mars H corona (*e.g.*, Chaffin *et al.*, 2014; Clarke *et al.*, 2014; Battacharya *et al.*, 2015; Mayyasi *et al.*, 2017; Halekas 2017). These studies found that the abundances, altitudes, column densities and escape rates of H reach an annual maximum around the Martian southern summer solstice (*i.e.*, solar longitude, L_s, ~270).

In a preliminary study of Martian H, MAVEN IUVS periapsis data spanning multiple Mars years were used to observe significant annual variability in Martian atmospheric H (Figure 1.3,

center). The H Ly- α intensities reach local maxima around $L_s \sim 270$ over the course of two Mars years. (Note that the general sinusoidal shape of the plot is associated with the precession of the MAVEN spacecraft, and annual variability is observed as an increased amplitude on top of this curve.) We also observe a significant dependence on solar zenith angle (SZA), where the highest H Ly- α intensities occur at low SZAs (*i.e.*, closer to the subsolar point). Note that this preliminary study did not distinguish between the independent H contributions from thermal H in the Mars corona and H-ENAs associated with proton aurora (nor did other previous observational studies of Martian atmospheric H), as it is not possible to uncouple observations of these two unique H populations. However, in subsequent chapters, the proton aurora contribution to the Ly- α profile is exclusively evaluated by subtracting out the background coronal H from profiles (explained in detail in Chapter 2).

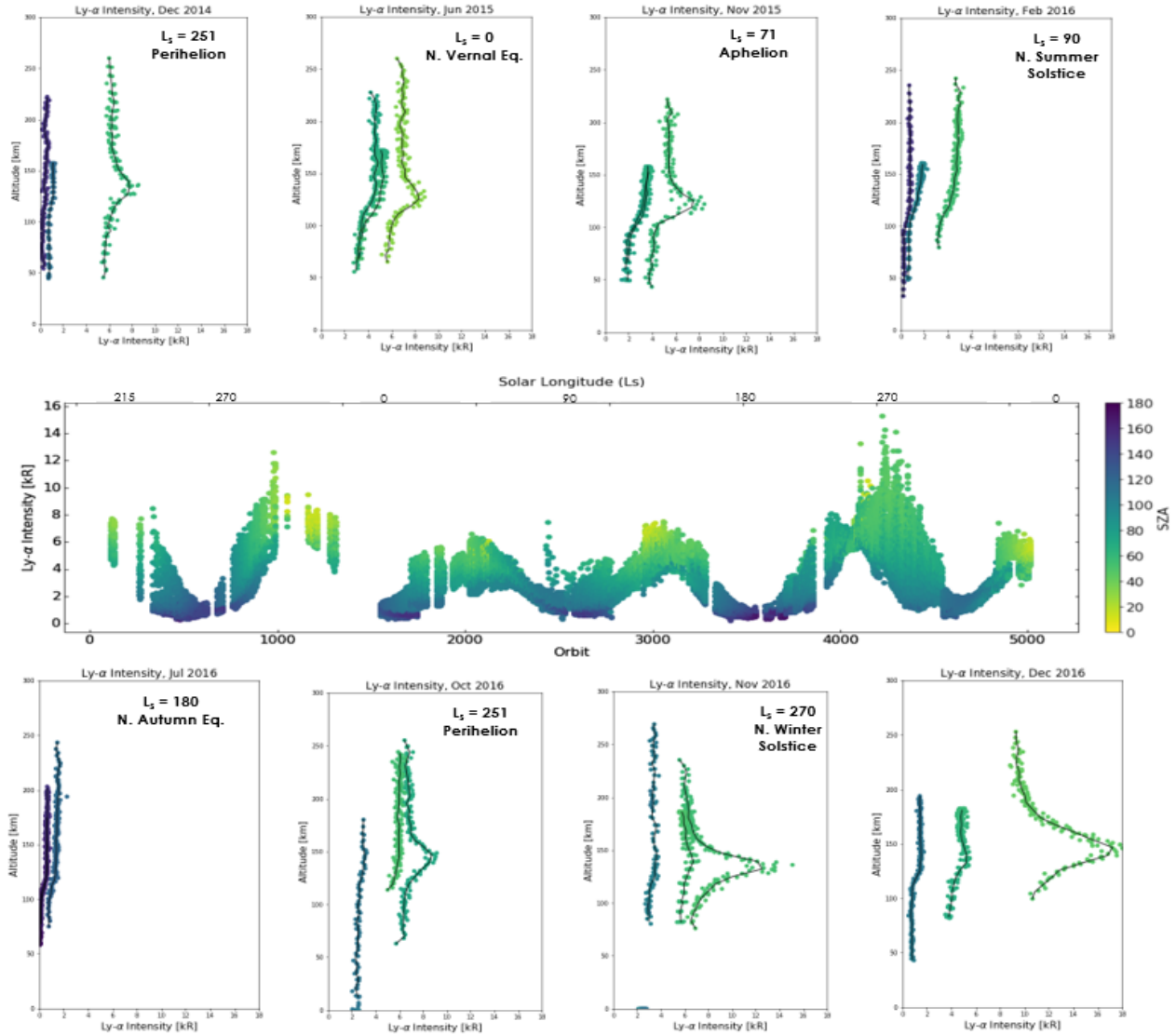


Figure 1.3: Observations of annual hydrogen variability at Mars. Center: Ly- α Intensities and SZAs for the first 5000 MAVEN orbits. Top and Bottom: Profiles of maximum, minimum, and median (at 150 km altitude) for select months; color corresponds to SZA & solid lines are altitude binned averages of the data.

1.6 Previous Observational Studies of Martian Proton Aurora

Proton aurora were first predicted to exist at Mars based on observations by the Solar Wind Ion Analyzer (SWIA) onboard the MAVEN spacecraft (Halekas *et al.*, 2015). A study by Halekas *et al.* (2015) initially identified an increased energy flux of “penetrating protons” (*i.e.*, solar wind protons that penetrate into the Martian atmosphere) having the same energy and velocity as the incident solar wind. A subsequent study by Deighan *et al.* (2018) found a strong

correlation between increased fluxes of solar wind penetrating protons and IUVS emission enhancements in Ly- α brightness, associated with proton aurora events. Additionally, Ritter *et al.* (2018) presented observations of proton aurora using UV data from the Spectroscopy for the Investigation of the Characteristics of the Atmosphere of Mars (SPICAM) spectrograph onboard Mars Express (Ritter *et al.*, 2018). Between these two UV spectroscopy observational studies of proton aurora at Mars, only nine definitive detections of proton aurora were previously identified.

1.7 Primary Dataset: MAVEN/IUVS

We use data from the Imaging UltraViolet Spectrograph (IUVS) onboard the Mars Atmosphere and Volatile Evolution (MAVEN) spacecraft, to identify/characterize proton aurora at Mars. IUVS has a Far-Ultraviolet (FUV) (110-190 nm) and Mid-Ultraviolet (MUV) (180-340 nm) channel (McClintock *et al.*, 2014). The combination of these channels provides coverage of important UV atomic and molecular spectral features at Mars (Figure 1.4). We specifically use IUVS limb scan data, taken during the periapsis portion of the MAVEN orbit. IUVS limb scans are built up as the instrument scanning mirror is slewed during data collection while observing across-track of the spacecraft travel direction (Figure 1.5). These data are used to create altitude-intensity profiles for given atomic/molecular species (*e.g.*, Figure 1.4 and Figure 1.7). Of interest to our study is the hydrogen (H) Lyman-alpha (Ly- α) emission at 121.6 nm (Figure 1.6). A Ly- α altitude-intensity profile is created by integrating under a Ly- α spectral line to determine the area of the Ly- α intensity for each altitude range observed in the limb scan (Figure 1.7, left). The intensity value from each of these spectral profiles can then be plotted at its corresponding tangent point altitude, resulting in the altitude-intensity profile for an observation (Figure 1.7, right).

In this study, I utilize IUVS Level 1C periapsis intensity data. In these data, which are created by the IUVS team, the background Ly- α emission is subtracted out, and the data are converted to kilorayleighs and binned into 5km altitude bins (e.g., Figure 1.7). Using data from MAVEN/IUVS in combination with multiple additional supporting datasets, I characterize the phenomenology of and observe variations in Martian proton aurora.

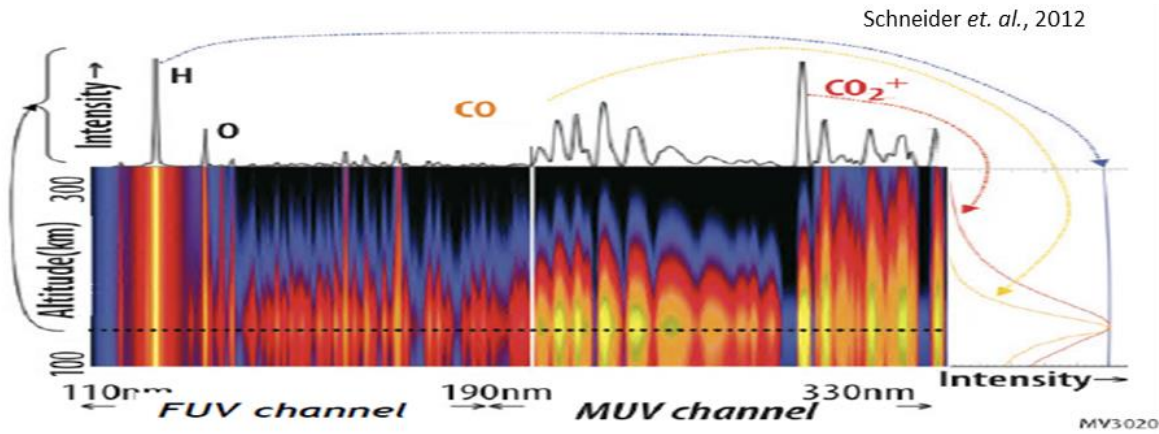


Figure 1.4: IUVS FUV and MUV example spectral observations and resulting altitude-intensity profile (Figure credit: Schneider et. al., 2012).

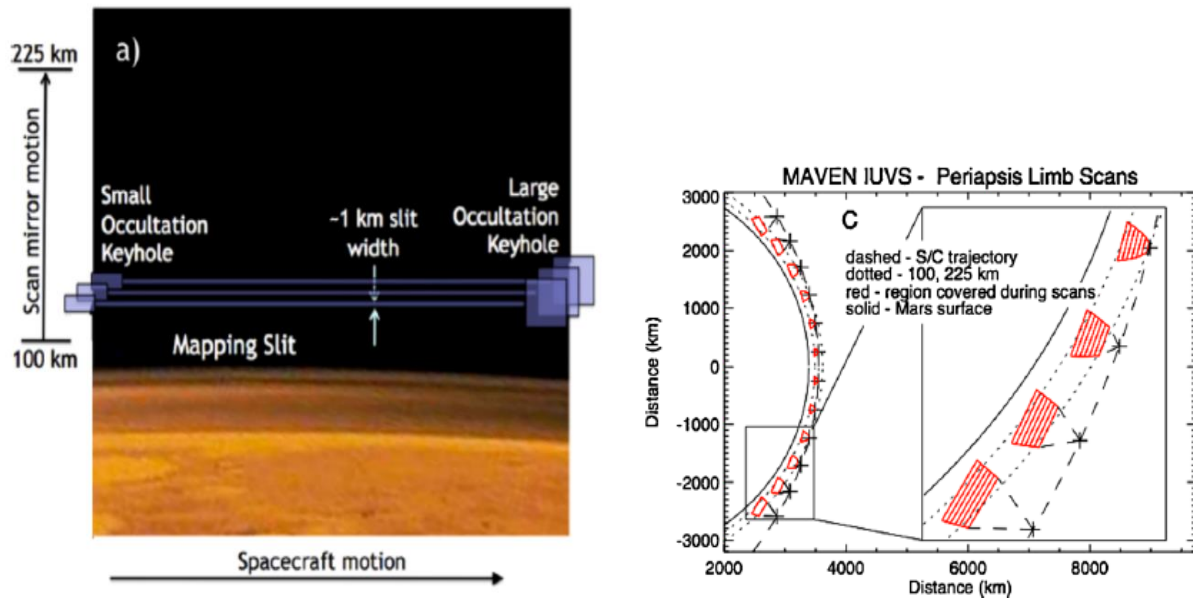


Figure 1.5: Example of IUVS periapsis limb scan data collection process. Note that the left image is a limb-viewing perspective, and the right image is a top-down perspective. (Figure credit: McClintock et al., 2014)

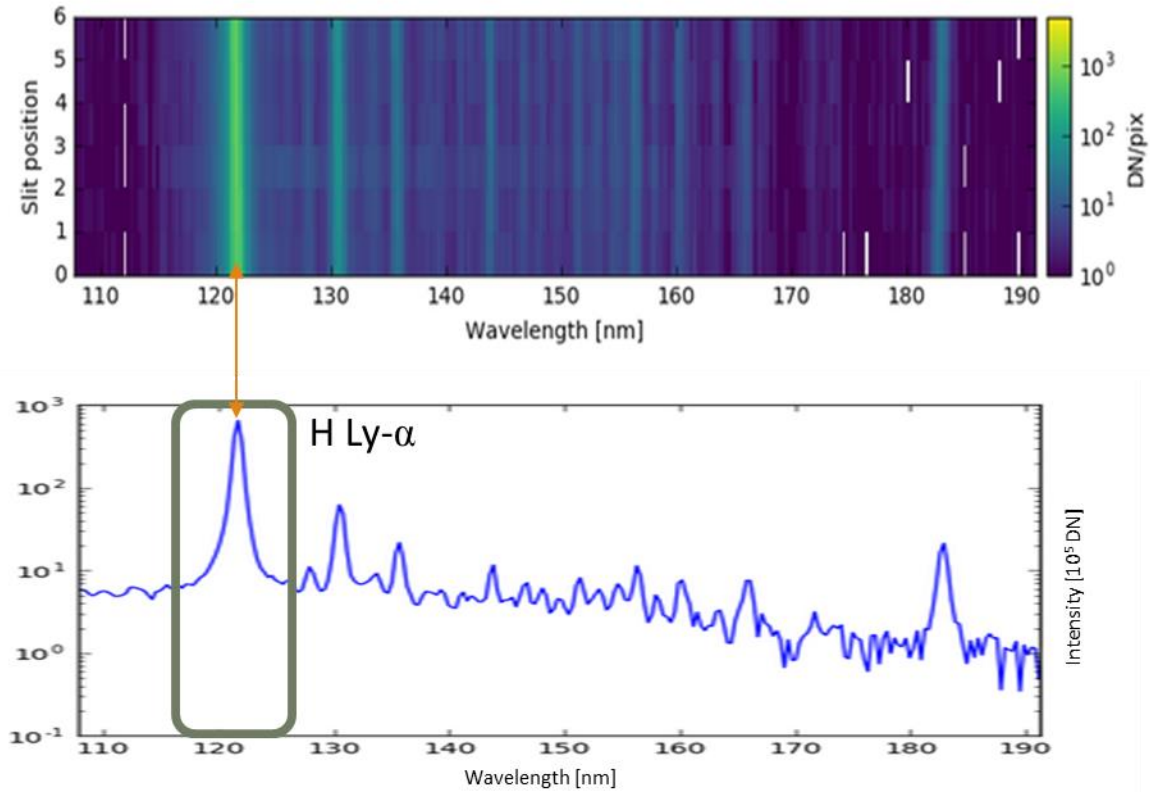


Figure 1.6: Example of IUVS raw detector data (using “detector-dark-subtracted” data) (Top) and resulting line spectra (Bottom).

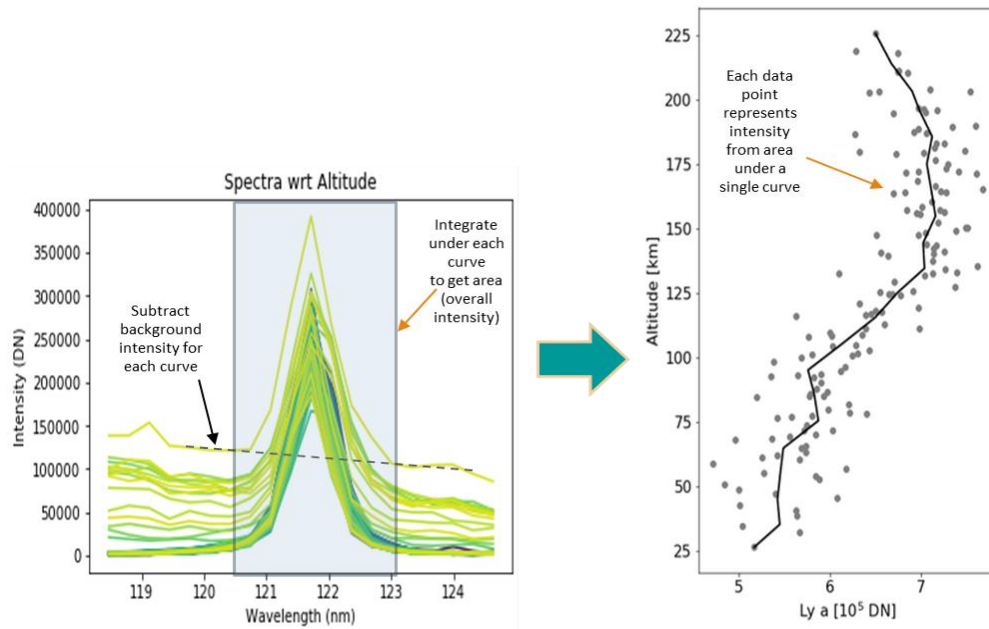


Figure 1.7: General data reduction procedure for creating altitude-intensity profiles. Left: IUVS line spectra at multiple altitudes from a single observation (i.e., data from different mirror and slit positions all from different corresponding limb altitudes). Right: Resulting altitude-intensity profile for a single IUVS observation.

1.8 Doctoral Dissertation Overview: Project Goals and Scientific Novelty

The purpose of this doctoral dissertation is to provide a deeper understanding of the phenomenology, variability and driving processes of proton aurora in the atmosphere of Mars. Proton aurora are the most newly identified, and therefore, the least studied and arguably the least understood type of aurora at Mars. Prior to this dissertation project, only two studies had observed Martian proton aurora (both in UV wavelengths) (*i.e.*, Deighan *et. al*, 2018 and Ritter *et. al*, 2018). This dissertation project builds upon the work of previous studies evaluating Martian proton aurora. In subsequent chapters, I present the results of the most in-depth analysis of Martian proton aurora to date.

In undertaking this project, I address many important research objectives, aiming to answer outstanding science questions and further develop our current understanding of Mars. These research objectives include:

- **Create a comprehensive database of Martian proton aurora and characterize the phenomenology of these events.** We undertake a rigorous statical analysis of proton aurora, identifying thousands of observations across the MAVEN/IUVS dataset and creating a simple/efficient automated detection method for proton aurora activity. We utilize the proton aurora detections to characterize the phenomenology of the events. (Chapter 2)
- **Evaluate the comparative variability between proton aurora and penetrating proton observations.** We compare H Ly- α remote sensing and *in situ* penetrating proton observations of proton aurora, identifying an unexpected deviation from nominal conditions that is associated with periods of high atmospheric dust activity and extreme solar activity. We identify a novel method for empirical estimation of

- Ly- α enhancement in proton aurora events based on the penetrating proton flux and local Martian environment. (Chapter 3)
- Constrain the geomagnetic locations of proton aurora occurrence at Mars to search for possible interaction with an upstream solar magnetic field. We evaluate connections between proton aurora activity and the magnitude/orientation of the upstream magnetic field, identifying possible preferential occurrence of proton aurora at specific cone/clock angles. (Chapter 3)
 - **Identify/characterize unusual variability in certain proton aurora observations.** We evaluate numerous detections of “atypical” proton aurora (including nightside and “variable” proton aurora detections) to gain a deeper understanding of the trends and unique formation mechanisms of these uncommon events. (Chapter 4)
 - Develop the current understanding of proton aurora formation and variability through a coordinated multi-modeling comparison campaign. We carry out a collaborative study to compare results from multiple models that effectively simulate proton aurora observations. These results help to constrain the dominant physics/driving processes that affect proton aurora. (Chapter 5)

Studying Martian proton aurora informs our understanding of the processes controlling Martian atmospheric loss and evolution, as the processes responsible for auroral formation at Mars are also responsible for stripping away the atmosphere. Further, by understanding proton aurora at Mars we may better understand the connection between the solar wind and Mars’ extended H corona. This understanding, in turn, informs our knowledge of interactions at other planetary bodies that exhibit a neutral H corona and lack a global magnetic field (*e.g.*, Venus, comets, and exoplanets), both in our solar system and beyond.

2. Proton Aurora on Mars: A Dayside Phenomenon Pervasive in Southern Summer

Previously published in the *Journal of Geophysical Research: Space Physics* (2019)

Hughes, A., Chaffin, M., Mierkiewicz, E., Deighan, J., Jain, S., Schneider, N.,

Mayyasi, M., Jakosky, B.

Chapter 2 Key Points

- Proton aurora form via interactions between the solar wind and H corona; as such, changes in the H corona strongly influence proton aurora
- Proton aurora occur in ~14% of dayside profiles in our data (varying with season), making them the most commonly observed aurora at Mars
- Proton aurora occurrence rates are highest in dayside southern summer observations, nearing 100% at low solar zenith angles at this time

Chapter 2 Abstract

We present observations of proton aurora at Mars made using the Imaging UltraViolet Spectrograph (IUVS) onboard the Mars Atmosphere and Volatile Evolution (MAVEN) spacecraft. Martian proton aurora display a prominent intensity enhancement in the hydrogen Lyman-alpha ($\text{Ly-}\alpha$) (121.6 nm) emission between ~110-150 km altitude. Using altitude-intensity profiles from periapsis limb scan data spanning nearly two Martian years, we create a comprehensive database of proton aurora and characterize their phenomenology. Due to Mars' lack of a global dipole magnetic field, Martian proton aurora are expected to form on the dayside via electron stripping and charge exchange between solar wind protons and the neutral corona. We observe proton aurora in ~14% of dayside periapsis profiles (with notable seasonal variability), making proton aurora the most commonly observed type of aurora at Mars. We determine that the primary factors influencing proton aurora occurrence rates are solar zenith angle (SZA) and season. The highest proton aurora occurrence rates are at low SZAs on the Mars dayside, consistent with known formation processes. Proton aurora have highest emission enhancements, peak intensities, peak altitudes, and occurrence rates (nearing 100%) around southern summer solstice. This time period corresponds with the seasonal inflation of the neutral

lower atmosphere, the onset of Martian dust storm season, seasonally increased coronal hydrogen column densities, and higher atmospheric temperature and solar wind flux following perihelion. The results of our study provide a new understanding of the primary factors influencing proton aurora, and the long-term variability of these phenomena as observed over multiple Mars years.

2.1 Introduction

Proton aurora have long been theorized to exist at Mars (*e.g.*, Kallio *et al.*, 1997; Kallio and Barabash, 2001), and have only recently been identified in orbital data (Deighan *et al.*, 2018; Ritter *et al.*, 2018). Using data from the Solar Wind Ion Analyzer (SWIA) (Halekas *et al.*, 2013) onboard the Mars Atmosphere and Volatile Evolution (MAVEN) spacecraft (Jakosky *et al.*, 2015), Halekas *et al.* (2015) observed a population of protons with the same energy and velocity as the incident solar wind that had penetrated to atmospheric altitudes below the Martian bow shock and magnetic pileup boundary (MPB) (*i.e.*, penetrating protons), and speculated that these might be associated with proton aurora.

Deighan *et al.* (2018) used data from the Imaging UltraViolet Spectrograph (IUVS) (McClintock *et al.*, 2015) onboard MAVEN to show that the penetrating proton population observed by Halekas *et al.* (2015) in SWIA *in situ* data were correlated with spectroscopic observations of emission enhancements in hydrogen Lyman-alpha ($H Ly-\alpha$) emission profiles (*i.e.*, the ultraviolet (UV) signature of proton aurora) (*e.g.*, Figure 2.1). Ritter *et al.* (2018) presented observations of proton aurora using UV data from the Spectroscopy for the Investigation of the Characteristics of the Atmosphere of Mars (SPICAM) spectrograph onboard the Mars Express spacecraft. The combination of these two previous UV observational studies provided fewer than ten examples of definitive Martian proton aurora detections. We expand on

these previous studies to include the entire IUVS dataset (spanning nearly two Martian years), identifying over four thousand new proton aurora detections and characterizing their phenomenology and variability over time.

Proton aurora on Earth were first observed by *Vegard* (1939) as doppler shifted hydrogen Balmer-alpha and -beta spectral lines within other auroral emissions. These phenomena were later characterized in detail in a review paper by *Eather* (1967). At Earth, proton aurora are strongly influenced by our planet's magnetosphere: protons are directed along Earth's magnetic field lines and deposited in an annular auroral region around the magnetic poles, where they create proton aurora.

The formation process of proton aurora at Mars is notably different than at Earth. Because hydrogen is the lightest constituent of the Martian upper atmosphere, the H corona is the most extended portion of the exosphere and influences initial interactions with the solar wind. The lack of a Martian global intrinsic magnetic field allows the solar wind to interact with the H corona on the sun-ward facing side of Mars before reaching the bow shock and being diverted around the planet by the magnetic structure of Mars' near-space environment (*i.e.*, the induced magnetic field; *e.g.*, *Akalin et al.*, 2010). Martian proton aurora form when solar wind protons strip electrons from H atoms in the extended corona and convert into energetic neutral atoms (ENAs) (*e.g.*, *Kallio and Barabash*, 2001). The thermal H⁺ ions produced in this way are then picked up by the solar wind convection electric field and mostly escape Mars' gravity (*e.g.*, *Rahmati et al.*, 2017). The created H-ENAs pass unimpeded through the bow shock and MPB and subsequently undergo additional charge exchanges and collisions with neutrals in the lower atmosphere. In so doing, the energetic hydrogen atom can be excited and emit Lyman alpha photons, creating proton aurora (Figure 2.1, left). Note that unlike typical aurora, where the

background gases emit, in this case it is the precipitating particle that emits. Martian proton aurora are expected to be confined to the dayside of the planet and not to exhibit the latitudinal constraints that exist at Earth. Moreover, as a result of the strong dependence on charge exchange processes with coronal H, any variations in the H corona or solar wind flux will inevitably affect proton aurora.

The dominant source of Ly- α at Mars is solar resonant fluorescence of H in the corona; the proton aurora emission appears on top of a broad, diffuse background emission from coronal H. Consequently, the typical non-auroral coronal H Ly- α altitude profile is relatively flat due to the diffusive separation of H from CO₂ above the homopause, the relatively large scale height of H in the Martian atmosphere, and the optically thick nature of Ly- α . By contrast, the Ly- α proton aurora emission is optically thin and Doppler shifted out of the thermal H distribution (the Doppler shift not resolvable in our dataset). Thus, proton aurora are identifiable in UV spectral data as an emission enhancement of intensities between ~110-150 km in the Ly- α altitude-intensity profile (compare in Figure 2.1). The emission is sharply peaked due to the energy deposition process, and the enhancement altitude range is consistent with previously determined predictions of the peak altitude of energy deposition for protons and H in the Mars atmosphere (*e.g.*, Halekas *et al.*, 2015; Deighan *et al.*, 2018).

In this study we focus on Martian proton aurora, which is one of three types of aurora at Mars, in addition to discrete (Bertaux *et al.*, 2005) and diffuse aurora (Schneider *et al.*, 2015). Studying Martian aurora can help us better understand how the Sun interacts with the upper atmosphere and near-space plasma environment of Mars. Studying proton aurora in particular can provide insight into the solar wind's direct interactions with Mars' extended hydrogen corona, and how these interactions change over time and with different influencing factors.

Moreover, this knowledge can also inform our understanding of the sun's interactions with other planetary bodies which we might not be able to directly observe, particularly those with a neutral hydrogen corona and no global magnetic field.

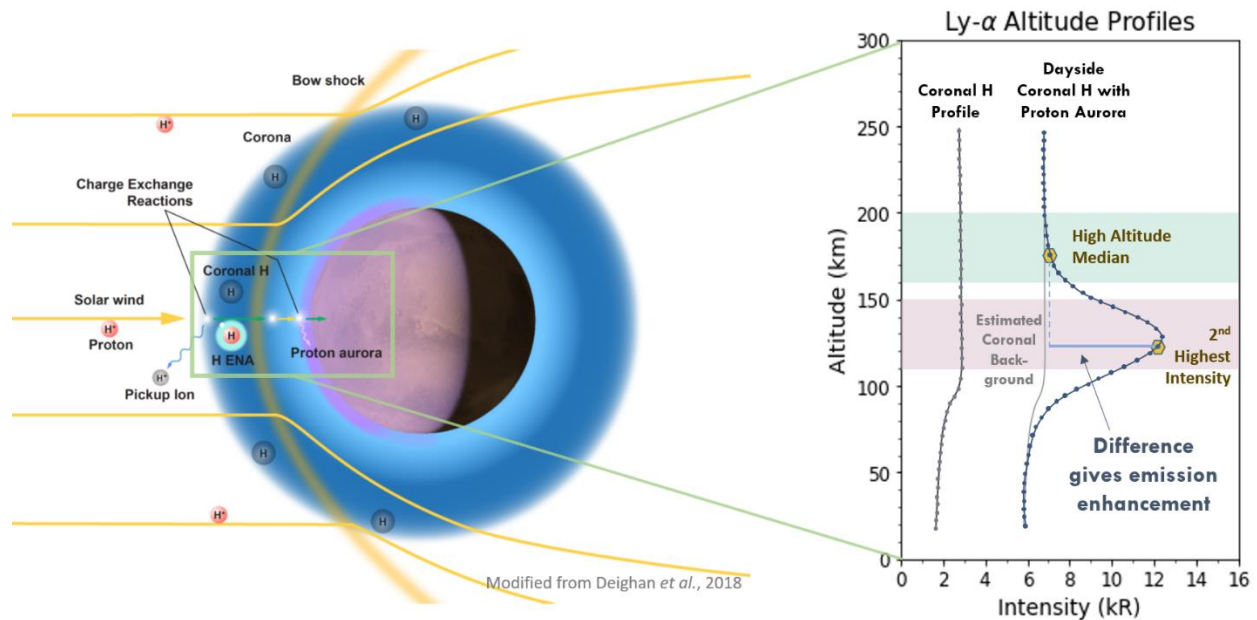


Figure 2.1: (Left): Proton aurora formation mechanism (modified from Deighan et al., 2018) showing how solar wind protons charge exchange with coronal H and convert to energetic neutral atoms (ENA) which pass unimpeded through the bow shock and subsequently charge exchange again to convert back into protons and deposit energy in the lower atmosphere as proton aurora. (Right): Example H Lyman- α altitude profile for coronal H (dark grey) and profile with proton aurora detection (blue) including a heuristic estimated coronal background profile for reference (light grey) (note that the background coronal profile is not distinguishable from proton aurora in the data). We detect and characterize proton aurora using the method indicated in the figure, where the second highest intensity in the peak altitude range is subtracted from the high altitude median of a profile; emission enhancement differences above a predetermined threshold (described in Figure 2.2) are considered detections.

2.2 Data and Methodology

2.2.1 Data

We use data from the IUVS instrument onboard the MAVEN spacecraft. IUVS has a Far-Ultraviolet (FUV) (110-190 nm) and Mid-Ultraviolet (MUV) (180-340 nm) channel (McClintock et al., 2015). We specifically use IUVS FUV limb scan data (taken during periapsis), to generate altitude-intensity profiles of the hydrogen Ly- α emission at 121.6 nm. (See supplementary material for more information about limb data and altitude-intensity profile creation). We

examine data spanning ~2 Martian years (from MAVEN arrival in October 2014 through August 2018), covering a wide range in season, geographic location, and SZA. In this study, we use standard periapsis Level-1C altitude-binned intensity data products, which give H Ly- α profiles for all periapsis data. The generation of these products is further described in Chapter 1, and in greater detail in the IUVS Software Interface Specification document (SIS).

2.2.2 Methodology

We began our study by searching for the characteristic proton aurora emission enhancement via visual inspection of Ly- α altitude profiles in the IUVS dataset. These results were later used to assess the effectiveness of multiple automated detection methods and to determine the most reliable method. We first tested the detection methods used by *Deighan et al. (2018)* and *Ritter et al. (2018)*. In the *Ritter et al. (2018)* detection method, the integral of the emission enhancement feature (*i.e.*, the area under the altitude-intensity curve) between 120-150 km in an altitude profile is compared to the area under the curve between 160-190 km; if the ratio of these areas is ≥ 1.1 (signifying a $\geq 10\%$ emission enhancement), the observation is considered a detection. With the *Deighan et al. (2018)* method, an observation is considered a detection if the difference between the median value in the 120-150 km range and the median value in the 160-190 km range is larger than 5 median absolute deviations away from the high altitude median.

By comparing the results of numerous methods, we found that the detection method most effective at accurately identifying proton aurora in IUVS data is a modified version of the *Deighan et al. (2018)* method. In this method, proton aurora are identified by: 1) separating the data of an altitude-intensity profile into high altitude (160-200 km) and peak altitude (110-150 km) data regions (Figure 2.1); 2) taking the difference between the second highest intensity

value from the peak altitude data region and the median intensity value from the high altitude data region; and 3) comparing the difference values for profiles from the entire dataset against a statistically determined threshold value (in this study, the mean plus 0.5 standard deviations, as discussed below). We use the second highest peak intensity in the difference to minimize false detections caused by cosmic ray hits on the instrument detector or other anomalous events that occur in a single altitude bin. Profiles with difference values greater than the threshold are considered detections, while those below the threshold are not (Figure 2.2).

Due to the typical lack of an airglow peak in the Ly- α profile, the mean and median of the emission enhancement values of all profiles in the dataset are close to zero. Figure 2.2 (top left) shows a histogram of emission enhancement values for the entire dataset. The proton aurora events with the largest emission enhancement differences are on the far-right side of the histogram (*e.g.*, orbits 4107, 4224, and 4235; profiles shown in Supplementary Figure 2.1).

To assist in identifying an appropriate proton aurora detection threshold, we plot normalized percentile-binned altitude profiles of the dataset (Figure 2.2, right). In creating these profiles, we first normalize each IUVS profile to account for variations in coronal H intensity caused by differing observation illumination conditions. In normalizing, we subtract out the low altitude median intensity (median between 50-100 km) from every intensity value in a profile; we then divide these intensities by the absolute value of the difference between the very high altitude median intensity (median between 175-225 km) and the low altitude median intensity. This makes the profiles run from zero to one, with a possible enhancement above one in the presence of proton aurora. Every normalized profile in the IUVS dataset is then binned based on the value of the emission enhancement associated with the profile, with one bin for each percentile enhancement, resulting in an altitude-intensity profile for each bin. The median

intensity values with respect to altitude are calculated for each percentile bin. This produces 100 median percentile-binned profiles. The strongest proton aurora detections are therefore shown in the highest percentile bin profiles. This characteristic enhancement due to proton aurora is clearly evident down to the ~90th percentile profile, where profiles become indistinguishable from neutral coronal H profiles. This trend indicates that the 90th percentile is an appropriate cutoff to use as a detection threshold for proton aurora.

Figure 2.2 (bottom left) shows that proton aurora can be identified as a tail of high enhancements attached to a symmetric underlying distribution. The figure compares positive and negative emission enhancement values to approximate the shape of the emission enhancement histogram (Figure 2.2, top left) in the absence of proton aurora events. The enhancement histogram in Figure 2.2 (top left) exhibits a positively skewed (non-Gaussian) distribution, where the asymmetric shape on the right-hand side is caused by the occurrence of proton aurora. It is likely that this histogram would be symmetric in the absence of proton aurora events. Using this assumption, we can identify an independent criterion for a proton aurora detection threshold. It is apparent in Figure 2.2 (bottom left) that ~0.5 standard deviations (σ) from the mean is approximately where positive and negative histogram values begin to diverge. Above this value, an individual measurement is far more likely to be a proton aurora event than part of a symmetric statistical distribution, making 0.5σ an appropriate detection threshold. Further supporting the choice of a 0.5σ threshold is the fact that 0.5σ from the mean corresponds with nearly the same difference value as that of the 90th percentile of the dataset, identified independently from the median-binned profiles. Thus, based on these two independently consistent determinations of a proton aurora detection threshold value, we use 0.5σ as our

detection threshold in this study. Note that σ in this context is simply a mathematical description of the underlying distribution and does not carry the usual connotation of statistical significance.

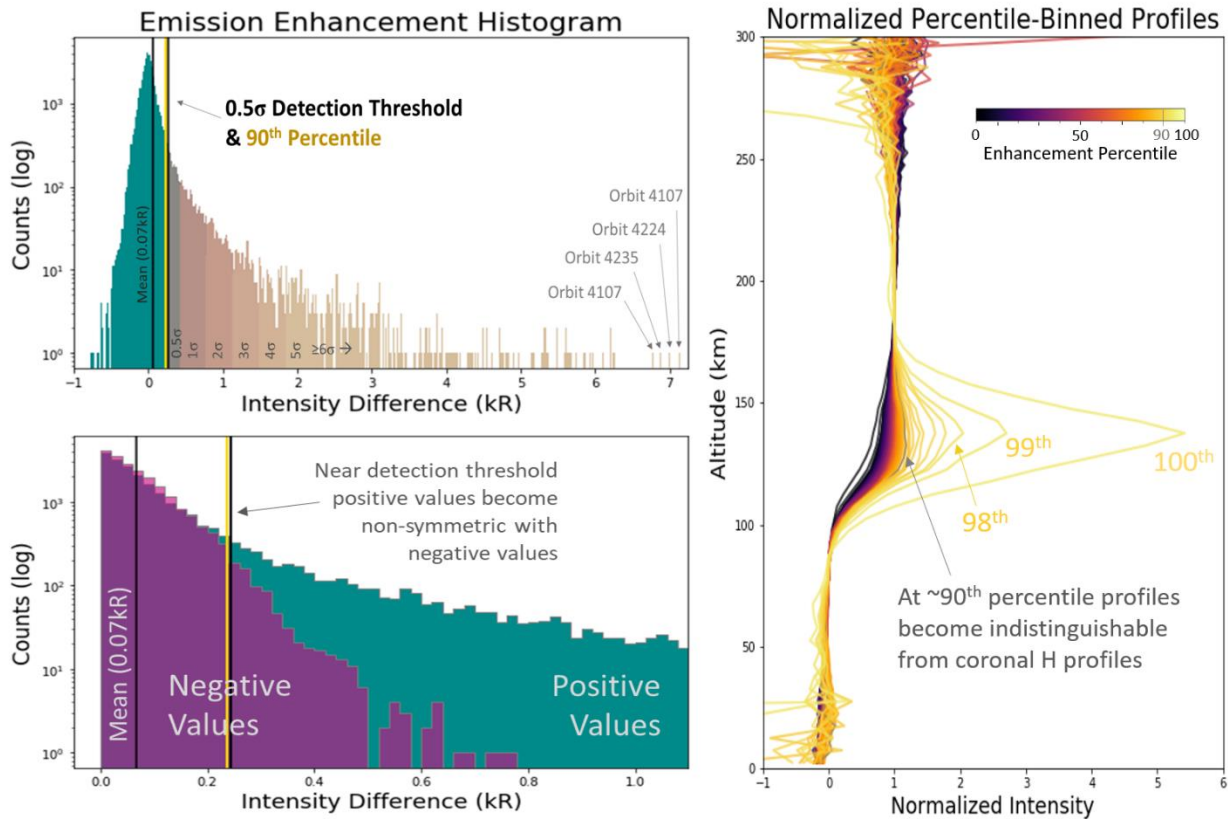


Figure 2.2: Detection methodology and threshold selection. (Top Left): Histogram of emission enhancement differences (as defined in Figure 2.1) of all H profiles in dataset. Chosen detection threshold is Mean + 0.5σ (which also closely coincides with the 90th percentile). (Bottom Left): Negative histogram values overlain on top of positive; note that positive values become non-symmetric with negative values near detection threshold, suggesting an appropriate threshold choice. (Right): Normalized percentile-binned altitude profiles; each profile represents median intensities from every emission enhancement percentile bin. An enhancement is prominent where proton aurora occur, and profiles become indistinguishable from coronal H profiles near ~90th Percentile. Using two independent criteria we establish a rigorous detection threshold for proton aurora.

2.2.3 Sensitivity to Detection Threshold

It is not always possible to determine the existence of proton aurora in a profile with absolute certainty (e.g., due to lower intensity events or very shallow emission enhancement features). Consequently, any chosen detection method will inevitably involve a threshold which excludes some potential proton aurora events and/or includes borderline detections. Our method,

like all other methods (*e.g.*, that of *Deighan et al. (2018)* or *Ritter et al. (2018)*), will therefore inevitably include/exclude some marginal detections and non-detections.

To assess the validity of our chosen 0.5σ threshold, we also tested numerous larger detection thresholds on the dataset. In Figure 2.3 we present histograms of the entire IUVS limb dataset over-plotted by histograms for proton aurora detections using both a 0.5σ threshold and a 3σ threshold. We include a 3σ threshold not because it is statistically significant for a non-normal distribution, but rather because there are no corresponding negative values in this histogram range and the identification of proton aurora events above this threshold value is certain. The detection threshold histograms are nearly identical in shape, differing only in their total number of counts. The 0.5σ threshold histogram on average has an order of magnitude more detections than the 3σ , as it includes most all plausible proton aurora detections; alternatively, the 3σ threshold is more selective, only including the brightest proton aurora detections. The close similarities between the detection threshold histograms demonstrates that the results of our study are not significantly impacted by the choice of a detection threshold. We therefore use the detection threshold of 0.5σ , so as to include both bright and faint events, and to thereby obtain the best statistics on the occurrences and phenomenology of proton aurora.

We have investigated the robustness and possible biases of our chosen methodology's ability to account for seasonal variations of the neutral CO_2 atmosphere (*e.g.*, *Jain et al., 2015*; *Bougher et al., 2017*). The peak altitude range for proton aurora (110-150 km) encompasses the majority of airglow peak altitudes observed by IUVS; thus, variations in the neutral atmosphere will also affect the altitude of peak energy deposition for H and protons. Our selected methodology uses a single threshold value to identify proton aurora throughout an entire dataset, irrespective of any variations that might influence the shape and intensity of the altitude profiles

(*e.g.*, intensity variations due to season or SZA). Using a single detection threshold could in some cases cause proton aurora events with relatively small emission enhancement values to go undetected (*e.g.*, a profile with a shallow peak). By using a 0.5σ threshold, we include even the comparatively small proton aurora events, thereby minimizing potential omissions associated with this method. And although the threshold value varies slightly when different data are included/excluded from the study (due to small changes in the standard deviation and mean), any statistical changes in the dataset are minimal and do not significantly impact the scientific results (as determined by including new data in our study as the mission progressed). Consequently, we find our chosen methodology to be most effective at automatically identifying proton aurora events in the dataset (having more positive detections and fewer false detections when compared with other methods).

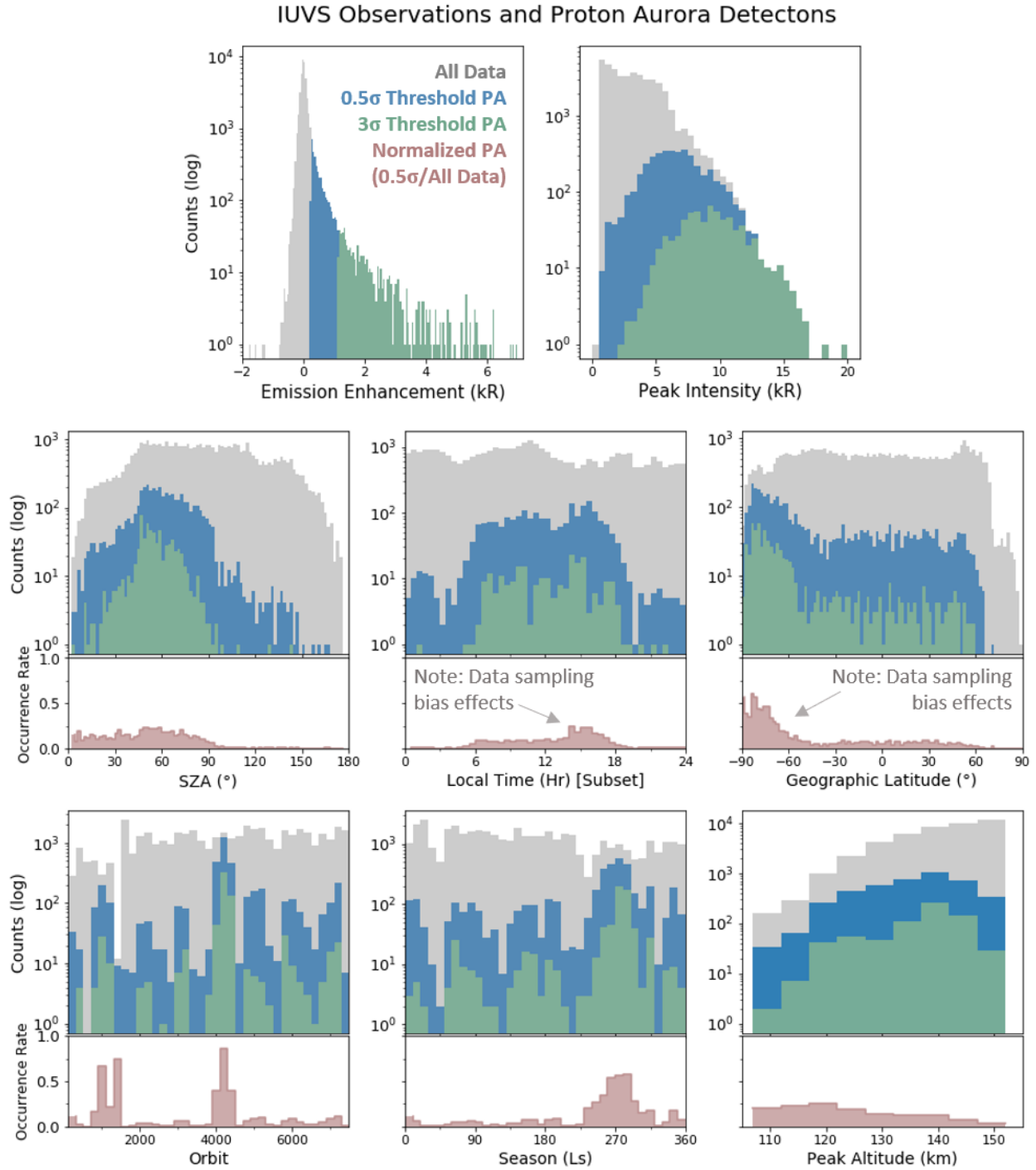


Figure 2.3: Histograms of all IUVS data (grey) and proton aurora detections using 0.5σ threshold (blue) and 3σ threshold (green) as a function of different observational variables. In each sub-panel we present normalized proton aurora detections showing occurrence rates (pink). Occurrence rates are determined by dividing 0.5σ detection counts by all data counts in each histogram bin. Note that potential data sampling biases affect the local time and geographic latitude histograms, and local time data have been subset to include only low- and mid-latitude data (discussed further in text). Highest proton aurora occurrence rates are observed on the dayside at low SZAs and around L_s 270 (southern summer solstice).

2.3 Proton Aurora Phenomenology and Variations

The normalized proton aurora histograms in Figure 2.3 (pink subplots) represent proton aurora occurrence rates. In creating these normalized histograms, values from proton aurora detection histograms have been divided by values in each bin from the entire dataset histograms. The highest proton aurora occurrence rates are correlated with low peak SZAs, daytime local times, peak altitudes between 110-120 km, and southern summer solstice (solar longitude, L_s , 270). There are apparent peaks in the occurrence rate histograms with respect to local time and latitude (Figure 2.3) in the late afternoon and near the southern pole; however, we note that these peaks are likely the result of a data sampling bias due to spacecraft observation location during certain seasons (explained in detail below). The largest emission enhancements are observed in orbits 4107, 4224, and 4235 (Figure 2.2), and occur around southern summer solstice (altitude-intensity profiles for these orbits are presented in Supplementary Figure 2.1).

2.3.1 Proton Aurora Correlations and Occurrence Rates: SZA, Season, Local Time, and Altitude Dependence

Figure 2.4 displays normalized histograms of proton aurora occurrence rates throughout the MAVEN mission. Note that the cyclic oscillations in peak intensity, SZA, and latitude are due to the precession of the MAVEN orbit, which changes the location of the spacecraft periapsis over time. The highest occurrence rates correspond with low SZAs, on the dayside ($< \sim 100^\circ$). Additionally, the highest occurrence rates are observed around orbits 1000 and 4200. These two orbit ranges occur near $L_s \sim 270$ (we note that daytime data are not available immediately before or during $L_s \sim 270$ near orbit 1000). During this season, proton aurora emission enhancements and peak intensities exhibit some of the highest observed values throughout the mission (as high as 7kR and 20 kR, respectively), reaching nearly three times

higher than average values in other seasons. Further, high occurrence rates primarily occur at low peak altitudes (110-130 km), with the notable exception being near southern summer solstice when high occurrence rates are observed at significantly higher altitudes (ranging between 110-150 km). This is coincident with the inflation of the lower atmosphere during this season.

In Figure 2.5 we present correlations between select variables for the entire dataset. We observe a strong correlation between low SZAs and high peak intensities (Figure 2.5A), confirming observations of high proton aurora intensity occurrence rates. (Note that apparent bands in intensity in Figure 2.5A are due to the precession of the MAVEN orbit causing the location of the periapsis to change during different seasons and SZAs.) We also observe a correlation between low SZAs and high emission enhancements for proton aurora events (Figure 2.5B). We find that proton aurora emission enhancements and peak intensities reach a maximum around southern summer solstice (Figure 2.5 D and E), further confirming previously identified seasonal trends in occurrence rates. Additionally, expanding on our findings of peak altitude occurrence rates, we find that proton aurora profiles have the highest peak altitudes and the largest range of altitudes (compared to other seasons) around southern summer solstice (Figure 2.5F and Supplementary Figure 2.2). (Note that altitude gaps in Figure 2.5F are due to the 5 km altitude binning of IUVS Level 1C data products.)

Proton aurora primarily occur during daytime local times, with an apparent peak in the late afternoon (Figure 2.3, Figure 2.4 and Figure 2.5C). We note that the data in local time plots presented herein have been subset to include only low- and mid-latitude data (*i.e.*, within $\pm 60^\circ$ of the equator), as local times near the poles during summer/winter are not physically meaningful (comparison local time plots which include the entire dataset can be found in Supplementary Figure 2.3). Around southern summer solstice, the highest proton aurora occurrence rates with

respect to local time occur in the afternoon near orbit 1000 and span a range of dayside times near orbit 4200 (Figure 2.4). The peak in occurrence rate around local time 15:00Hr in Figure 2.3 is likely due to an abundance of data at this local time during southern summer (see Figure 2.4 and Supplementary Figure 2.4). And the few apparent proton aurora detections at local times in the nighttime are primarily at high latitudes during local hemispheric summer (see Supplementary Figure 2.4). Thus, we do not identify any proton aurora dependence on local time, but rather, only a dependence on dayside occurrence, which is more appropriately characterized by SZA.

We note that although the highest proton aurora peak intensities, emission enhancements, and occurrence rates are observed near southern summer solstice, we also observe some high values for all of these variables throughout the rest of the year (*e.g.*, just after orbit 3000 and before orbit 6000 in Figure 2.4). Enhancements and peak intensities of proton aurora are, however, much smaller during other times of the year. Further, the high occurrence rates that do not occur near L_s 270 tend to be short-lived, typically spanning only weeks, rather than months at a time when observed around L_s 270. These events are likely correlated with either increased solar activity or regional/global dust activity on the planet (explained in more detail in the Discussion section).

Figure 2.6 shows proton aurora detection and occurrence rate plots (similar in style to those of Figure 2.3) that are further binned to identify variations in season and latitude. The lack of data at low SZAs in many bins in Figure 2.6 (*i.e.*, beige regions in occurrence rate plots) makes it challenging to determine occurrence rates near the subsolar point. Proton aurora occurrence rates with respect to SZA reach nearly 100% around L_s 270 in the southern hemisphere, providing quantitative confirmation of the seasonal increase in occurrence rates

described above. During this season and latitude, the SZA histogram exhibits the expected shape of a proton aurora SZA histogram: having highest occurrence rates at low SZAs and dropping off sharply at higher SZAs. We also observe high occurrence rates (>60%) and a similar decreasing histogram shape at mid-latitudes during this season. While the majority of bins have lower occurrence rates (averaging ~25%, with the exception of the before-mentioned L_s 270 season), an apparent exception to the very low occurrence rates outside of L_s 270 may be the southern and mid-latitude plots in the L_s 360 bins, having occurrence rates between 40-50%. Although these rates are still far below the highest values observed near L_s 270, they are likely due to the extended period of high occurrence rates near orbit 1000 (see Figure 2.4), which began just after L_s 270 and continued into the beginning of L_s 360; hence, these are associated with a prolonged period of proton aurora events at the end of southern summer.

2.3.2 Variables with No Apparent Correlations: Geographic Location and Spacecraft

Observation Parameters

Due to the minimal data available at northern latitudes and low SZAs during the L_s 270 season (and because there are far fewer total data counts in the mid-latitude bin in Figure 2.6), it would be inaccurate to infer a latitudinal dependence from Figure 2.6. High occurrence rates in the orbit 1000 range are from mid-latitude data, and southern latitude data in the orbit 4200 range. Because the MAVEN spacecraft periapsis was primarily located in the southern hemisphere around L_s ~270, when the highest proton aurora rates occur, comparable periapsis data for northern hemispheric summer months are not abundant. This data bias, therefore, gives the appearance of a latitudinal dependence that likely does not exist (*e.g.*, Figure 2.3 and Figure 2.4). We further discuss the geographic dependence of proton aurora (or rather, lack thereof) in the Discussion section.

Ritter et al. (2018) proposed that spacecraft observational parameters such as spacecraft altitude might play a role in the detectability and observed intensities of proton aurora. We do not observe any dependence on spacecraft altitude, or tangent point distance for proton aurora occurrence or intensity.

2.3.3 Atypical Proton Aurora Detections

In addition to the typical proton aurora events outlined thus far (which usually have continuous detections in all similar SZA swaths within an orbit), we also observe many instances of proton aurora which only display detections in a few discontinuous mid-orbit swaths, which we refer to as “variable” proton aurora. This type of proton aurora has recently been found to be potentially associated with transient layers in the Martian ionosphere (*Crismani et al.*, 2019). Similar variations in proton aurora have also been observed on Earth and are often referred to as “pulsating” proton aurora (*e.g.*, *Eather*, 1967; *Nomura et al.*, 2016; *Ozaki et al.*, 2016). It remains uncertain based on current observations of these features at Mars whether they vary spatially and/or temporally, as there is plausible evidence suggesting both. More work needs to be done to unambiguously determine the frequency of these events in the dataset, and to characterize the driving factors for this type of variation.

Finally, we note that a small number of proton aurora events have been identified on the nightside of the planet (*e.g.*, Figure 2.3 SZA subplots, Figure 2.6, and Figure 2.5C). Work is ongoing to better understand the formation mechanisms responsible for producing nightside Martian proton aurora, but a detailed assessment of these events is beyond scope of what we present in this study. We defer discussion of nightside proton aurora to a forthcoming paper.

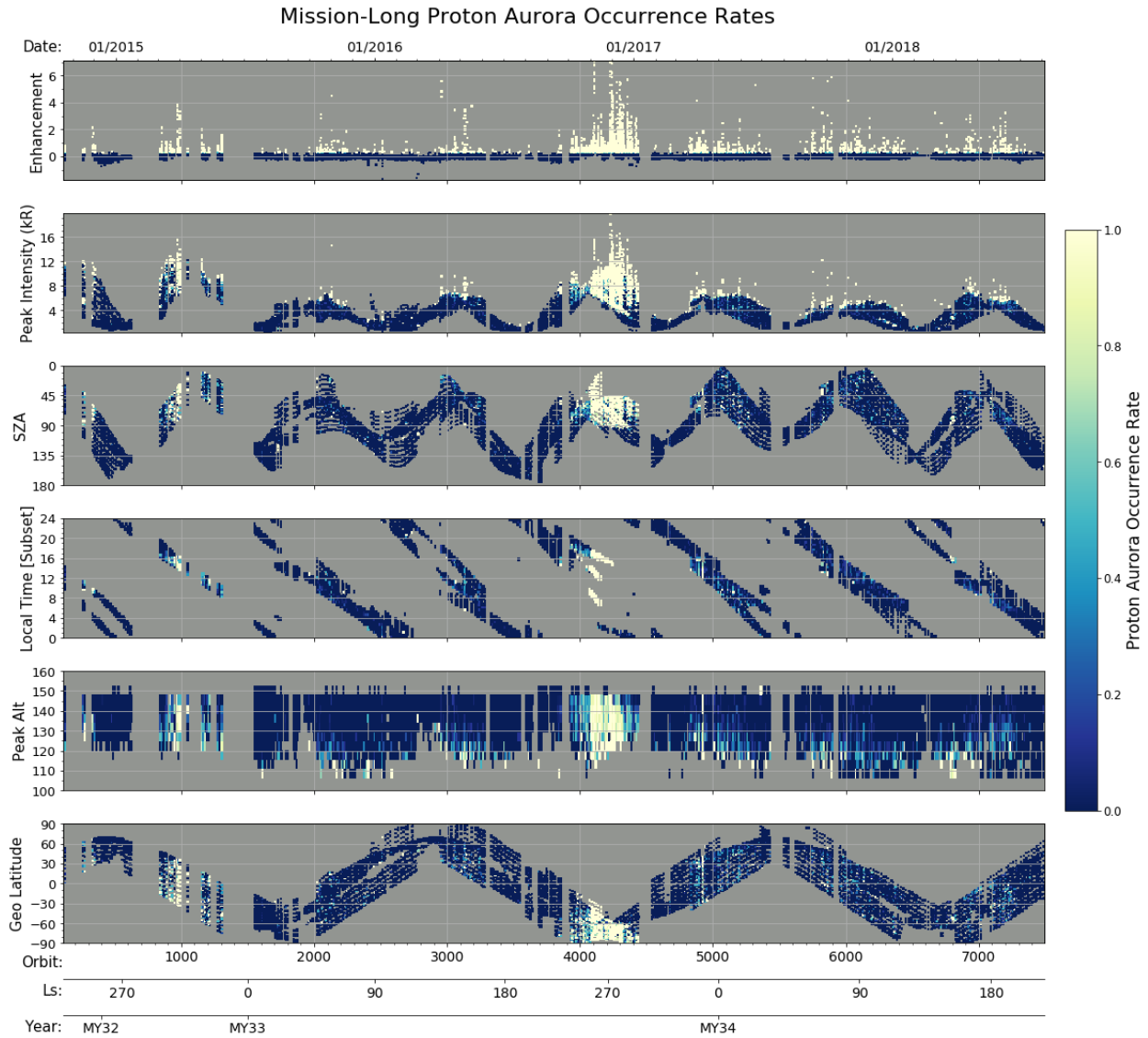


Figure 2.4: Normalized 2-D histograms showing proton aurora occurrence rates as a function of different observational variables and MAVEN orbit (occurrence rates determined as in Figure 2.3). Note that local time data have been subset to include only low- and mid-latitude data (discussed further in text). Highest occurrence rates, emission enhancements, peak intensities, and peak altitudes are observed around southern summer solstice ($L_s \sim 270$), and correspond with low SZAs (i.e., daytime occurrences).

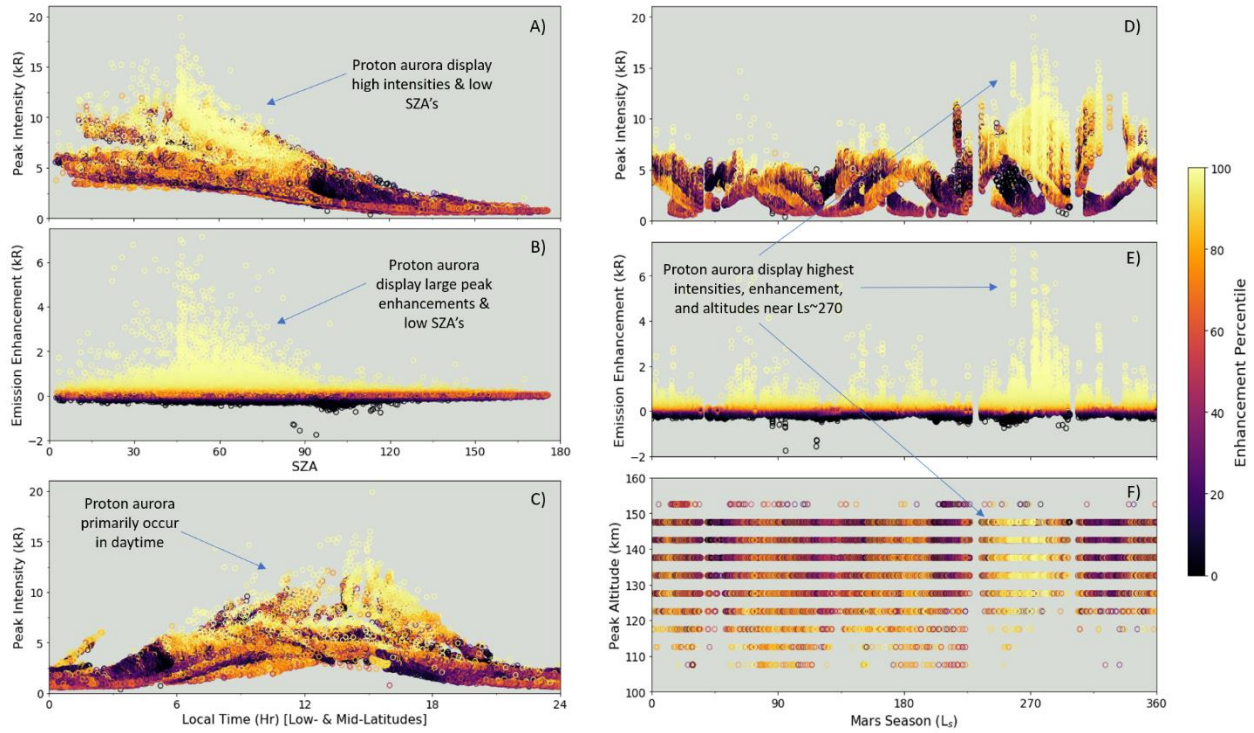


Figure 2.5: Proton aurora variations with respect to SZA (A&B), local time (C), and season (L_s) (D-F). Color represents emission enhancement percentile bin (as in Figure 2.2, right), and proton aurora detections correspond with percentiles greater than $\sim 90^{\text{th}}$ percentile. Note that local time data have been subset to include only low- and mid-latitude data (discussed further in text). Proton aurora display high intensities, large peak enhancements, and low SZAs (occurring in daytime), and display highest intensities, enhancement, and altitudes near southern summer solstice ($L_s \sim 270$).

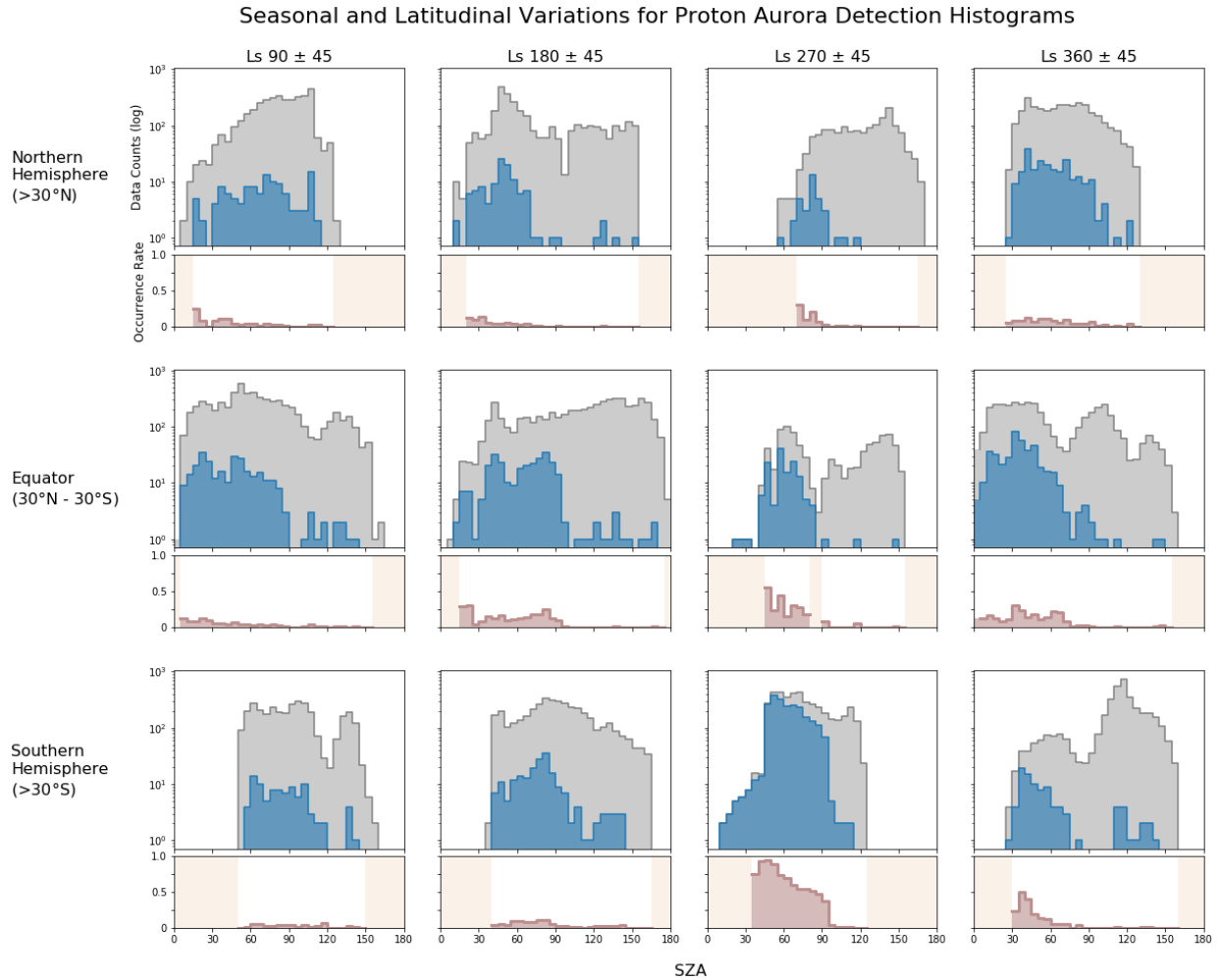


Figure 2.6: Seasonal and latitudinal variations of SZA for proton aurora. Horizontal bins correspond with latitude (60° bin size) and vertical bins with Mars season (90° bin size, around each major season). Top plots: All IUVS data (grey) and proton aurora detections (blue). Bottom subplots: Proton aurora occurrence rates (pink) (occurrence rates determined as in Figure 2.3). Beige areas on normalized subplots represent bins where the total number of counts is less than or equal to ten. Note that apparent latitudinal dependence is likely due to a data sampling biases (discussed further in text). Occurrence rates reach nearly 100% at low SZAs around southern summer solstice (L_s 270).

2.4 Discussion

In this study we determine occurrence rates and seasonal variations of Martian proton aurora for the first time. We identify proton aurora detections as profiles with an enhancement difference greater than a chosen threshold. Using a detection threshold of 0.5σ plus the mean, we identify proton aurora detections in 9.7% of IUVS altitude-intensity profiles from 26.5% of orbits (corresponding with detections in 4254 of all profiles from 1074 different orbits). When

considering only dayside profiles (*i.e.*, $SZA < 105$), the detection rate increases to 14.1%, with notable seasonal variability (*e.g.*, annual proton aurora occurrence rates with respect to SZA ranging between ~25-100%). By comparison, IUVS has detected diffuse aurora on Mars in a few percent of orbits with favorable geometry (based on *Schneider et al.*, 2018, and references therein); and discrete aurora detections are rarer still in the IUVS dataset. Based on these results, we find that proton aurora are currently the most commonly observed type of aurora at Mars.

The two factors having the largest influence on proton aurora intensity and occurrence rate are SZA and season. The highest emission enhancements, intensities, peak altitudes, and occurrence rates are all observed around southern summer solstice, and occurrence rates are highest at low $SZAs$ (on the planet's dayside) (Figure 2.3, pink subplots). Occurrence rates approach 100% in southern summer at low $SZAs$, and average less than 25% (peaking at 25-50%) during other seasons. A correlation between proton aurora occurrence rate and low $SZAs$ was expected based on the ENA-driven formation process (confining proton aurora to the Mars dayside). *Kallio and Barabash* (2001) predict a quantitative dependence on SZA in modeled correlations of SZA with precipitating H atom particle flux and energy flux; it is tempting to compare this dependence to our occurrence rates but due to the differences in observed variables, these cannot be directly quantitatively compared. A closer (though still incomplete) qualitative comparison to the *Kallio and Barabash* (2001) predictions would be Figure 2.5A, which shows the peak intensity of H-ENAs from proton aurora (yellow data points) falling off as a function of SZA .

2.4.1 Dependence on Local Time, SZA , and Induced Magnetic Field

We do not observe any correlation in our dataset between proton aurora and dawn/dusk local times. However, we might expect these asymmetries to exist based on dawn-dusk

asymmetries in other geophysical parameters such as those predicted via modeling of H density and escape flux (*Chaufray et al., 2015*), as well as for the induced magnetic field (*Liemohn et al., 2017; Fang et al., 2018*). These factors are expected to create a bulge in H at the dawn or dusk terminator that alternates between the terminators with changing season and/or solar cycle. Such variations could indeed lead to a local time dependence for proton aurora. We note that there is a lack of data spanning all local times for latitudes/seasons when an observed region is not continually illuminated by sunlight (*i.e.*, most proton aurora data are from the poles during local summer). Case studies spanning a larger range of local times and diurnal illumination conditions would need to be conducted in order to determine a dependence on local time with certainty.

The shape of the histogram of proton aurora occurrence rate with respect to SZA in Figure 2.3 does not follow the predicted decreasing trend with highest occurrences near the sub-solar point, and motivates further examination of the factors controlling the occurrence rate with respect to SZA. Since most of the histograms in Figure 2.6 have very low occurrence rates at low SZAs (when sufficient data exist), it is possible that some mechanism is responsible for suppressing proton aurora occurrence at low SZAs. One possible mechanism is given by *Gerard et al. (2019)*, who model Martian proton aurora under varying induced magnetic field intensities and orientations. They show that the magnitude and direction of the induced magnetic field at Mars can lead to a magnetic barrier effect, stopping protons from penetrating into the atmosphere. Prior studies have measured an induced field around Mars with a magnitude that is inversely dependent on SZA and reaches values as high as 40nT near the sub-solar point (*e.g.*, *Brain et al., 2003; Akalin et al., 2011*). Based on the results of their modeling, *Gerard et al. (2019)* predict that this SZA-dependent induced magnetic field could lead to a lack of proton aurora near the sub-solar Mars point, where magnetic field intensities are highest. Thus, we may be

observing the SZA effects of this field on proton aurora occurrence rate in our dataset, leading to suppressed occurrence rates at low SZAs in the SZA histogram of Figure 2.3. *Gerard et al.* (2019) also note that deviations in orientation from a horizontal induced magnetic field can guide protons deeper into the atmosphere rather than act as a magnetic barrier. During times of southern summer observations, when we observe the expected decreasing SZA histogram shape (Figure 2.6), it is possible that the induced magnetic field may have had a different magnitude or orientation favoring proton penetration at low SZAs; however, as the likelihood of favorable magnetic field conditions only during this season is small, we do not expect this to be the case. Another explanation is that the histogram shape during this time period is due to the much higher occurrence rates in this season relative to other seasons (*i.e.*, nearing 100% in southern summer versus <25% in most other seasons), allowing the shape of the histogram to be more clearly discerned.

In addition to SZA effects on proton aurora, *Gerard et al.* (2019) also demonstrate that both the presence of a horizontal induced magnetic field and the ratio of H^+ /H-ENAs in the incident beam can significantly decrease the intensity and peak altitude in a proton aurora altitude-intensity profile. They also find that a horizontal induced magnetic field, which leads to the magnetic barrier effect and blocks proton precipitation, would slightly widen the Ly- α spectral line. While we do not address the influence of local magnetic field strength and orientation in our study, changes in the peak altitude and intensity of a profile are detectable in IUVS data. However, it is worth noting that emission feature spectral line shape effects are below the resolution of IUVS so line broadening would not be observable in our dataset, and H^+ /H-ENA ratios cannot be determined using currently available MAVEN data. While individual case studies may reveal these effects, our current statistical study does not. In a future study, we

intend to constrain the effects of variability in the interplanetary magnetic field (IMF) and induced magnetic field, as well as that of the remanent crustal magnetic fields on the distribution of Martian proton aurora detections.

2.4.2 Seasonal and Intermittent Drivers on Proton Aurora

Below we discuss some additional drivers that influence Martian proton aurora magnitude and variability on short and long timescales. As with all planetary aurora, increased solar activity affects the intensity of Martian aurora. Proton aurora and penetrating protons have been previously found to be associated with high solar wind flux and solar events such as coronal mass ejections (*e.g.*, *Deighan et al.*; 2018, *Ritter et al.*, 2018; *Halekas et al.*, 2015).

We observe the highest annual proton aurora intensities near southern summer solstice (L_s 270), rather than immediately following perihelion (L_s 250). Due to Mars' highly elliptical orbit, the planet is ~ 0.3 AU closer to the sun at perihelion than aphelion. This substantial change in the sun-planet distance would cause higher solar extreme ultraviolet (EUV) irradiance, as well as increased solar wind flux and temperatures in the upper atmosphere near perihelion. Because increasing the temperature of H atoms (and/or the abundance of H atoms along an observational line of sight) causes an increase in Ly- α brightness (*e.g.*, *Chaufray et al.*, 2008; *Bhattacharyya et al.*, 2017; *Chaffin et al.*, 2018), the changes in the neutral atmosphere following perihelion would lead to increased Ly- α intensities in the H corona. Further, because it is not possible to distinguish between background Ly- α emitted by the neutral H corona and Ly- α emitted by H-ENAs in a proton aurora profile, the increased intensities of coronal H could also then partially contribute to higher intensities in proton aurora profiles.

Because of the essential role of the coronal H in proton aurora formation, any variations in the neutral H corona will strongly influence Martian proton aurora. Seasonal trends in coronal H

have previously been observed at Mars by multiple different spacecraft/instruments (*Chaffin et al.*, 2014; *Clarke et al.*, 2014; *Battacharya et al.*, 2015; *Mayyasi et al.*, 2017), finding that H abundances and altitudes are highest around southern summer solstice (L_s 270). *Halekas* (2017) proposes that the timing of the increased coronal H abundance may be due to “either a lag in the response of the upper atmosphere to solar input or a seasonal influence in addition to the direct effects of the solar EUV.” *Halekas* (2017) also reported a peak in H column density upstream of the Mars bow shock near southern summer solstice, finding that the column density increases nearly ten-fold over the course of a year (leading to higher escape rates during this time). *Chaffin et al.* (2017) demonstrate, using a photochemical model, that if atmospheric water is lofted to high altitudes during southern summer it can be photodissociated into H, and subsequently inflate the H corona. The increased coronal H abundances around southern summer solstice would thereby increase the background coronal brightness and move more H upstream of the bow shock. This additional upstream coronal H would lead to more charge exchange interactions between solar wind protons and the H corona, increasing production of the H-ENAs that penetrate the atmosphere, and ultimately leading to higher proton aurora occurrence rates and intensities during this season.

The major contributor to the increased peak altitude of proton aurora during southern summer is an inflated neutral CO₂ atmosphere and larger scale height (*e.g.*, *Jain et al.*, 2015; *Bougher et al.*, 2017). Ly- α is absorbed by CO₂ at low altitudes, being partially absorbed below ~130 km and completely absorbed by 80 km (*e.g.*, *Gerard et al.*, 2019). *Gerard et al.* (2019) demonstrate via modeling that CO₂ absorption increases the peak altitude (and decreases the peak intensity) in an observed proton aurora Ly- α altitude-intensity profile. Because the CO₂ density in the Martian thermosphere changes with season, this variation should alter the altitude

of proton aurora profiles over the course of the year. Thus, higher CO₂ densities and altitudes near L_s 270 contribute to higher proton aurora peak altitudes in this season by inflating the neutral lower atmosphere, thereby increasing the peak altitude of energy deposition for H and protons in the atmosphere. This annual CO₂ variation on its own, however, cannot explain the higher peak intensities observed in proton aurora profiles during this season, meaning that an alternate process(es) must be responsible for seasonally increased proton aurora brightness.

Regional/global dust storms and other dust activity can also contribute to increasing the peak altitude, intensity, and occurrence rates of proton aurora on Mars. Dust activity increases the temperature of the atmosphere, thereby also increasing the scale height and peak altitude of thermospheric CO₂ (*e.g.*, Jain *et al.*, 2015; Liu *et al.*, 2018; Heavens *et al.*, 2018). Vandaele *et al.* (2019) found that dust storms on Mars lead to a significant increase in H₂O and HDO at high altitudes (40-80 km) on timescales as short as days. This increased high altitude water can then photodissociate into H and supply more H to regions of the corona upstream of bow shock, thereby increasing proton aurora occurrence, intensity, and peak altitude. Thus, dust activity affects proton aurora similarly as the inflated CO₂ atmosphere and H corona, but over shorter timescales (*e.g.*, days to weeks). We might expect to see the most pronounced effects of dust activity on proton aurora during southern summer (just after the Martian dust storm season begins).

2.4.3 Influence of the Bow Shock and Geographic Location on Proton Aurora

Because proton aurora form as a result of charge exchanges with coronal H present upstream of the bow shock, changes in the bow shock shape/location can affect proton aurora in similar ways as the previously described H corona variations. The location of the Martian bow shock has been observed to move with season, becoming more inflated and moving further away

from the planet near perihelion (*e.g.*, *Hall et al.*, 2016; *Halekas et al.*, 2016). And because the bow shock radius reaches a maximum around southern summer solstice, it is likely that the mechanisms responsible for this variation also influence seasonal variations in proton aurora. *Hall et al.* (2016) observe the bow shock altitude at the terminator increase by 11% at perihelion compared to aphelion and theorize that it is likely most heavily influenced by solar EUV irradiance (as opposed to dynamic pressure). However, it should be noted that compared to the bow shock inflation, the corresponding inflation of the H corona (*i.e.*, increased H abundance and column density) must be significantly higher, so as to inflate further beyond the bow shock than in other seasons and allow an increase in proton aurora occurrence rates during this time.

We do not observe any clear geographic variability in Martian proton aurora. *Hall et al.* (2016) note that the Mars bow shock in the southern hemisphere is on average located slightly farther away (2.4%) from the planet than in the northern hemisphere. Although such a difference could create latitudinal variations in proton aurora occurrence, we note that this small difference moves the location of the bow shock by only a fraction of a H scale height, and thus should not strongly influence locations of occurrence (though larger changes in bow shock altitude could cause a presumably larger change in proton aurora occurrence rate). It is plausible that proton aurora could theoretically exhibit a latitudinal dependence caused by remanent southern hemispheric crustal fields (*e.g.*, *Brain et al.*, 2003). But because we observe high occurrence rates at all latitudes where data exist around southern summer solstice (*i.e.*, mid- and southern latitudes), we determine that any apparent latitudinal dependence in the southern hemisphere (*e.g.*, Figure 2.3 and Figure 2.6) is likely an observational bias caused by the location of periapsis during these times of observation (*e.g.*, in Figure 2.4 compare latitude subplot with observation periods around $L_s \sim 270$ and at low SZAs). We note that there is a lack of data at northern

latitudes and low SZAs in southern summer; as more northern latitude data become available in this season, we will be able to rule out a latitudinal dependence with more certainty. We also do not observe a strong dependence on geographic longitude for proton aurora occurrence (see Supplementary Figure 2.5). We might expect longitudinal trends to exist in the data at some low level based on the presence of nonmigrating atmospheric waves and tides (*e.g.*, *Lo et al.*, 2015; *England et al.*, 2016) and also in the southern hemisphere due to localized remanent crustal fields. These waves and tides can cause local CO₂ density variations, which could lead to density variations in the H corona. Such a longitudinal dependence may become visible if the data are detrended to account for SZA and seasonal variations in specific case studies.

2.4.4 *Solar Cycle Variations*

Because the MAVEN mission has only spanned a fraction of a solar cycle, we cannot observe long-term effects of solar cycle variation on proton aurora in our data. However, we can hypothesize on these effects based on our observations and knowledge of the driving processes of Mars proton aurora. Data used in this study were collected during the declining phase of the solar cycle (immediately following solar maximum). The *Ritter et al.* (2018) study (another multi-year Mars proton aurora study) also used data taken during the declining and minimum parts of the previous solar cycle, limiting our ability to directly compare results from different solar cycle phases. The higher occurrences of CME's and solar energetic particle (SEP) events (*e.g.*, increased proton flux) during solar maximum periods would initially suggest an increase in proton aurora occurrence rates during solar maximum conditions. However, *Kallio and Barabash* (2001) propose that due to the denser H corona at solar minimum than maximum, the penetrating H-ENA particle flux (and consequently, proton aurora occurrence) will be higher during solar minimum periods. Models of Mars dayside exospheric temperatures show that

average temperatures change by 100-150K over the course of a solar cycle, and annual changes in temperature between aphelion and perihelion are higher during solar maximum than solar minimum conditions (*Bougher et al.*, 2014). *Chaufray et al.* (2015) demonstrate via modeling that EUV heating at solar maximum leads to an increased coronal H Jeans escape flux and decreased H density at the exobase compared to solar minimum. Moreover, *Mayyasi et al.* (2018) observed that even temperature changes due to impulsive events can significantly impact the H corona: finding that an 80K increase in exospheric temperature (due to a CME and solar flare in their study) led to increased H brightness on the dayside, decreased H density at the Mars exobase, and a nearly five-fold increase in instantaneous H escape flux due to Jeans escape. We expect that increased temperatures during solar maximum will lead to inflation of the H corona further beyond the bow shock (decreasing H density at the exobase but increasing H column density upstream of the bow shock) and cause higher intensities and occurrence rates for proton aurora, similar to currently observed seasonal variations. Future MAVEN measurements spanning a complete solar cycle will be beneficial in gaining a more robust understanding of the sun's interaction with Mars' upper atmosphere, as well as the long term influences of these interactions on proton aurora caused by solar cycle variations.

2.5 Summary and Conclusions

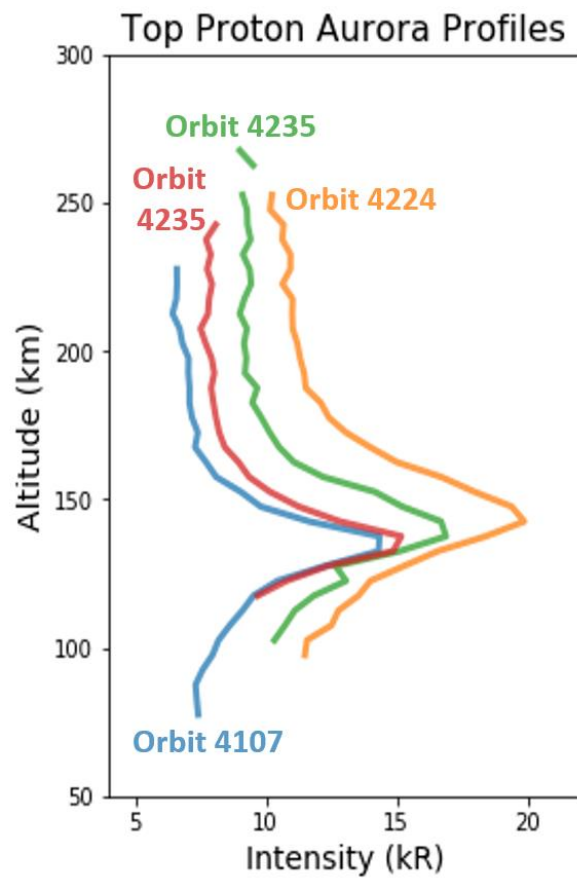
The results of our study provide a new understanding of the major factors driving proton aurora, and the long-term phenomenology and variability of these events as observed over multiple Martian years. We find that that the two primary factors influencing proton aurora rates are solar zenith angle (SZA) and season. Proton aurora primarily occur on the dayside at low SZAs, and the highest occurrence rates, emission enhancements, intensities, and peak altitudes occur around southern summer solstice ($L_s \sim 270$). Proton aurora are prevalent at Mars,

occurring in ~14% of dayside IUVS periapsis data, with significant seasonal variability (having occurrence rates approaching 100% near southern summer solstice at low SZAs); this makes proton aurora the most commonly observed type of aurora at Mars. The annual variation in proton aurora occurrence rate is in keeping with previously observed variations of the Mars H corona. More specifically, seasonally induced lower atmospheric dynamics and chemistry around southern summer solstice lead to inflation of the H corona further beyond the bow shock and magnetic pileup boundary (MPB) relative to other seasons, exposing more neutral H to interact with incident solar wind protons. The combination of these influencing factors, along with higher atmospheric temperatures and solar wind flux near perihelion, increase occurrence rates and intensities of Martian ENA-driven proton aurora around southern summer solstice.

Proton aurora are one of the few observable Mars phenomena that are created by direct interactions between solar wind protons and the H corona. Thus, by studying Martian proton aurora we can better understand the connection between the sun, Mars' H corona, and its near-space plasma environment. Moreover, proton aurora occurrence and intensity may serve as a proxy for variations in each of these regions, as well as tracking changes in lower atmospheric dynamics (*e.g.*, the neutral CO₂ atmosphere and dust activity). Studying Martian proton aurora may also provide additional context in understanding atmospheric loss and evolution, as the processes responsible for aurora formation at Mars (*e.g.*, solar wind interactions and electron stripping/ionization in the H corona) are also responsible for stripping away the atmosphere. More work needs to be done to better understand these phenomena, including case studies of the effects of dust activity, the influence of changes in the induced magnetic field, modeling of absorption in the lower CO₂ atmosphere, and longer temporal coverage showing variations over a full solar cycle. As we learn more about Martian proton aurora, we also learn more about the

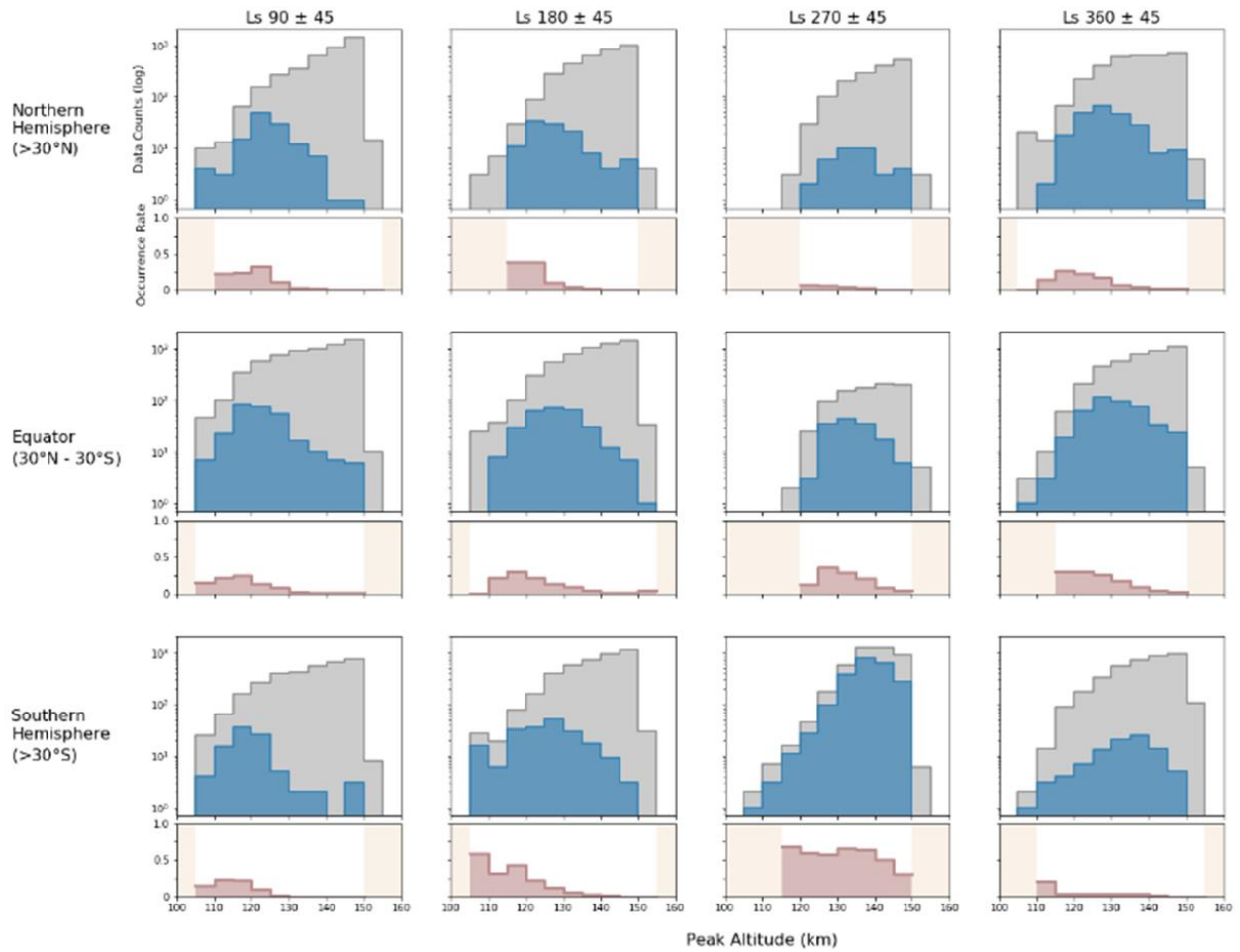
Sun-Mars system as a whole and gain an understanding of interactions at other planetary bodies that lack a global magnetic field and exhibit a neutral H corona.

Chapter 2 Supplementary Figures

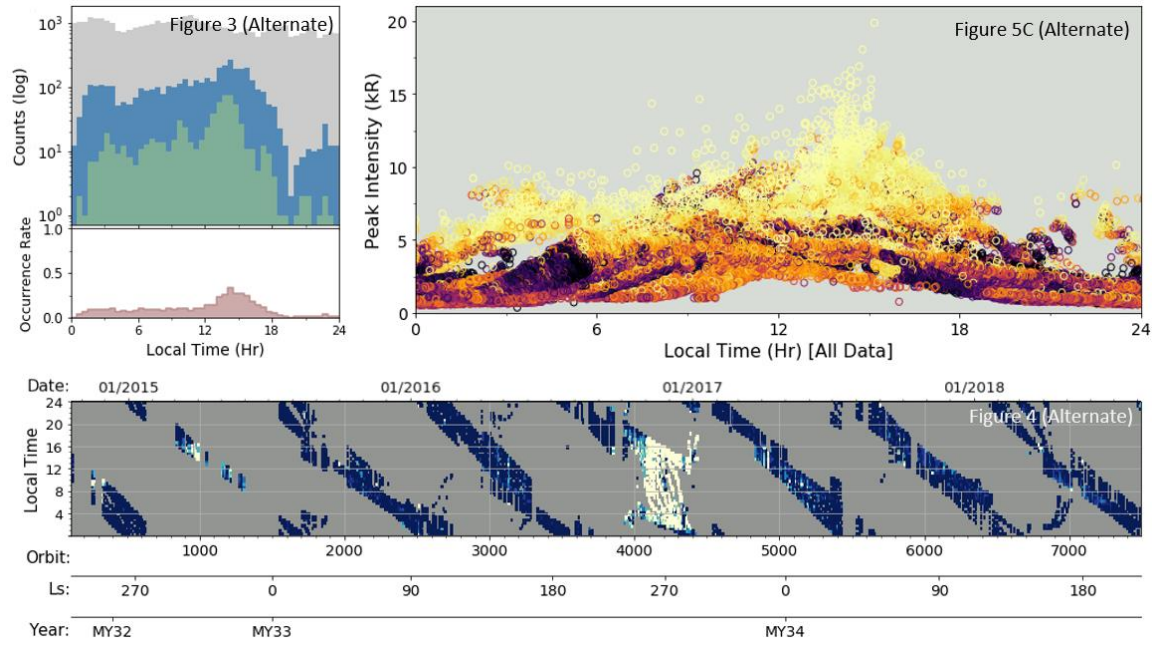


Supplementary Figure 2.2: Altitude-intensity profiles for the top four orbits with the highest emission enhancement differences (Orbits 4107, 4224, 4235, and 4107). These orbits have corresponding enhancement values of 7.13kR, 6.99kR, 6.87kR, and 6.77kR, respectively.

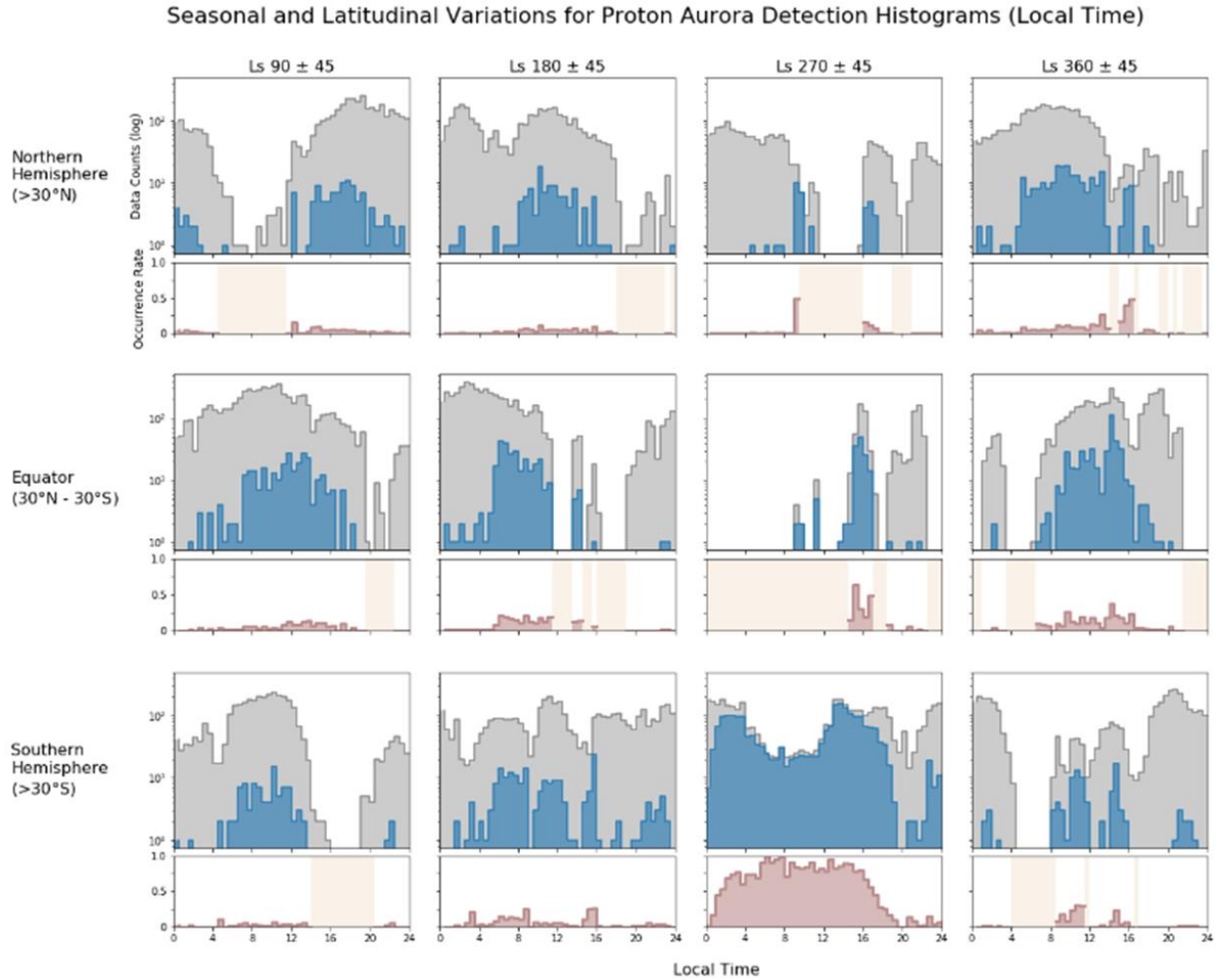
Seasonal and Latitudinal Variations for Proton Aurora Detection Histograms (Peak Altitude (km))



Supplementary Figure 2.3: Seasonal and latitudinal variations of peak altitude for proton aurora. Histogram plots are as described in Figure 2.6: All IUVS data (grey), proton aurora detections (blue), and proton aurora occurrence rates (pink). Beige areas on normalized subplots represent bins where the total number of counts is less than or equal to ten. Note that apparent latitudinal dependence is likely due to a data sampling biases and the location of MAVEN periapsis during this time (discussed in the text). The highest proton aurora occurrence rates are observed around southern summer solstice (L_s 270) spanning a wide range of altitudes.

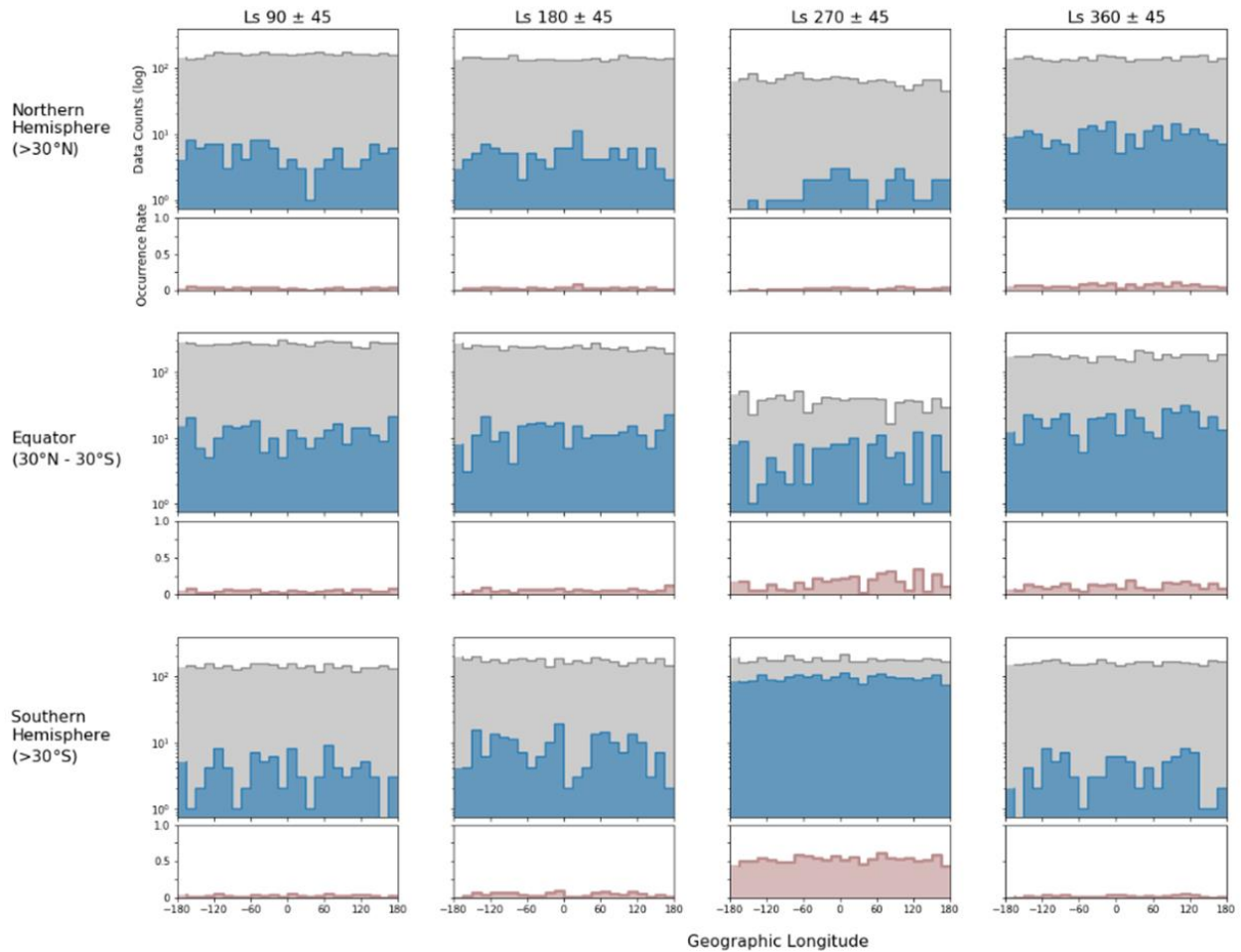


Supplementary Figure 2.4: Proton aurora variations with respect to local time. These plots show the same correlations as corresponding plots in the main text (Figure 2.3, Figure 2.4, and Figure 2.5C), but here the entire local time dataset is plotted (i.e., data from all latitudes) for comparison to plots in the main text that include only local time data from low- and mid-latitudes ($\pm 60^\circ$ latitude).



Supplementary Figure 2.5: Seasonal and latitudinal variations of local time for proton aurora. Histogram plots are as described in Figure S2 (and Figure 2.6). Note that apparent latitudinal dependence is likely due to a data sampling biases and the location of MAVEN periapsis during this time (discussed in the text). The highest proton aurora occurrence rates are observed around southern summer solstice (L_s 270), covering a wide range of local times due to the location of the MAVEN periapsis in this season.

Seasonal and Latitudinal Variations for Proton Aurora Detection Histograms (Geographic Longitude)



Supplementary Figure 2.6: Seasonal and latitudinal variations of geographic longitude for proton aurora. Histogram plots are as described in Figure S2 (and Figure 2.6). Note that apparent latitudinal dependence is likely due to a data sampling biases and the location of MAVEN periapsis during this time (discussed in the text). The highest proton aurora occurrence rates are observed around southern summer solstice ($L_s 270$); however, no clear longitudinal dependence is discernable.

3. A Combined Remote Sensing and *In Situ* Evaluation of Martian Proton Aurora

For submission to *Journal of Geophysical Research: Space Physics*

Hughes, A., Chaffin, M., Mierkiewicz, E., Halekas, J., Schneider, N.,

Deighan, J., Jain, S., *et al.*

Chapter 3 Key Points

- We identify a correlation between orbit-averaged H Lyman-alpha emission enhancements and penetrating proton fluxes for ~two Mars years of proton aurora events.
- Large offsets from the expected correlation are caused by major dust storm or extreme solar activity, causing variability in the observed proton-hydrogen ratio.
- Using the penetrating proton flux, we may empirically estimate the proton aurora Ly- α emission enhancement for different atmospheric/solar conditions.

Chapter 3 Abstract

In this study, we compare remote sensing and *in situ* observations of Martian proton aurora events. Based on the relationship between penetrating protons and hydrogen (H) energetic neutral atoms (ENAs) in the formation of proton aurora, we observe an expected correlation between the H Lyman-alpha (Ly- α) emission enhancement (used as a proxy for H-ENAs) and penetrating proton flux. However, we observe a large spread in the relative comparison of these two datasets. We determine that this spread is correlated with one of two major impacting events: high dust activity or extreme solar activity. Proton aurora events exhibiting a relative excess in penetrating proton flux compared to Ly- α enhancement tend to occur during periods of high dust activity (caused by an increased equilibrium charged fraction and muted Ly- α peak brightness, due to the associated higher neutral atmospheric density and corresponding absorption by CO₂ on the bottom-side of the Ly- α profile). Conversely, proton aurora events exhibiting a relative deficit of penetrating proton flux compared to Ly- α enhancement tend to occur during periods of extreme solar activity (caused by larger Ly- α enhancements due to higher solar wind particle temperatures). We also find that the largest proton aurora events occur during both dust storm and solar events, due primarily to the intensified increase in H column

density above the bow shock. We present a simplified yet novel method for empirically estimating the Ly- α emission enhancement of proton aurora events based on the penetrating proton flux and a knowledge of local dust/solar activity at the time. Lastly, we compare proton aurora observations with interplanetary magnetic field (IMF) magnitudes and orientations upstream of the Martian bow shock. We identify a possible correlation between proton aurora activity and specific IMF cone/clock angles, and a possible preferential occurrence during near-radial IMF orientations.

3.1 Introduction

Martian proton aurora are understood to form by solar wind protons interacting with neutral hydrogen (H) in the extended Martian corona to convert into energetic neutral atoms (ENAs). These ENAs, maintaining the same energy and velocity as the incident solar wind can then bypass the bow shock and magnetic pileup boundary (MPB) to penetrate into the upper portions of the atmosphere (*i.e.*, the Martian thermosphere). The incident solar wind protons convert between ENAs and protons through charge exchange and/or electron stripping many times before reaching a stopping altitude (*e.g.*, Supplementary Figure 3.1) and de-exciting from their neutral state to emit a photon that can be observed in the H Lyman-alpha (Ly- α) emission (121.6 nm). This process was initially identified to occur at Mars by Halekas *et al.* (2015) based on observations by the Solar Wind Ion Analyzer (SWIA) (Halekas *et al.*, 2013) onboard the Mars Atmosphere and Volatile Evolution (MAVEN) spacecraft (Jakosky *et al.*, 2015). Halekas *et al.* (2015) observed a population of solar wind protons (as identified by the bulk energy and velocity) that had penetrated into the Martian thermosphere (referred to as “penetrating protons”) and speculated that they may be associated with proton aurora.

Following the study by Halekas *et al.* (2015), Deighan *et al.* (2018) identified proton aurora using the Imaging UltraViolet Spectrograph (IUVS) (McClintock *et al.*, 2015) onboard the MAVEN spacecraft (Jakosky *et al.*, 2015). Proton aurora are observed in ultraviolet limb scan data as an enhancement in the Ly- α emission above the background coronal H brightness between an ~110-150 km in altitude. Deighan *et al.* (2018) observed multiple instances of proton aurora over the span of ~one month and compared IUVS Ly- α and SWIA penetrating proton observations during this period. They observed that increases in SWIA penetrating proton fluxes clearly corresponded with increases in the IUVS proton aurora Ly- α “emission enhancement” (*i.e.*, the difference between the Ly- α brightness at the peak and at high altitude for a Ly- α altitude-intensity profile – *e.g.*, Figure 1 in Hughes *et al.*, 2019).

A previous study by Hughes *et al.* (2019) undertook a detailed statistical analysis of proton aurora using multiple Mars years of IUVS data. Hughes *et al.* (2019) identified both a strong dependence on solar zenith angle (SZA) and season: with the most frequent and largest proton aurora events occurring on the dayside of the planet (*i.e.*, at low SZAs) around southern summer solstice (*i.e.*, solar longitude, L_s , ~270). This increase in proton aurora activity near southern summer solstice was found to coincide with increases in the H column density and escape rate of the H corona, caused by seasonally increased atmospheric dust activity (*e.g.*, Hughes *et al.*, 2019; Chaffin *et al.*, 2021; Chaffin *et al.*, 2014; Clarke *et al.*, 2014; Halekas, 2017). This increased H abundance beyond the Martian bow shock allows a larger fraction of solar wind protons to be converted into H-ENAs, causing a seasonal increase in proton aurora frequency and emission enhancement.

In this study we combine observations from remote sensing and *in situ* datasets to better understand Martian proton aurora. While many previous MAVEN studies have compared

remote sensing and *in situ* datasets, only the Deighan *et al.* (2018) has used such datasets to specifically evaluate proton aurora. However, the very limited time period of the Deighan *et al.* (2018) study (~1 month), precluded their ability to observe any seasonal variability or large-scale correlations between the datasets. We undertake the first large-scale statistical comparison of IUVS and SWIA observations of proton aurora for multiple years of MAVEN data.

3.2 Data and Databases

3.2.1 MAVEN/IUVS proton aurora detections

We use a database of proton aurora detections compiled in a previous statistical study by Hughes *et al.* (2019) and expand on this list by including observations through MAVEN orbit ~8400 (note that the previous study considered data through MAVEN orbit ~7500). These proton aurora detections were made using IUVS Level 1C periapsis limbs scans of Ly- α altitude-intensity profiles. (Further details on the proton aurora detection methods used can be found in the Methodology section of Hughes *et al.*, 2019.) Using the previously compiled database of individual limb scan Ly- α emission enhancements, we average the peak emission enhancement values for every limb scan within each MAVEN orbit to determine a single orbit-averaged enhancement for proton aurora events. Averaging the orbit emission enhancement values in this study allows for better comparison of IUVS observations with the *in situ* orbit-averaged observations (which are typically averaged for inter-orbit comparisons to remove variability caused by the motion/viewing angle of the spacecraft, *e.g.*, altitude and SZA). Using orbit-averaged values also helps to avoid discrepancies that arise from the different sampling times and locations of the remote sensing and *in situ* instruments for each of the comparison datasets. We exclude orbits with negative orbit-mean enhancements, as these are typically caused by observational/instrumental effects.

By evaluating the Ly- α emission enhancement (*i.e.*, the Ly- α brightness due to proton aurora with the background coronal H brightness subtracted out), we effectively observe only the proton aurora contribution to the Ly- α emission. Thus, while IUVS does not directly measure the H-ENA particles associated with proton aurora, the Ly- α emission enhancement serves as a *proxy* for evaluating neutral H associated with proton aurora events.

3.2.2 MAVEN/SWIA penetrating proton observations

In this study we use SWIA orbit-averaged penetrating proton fluxes (*i.e.*, the product of the average penetrating proton density and velocity for each orbit). We consider proton flux as opposed to density as it also incorporates any changes associated with varying solar wind velocity. By evaluating the average SWIA penetrating proton flux from the periapsis portion of each orbit, we exclude any major variability associated with the spacecraft location (*e.g.*, altitude and/or SZA) or small-scale intra-orbit variations. Because SWIA does not measure of the penetrating proton population during every orbit (due to the varying altitude and orbit precession of the MAVEN spacecraft), we consider only MAVEN orbits with pristine measurements of the penetrating proton population (*e.g.*, at altitude ranges below the planet's bow shock and MPB) (*e.g.*, Halekas *et al.*, 2015). A more detailed description of the parameters used in identifying and characterizing penetrating protons in SWIA data is described by Halekas *et al.* (2015 and 2016).

The MAVEN orbits used in this study were selected by identifying orbits that had overlapping coverage of both IUVS proton aurora detections and SWIA penetrating proton observations.

3.2.3 *MAVEN/MAG observations*

The Magnetometer instrument onboard the MAVEN spacecraft measures interplanetary magnetic fields as well as local planetary magnetic fields in the Martian ionosphere (Connerney *et al.*, 2015). We use a database of orbit-averaged upstream magnetic field magnitudes in the x, y, and z directions of the Mars-Sun-Orbit (MSO) coordinate system (we convert these orientations to the commonly used cone and clock angles). This database was compiled alongside SWIA measurements to identify and include average values from only MAVEN orbits that made pristine measurements of the upstream solar wind (as the changing MAVEN orbit limits the possibility of consistency in the location of the spacecraft during every orbit). Only those MAVEN orbits with overlapping proton aurora detections and pristine upstream solar wind measurements were included in the IUVS-MAG data comparison. A detailed description of the algorithm used to determine the parameters from MAG and SWIA data is described in Halekas *et al.*, 2016 (Section 3.1).

3.2.4 *MAVEN Science Impacting event database*

The MAVEN Science Data Center website contains publicly available MAVEN data and spacecraft/instrument information. This website also contains a database of MAVEN events that were observed by spacecraft instruments throughout the mission, as compiled by the MAVEN team. The database can be filtered to include only major MAVEN science impacting events (*e.g.*, dust storms, solar wind streams, solar flares, coronal mass ejections (CMEs), solar energetic particles (SEPs), and diffuse/discrete aurora). It should be noted that this database is not inclusive of all events, but rather only the most significant events observed by MAVEN. Thus, any detailed analyses performed using this database should also incorporate observations from specific MAVEN instruments.

3.2.5 *Mars Climate Database (Montabone et al. (2015) Dust Optical Depths)*

The Mars Climate Database (MCD) is a free resource that provides climatological information about Mars. The MCD is primarily derived from a General Circulation Model (GCM) of the Martian atmosphere and validated with observational data (Forget *et al.*, 1999). A particularly useful MCD product for our study is the “Climatologies of the Martian Atmospheric Dust Optical Depth”, which provides combined-data gridded maps and derived GCM maps of column dust optical depth ($9.3 \mu\text{m}$ absorption) spanning all geographic locations during ten Mars years (Montabone *et al.*, 2015).

We use the MCD database to determine a globally averaged normalized column dust optical depth (CDOD) during each MAVEN orbit. An increasing CDOD value corresponds with increasing dust activity on the planet. We look for time periods of high dust activity that occur just before or during MAVEN/IUVS observations of proton aurora. (We note that globally averaging CDOD values provides an appropriate comparison for assessing large-scale variability that would lead to dust-induced H escape and expansion of the H corona; however, it also removes localized small-scale variability caused by intense regional dust storms.)

3.2.6 *MAVEN/SEP solar activity database*

The Solar Energetic Particle (SEP) instrument onboard MAVEN measures the impact of SEPs on the Martian upper atmosphere (Larson *et al.*, 2015). It is used to measure the energy fluxes of high energy solar wind electrons and ions (including protons). In this study, we compare IUVS proton aurora detections to a SEP database of major proton-related solar events (compiled by the MAVEN/SEP team) in order to evaluate the effects of high energy solar particles on proton aurora.

3.2.7 *Potential caveats of remote sensing-in situ data comparisons*

It is important to consider the potential caveats that may be associated with comparing remote sensing and *in situ* datasets, (*e.g.*, IUVS and SWIA). First, there are notable differences in the spatial and temporal scales of the measurements. SWIA observes the local particle environment in the immediate vicinity of the spacecraft as MAVEN moves along its orbit. Alternatively, IUVS builds up each limb scan observation by integrating the number of photons along the line of sight between the spacecraft out to infinity (hence why IUVS ephemeris parameters – *e.g.*, altitude, SZA, and geographic location - are typically given as the “tangent point” of the parameter). Thus, while SWIA observes the penetrating proton population along-track of the spacecraft as it passes through different altitude ranges and locations during the periapsis segment of a given orbit, IUVS observes the tangent point altitudes and intensities of proton aurora thousands of km away from MAVEN (and perpendicular to the spacecraft movement) during the MAVEN orbit periapsis.

The possible variations in observations pertain not only to differences in the location/volume measured by each instrument, but also to the temporal resolution. Each IUVS limb scan is built up by integrating over different altitude ranges during a ~two minute period, with a short period between each subsequent limb scan within a given orbit. Alternatively, SWIA typically collects data at a ~4 second cadence during periapsis. As such, SWIA is better suited for observing any small scale variability that is below the temporal resolution of IUVS. If any localized variability occurs in space and/or time during an orbit, it would be extremely unlikely that both instruments would simultaneously observe the event. Thus, in undertaking a statistical comparison with the datasets in this study, we assume minimal spatial and/or temporal variation between the MAVEN spacecraft and IUVS tangent point (*i.e.*, that no local structures

or processes are significantly affecting the in-between region). Any deviations from this assumption would lead to discrepancies in the comparisons.

Thus far we have described possible caveats for comparing remote sensing and *in situ* datasets onboard MAVEN. However, it is also important to note that even comparisons between different *in situ* datasets can present challenges due to the different look directions and fields of view of certain MAVEN instruments. For example, the fields of view of the SWIA and SEP instruments do not overlap. Thus, while uncommon for most observations, it should be considered that any small scale perturbations in the local particles/fields environment could potentially cause inconsistencies between even the different *in situ* MAVEN observations.

3.3 Observations and Results

3.3.1 Proton aurora correlation with MAVEN science-impacting events

When comparing proton aurora detections with major science impacting events detected by MAVEN, we find that almost all proton aurora events correspond with a simultaneous MAVEN science impacting event (*e.g.*, dust storms and solar activity). Figure 3.1 shows a comparison of proton aurora detections with other major science impacting events as identified by MAVEN during the first ~three Earth years of the MAVEN mission. The type and duration of each major science impacting event is shown on the bottom half of the plot as a discrete point, along with the corresponding MAVEN orbit numbers. The top half of the plot present orbits containing proton aurora detections (as identified by Hughes *et al.*, 2019), with the vertical distribution and color of the points corresponding with the size of each proton aurora event (*i.e.*, orbits containing relatively large proton aurora activity have the largest emission enhancements that are farthest offset above the horizontal threshold line). Based on this preliminary comparison it is evident that the primary sources that influence the formation and magnitude of proton aurora on Mars

must be either from the “top-down” (*i.e.*, major solar events) or the “bottom-up” (*i.e.*, dust storm activity). In the subsequent sections, we explore these different (and at times, complementary) sources for Martian proton aurora variability.

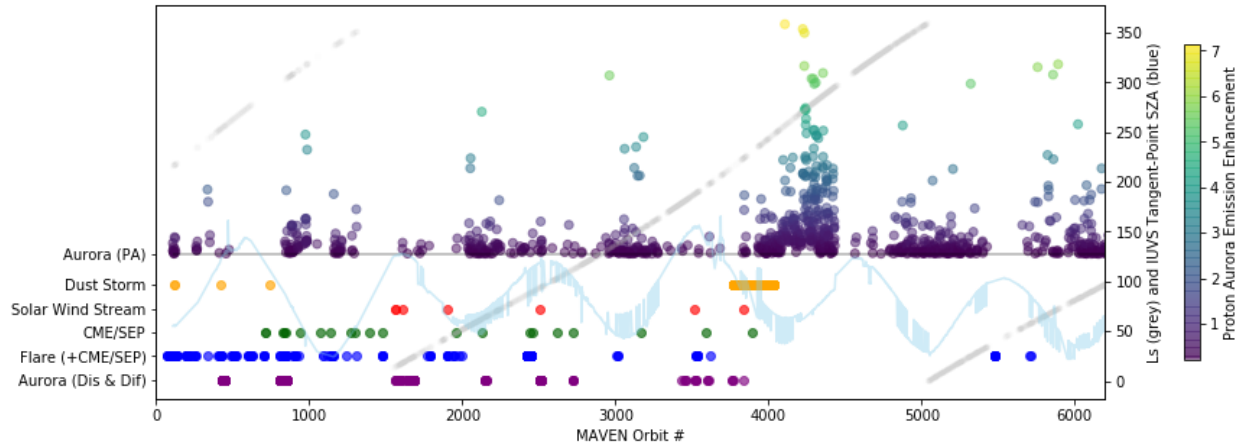


Figure 3.1: Proton aurora detections are shown on the top of the plot with offset and color corresponding to Ly- α emission enhancement. The bottom portion of the plot shows most major MAVEN science impacting events observed in the first few years of the mission. These science events include dust storms, solar winds streams, CME/SEP events, solar flares (including CME and/or SEP events), and discrete and/or diffuse aurora. The season (L_s) and orbit-maximum IUVS limb scan tangent point SZA are overplotted for reference as grey linear and light blue sinusoidal plots, respectively.

3.3.2 Comparison of IUVS Ly- α emission enhancements and SWIA penetrating proton fluxes for proton aurora detections

In comparing orbit-averaged SWIA penetrating proton fluxes with orbit-averaged IUVS Ly- α emission enhancements for proton aurora detections (Figure 3.2, left), we identify a clear correlation between these datasets. The trend of the plot of these two variables is mostly linear, with some notable deviations from the heuristic line-of-best-fit (which is created using a linear least-squares regression fitting routine). As the penetrating proton flux and Ly- α enhancement generally track with each other throughout the MAVEN mission (*e.g.*, Supplementary Figure 3.2), the same driving processes are likely responsible for variability in both of these parameters. Most of the spread from the best-fit line appears to be strongly correlated with season, with orbits occurring near/during southern summer solstice ($L_s \sim 270$) exhibiting the most spread away

from the best-fit trendline (see Figure 3.2 and Supplementary Figure 3.3; note that point colors corresponds with L_s in Figure 3.2).

By considering the offset of each point from the best-fit trendline, we may more thoroughly quantify the spread of the data in Figure 3.2 (left). Figure 3.2 (right) shows each of these points plotted as a y-distance offset from the line of best fit for each respective MAVEN orbit numbers (note that the area of each data point corresponds with Ly- α emission enhancement, a measurement of the magnitude of a proton aurora event). Orbits with a relatively high SWIA penetrating proton flux in comparison with the corresponding proton aurora emission enhancement (*i.e.*, the data points mostly in the upper left quadrant of Figure 3.2, left) are offset above the horizontal trendline location in Figure 3.2 (right). Alternatively, orbits with a relatively small SWIA penetrating proton flux in comparison with the corresponding proton aurora emission enhancement (*i.e.*, the points far below the trendline in the lower quadrants of Figure 3.2, left) are offset below the horizontal trendline in Figure 3.2 (right). It is important to consider that the location of the best-fit trendline is affected by the large spread in the data (especially due to seasonal variability); thus, while the exact offset distance of any specific data point from the trendline should not be held in high regard, the large offsets above/below the line are indeed associated with significant deviation from the trendline. Reasons for the extreme offsets from the line of best fit are examined in the following section.

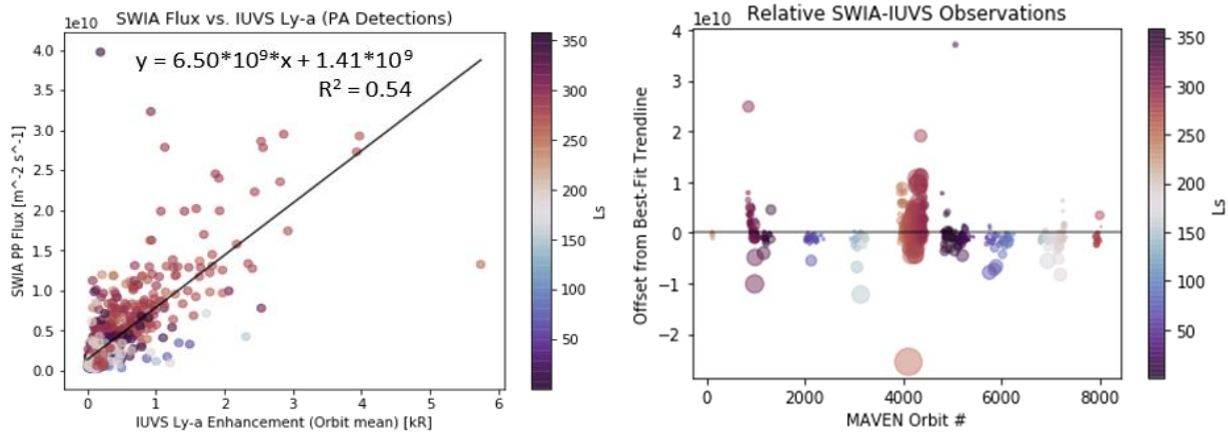


Figure 3.2: Left: comparison of orbit-averaged IUVS Ly- α emission enhancement values and SWIA penetrating proton fluxes for orbits containing proton aurora detections (color corresponds with solar longitude, L_s). We identify a quasi-linear correlation between the two observables, with notable spread in the data (corresponding with orbits near southern summer solstice). Right: for each point in the left panel, y-distance offset from the line of best fit versus MAVEN orbit number. The offsets from the best-fit line correspond to a relative excess (positive offset) or deficit (negative offset) of penetrating proton flux compared with Ly- α emission enhancement (area of each data point corresponds with the orbit-averaged Ly- α emission enhancement). We note that these plots are constrained to only orbits containing proton aurora detections.

3.3.3 Proton aurora observations compared with dust optical depth and solar activity

A comparison of MAVEN science impacting events from Figure 3.1 with the line distance offsets in Figure 3.2 (right) provides even further illumination into reasons for the large spread in the data on the IUVS-SWIA comparison plot. It becomes evident that the data points that exhibit a very large positive offset from the best-fit trendline (*i.e.*, those with an excess SWIA flux relative to IUVS Ly- α enhancement) appear to correspond with major global dust storms. Alternatively, points that exhibit a very large negative offset from the best-fit trendline (*i.e.*, those with an excess IUVS Ly- α enhancement relative to the SWIA flux) appear to correspond with major solar events (*i.e.*, SEP, CIR, CME, etc.).

In order to further evaluate the apparent correlations in our results, we compare proton aurora detections with observations from other instruments onboard MAVEN and different Mars-orbiting spacecraft. In considering the association with dust activity, we compare our results with dust optical depth measurements from the MDC database compiled by Montabone *et al.*, 2015; and to evaluate correlations with extreme solar activity we compare our findings with

major solar events observed by the MAVEN SEP instrument. In Figure 3.3 we plot normalized globally-averaged CDOD data from the MCD on top of the data offset distances from the best-fit trendline shown in Figure 3.2 (right). This comparison confirms the identified trends that orbits exhibiting a relative excess in SWIA flux (*i.e.*, orbits with highly positive offsets from the SWIA-IUVS best-fit trendline) correspond with periods of high CDOD (an indication of major dust activity during that time). And orbits that exhibit a relative excess of IUVS Ly- α enhancement (*i.e.*, orbits with highly negative offset from the best-fit trendline) correspond with extreme solar events. We note that the major peak in CDOD between MAVEN orbits ~7000-8000 corresponds with the planet encircling dust event (PEDE) of 2018. However, because the MAVEN periapsis was observing on the planet's nightside/terminator during this time (*i.e.*, at high SZAs when the Ly- α enhancement is small or non-existent), there were no major proton aurora detections.

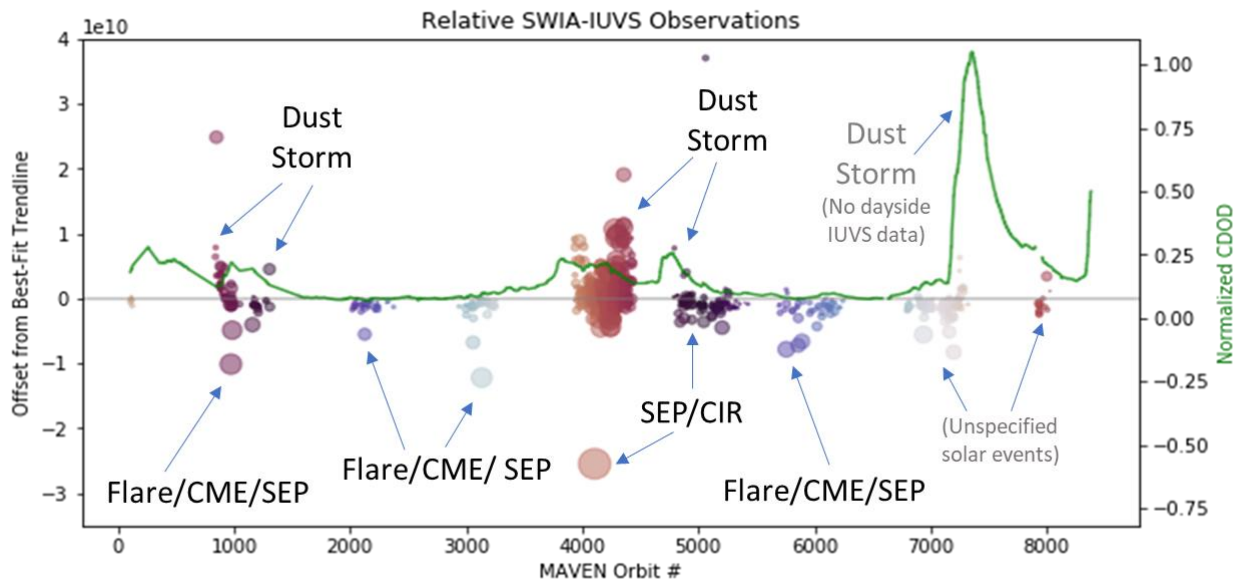


Figure 3.3: Same as Figure 2 (Right) with annotations showing major dust and solar activity as observed in the Mars Climate Database (MCD) and by the MAVEN/SEP instrument, respectively. The overplotted green line represents globally averaged normalized column dust optical depth (CDOD) from the MCD. By comparing the datasets in this manner, we observe a trend that proton aurora events during orbits with a very large positive offset from the best-fit line appear to correspond with major dust storm activity; conversely, proton aurora events during orbits with a very large negative offset from the best-fit line appear to correspond with major solar events. (Description of data colors and area are provided in the caption of Figure 2.)

We can further examine the correlation between CDOD and offset from the line of best fit by plotting these two quantities against each other, as shown in Figure 3.4A. However, because the data points on the far right side of Figure 3.4A correspond with proton aurora detections at very high SZAs just before and during the PEDE, we exclude these uncharacteristic events from our analysis and focus on orbits that exemplify typical variability (as shown in Figure 3.4B). Based on the comparison in Figure 3.4B, it becomes apparent that all orbits that exhibit a relative excess in SWIA flux (*i.e.*, all points positively offset from the best-fit trendline) correspond with relatively high CDOD values. (We note, however, that it is not the case that all orbits which exhibit high CDOD values are necessarily positively offset from the trendline.)

The connection between increasing dust activity and Ly- α enhancement for proton aurora is especially prevalent for orbits with very high SWIA penetrating proton fluxes. Figure 3.4C, shows that there is not an apparent correlation between CDOD and Ly- α enhancement for all MAVEN orbits; however, in considering only the data points that are positively offset from the trendline (*i.e.*, those with a relative excess of penetrating proton flux), a clear correlation becomes apparent between these two variables (Figure 3.4D). (We note that a similar plot of CDOD versus Ly- α enhancement for points negatively offset from the trendline does not reveal any correlation, *e.g.*, Supplementary Figure 3.4.) We may further consider orbits that exhibit a significant relative excess of penetrating proton flux (*i.e.*, with a large positive offset from the SWIA-IUVS best-fit trendline) by including only orbits with high SWIA penetrating proton fluxes (*i.e.*, $>1.5 \times 10^{10} \text{ m}^{-2} \text{ s}^{-1}$) (and again excluding high SZA observations during the PEDE) (Figure 3.4E). The plot in Figure 3.4E shows a clear linear correlation between CDOD and Ly- α enhancement for proton aurora detections. This clear correlation confirms the trends from Figure

3 of the strong dependence on dust activity for proton aurora enhancement and the relative penetrating proton flux to Ly- α enhancement ratio.

Lastly, we note that no significant difference is observed in the penetrating proton velocities of orbits that have a relative excess or deficit of SWIA penetrating proton flux (*i.e.*, positively or negatively offset from the best-fit trendline) (Supplementary Figure 3.5). However, we observe a clear correlation between high penetrating proton density orbits and those with a relative excess of penetrating proton flux in comparison with Ly- α enhancement (*i.e.*, those that are positively offset from the best-fit trendline) (Supplementary Figure 3.5). This trend indicates that the observed variability in SWIA penetrating proton flux is primarily driven by changes in solar wind density rather than velocity during these orbits.

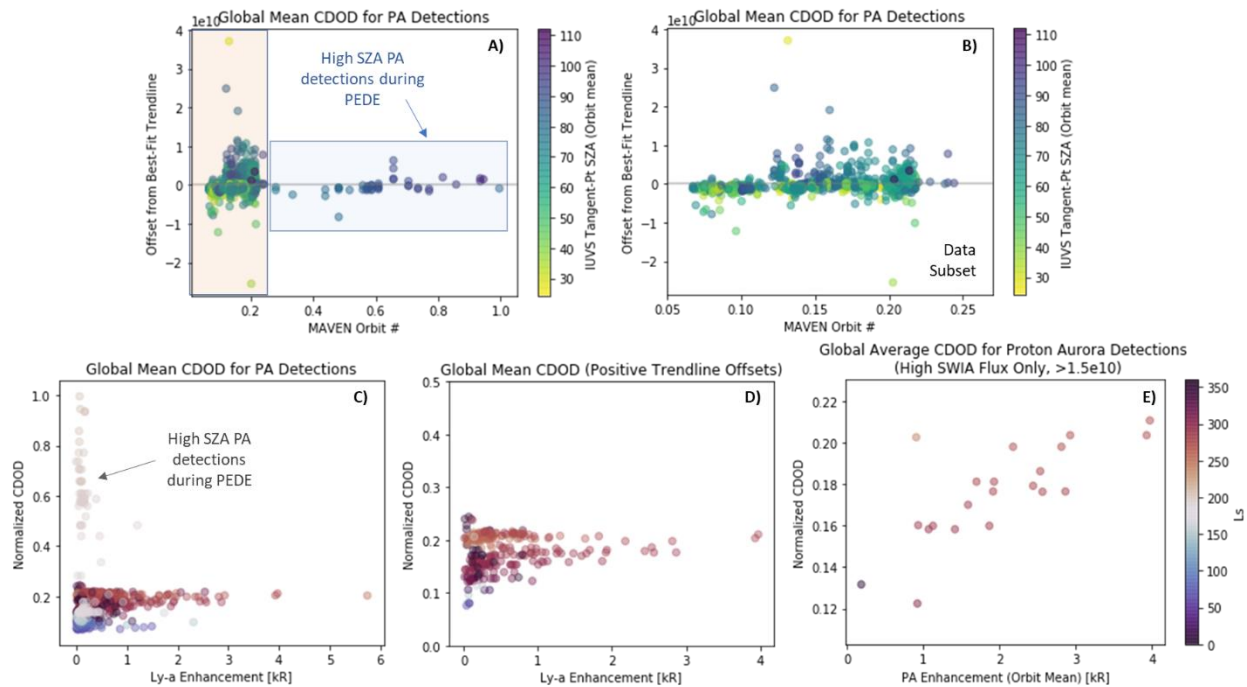


Figure 3.4: A) Perpendicular distance from line of best fit (as described in Figure 2, Right) plotted against globally averaged normalized column dust optical depth (CDOD) values for each orbit. Note that the points on the far right side of the plot correspond with the small number of proton aurora events occurring during the 2018 planet encircling dust event (PEDE) as the location of the MAVEN periapsis was moving onto the night side (causing unusually high IUVS tangent point SZAs during these orbits). B) Subset of data highlighted in yellow from plot (A); a trend become evident that relatively high CDOD values generally correspond with a positive offset from the line of best fit. C) Comparison between CDOD values and emission enhancement for

proton aurora events. D) Same as plot (C) but subset to only the orbits that are positively offset from the best-fit line, revealing an apparent correlation between dust activity and proton aurora enhancement for positively offset orbits. E) Same as (C) but subset to evaluate only orbits with high SWIA penetrating proton flux values. We observe a strong linear correlation between CDOD and proton aurora enhancement during orbits with the highest SWIA fluxes.

3.3.4 **Comparison of IUVS proton aurora detections with MAG upstream magnetic field observations**

Figure 3.5 shows orbit-mean IUVS proton aurora emission enhancements in comparison with the magnitude (Figure 3.5A) and orientations (*i.e.*, cone and clock angle in Figure 3.5B and Figure 3.5C, respectively) of the upstream interplanetary magnetic field (IMF). We do not observe a clear correlation between proton aurora enhancement and IMF magnitude. However, a double peak structure is apparent in the proton aurora enhancement at specific cone and clock angles. (We note that similar trends are observed when plotting the results in MSO coordinates, *e.g.*, Supplementary Figure 3.6.)

Histograms of proton aurora observations with respect to IMF cone and clock angle are shown in Figure 3.6A and Figure 3.6C, respectively (and compared with histograms of all IUVS observations). The proton aurora histograms closely follow the trends present in the entire dataset. We also present normalized histograms of proton aurora occurrence rates (*i.e.*, proton aurora detections/all observations) for cone/clock angle in Figure 3.6B and Figure 3.6D, respectively. The normalized histograms may indicate slightly higher proton aurora occurrence rates for high (and possibly also low) cone angles (*i.e.*, more radially oriented IMF angles). We do not observe any preferential occurrence rates for clock angle.

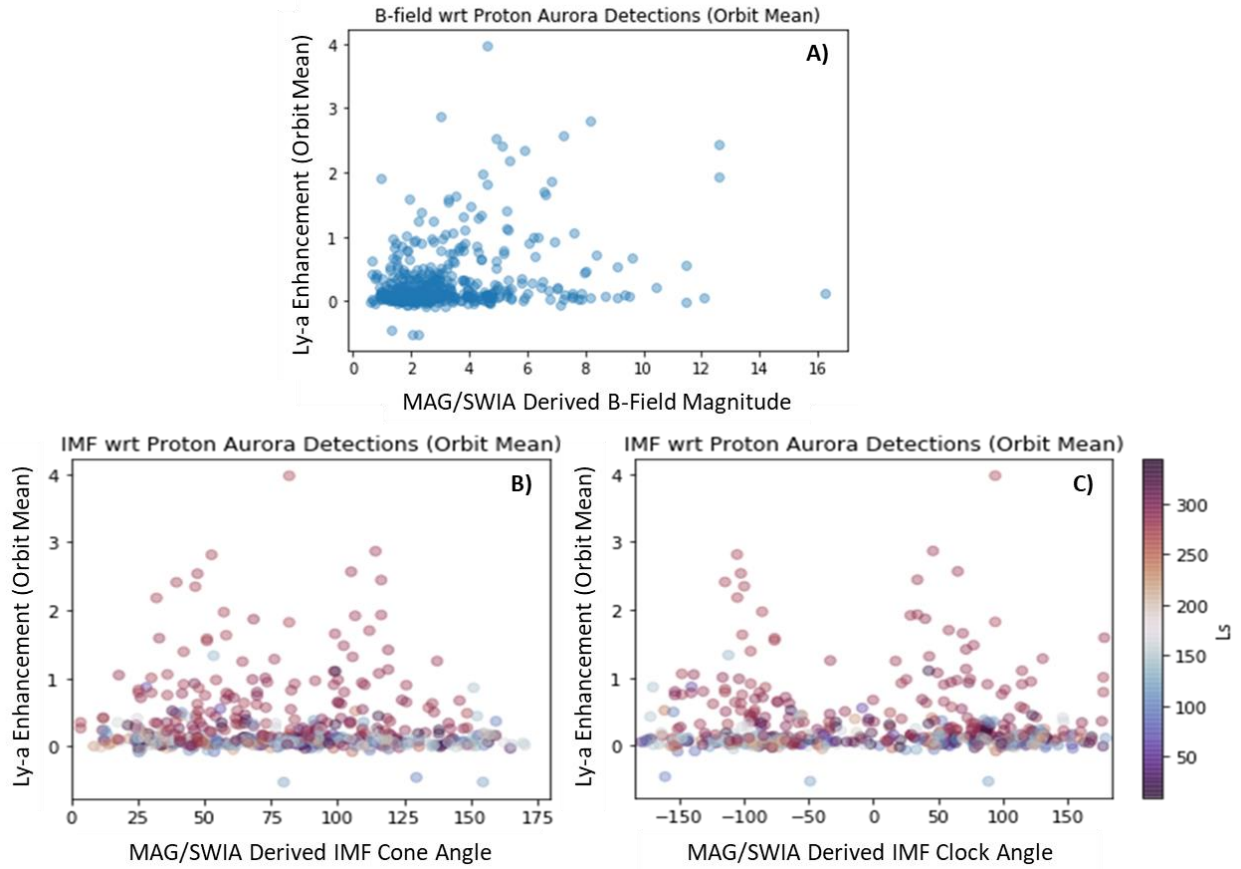


Figure 3.5: Orbit-mean IUVS proton aurora emission enhancements compared with the magnitude (A) and orientation (i.e., cone angle (B) and clock angle (Figure 3.5C)) of the upstream interplanetary magnetic field (IMF). No clear correlation is observed between proton aurora enhancement and IMF magnitude, but a double peak proton aurora enhancement is apparent in both the cone angle and clock angle plots.

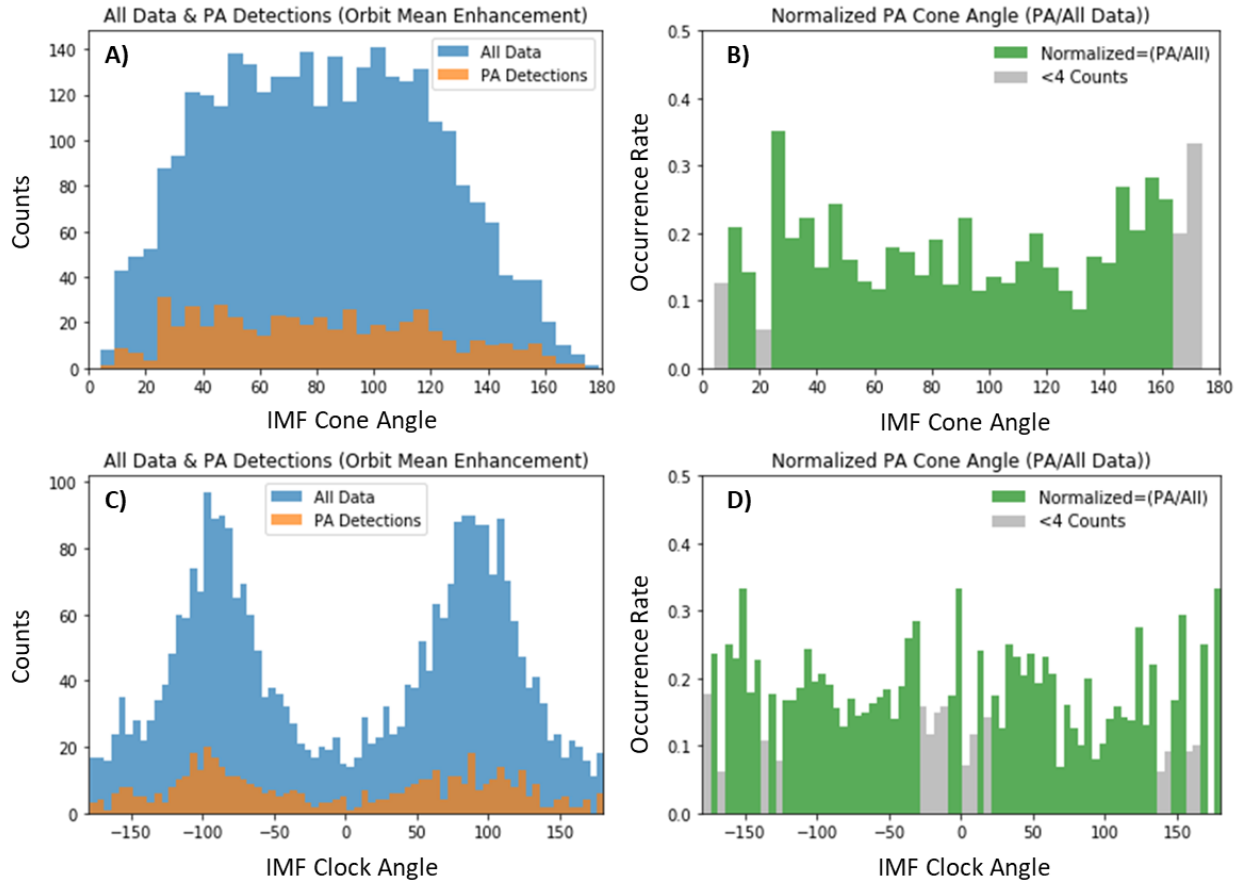


Figure 3.6: Proton aurora observations with respect to IMF cone angle (A) and clock angle (C) (Note that blue histograms shows all IUVS observations and orange histograms show only proton aurora observations). Proton aurora occurrence rates are also shown these respective angles (B and D, respectively).

3.4 Discussion

3.4.1 Expected results based on previous studies and observations

Case studies have previously performed for Earth to simultaneously observe UV proton aurora emissions and the incident protons using remote sensing and *in situ* data (e.g., Gérard *et al.*, 2001; Frey *et al.*, 2001). Gérard *et al.* (2001) identified minor discrepancies between the proton and the Ly- α pre-midnight ovals which they attributed to a combination of instrumental and/or physical effects. And overall, these studies found good agreement between the Ly- α and *in situ* proton observations for terrestrial proton aurora events, demonstrating the usefulness and relevance of this type of comparative analysis.

Based on the results of the Deighan *et al.* (2018) study (*i.e.*, IUVS Ly- α emission enhancements found to increase with increasing SWIA penetrating proton fluxes) one might expect to observe a clear correlation in a multi-year statistical comparison of these different instrument observations during proton aurora events. We do in fact observe this general expected correlation between IUVS and SWIA observations, where an increasing Ly- α enhancement typically corresponds with an increasing penetrating proton flux (indicating that similar influencing factors affect both variables). While both the penetrating proton fluxes and Ly- α emission enhancements increase due to dust activity and extreme solar activity, of particular interest in this study is the *relative* increase of each of these variables in comparison with each other during these major events. The significant amount of deviation from a constant correlation in the observed variability of each dataset is not consistent with expectations.

Because some extreme solar events are commonly associated with enhanced solar wind proton velocities and densities, one might initially predict that orbits with a high penetrating proton flux to Ly- α enhancement ratio would be associated with extreme solar activity (which is opposite to the observed trends). Indeed, one should expect that the solar wind velocity would play a significant role in shaping the results, as higher velocity solar wind protons produce a larger fraction of penetrating protons relative to ENAs or Ly- α (*e.g.*, Halekas, 2017). This is because the electron stripping cross section (associated with converting H to H⁺) increases with energy in the typical solar wind energy range. Alternatively, the charge exchange cross section (associated with converting H⁺ to H) is flat (or slightly decreasing for very high energies), as is the Ly- α cross section in the solar wind energy range. Thus, for a relatively high solar wind velocity, one would expect a higher ratio of penetrating proton flux to Ly- α emission enhancement for proton aurora. While this may be the case for a few orbits with an extremely

high velocity (*e.g.*, near MAVEN orbit ~ 1000), we do not observe any notable correlation between velocity and the penetrating proton flux to Ly- α enhancement ratio (either during dust or solar activity). The lack of correlation between the observed trends in this study with penetrating proton velocities (and thereby, also solar wind velocities) implies that particle velocity is not the primary cause for the large inter-orbit variability that is observed.

3.4.2 Causes for discrepancies between proton aurora IUVS Ly- α emission enhancement and SWIA penetrating proton flux

There are numerous possible causes for the observed discrepancies in the IUVS proton aurora enhancement and SWIA penetrating proton flux comparison. The apparent trends may be due to observational and/or geophysical effects. One possible observational explanation may be due to discrepancies between the observation location of SWIA and IUVS (*e.g.*, differences between the spacecraft and IUVS tangent point distance, SZA, altitude, etc.). It is also possible that one or both of these instruments are not always observing at an altitude where the equilibrium charged fraction between protons and H-ENAs has been reached. This would lead to discrepancies in the expected proton/ENA ratio. Given the difference in observing locations/altitudes of SWIA and IUVS, we consider this cause to be a possible contributor to some of the observed discrepancies. Another possible observational effect may be orbit-to-orbit variations in the viewing angle of MAVEN/IUVS, which could cause an apparent increase/decrease in Ly- α intensity (and thereby, emission enhancement). If the IUVS observational phase angle is oriented at $\sim 90^\circ$, a wavelength shift could lead to absorption of the Ly- α proton aurora spectral emission by the coronal Ly- α spectral emission. A preliminary assessment shows that this effect may be occurring in a few orbits that exhibit very high penetrating proton flux/Ly- α enhancement ratios with IUVS orbit-mean phase angles of $\sim 90^\circ$;

however, generally we do not observe a clear correlation between phase angle and high penetrating proton flux/Ly- α enhancement ratios (see Supplementary Figure 3.7). While it is likely that the results of this study are partially influenced by observational effects, the observed trends of variations in penetrating proton/Ly- α emission enhancement ratios correlating with unique physical events (*i.e.*, dust or solar activity) spanning multiple Martian years is a strong indicator that these observational effects alone cannot be entirely responsible for the observed discrepancies.

Chaffin *et al.* (2021) found that Martian dust activity plays a significant role in increasing the column density of the H corona, leading to increased H escape. A higher column density causes inflation of the H corona further beyond the bow shock, creating larger proton aurora enhancements due to more charge exchange interactions between solar wind protons and coronal H (*e.g.*, Hughes *et al.*, 2019; Chaffin *et al.*, 2021). The increased H column density beyond the bow shock causes an increase in both the densities of the penetrating protons and ENAs. However, the dust storm related increase in the neutral atmospheric CO₂ density leads to a higher equilibrium charged fraction (F_{eq}^+), causing a higher relative fraction of penetrating protons to ENAs. In the context of considering the Ly- α emission enhancement as a proxy for the H-ENA flux related to proton aurora, we would expect to observe a similar increase the ratio of penetrating protons to Ly- α emission enhancement. Additionally, a dust-induced increase in the neutral atmospheric scale height will also cause absorption by CO₂ on the bottom side of the Ly- α altitude-intensity profile (causing a decreased Ly- α brightness and higher altitude at the profile peak). Consequently, the combined effects of increased neutral atmospheric density during dust storms (*i.e.*, an increased F_{eq}^+ and the muted brightness of the Ly- α profile) result in the observed relative increase in the SWIA penetrating proton flux/IUVS Ly- α enhancement ratio during

major dust activity. This variability leads to a seasonal variability in the penetrating proton flux/Ly- α enhancement ratio that tracks with annual changes in H escape/column density due to Martian dust storm activity (Supplementary Figure 3.8 and Supplementary Figure 3.9). We note, however, that this change in the ratio (*i.e.*, the *relative* variability) between these variables should not be confused with the absolute variability in Ly- α emission enhancement with season, as the largest and most frequent annual proton aurora activity on Mars occurs around the southern summer solstice, corresponding with the maximum annual H column density (Hughes *et al.*, 2019; Halekas, 2017). Thus, if not for the effect of CO₂ absorption on the Ly- α profile, it is interesting to speculate that the Ly- α intensities and emission enhancements during this season would be even larger than those observed.

The Ly- α emission enhancement serves as a proxy for ENAs incident on the Martian atmosphere. While SIWA measures quantities of the incident particles themselves (*i.e.*, proton velocities and densities), IUVS observes Ly- α photons emitted by H atoms to calculate an integrated column H brightness. Thus, it is important to consider that the Ly- α intensity can vary based not only on H abundance (*e.g.*, the number density of photons), but also due to the particle temperature and/or observation angle of the spacecraft. One way that the Ly- α enhancement could produce inaccurate results as a proxy for the penetrating H-ENA is if the H temperature increases but the H number density does not. Increased particle temperatures associated with extreme solar events could lead to a higher Ly- α emission enhancement without a corresponding increase in the H-ENA number density (and thereby, the penetrating proton density and flux). However, as extreme solar events usually involve increased solar wind particle fluxes, it is likely that both the incident solar wind proton temperature and density are increasing during these orbits. A study by Mayyasi *et al.* (2018) observed a rapid 80K increase in the exospheric

temperature induced by a CME/solar flare. This impulsive solar event also caused a dramatic increase in the observed Ly- α brightness and a decrease in the H density at the exobase (corresponding with an increased column density above the exobase), resulting in a ~five-fold increase in H escape flux due to Jeans escape. Although the H column density is found to increase during both dust storms and extreme solar activity, seasonal atmospheric escape due to dust activity is twice as large (an order of magnitude annual variation as calculated by Halekas, 2017) and persistent for an extended period of the year (compared with only a few days of increased escape due to solar events). Because we observe absolute increases in *both* the Ly- α enhancement and penetrating proton flux in most orbits during extreme solar events (Supplementary Figure 3.2), the solar wind proton flux and/or H column density (induced by higher exospheric temperatures and escape rates) must be increasing during these periods. However, an increase in one or both of these parameters alone could not account for the observed decrease in the relative ratio of the penetrating proton flux to Ly- α enhancement during these times. And because we are observing Ly- α emission enhancements (*i.e.*, subtracting out the contribution from coronal H) it must be the case that the increasing Ly- α enhancements are caused by the solar wind particle temperatures rather than the exospheric temperature. Thus, we determine that the increased solar wind proton (and thereby, ENA) temperatures during extreme solar events is primarily responsible for the uncharacteristically high Ly- α proton aurora enhancements.

Independent of the penetrating proton flux to Ly- α enhancement ratio, the largest proton aurora events throughout the MAVEN mission (*i.e.*, those exhibiting the largest Ly- α emission enhancements) occur during periods of *both* high dust and extreme solar activity. This is due to the combination of the effects described above: 1) the increased H column density due to dust

activity facilitates a larger H-ENA conversion rate upstream of the bow shock, and thereby a higher density of ENAs that penetrate the atmosphere; 2) increased solar wind proton densities during extreme solar events supply a larger number of incident protons that can convert into ENAs; and 3) increased exospheric temperatures during extreme solar events produce even further expansion of the H corona and H column density above the bow shock (further increasing the ENA conversion rate) and create larger enhancements in the Ly- α profile (due to increased particle temperatures).

A possible source of discrepancy between SWIA and IUVS observations that has not been evaluated in this study is the influence of global and crustal magnetic fields. Although changes in the magnetic environment do not affect ENAs, they could indeed affect the incident and penetrating proton populations. In a future study we will evaluate the effects of remnant crustal fields and IMF strength and orientation on proton aurora observations. We have also not considered the direct effects of the solar wind EUV, ram pressure, or Mach speed; these three parameters have been previously found to influence the bow shock location, and thereby the exposed H column density upstream of the bow shock (*e.g.*, Halekas *et al.*, 2016). More work needs to be done to determine how seasonal and/or instantaneous variability in these factors (*e.g.*, heliocentric distance or extreme solar events) might influence the results of this study. Finally, there may be possible effects associated with using orbit-averaged values and constraining the study to only orbits with overlapping SWIA and IUVS observations. While averaging the measurements from the periapsis segment of each MAVEN orbit is the most effective method for comparing these two large datasets, this analysis method could obscure any inter-orbit temporal variability. If the penetrating proton flux or the Ly- α emission enhancement respond on different timescales to the varying input parameters (*e.g.*, if there is a lag in the

response time of one of the observed quantities), we would not observe the related variability between the IUVS and SWIA datasets.

3.4.3 *Empirical estimation of proton aurora Ly- α emission enhancement*

We present a direct application of the results of our study in estimating a Ly- α emission enhancement for proton aurora events. Thus far we have considered the Ly- α emission enhancement as a proxy for the ENA flux associated with proton aurora. However, as discussed above, there are certain circumstances in which Ly- α does not act as a sufficient proxy for ENA variability. Based on the established relationship between penetrating proton flux and Ly- α enhancement for proton aurora, we may determine a quantifiable correlation for these two parameters. As shown in Figure 3.7, if the Ly- α emission enhancement is considered as the dependent variable and penetrating proton flux the independent variable, creating a trendline for this plot (using linear least-squares regression) provides an equation (shown on plot) that maybe used to approximate the observed Ly- α enhancement for proton aurora events during “nominal conditions” (*i.e.*, not during periods of high dust or solar activity) based on measurements of the penetrating proton flux. Moreover, by subsetting the data on this plot into regions of relatively high and low penetrating proton to Ly- α enhancement ratios (*i.e.*, points far below and above the best-fit trendline, respectively), we may more accurately determine the Ly- α enhancement for a proton aurora event based on a knowledge of the local neutral atmospheric density (particularly relating to dust activity and/or season) or solar activity during the period of interest. This type of empirical estimate provides a useful and new tool for observations of future auroral events, particularly during periods when direct observations may not be possible due to spacecraft location/geometry. We note, however, that this estimate does not take into account variability associated with observational parameters such as SZA and altitude.

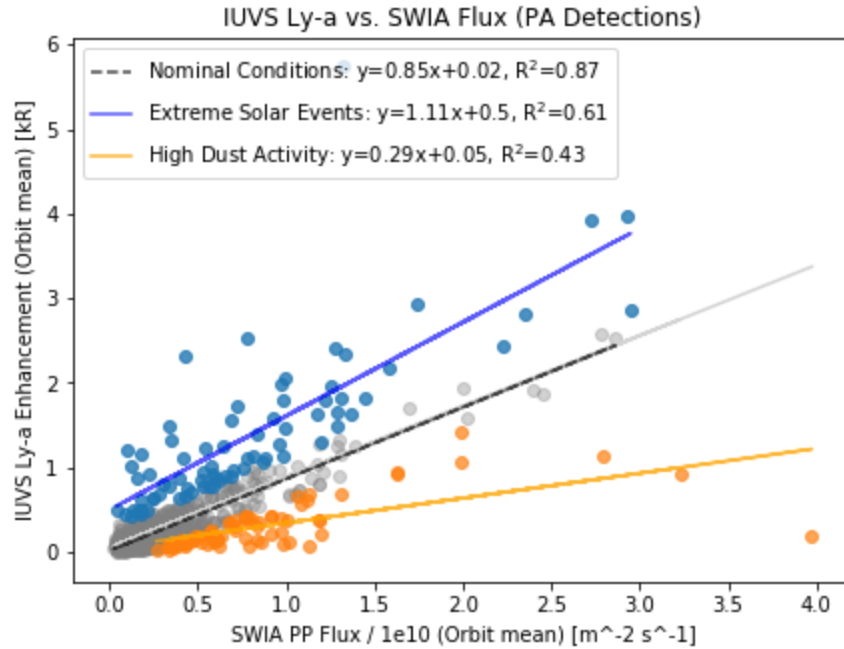


Figure 3.7: IUVS Ly- α emission enhancement versus SWIA penetrating proton flux (inverted plot of Figure 3.1, considering Ly- α enhancement as the dependent variable). The trendlines give an estimate of the Ly- α enhancement for proton aurora event assuming a foreknowledge of the penetrating proton flux and the local dust/solar activity conditions.

3.4.4 Connections between proton aurora and the upstream magnetic field environment

In order to better quantify correlations between proton aurora and the local magnetic/plasma environment, we look for connections between Martian proton aurora and the upstream magnetic field: comparing proton aurora detections with magnitudes and orientations of the upstream magnetic field that influences the Mars induced magnetic field environment.

The possible preferential occurrence of proton aurora during periods of more radial IMF orientations could be caused by unique interaction between the IMF and the Mars induced magnetosphere. A modeling study by Gérard *et al.* (2018) found that any deviation from a horizontal induced magnetic field (*e.g.*, during near-radial IMF conditions) could “decrease the efficiency of the magnetic barrier and actually guide protons deeper into the atmosphere.” It would be interesting to search for evidence of variability in the penetrating proton flux (as well as the penetrating proton flux to Ly- α enhancement ratio) at different IMF angles, as such an

observation would add credence to the modeling predictions of Gérard *et al.* (2018). We defer such a project for a more detailed forthcoming study.

The double peak structure in the cone/clock angle plots in Figure 3.5 (*i.e.*, relating proton aurora emission enhancement to IMF orientation), implies a connection between the largest proton aurora enhancements/activity and specific IMF cone and clock angle orientations. (It is interesting to note that the locations of the peaks may be consistent with orientations of the Parker spiral under nominal conditions.) However, we also note that a possible observational bias may exist in the results due to limited data availability. Thus, more work needs to be done before these findings can be interpreted with confidence.

In a future study, we will carry out specific case studies to evaluate the effects of crustal fields on proton aurora. We will also look for corresponding variability between unique IMF orientations, penetrating proton fluxes, and the penetrating proton flux to Ly- α enhancement ratio. Lastly, it may also be useful to consider the results in a different Mars coordinate system (*e.g.*, relative to the electric field environment) to determine if new trends arise in the dataset. These results will aid in our understanding of the interactions between Martian proton aurora and the upstream/local magnetic environment.

3.5 Conclusions

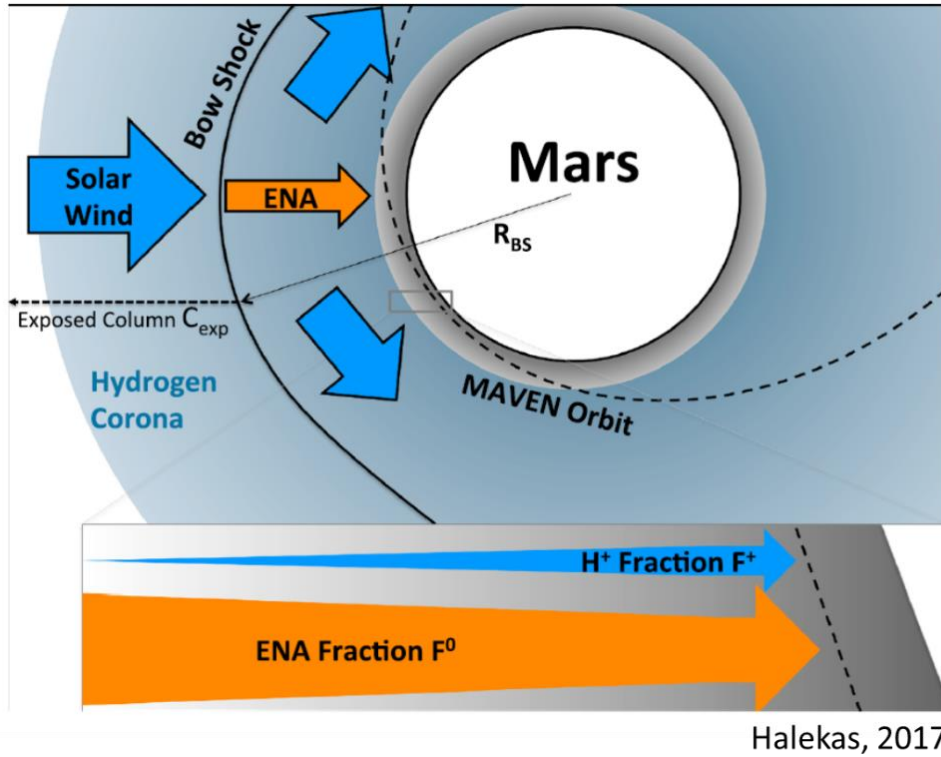
In this study, we focus on large scale statistical comparisons of proton aurora observations by a remote sensing and *in situ* instrument. We determine that the observed trends in the data (*i.e.*, an excess in penetrating proton flux relative to Ly- α enhancement during dust activity and a deficit during extreme solar events) are due to the compounding effects of multiple physical and observational causes. During major dust activity, an increase in the equilibrium charged fraction combined with a decreased maximum Ly- α brightness (due to CO₂ absorption on the bottom side

of the Ly- α profile) lead to an observed excess in penetrating proton flux relative to Ly- α emission enhancement. And increased solar wind particle temperatures during extreme solar activity cause an increased Ly- α brightness, leading to an apparent deficit in penetrating proton flux relative to Ly- α emission enhancement.

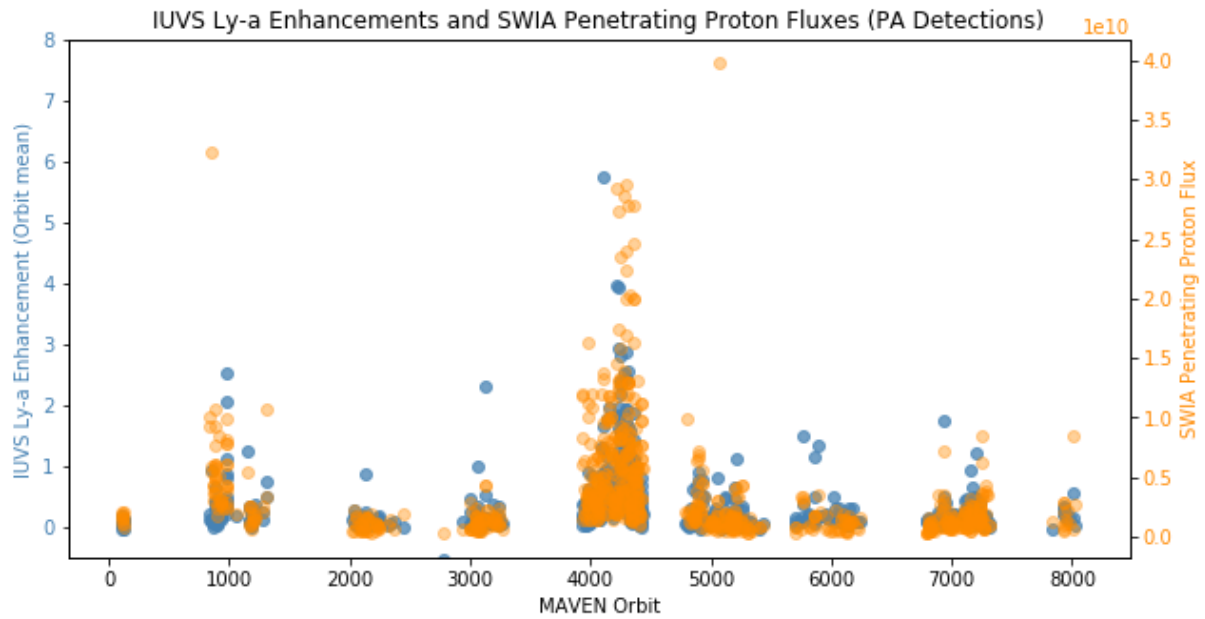
We compare proton aurora detections with orbit averaged measurements of the magnitude and orientation of the local IMF upstream of the Martian bow shock. We identify a possible correlation between high proton aurora activity and certain IMF cone/clock angles, and a possible preference for proton aurora occurrence during near-radial IMF orientations. Work is ongoing to authenticate and expand upon these findings.

Some questions that may yet be addressed in a future study are the specific effect of dust and extreme solar activity on atmospheric H and CO₂ column densities and temperatures. It would also be of interest to evaluate if any additional factors could be affecting or concealing any apparent trends between the datasets (*e.g.*, SZA, L_s, CO₂ absorption, etc.). In a future study, it would also be interesting to compare our results with direct measurements of ENAs made by another spacecraft (as MAVEN is not equipped with an ENA detector). One would expect to observe a close correlation between penetrating protons and the ENAs, with similar seasonal variability in the charged fractions around southern summer. Concurrent Ly- α observations would provide useful comparative context for assessing variability in the local dust and solar wind environments. Lastly, in order to better understand the unique variability within certain orbits, it would be beneficial to undertake specific case studies of different time periods. In a forthcoming publication, we examine numerous orbit case studies of “atypical” proton aurora, further developing our understanding of the unique processes that can cause these events to deviate from the expected correlation.

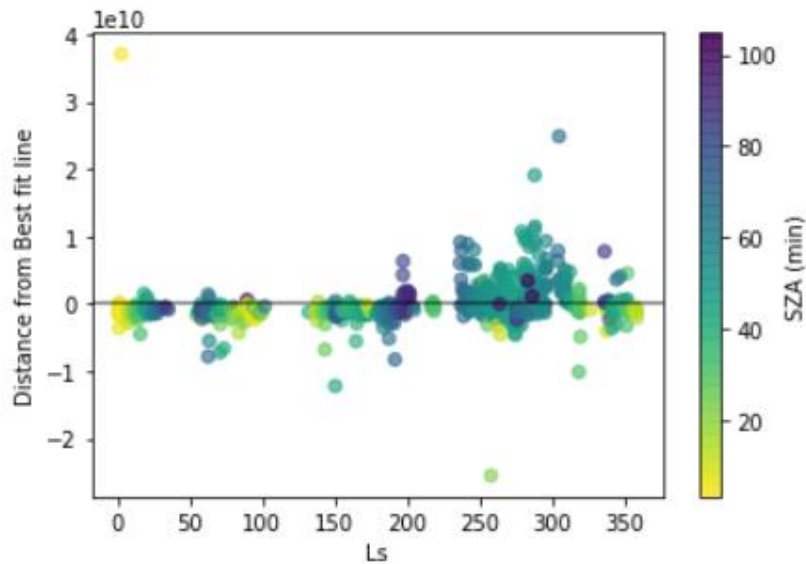
Chapter 3 Supplementary Figures



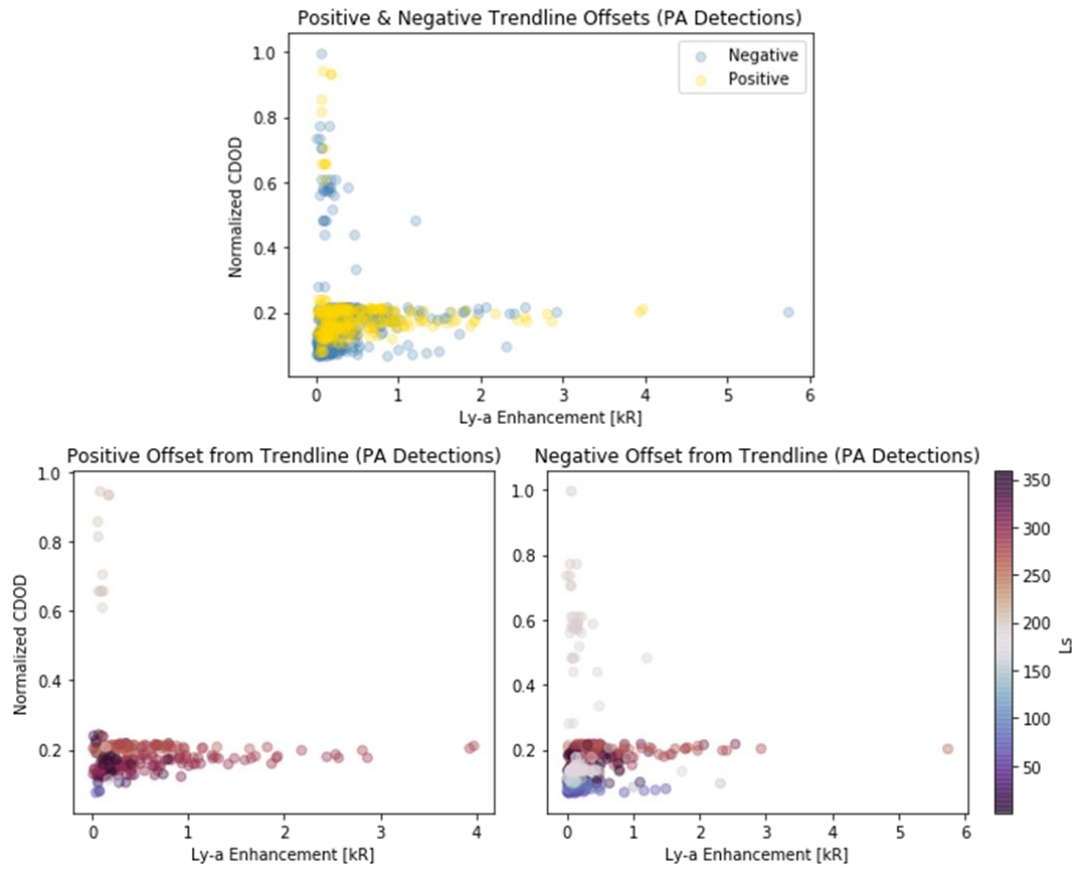
Supplementary Figure 3.1: Representation of the interaction between solar wind protons and the extended Martian H corona to create H-ENAs and penetrating protons during the proton aurora formation process (Figure 1 from Halekas, 2017).



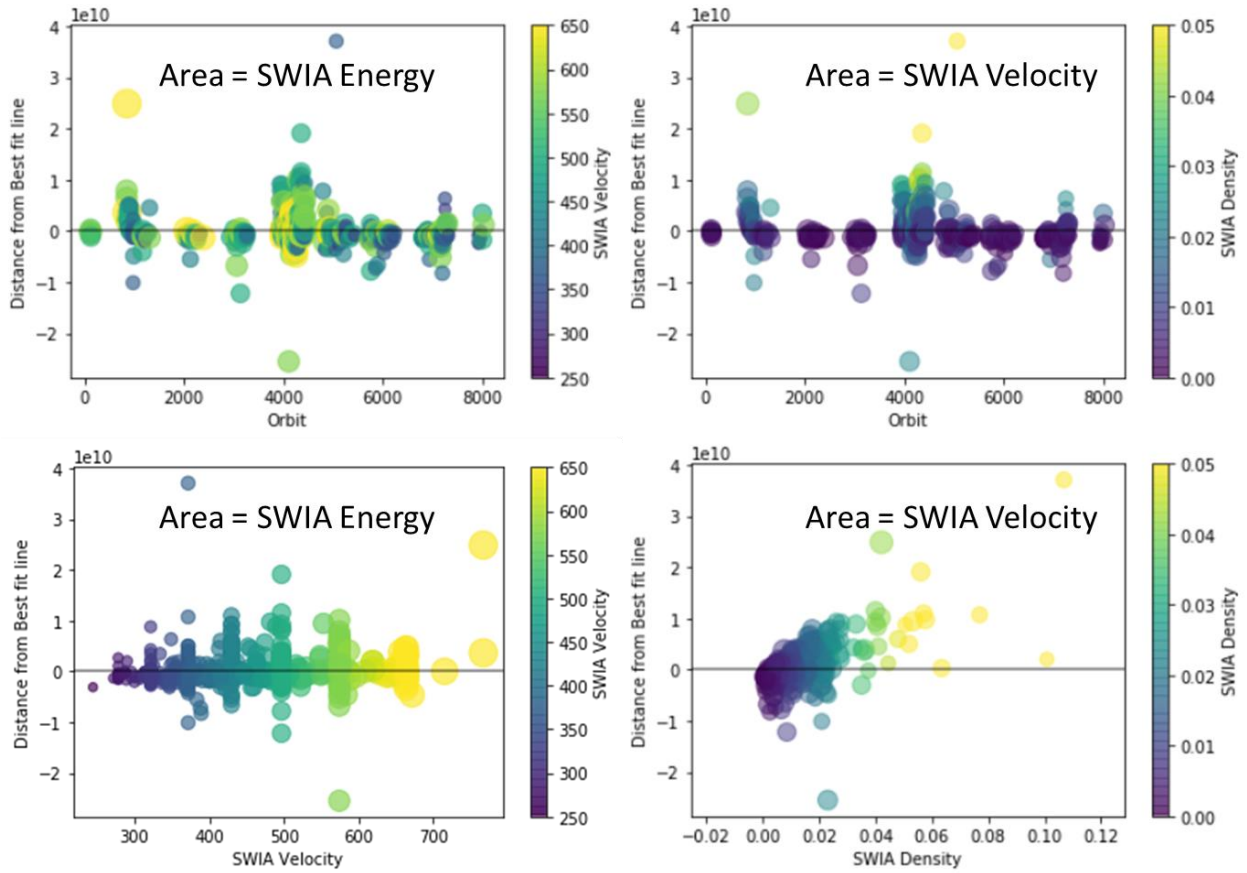
Supplementary Figure 3.2: Overlapping observations of IUVS Ly- α emission enhancement and SWIA penetrating proton flux for proton aurora detections in the first few years of MAVEN orbits.



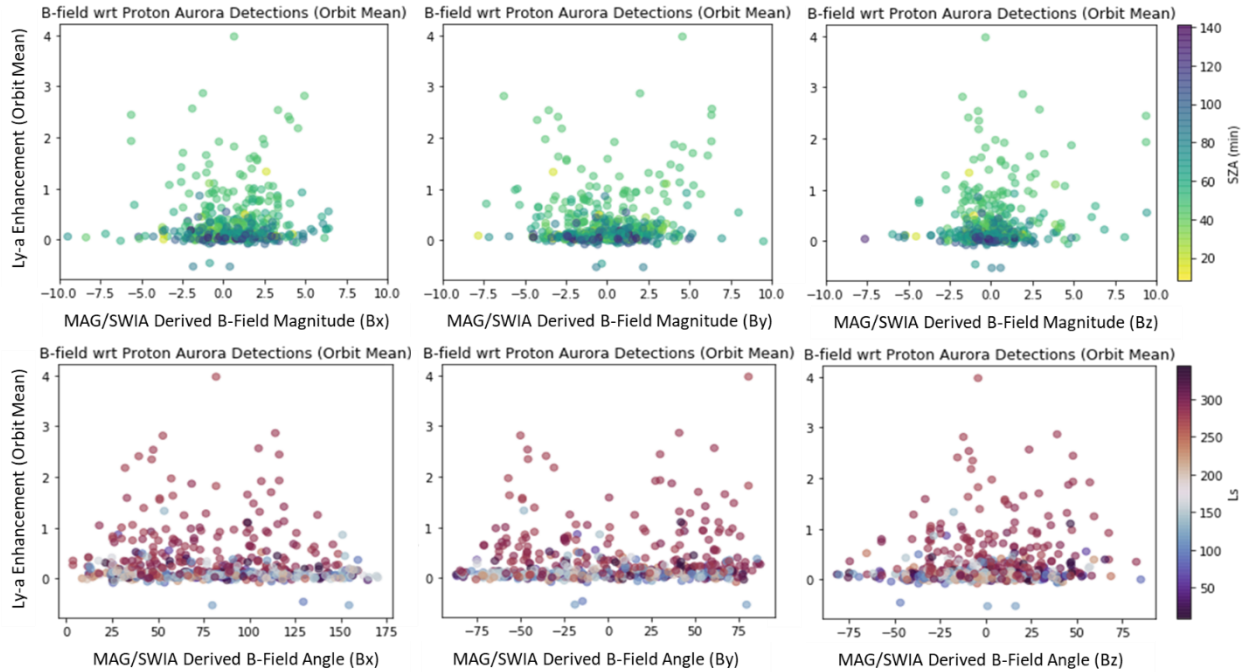
Supplementary Figure 3.3: Offsets from the SWIA-IUVS best-fit trendline compared with season (solar longitude, L_s). The largest offsets (corresponding with a relative excess of penetrating proton flux compared with Ly- α emission enhancements) occur around southern summer solstice ($L_s \sim 270$). Note that color corresponds with the orbit minimum peak IUVS tangent point SZA.



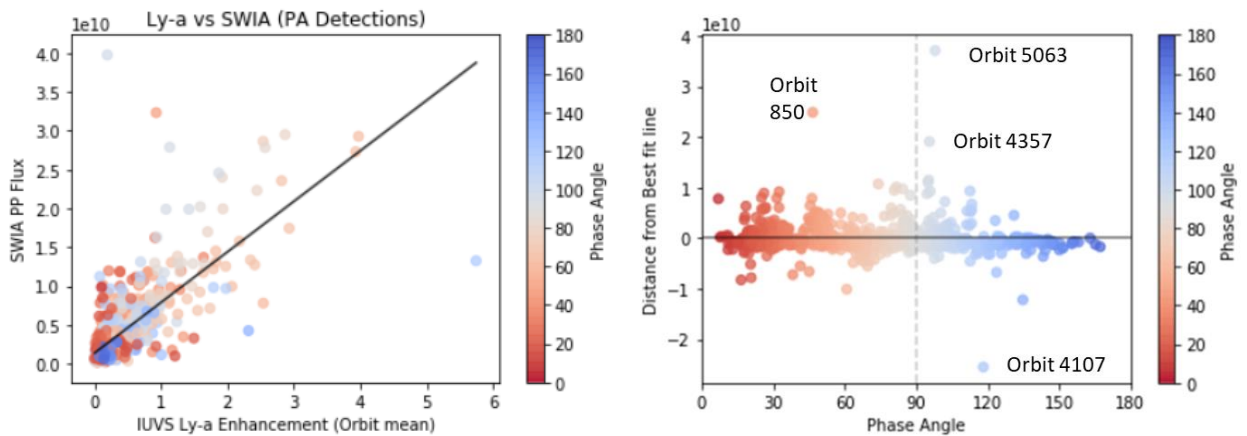
Supplementary Figure 3.4: Same as Figure 3.4C but showing positive and negative offsets from the best-fit trend line overplotted in blue and gold, respectively (top plot), as well as on individual plots with season as the color (bottom).



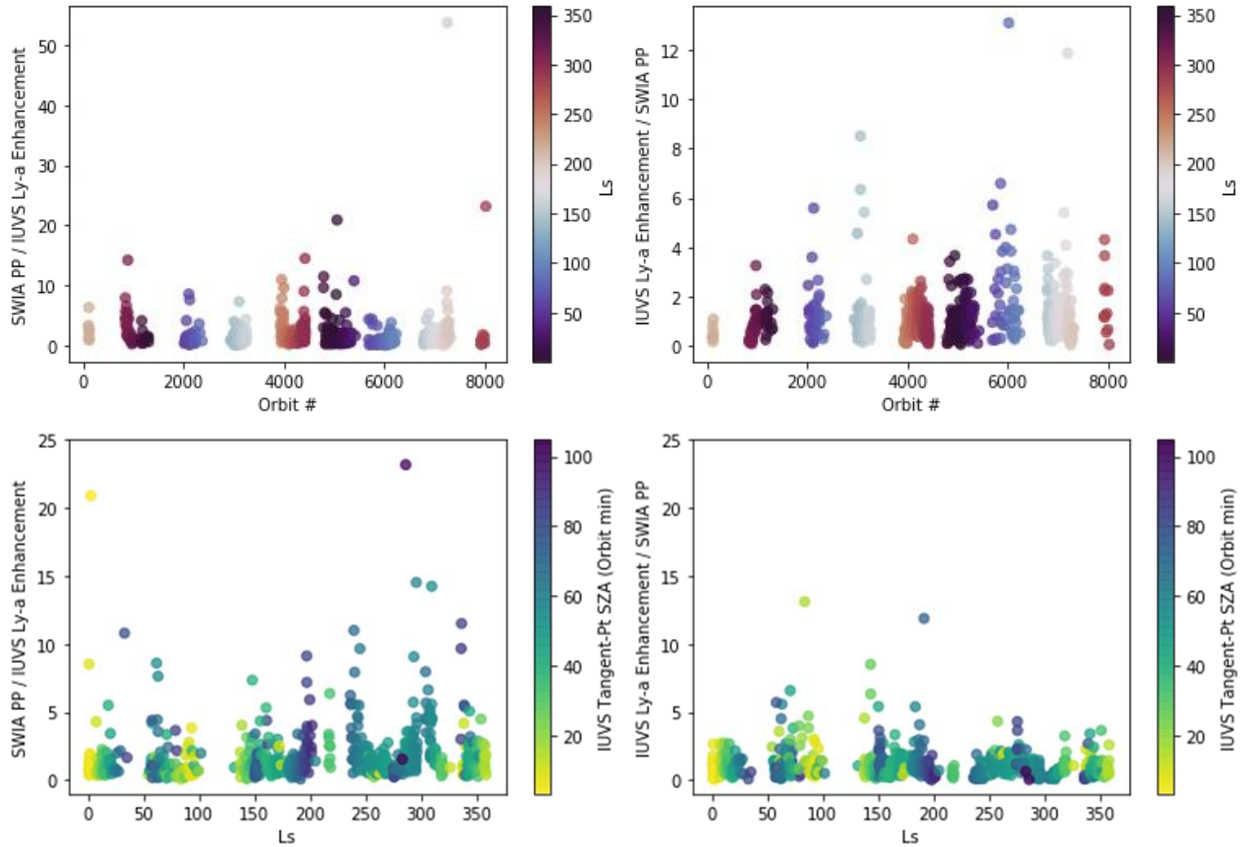
Supplementary Figure 3.5: Top plots: Same as Figure 2, Right (offsets from the SWIA-IUVS best-fit trendline compared with MAVEN orbit numbers) showing SWIA penetrating proton velocity (top left) and density (top right) as the color. Bottom plots: Offsets from best-fit trendline compared with SWIA penetrating proton velocity (bottom left) and density (bottom right).



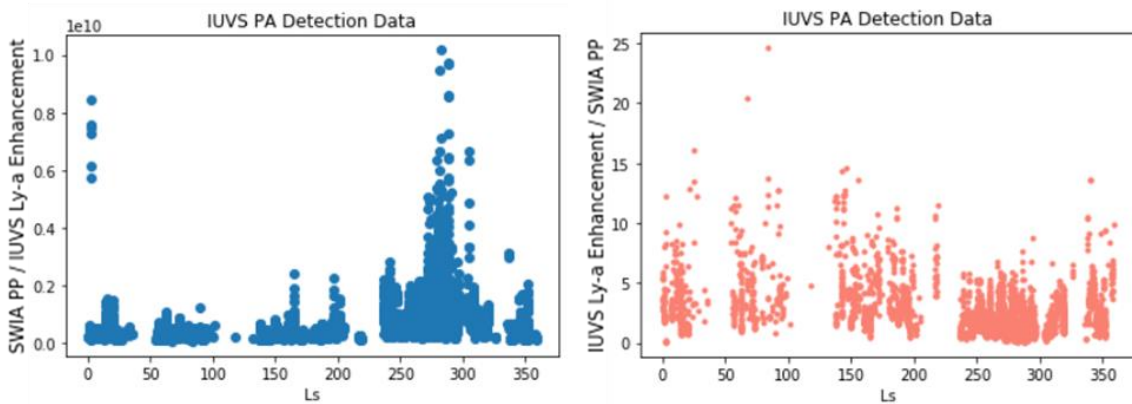
Supplementary Figure 3.6: Same as Figure 3.5, but the IMF magnitude and orientations are shown in different MSO coordinates. Note that color on the corresponds with IUVS orbit mean tangent point SZAs (top), and season (shown as L_s) (bottom).



Supplementary Figure 3.7: (Left) Same as Figure 3.1, Left, but showing IUVS phase angle observations as the color. (Right) Offsets from the SWIA-IUVS best-fit trendline compared with IUVS phase angle.



Supplementary Figure 3.8: Ratios of orbit-averaged SWIA penetrating proton flux to IUVS Ly- α emission enhancement (left plots) and Ly- α emission enhancement to penetrating proton flux (right plots), compared with MAVEN orbit numbers (top plots) and season, as L_s (bottom plots). (Note that SWIA penetrating proton flux is scaled down by dividing by 1×10^{10} .)



Supplementary Figure 3.9: Same as Supplementary Figure 3.8, but for each individual IUVS orbit periapsis limb scan (as opposed to orbit-averaged values). The seasonal variability of the penetrating proton flux/Ly- α emission enhancement ratio is somewhat more evident in individual detections (as averaging over an entire orbit can mask small scale variability in some cases). (Note that the SWIA penetrating proton flux is scaled down by dividing by 1×10^{10} in the right plot.)

4. Atypical Observations of Martian Proton Aurora

For submission to *Journal of Geophysical Research: Space Physics*

Hughes, A., Chaffin, M., Mierkiewicz, E., Fowler, C., Halekas, J., Schneider,

N., Deighan, J., Jain, S., *et al.*

Chapter 4 Key Points

- We identify different types of Martian proton aurora events that deviate from the typical characteristics of previous observations and known formation mechanisms.
- “Atypical” proton aurora exhibit variability in the peak altitude and/or intensity of the hydrogen Lyman-alpha profile between limb scans within a single orbit.
- Nightside proton aurora detections account for ~4% of all IUVS proton aurora detections, however, they are only observed to occur <1% of the time in all nighttime IUVS data.

Chapter 4 Abstract

Due to the lack of a planetary-wide magnetic field on Mars, proton aurora are expected to form on the planet’s dayside by electron stripping and charge exchange with the neutral corona. Previous studies have found a strong solar zenith angle (SZA) and seasonal dependence for Martian proton aurora, primarily constraining these events to the dayside and causing highest occurrence rates during southern summer. However, we identify unique types of Martian proton aurora that deviate from typically observed characteristics of previous detections and known formation mechanisms. Herein we present the results of a study of unusual Martian proton aurora observations. We identify detections of numerous types of “atypical” proton aurora (*e.g.*, “variable” and nightside events), evaluating the variability and investigating possible formation mechanisms for these phenomena. “Variable” proton aurora are observed to exhibit variability in the peak altitude and/or intensity of the hydrogen Lyman-alpha (Ly- α) profile between limb scans within a single orbit; these observations are understood to correspond with spatial and/or temporal variability within a proton aurora event. We present case studies of observations of variable proton aurora that are found to be associated with variability caused by neutral atmospheric waves/tides and the upstream solar wind. Additionally, despite formation

mechanisms that should constrain proton aurora to the dayside, we identify a small number of detections on the planet's nightside. We present the results of a statistical evaluation of nightside proton aurora events (defined as $SZA > 100^\circ$). We find that nightside proton aurora detections account for ~4% of all IUVS proton aurora observations and 10% of the MAVEN orbits exhibiting proton aurora; however, nightside detections are only observed in <1% of all nighttime observations, making them extremely uncommon. We consider the potential effects of magnetic fields on nightside proton aurora events and propose possible formation mechanisms for these phenomena.

Studying “atypical” proton aurora events aids in characterizing the different influencing factors on unique sub-types of Martian proton aurora. The results of this study provide a deeper understanding of interactions between the solar wind, the local magnetic/plasma environment, and the Martian upper and neutral atmosphere. Furthermore, we report the first known observation of energy transport from the lower/middle-atmosphere via waves/tides affecting upper atmospheric auroral variability at Mars. Thus, the results of this study will provide useful context for future investigations that aim to develop our understanding of the interconnectedness between dominant processes in the lower-, middle-, and upper-atmosphere of Mars and the transport of energy throughout the Martian atmosphere.

4.1 Introduction and Background

Three types of aurora that have been observed at Mars: discrete (Bertaux *et al.*, 2005), diffuse (Schneider *et al.*, 2015), and proton aurora (Deighan *et al.*, 2018; Ritter *et al.*, 2018; Hughes *et al.*, 2019). Of these three types of aurora, proton aurora are the most recently identified and the most commonly observed at Mars (Hughes *et al.*, 2019). Although previous studies have evaluated the phenomenology and statistical properties of proton aurora, few studies have

assessed the characteristics of abnormal proton aurora events. In this study, we build on previous work by presenting multiple case and statistical studies of unusual, or “atypical”, proton aurora observations.

Unlike terrestrial aurora, Martian proton aurora form via interactions between solar wind protons and the extended Martian hydrogen corona. Through electron stripping and charge exchange processes, incident solar wind protons are able to remove electrons from neutral coronal hydrogen (H) and convert into energetic neutral atoms (ENAs). This process allows the solar wind protons to bypass the Martian induced magnetic field environment (*e.g.*, the bow shock and magnetic pileup boundary (MPB)) and be transported to the lower parts of the atmosphere. When these excited ENAs de-excite, they emit a Lyman-alpha ($\text{Ly-}\alpha$) photon, which is detected as proton aurora (see Deighan *et al.*, 2018 and Hughes *et al.*, 2019 for a more detailed discussion of formation processes). During the formation of proton aurora, the incident solar wind protons can convert back and forth between protons and H-ENAs many times before ultimately deexciting when in the ENA state and emitting a $\text{Ly-}\alpha$ photon.

4.1.1 Relationship between Penetrating Protons and Proton Aurora on Mars

Martian penetrating protons (*i.e.*, solar wind protons that penetrate into the upper atmosphere) and proton aurora have previously been found to be strongly correlated. The existence of proton aurora was initially predicted at Mars based on models (*e.g.*, Kallio and Barabash, 2001) and observations of a penetrating proton population (Halekas *et al.*, 2015). The preliminary observations of penetrating protons by Halekas *et al.* (2015) were made using the *in situ* SWIA instrument (*i.e.*, Solar Wind Ion Analyzer, Halekas *et al.*, 2013) onboard the MAVEN (Mars Atmosphere and Volatile Evolution mission) spacecraft (Jakosky *et al.*, 2015). The SWIA observations were subsequently found to be correlated with enhancements in remote sensing

observations of the hydrogen Ly- α emission (121.6 nm) (Deighan *et al.*, 2018), which were made using the IUVS instrument (*i.e.*, Imaging UltraViolet Spectrograph, McClintock *et al.*, 2014) onboard MAVEN. Deighan *et al.* (2018) found that increased Ly- α intensities during proton aurora events (identified as a Ly- α emission enhancement between \sim 110-150 km in altitude) corresponded with periods of increased SWIA penetrating proton flux.

A recent study by Hughes *et al.* (2021) identified strong correlations between MAVEN orbit-averaged SWIA penetrating proton fluxes in connection with orbit-averaged IUVS Ly- α emission enhancements of proton aurora events. Hughes *et al.* (2021) also found that proton aurora can be influenced from the “top down” (*e.g.*, due to extreme solar activity) or from the “bottom up” (*e.g.*, due to strong dust storms). Both influencing processes can act to increase the H column density above the exosphere, providing more available H to interact with solar wind protons through charge exchange.

4.1.2 “Typical” vs. “Atypical” Martian Proton Aurora

Due to the unique formation mechanism of proton aurora, and the strong connection with the Martian hydrogen corona, these aurora have been found to exhibit a strong SZA and seasonal dependence. A previous statistical study by Hughes *et al.* (2019) used IUVS observations of Martian proton aurora to determine that these events are primarily constrained to the dayside of the planet ($SZA < \sim 90^\circ$) and have highest Ly- α intensities, emission enhancements, peak altitudes, and occurrence rates (nearing 100%) around southern summer solstice (*i.e.*, solar longitude (L_s) ~ 270). This seasonal dependence of proton aurora was found to be directly related to the dust-induced increase in the H column density above the exobase and escape rate during this period (*e.g.*, Hughes *et al.*, 2019; Chaffin *et al.*, 2021; Chaffin *et al.*, 2014; Clarke *et al.*, 2014; Halekas, 2017). They identified proton aurora events in $\sim 14\%$ of dayside periapsis

profiles (with notable seasonal variability), making proton aurora the most commonly observed type of aurora at Mars.

Proton aurora events have been observed to change significantly in the ~4-5 hours between MAVEN orbits, at times appearing or ceasing altogether within that period (*e.g.*, Deighan *et al.*, 2018). While inter-orbit and seasonal variability is common in proton aurora, major variations within a single orbit (*i.e.*, intra-orbit variations) are rare. Apart from the variability associated with changing SZA, the altitudes and intensities of proton aurora observations generally show little variability between IUVS limb scans within an orbit.

Previous studies have identified variations within individual proton aurora events, referred to as “variable” or “patchy” proton aurora (*e.g.*, Hughes *et al.*, 2019; Crismani *et al.*, 2019). In these observations, the Ly- α profile intensity is seen to increase/decrease during a single orbit, indicating spatial and/or temporal variability. Hughes *et al.* (2019) reported observing this type of atypical variability in Ly- α profiles in their statistical IUVS proton aurora study. And a study by Crismani *et al.* (2019) used MAVEN radio occultation data in combination with IUVS and SWIA observations of variability in a proton aurora event to characterize variability in localized ionization in the Martian ionosphere.

4.1.3 “Modulated” H and Penetrating Proton Detections at Mars

A recent study by Fowler *et al.* (2019) identified numerous instances of a quasi-periodic structure in the upstream solar wind conditions at Mars (*e.g.*, in the proton flux, energy flux, magnetic field strength, and velocity). Further, these observations were found to coincide with similar quasi-periodic behavior in the SWIA penetrating proton observations (Supplementary Figure 4.1). Because there were no corresponding variations observed in the neutral atmosphere,

it was determined that these variations in penetrating protons were caused by variations in the upstream solar wind.

Further, Fowler *et al.* (2019) found a strong correlation between the orientation of the interplanetary magnetic field (IMF) and the mean amplitude of the density variations (and/or the period of the variability) for highly modulated penetrating proton events. They determined that the highest amount of density and/or temporal variation (*i.e.*, the most modulated events) occur during periods when the IMF orientation is nearly or “quasi-” radial. It was determined that this radial IMF creates an ideal orientation of the foreshock region upstream of the bow shock, causing convection in foreshock structures and localized enhancements of charge exchange. Because of the interconnected relationship between penetrating protons and H-ENAs to bypass the MPB, Fowler *et al.* (2019) made correlations between their findings of modulated penetrating protons and modulated H in the Martian atmosphere. However, the Fowler *et al.* (2019) study did not entail unique observations of Martian H, nor did it entail a correlation with observations of proton aurora. Herein we expand on the previous study by Fowler *et al.* (2019) to identify modulated proton aurora and characterize other unique/atypical variations in Martian proton aurora.

4.2 Data and Methods

The Imaging Ultraviolet Spectrograph (IUVS), onboard the Mars Atmosphere and Volatile Evolution mission (MAVEN) spacecraft observes the upper atmosphere and ionosphere of Mars in far- and mid-ultraviolet (UV) wavelengths (110–340 nm) (McClintock *et al.*, 2014). We use Level-1C H Ly- α observations from periapsis limb scans (*i.e.*, altitude-intensity profiles) to identify and characterize proton aurora detections. We additionally incorporate IUVS CO₂⁺ UV-Doublet (UVD) profiles as a proxy for assessing neutral atmospheric variations. We use a

database of Martian proton aurora detections compiled in a previous statistical study by Hughes *et al.* (2019), expanding on this list by including observations through MAVEN orbit ~8400 (which includes the southern summer season from Mars Year 34). (See Hughes *et al.*, 2019 for more information on proton aurora detection methodology.)

In order to compare IUVS observations with variability in the neutral CO₂ and plasma environments (*e.g.*, penetrating protons and local magnetic fields), we compare IUVS observations with data from multiple other instruments onboard MAVEN: the Neutral Gas and Ion Mass Spectrometer (NGIMS) (Mahaffy *et al.*, 2015), the Solar Wind Ion Analyzer (SWIA) (Halekas *et al.*, 2013), and the Magnetometer instrument (MAG) (Connerney *et al.*, 2015).

In this study we consider proton aurora detections throughout the entire MAVEN mission. However, in evaluating IUVS comparisons with the observations in the Fowler *et al.* (2019) study, we consider only detections from the ~3 week time period of their study (*i.e.*, November/December 2016).

4.3 Observations of “Atypical” Proton Aurora

4.3.1 “Variable” proton aurora

We describe detections of “variable” proton aurora, *i.e.*, observations displaying variability in altitude and/or intensity within a single MAVEN orbit. For the purposes of this study, we distinguish between two general types of “variable” proton aurora: 1) observations that exhibit corresponding variability with the neutral CO₂ atmosphere, and 2) observations that do not correspond with variability with the neutral atmosphere.

4.3.1.1 “Variable” proton aurora associated with neutral atmospheric variability

We first consider proton aurora variability that is correlated with the neutral atmosphere. Although MAVEN does not observe neutral CO₂, the CO₂⁺ UV-Doublet (UVD) emission

directly tracks with CO₂ and is a commonly used proxy. Thus, we may assess the concurrent variability of H and CO₂ by comparing peak altitudes and intensities of the Ly- α and CO₂⁺ UVD profiles for each IUVS limb scan in a MAVEN orbit.

In certain proton aurora detections, we observe an increase in altitude and/or intensity of proton aurora Ly- α observations between IUVS limb scans that tracks with similar profile variability in the corresponding CO₂⁺ UVD limb scan from the same orbit. Figure 4.1 presents an example of this sort of variable proton aurora event observed during MAVEN orbit 4107. As shown in Figure 4.1, the Ly- α peak altitude in this orbit increases by ~5km in the fourth through seventh limb scans, and subsequently goes back down in later orbit scans. The peak altitudes in the offset Ly- α and CO₂⁺ UVD altitude-intensity profiles are observed to concurrently vary with each other in the same mid-orbit limb scans. (We note a lack of corresponding variability in other IUVS emissions, verifying that the observed changes are physical rather than instrumental/observational.)

In addition to variability in the IUVS Ly- α limb scan peak altitudes, the Ly- α emission enhancements during this orbit are also observed to fluctuate between limb scans. Moreover, observations made by MAVEN's SWIA and NGIMS instruments during this orbit show similar mid-orbit fluctuations in the penetrating proton flux and neutral CO₂ density, respectively (Figure 4.1). (Note that the general sinusoidal shape of the SWIA and NGIMS curves throughout the orbit is associated with the changing spacecraft altitude during periapsis; see Supplementary Figure 4.2 and Supplementary Figure 4.3 for details on spacecraft and IUVS observation geometries, and Supplementary Figure 4.4 for additional Ly- α information for this orbit.)

4.3.1.2 “Variable” proton aurora independent of neutral atmospheric variability

There are also observations of variable proton aurora that are not associated with variability in the neutral atmosphere. One unique example of this type of variable proton aurora are detections corresponding with modulated penetrating proton events, which were found by Fowler *et al.* (2019) to be associated with variability in the upstream solar wind caused by a radial orientation of the IMF. We examine detections of modulated H deposition (observed by SWIA as penetrating protons) from the study by Fowler *et al.* (2019), spanning a multi-week period in late 2016.

The plots in Figure 4.2 display IUVS Ly- α intensity data for three proton aurora events; here Ly- α altitude-intensity profiles of each limb scan in the orbit are overlain on top of a synthetic image format of the un-binned periapsis Ly- α data (*i.e.*, each of the IUVS orbit limb scans (horizontal) displays the Ly- α intensity for each of the 21 IUVS mirror integrations (vertical) and seven spatial bins within each limb scan; *e.g.*, similar to Figure 2 from Deighan *et al.*, 2018). The top plot in Figure 4.2 shows an example of an orbit with minimal modulation of penetrating protons and a non-radial IMF (*i.e.*, $\sim 85^\circ$ IMF orientation). The middle and bottom orbits in Figure 4.2 show examples of “modulated” proton aurora (*i.e.*, corresponding with highly modulated events from the Fowler *et al.* (2019) study) in MAVEN orbits 4223 and 4261, respectively. Both of these orbits occur during near-radial IMF conditions (with respective IMF orientations of $\sim 23^\circ$ and $\sim 37^\circ$ from radial). The peak altitudes of the Ly- α proton aurora profiles in each limb scan during orbit 4223 are mostly consistent, with the exception of a 15 km mid-orbit increase in the peak altitude of Ly- α profile of the sixth limb scan in the orbit. (We note that the maximum peak altitude in orbit 4223 is ~ 160 km, far larger than the typical altitude range in which proton aurora have previously been observed or predicted to occur.) Similarly, orbit

4261 shows a sudden mid-orbit decrease in the peak Ly- α intensity of the proton aurora profile in the sixth limb scan. Although we observe significant variability between Ly- α limb scans within these orbits, we do not observe any corresponding variability in the IUVS CO₂⁺ UVD profiles (*e.g.*, Supplementary Figure 4.5). Similarly, the Fowler *et al.* (2019) study also did not identify any corresponding variability in the NGIMS CO₂ observations during this orbit.

In our comparative study, we identify proton aurora during all eight of the top most highly modulated orbits from the Fowler *et al.* (2019) study that have overlapping IUVS and SWIA observations (*i.e.*, MAVEN orbits 4223, 4249, 4260, 4261, 4262, 4303, 4304, and 4276). We observe definitive signs of variability in the IUVS data (*i.e.*, changes in peak altitudes and/or intensities in proton aurora detections between limb scans within a single orbit) in four of these eight orbits (*i.e.*, orbits 4223, 4261, 4262, and 4303; see Supplementary Figure 4.6 for Ly- α observations of all four orbits), and potential signs of variability in another three orbits (*i.e.*, 4249, 4260, and 4304). (We note that it is not possible to identify intra-orbit proton aurora variability in orbit 4276, as only a very small proton aurora enhancement is observed in a single limb scan during this orbit; however, we do observe possible signs of altitude variability in the subsequent orbit.) Additionally, we also observe similar variations in many other MAVEN orbits that do not have overlapping SWIA penetrating proton observations (and were thereby not included in the Fowler *et al.* (2019) study). Lastly, we note that we do not observe any evidence of the described variability in proton aurora profile peak altitude or intensity (*i.e.*, variability that is uncoupled from the CO₂⁺ UVD) during the orbits from the Fowler *et al.* (2019) study that were found to exhibit little/no modulation in SWIA penetrating proton observations.

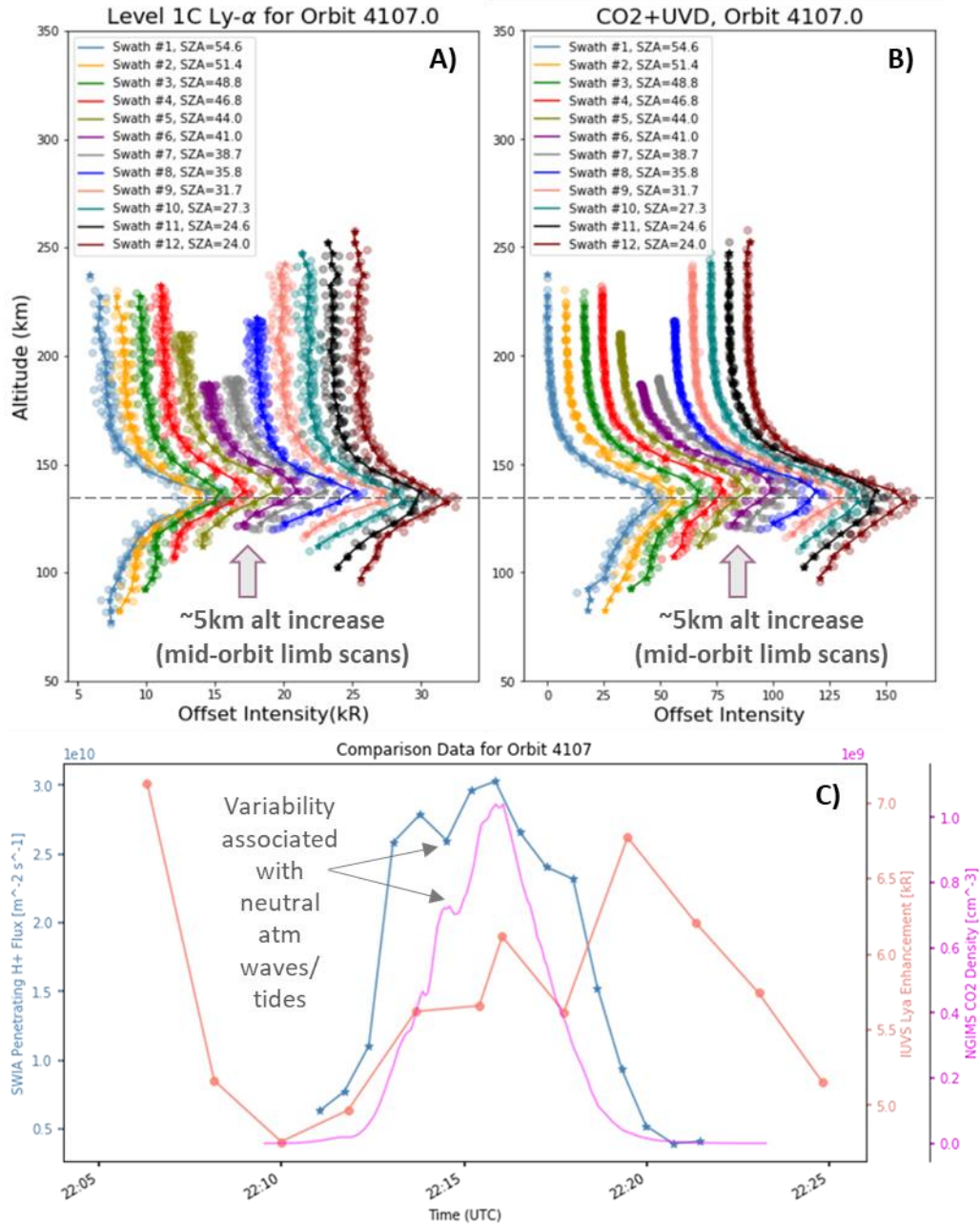


Figure 4.1: (Top) Offset IUVS limb scan altitude-intensity profiles from MAVEN orbit 4107 for A) Ly- α and B) CO₂⁺ UVD emissions. Variations in Ly- α peak altitude between the scans within the orbit (observing a single proton aurora event) track with altitude variations in the CO₂⁺ UVD profiles (note that such variations in the CO₂⁺ UVD are consistent with previous observations of lower atmospheric waves/tides). C) Concurrent observations of IUVS emission enhancement, SWIA penetrating proton flux, and NGIMS CO₂ density during the periapsis portion of MAVEN orbit 4107. We observe similar fluctuations in the different instrument measurements on roughly the same temporal scale during this orbit, consistent with being caused by the same driving mechanisms.

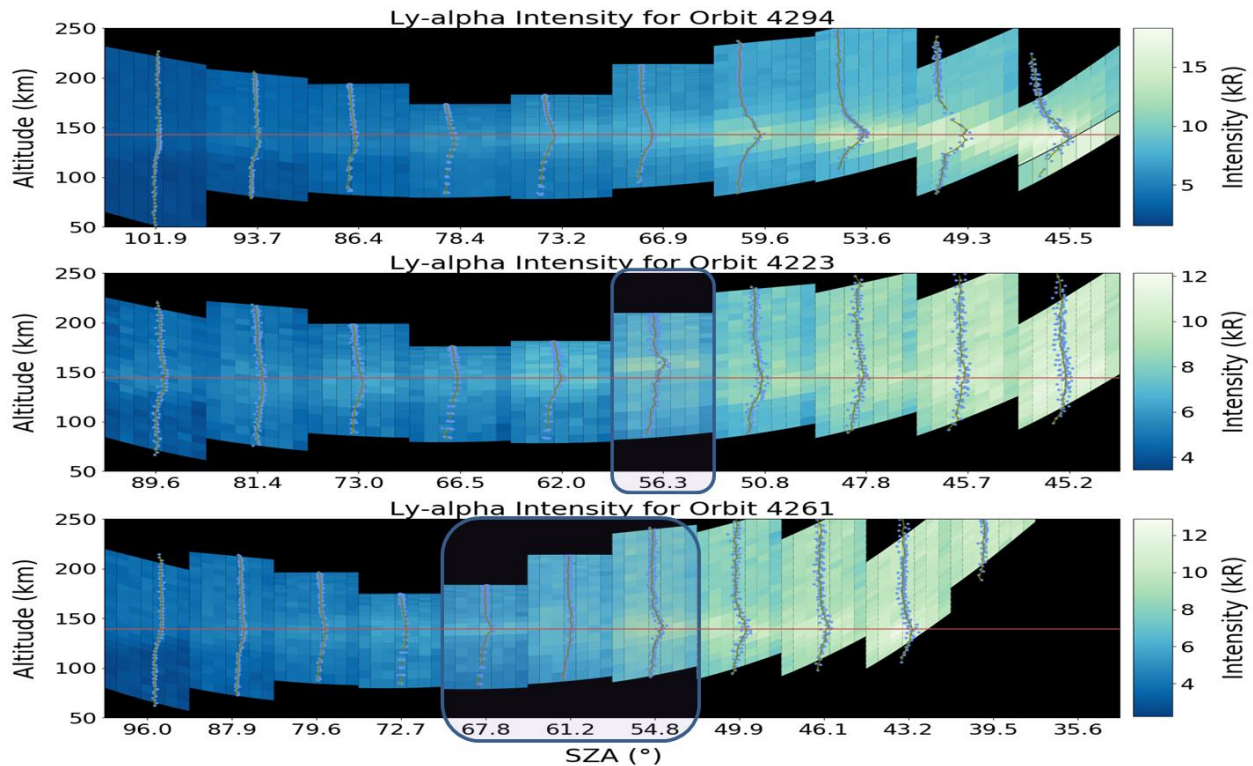


Figure 4.2: Altitude-intensity profiles overlain on top of a synthetic image format of Ly- α intensities for each IUVS limb scan/mirror angle in MAVEN Orbit 6753 (e.g., Figure 2 from Deighan et al. 2018). Examples of “modulated” proton aurora (middle and bottom plots) in comparison with a proton aurora event with minimal variability (top). The middle plot shows altitude variation in a central orbit limb scan (during near-radial IMF conditions) and the bottom plot shows intensity variation in a central orbit limb scan (also during near-radial IMF conditions). Note that the given SZA values given correspond with the median SZA in each IUVS scan; the boxes highlight the variability within each orbit, and the horizontal lines represent the average peak altitude for each orbit.

4.3.2 Nightside proton aurora

Although Martian proton aurora occur almost entirely on the dayside of the planet, we observe some proton aurora events on the planet’s nightside. Figure 4.3 shows an example of a proton aurora event that occurs on the nightside of the planet, having IUVS peak limb scan SZAs between $\sim 120^\circ$ - 145° . This detection in MAVEN orbit 6753 also exhibits significant variability in the Ly- α proton aurora peak intensities (and a minor decrease in altitude with increasing SZA) between limb scans within the orbit.

Nightside proton aurora detections account for 3.9% of all IUVS limb scan proton aurora detections and exhibit many notable differences from the more common dayside events. Figure 4.4 shows a comparison between IUVS dayside and nightside proton aurora observations

(defining day/night detections as $\pm 10^\circ$ of a peak SZA=90°, respectively). Based on this statistical comparison, we find that nightside events exhibit much smaller Ly- α peak intensities (*i.e.*, mean nightside peak intensity is $\sim 3.8\times$ smaller than mean dayside peak intensity; Figure 4.4A), emission enhancements (*i.e.*, mean nightside enhancement $\sim 1.9\times$ smaller than dayside enhancement) (Figure 4.4B), and peak altitudes (*i.e.*, nightside altitude histogram peaks $\sim 20\text{km}$ lower than dayside histogram: $\sim 120\text{km}$ versus $\sim 140\text{km}$, respectively) (Figure 4.4 C). Nightside proton aurora do not exhibit any clear seasonal dependence (in contrast to the strong seasonal dependence of dayside events, reaching a maximum occurrence near $L_s \sim 270$) (Figure 4.4D). And nightside events do not appear to be geographically constrained on the planet (Figure 4.4E). It is also interesting to note that nightside proton aurora peak altitudes appear to decrease with increasing SZA (consistent with previous observations of the SZA dependence of nightside ion peak altitudes, *e.g.*, Girazian *et al.*, 2019), and that both day- and nightside observations exhibit higher peak altitudes during the southern summer season (*i.e.*, around $L_s \sim 270$) (Supplementary Figure 4.7), when the H column density and escape rate reach an annual maximum (*e.g.*, Chaffin *et al.*, 2014; Halekas *et al.*, 2017).

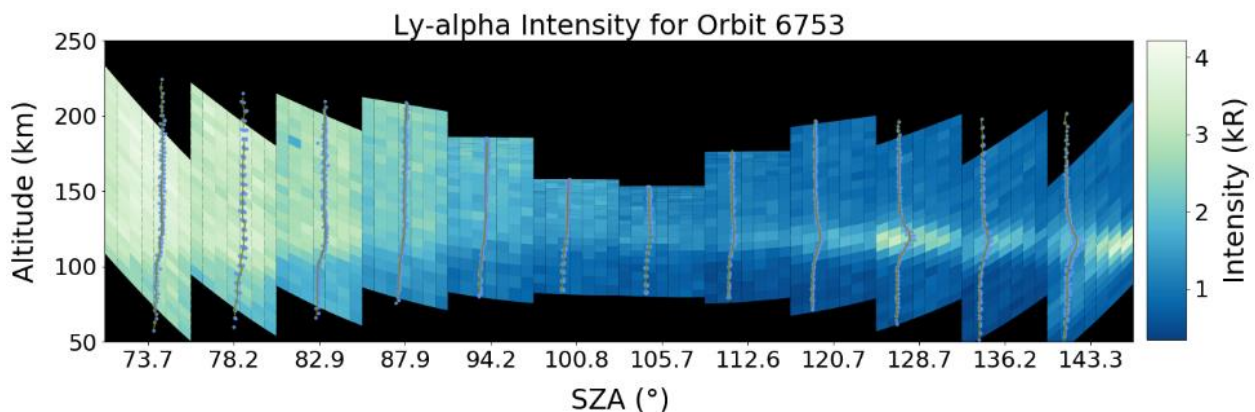


Figure 4.3: Altitude-intensity profiles overlain on top of a synthetic image format of Ly- α intensities for each IUVS limb scan/mirror angle in MAVEN Orbit 6753 (*e.g.*, Figure 2 from Deighan *et al.* 2018). This orbit shows an example of a nighttime proton aurora event. Note that the given SZA values given correspond with the median SZA in each IUVS scan.

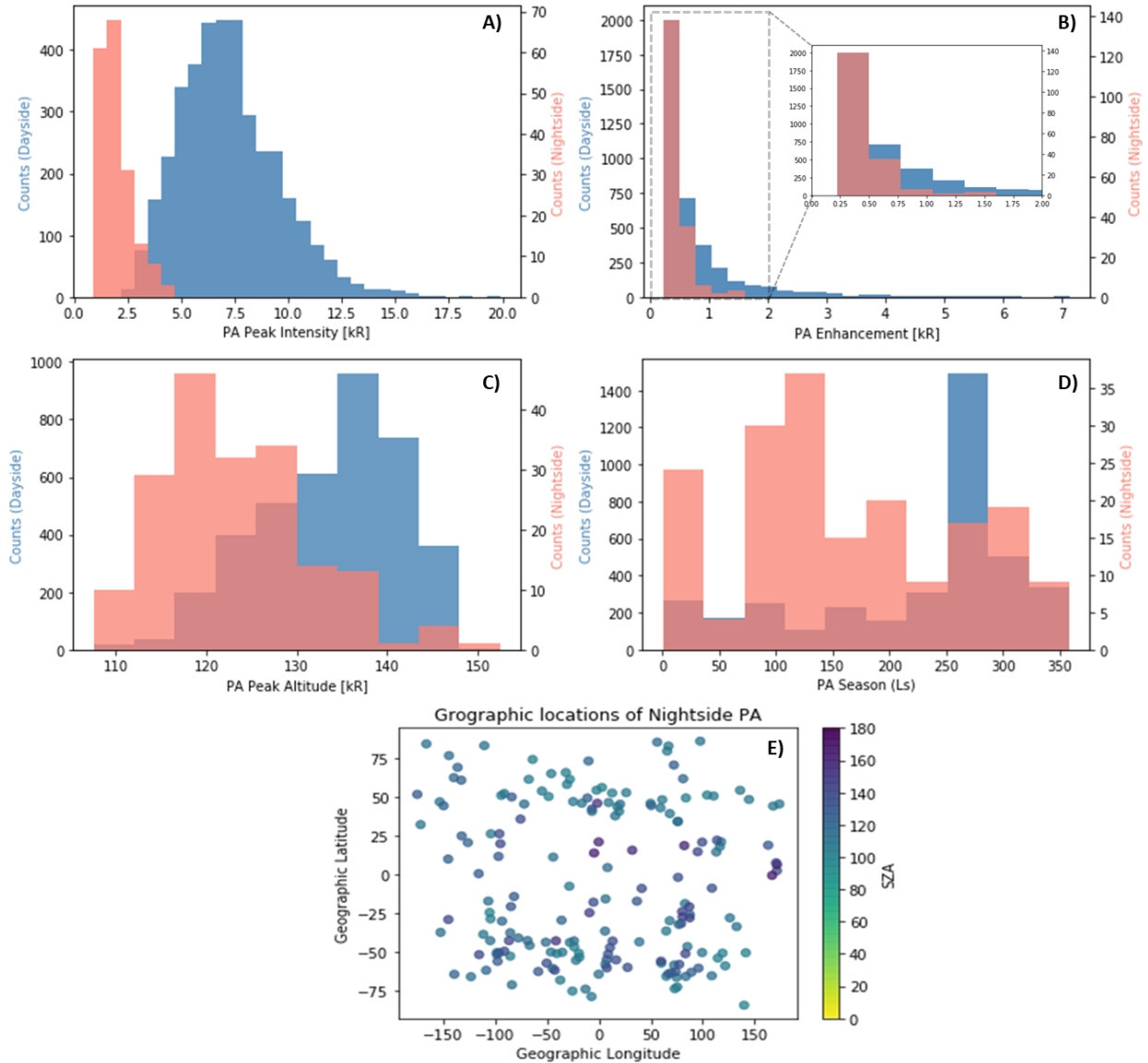


Figure 4.4: Statistical comparisons of proton aurora observational parameters for dayside versus nightside events. Nightside events exhibit smaller peak Ly- α intensities (A), emission enhancements (B), and altitudes (C); they do not appear to exhibit a clear seasonal dependence (D), or to be geographically constrained on the planet (E). Note the difference on the scales between the day/night axes. (Note: day and night observations are defined as $\pm 10^\circ$ of SZA=90°, respectively.)

4.4 Discussion

There are many inherent difficulties associated with comparative observations between remote sensing and *in situ* datasets such as IUVS and SWIA (*e.g.*, see Hughes *et al.*, 2021 for a thorough evaluation). One such difficulty is due to the ~two minute integration period for IUVS limb scans. If the variability being observed occurs on a period larger than the IUVS integration

time, the instrument will not be able to detect any variability within a single limb scan. If the variability is small enough, such that it can be observed within a single limb scan or in subsequent IUVS limb scans (but still large enough so as to not be “washed out” during the integration period), the instrument may observe that variability. However, any large scale periodic variability could not be detected during the ~20 minute periapsis portion of the MAVEN orbit. It is also important to consider the spatial extent of any variability. Because SWIA observes in the immediate vicinity of the spacecraft and IUVS observes ~100’s of km away from the spacecraft, IUVS would not observe any variability occurring on a small spatial extent near the spacecraft and vice versa.

As previously mentioned, “typical” observations of Martian proton aurora occur on the dayside of the planet at low SZA’s with minor variability in the Ly- α emission enhancement between limb scans. For a typical IUVS proton aurora observation, the Ly- α peak altitudes of limb scan profiles within a single orbit are mostly constant and the intensity only varies as a function of the cosine squared of the SZA. Thus, the Ly- α profiles of proton aurora observations could only exhibit dramatic/rapid changes (*i.e.*, on the order of minutes between IUVS limb scans) in the altitude and/or intensity as a result of corresponding variations in the density, temperature, and/or velocity of either the incident solar wind protons, the H corona, or the neutral CO₂ atmosphere.

The previous study by Fowler *et al.* (2019) found that the modulated H in their study was caused by temporal variability in the upstream solar wind. Alternatively, the study by Crismani *et al.* (2019) determined that the observed “patchy” proton aurora event in their case study was the result of spatial variability, presumed to have been caused by a geometric observational effect related to localized ionization. We have presented two unique types of variable proton

aurora that can be caused by localized geographic spatial variability (*i.e.*, observations associated with atmospheric waves/tides) or temporal variability (*i.e.*, “modulated” proton aurora). Because there are multiple processes that can be responsible for intra-orbit spatial/temporal variability in proton aurora, it is not possible to determine a causal mechanism for observed variability via the exclusive evaluation of the Ly- α profiles for proton aurora events. Multi-instrument case studies must be undertaken for different variable proton aurora detections in order to identify/characterize the unique mechanisms in each observation responsible for driving the variability.

4.4.1 Variability associated with neutral atmospheric waves/tides

The observed peak altitude variability in the IUVS CO₂⁺ UVD emission during orbit 4107 is consistent with previous observations of atmospheric tides (*e.g.*, Lo *et al.*, 2015; England *et al.*, 2016). Additionally, the observed variability in the NGIMS and SWIA measurements is also consistent with typical observations of atmospheric waves and/or tides. These observations correspond with altitudinal and/or geographic variability (*e.g.*, latitudes, longitudes, and local solar times) in the neutral atmospheric density as the MAVEN spacecraft progresses through the periapsis portion of its orbit. The concurrent/independent observations of atmospheric waves and/or tides by three different MAVEN instruments during this orbit (*i.e.*, IUVS, NGIMS, and SWIA), in combination with the correlated timescales of variability with proton aurora suggests the influence of neutral atmospheric waves and/or tides in creating the observed variability during this orbit.

Atmospheric waves and tides can affect the structure, energy transport, and dynamics in the lower- and middle-atmosphere (*e.g.*, Guzewich *et al.*, 2012; Guzewich *et al.*, 2016; Lo *et al.*, 2015; England *et al.*, 2016). A change in neutral atmospheric density and/or temperature

(induced by waves and/or tides) during the observed orbit could cause a localized increase in the atmospheric scale height, in turn causing an increased proton aurora peak altitude and a decreased peak intensity (*i.e.*, due to CO₂ absorption on the bottomside of the profile). The location/local solar time of the observations during this orbit may be consistent with possible influence by the diurnal thermal tide (*e.g.*, see IUVS orbit observation geometry in Supplementary Figure 4.2) and/or topographically-forced stationary waves (as IUVS is observing near Hellas Basin during this orbit).

To our knowledge, we report the first observation of the influence of energy transport from the lower/middle neutral atmosphere (*i.e.*, via waves and/or tides) on upper atmospheric auroral variability at Mars. Previous studies have reported on the effects of non-migrating thermal tides on Martian ionospheric variability (*i.e.*, the peak altitude & density of M2 layer) (*e.g.*, Withers, 2009 & references therein), as well as the effects of topographically-controlled thermal tides on variability in the upper atmosphere (*e.g.*, Withers *et al.*, 2003). Connections between neutral atmospheric waves and auroral variability has also been previously observed at Earth: a study by Palmroth *et al.* (2020) found that upward propagating gravity waves from the lower atmosphere can be bent and made to travel horizontally through the thermosphere; when penetrating particles subsequently interact with these waves, they create “auroral dunes”, a unique type of aurora that exhibits small scale variability in altitude and brightness across a large spatial extent.

Combined multi-instrument observations of different concurrent atmospheric phenomena (such as has been presented in this study) can provide new information to investigate coupling and energy transport between the lower/middle- and upper-atmosphere on Mars. Additional datasets, including observations of local atmospheric temperature/density profiles (*e.g.*, Mars

Climate Sounder (MCS) onboard the Mars Reconnaissance Orbiter (MRO) spacecraft), may be helpful in identifying/characterizing the atmospheric variability caused by waves/tides during this period. However, the restricted observation times of MCS (*i.e.*, ~3pm local solar time observations on the planet's dayside) may limit the ability to directly compare with IUVS observations in this orbit.

We have presented a detailed case study of the influence of waves/tides on proton aurora, however, many similar observations have been identified in the IUVS dataset. As previously discussed, every orbit exhibiting intra-orbit limb scan variability in proton aurora profiles does not necessarily corresponds with variability in the CO₂⁺UVD emission; and conversely, all intra-orbit variability observed in the CO₂⁺UVD profiles does not necessarily corresponds with similar observed variability in Ly- α proton aurora profiles. This lack of observed correlation in variability may be due to unfavorable observation geometries (*e.g.*, high SZAs), relatively small amplitudes of temperature/density variations (such that the variability would not be observable in the Ly- α emission), or large CO₂ scale heights (causing absorption on the bottomside of the Ly- α profile and obscuring any intra-orbit variability between limb scans).

4.4.2 Variability associated with “modulated” H and penetrating protons

Based on the connection between penetrating protons and ENAs, one would expect that any variability in the penetrating proton density would lead to variability in the deposited H, and thereby, the Ly- α profiles of proton aurora. The observed variations in “modulated” proton aurora events are consistent with formation by a fluctuating energy source and quasi-periodic penetrating proton density, as observed in the SWIA modulated penetrating proton events in the Fowler *et al.* (2019) study. This temporal variations in the upstream solar wind energy and density could indeed cause corresponding variability in the proton aurora peak altitude and

brightness (due to the energy dependence of the electron stripping/charge exchange cross sections and H/H^+ stopping altitude, and Ly- α profile variability with H density). We estimate that the range of variability in energy observed in the Fowler *et al.* (2019) study would correspond with ~10-15km variability in the proton stopping altitude; this value is consistent with the ~15km altitude variability observed between limb scans in orbit 4223.

Fowler *et al.* (2019) identified periods of temporal variability on the order of 10's of seconds (~15-55 seconds for the highest modulated events). Because IUVS has a ~two minute integration time for each limb scan, it is likely that the instrument is observing this variability in proton aurora altitude and intensity (caused by the upstream energy and density variations) between orbit limb scan observations. However, due to the relatively long integration time of IUVS, such differences between scans can be difficult to consistently observe, depending on the amplitude and period of the upstream variation. We note that (by definition) all of the most highly modulated orbits from Fowler *et al.* (2019) exhibit large mean amplitude of density variations in the penetrating protons and/or relatively large time periods of proton density modulation. Indeed, of the most highly modulated events, we observe clear evidence of variability in the Ly- α profiles from orbits that exhibit the largest density variations and/or periodicities. Comparatively, almost all of the highly modulated event orbits that do *not* exhibit clear evidence of Ly- α variability have comparatively low density variations and/or periodicities. Thus, we find that the factors that determine whether or not IUVS will observe variability between Ly- α profiles during a modulated proton aurora event are the amplitude of the density variation and the periodicity of the modulation events (as variations on timescales significantly smaller than the IUVS integration times cannot be observed between limb scan integrations).

Finally, we note that variability in proton aurora events has also been observed at Earth. One of the first of such observations was presented by Eather (1967), who observed what was referred to as “pulsating” proton aurora (*e.g.*, Nomura *et al.*, 2016; Ozaki *et al.*, 2016). Observations of pulsating proton aurora have more recently been made from UV space-based instruments, including a study by Yahnin *et al.* (2009) in which they used the IMAGE spacecraft to observe the brightness of the proton aurora arc grow and diminish multiple times during a series of images spanning ~20 minutes (Figure 4.5). The formation processes of aurora on Earth and Mars are fundamentally different due to the presence/absence of an intrinsic magnetic field, respectively. However, the similarities between these terrestrial and Martian observations makes for a useful comparison in considering how such events might be observed at Mars in a similar sequence of images.

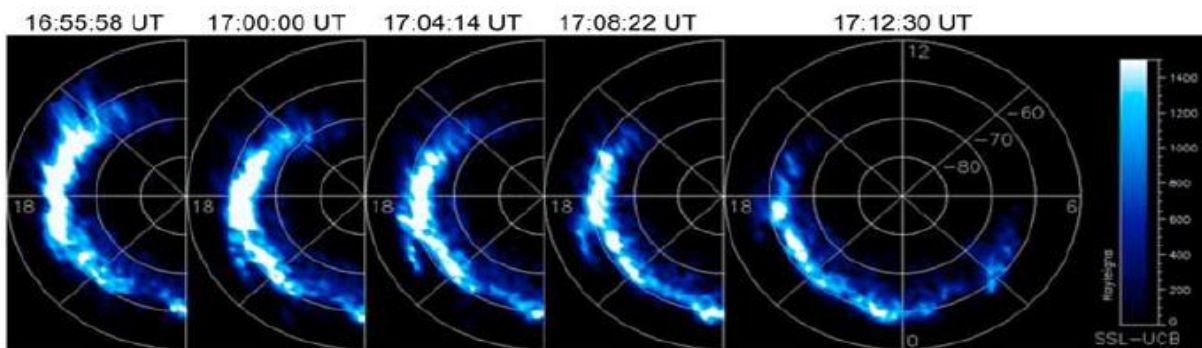


Figure 4.5: Sequence of images from IMAGE spacecraft showing “pulsating” proton aurora at Earth on 9 March 2004 (credit: Yahnin+2009).

4.4.3 Nighttime proton aurora detections

Nighttime proton aurora are one of the most unique subtypes of Martian proton aurora, as their existence is not easily explained by the commonly understood formation processes. Nightside proton aurora account for ~4% of all individual IUVS limb scan proton aurora detections (184 out of 4705 detections in this study) and 10.0% of the MAVEN orbits exhibiting proton aurora (122 out of 1225). (We note that dayside detections account for ~81% of

detections in this study, and near-terminator detections ~15%.) Hughes *et al.* (2019) previously reported observing proton aurora in 9.7% of all IUVS limb scan profiles from 26.5% of all MAVEN orbits included in their study. We find similar results here and identify proton aurora in 18.8% of all dayside IUVS observations (slightly larger than the 14.1% reported by Hughes *et al.* (2019) due to a different SZA cut off for dayside events, *i.e.*, $SZA < 80^\circ$ in this study versus $SZA < 105^\circ$ in the Hughes *et al.* (2019) study). Contrastingly, we observe proton aurora occurrence in only 0.85% of all nightside IUVS limb scan observations. This extremely low occurrence rate of less than 1% speaks to the rarity of nightside proton aurora events.

Previous studies have proposed that nightside H-ENAs could be the result of highly scattered solar wind ENAs or magnetosheath protons/ENAs (*e.g.*, Brinkfeldt *et al.*, 2006; Wang *et al.*, 2018). Due to the unlikelihood of producing significant localized enhancements in in the Ly- α emission through scattering processes alone (*i.e.*, such that it is observable above the background thermal H), we do not consider the former process to be exclusively capable of creating nightside proton aurora events and instead evaluate alternative possible formation mechanisms.

A modeling study by Wang *et al.* (2018) proposed that nightside H-ENAs are generated by proton precipitation in the magnetosheath onto the nightside (primarily aided by a convection electric field that points away from the planet). Wang *et al.* (2018) suggest a possible formation mechanism for nightside proton aurora: that magnetosheath penetrating protons, which contribute in part to the population of planetward-moving protons in the magnetotail, can travel back toward the planet and subsequently precipitate into the nightside exosphere as H-ENAs and protons. Wang *et al.* (2018) predicted that the Ly- α intensities of nightside proton aurora should be ~one order of magnitude lower than those of dayside proton aurora events. While our observations of nightside Mars proton aurora do indeed exhibit relatively low Ly- α peak intensities in

comparison with dayside events, we observe a difference of only a factor of ~ 3.8 between the mean day- and nightside peak Ly- α intensities. However, Wang *et al.* (2018) suggest that discrepancies in their predictions may be due to their assumption of a spherically symmetric exosphere, leading to an overestimation of the nightside exospheric density and therefore, H-ENA precipitation flux.

Previous studies of proton/ENA precipitation at Mars found that magnetosheath protons and ENAs exhibit uniquely different fluxes and energy spectra than their penetrating solar wind counterparts: having higher fluxes and a broader energy spectrum with a lower energy peak (*e.g.*, Halekas *et al.*, 2015; Wang *et al.*, 2018). Thus, an evaluation of the energy spectrum during nighttime events could help to shed light on the source of nightside protons. Although SWIA has made some measurements of terminator/nightside penetrating protons, due to the rarity of nightside proton aurora detections, there are very few nighttime orbits exhibiting proton aurora that have overlapping IUVS and SWIA observations.

Because solar wind particles do not have direct access to the nightside of the planet, nightside proton aurora may alternatively form via unique interactions between the upstream IMF with the Martian induced magnetosphere and/or remnant crustal fields, perhaps similar to formation processes responsible for creating discrete and diffuse electron aurora on the nightside of Mars. Martian discrete aurora have been found to be constrained to locations near the southern hemispheric remnant crustal fields, and form via solar particles accelerated along diverging magnetic flux tubes above magnetized crustal fields (Bertaux *et al.*, 2005; Lundin *et al.*, 2006). Discrete aurora can occur in “cusp”-like regions between strong remnant crustal magnetic fields or along open field lines connected to crustal fields (Lundin *et al.*, 2006). Alternatively, Martian diffuse aurora are not geographically constrained on the planet and are understood to form via

solar particle interactions with draped solar wind field lines around Mars (Schneider *et al.*, 2015). Magnetic field interactions could transport protons to the nightside of the planet, perhaps due to similar magnetic field alignment constraints as cusp proton aurora observed at Earth (*e.g.*, Frey, 2002). A comparison of nightside proton aurora detections with locations of open/closed magnetic field lines shows that these nightside events do not appear to be restricted to locations of a single type of open/closed magnetic field topology (Supplementary Figure 4.8, Top). However, proton aurora events that occur near remnant crustal fields in the southern hemisphere appear to be constrained by the locations of the crustal fields, primarily occurring in between/bordering locations of strong radially-oriented magnetic fields (Supplementary Figure 4.8, Bottom). Thus, the similarities in locations to both discrete and diffuse aurora suggest that it is possible that nightside proton aurora may also be driven by the two processes responsible for creating discrete/diffuse aurora on Mars. A thorough comparison of nightside proton aurora events with discrete/diffuse aurora observations will be necessary to better understand the connections between these auroral types. However, such an assessment is beyond of purview of this current study.

Future detailed case studies of these nightside detections (*e.g.*, evaluating penetrating proton fluxes/energy spectra, local magnetic field variations, solar energetic particles, and overlapping observations of discrete/diffuse aurora) will be beneficial in developing our understanding of the formation processes of these phenomena.

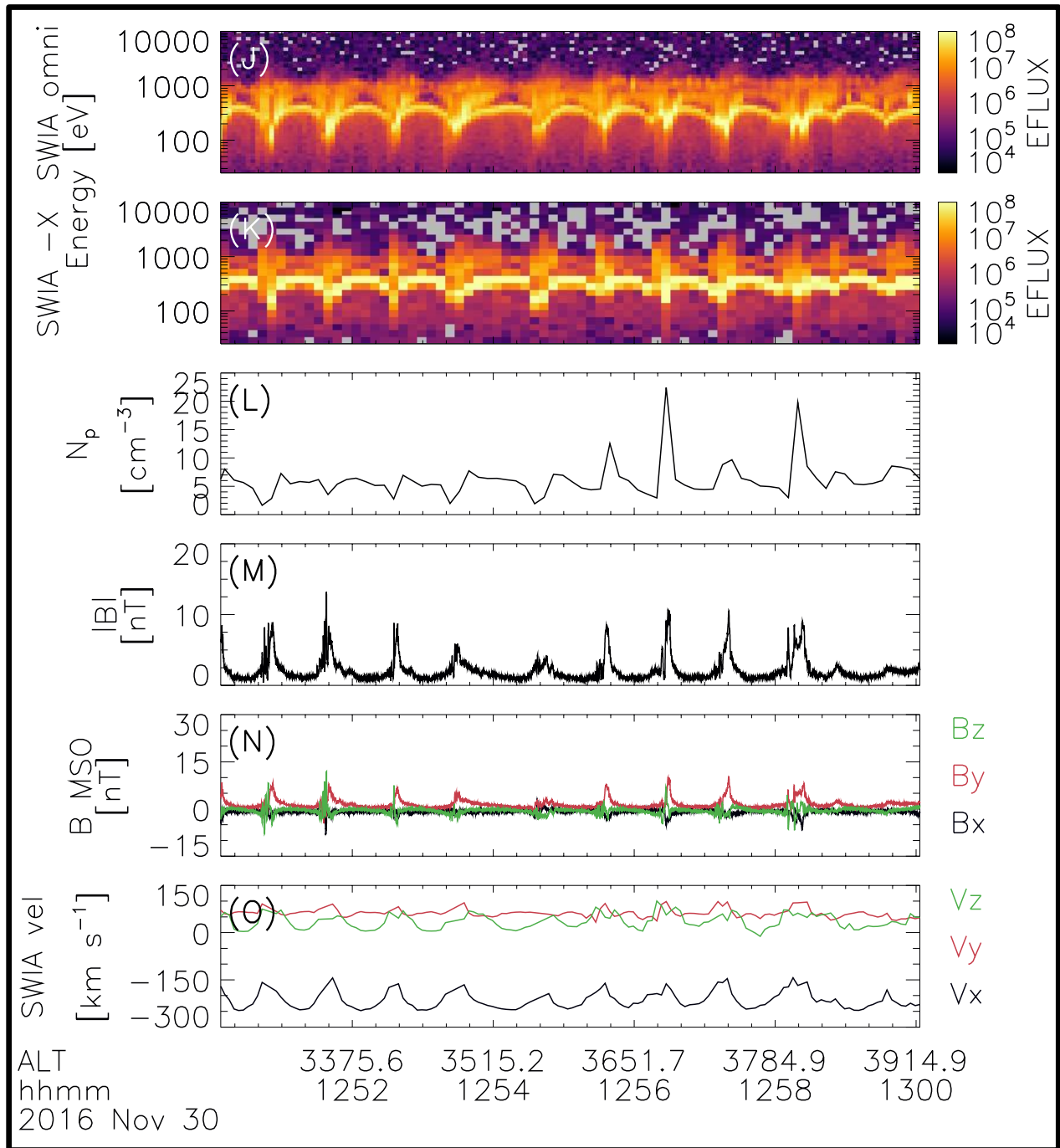
4.5 Conclusions & Future work

Herein we have presented multiple case studies of “variable” proton aurora, which are found to be associated with spatial and/or temporal variability in the neutral atmosphere or upstream solar wind. Because of the range of potential formation processes that could be responsible for

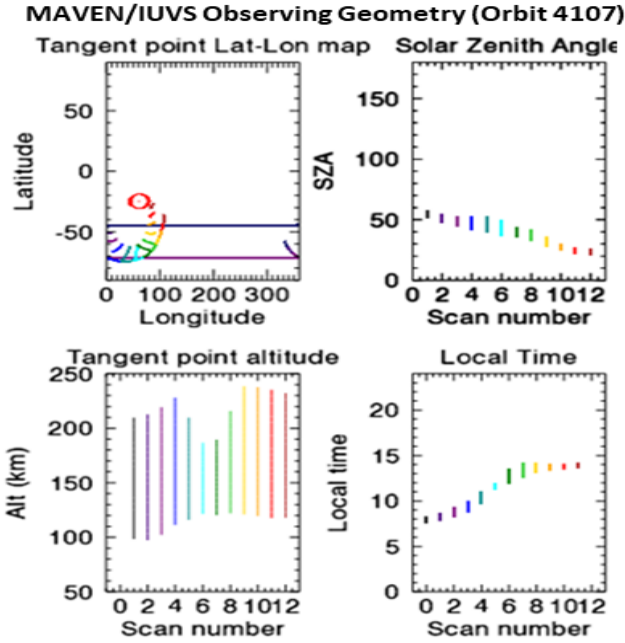
variable proton aurora, multi-instrument case studies must be utilized to understand the unique causes for variability in individual events. We have also presented results of a statistical study of nightside proton aurora events and compare these observations with the more common dayside detections. We find that nightside proton aurora exhibit much smaller Ly- α intensities, emission enhancements, and peak altitudes. Nightside events make up a very small subcategory of proton aurora (*i.e.*, ~4% of all IUVS proton aurora detections, but observed in less than ~1% of all nightside IUVS Ly- α observations), making them extremely rare in the dataset.

In a future study we will aim to further quantify the frequency and phenomenology of variable proton aurora events in the IUVS dataset. It will also be beneficial to compare proton aurora variations with observations of atmospheric waves/tides, in order to assess the extent to which energy (and possibly also mass) transport and dynamic processes of waves/tides in the lower- and middle-atmosphere affect upper-atmospheric dynamics and auroral activity.

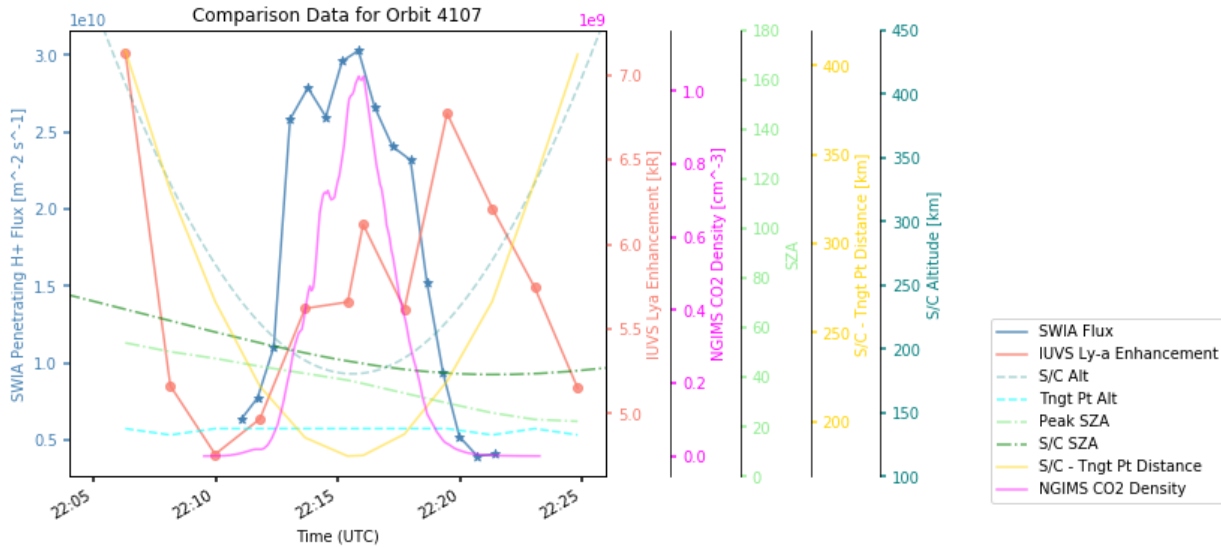
Chapter 4 Supplementary Figures:



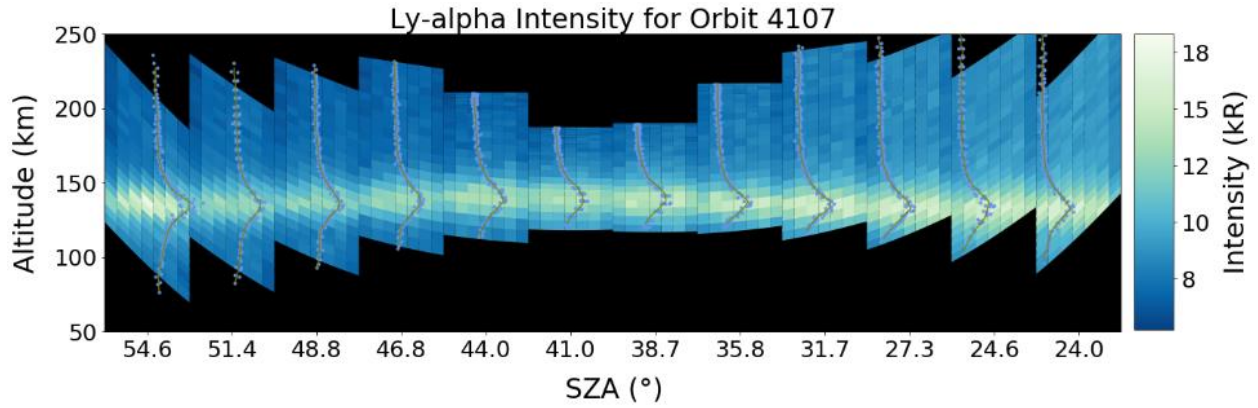
Supplementary Figure 4.1: Example of a modulated penetrating proton event from Fowler et al. (2019), showing quasi-periodic fluctuations in the upstream magnetic field and proton energy, density, velocity.



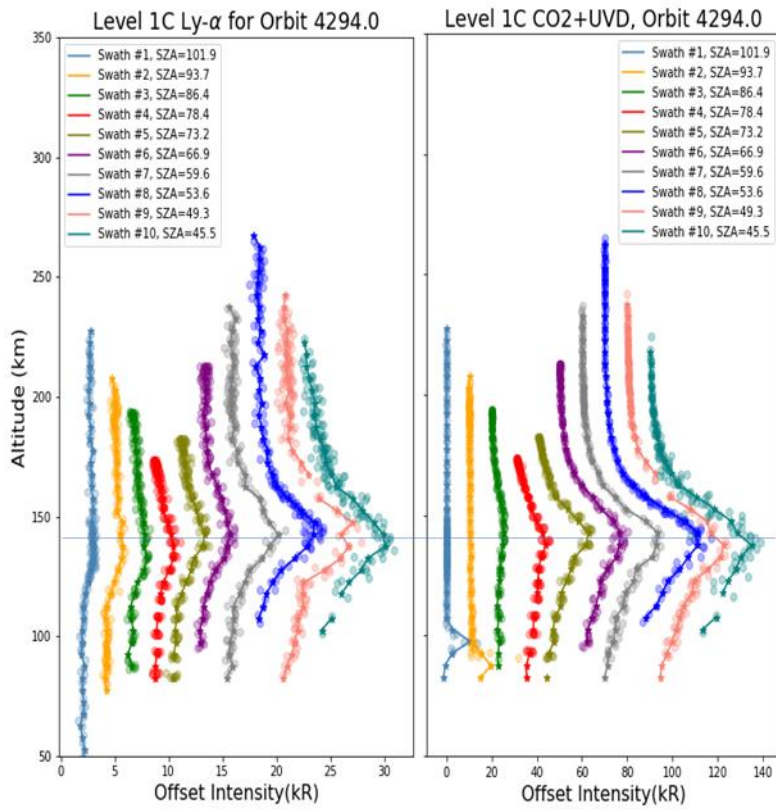
Supplementary Figure 4.2: IUVS orbit geometry plots for MAVEN orbit 4107, showing the locations of IUVS limb scan observations across different latitudes, longitudes, and local solar times during the orbit.

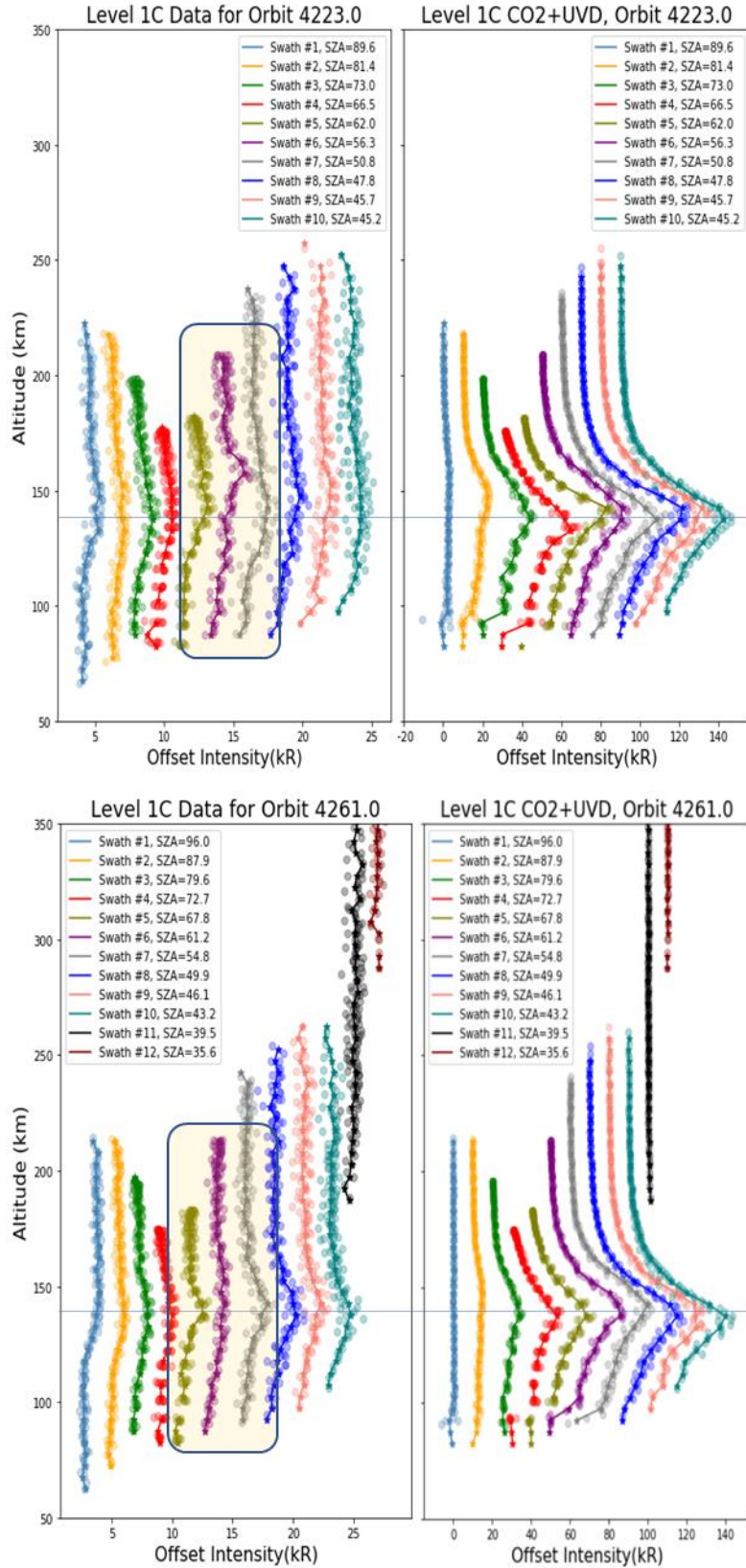


Supplementary Figure 4.3: Same as Figure 4.1, with IUVS tangent point observation angles and spacecraft angles overlain (e.g., SZA and altitude).

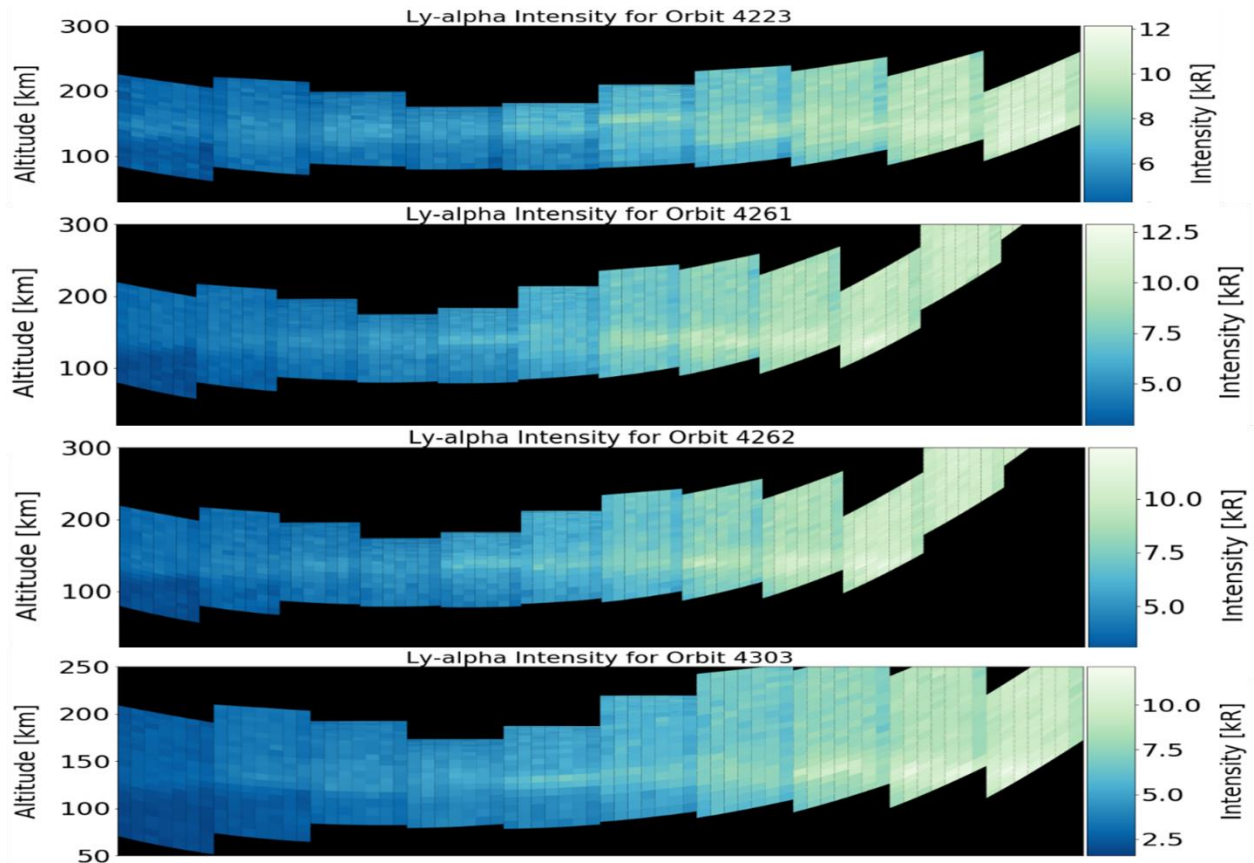


Supplementary Figure 4.4: Altitude-intensity profiles overlain on top of a Ly- α synthetic image format for MAVEN orbit 4107.

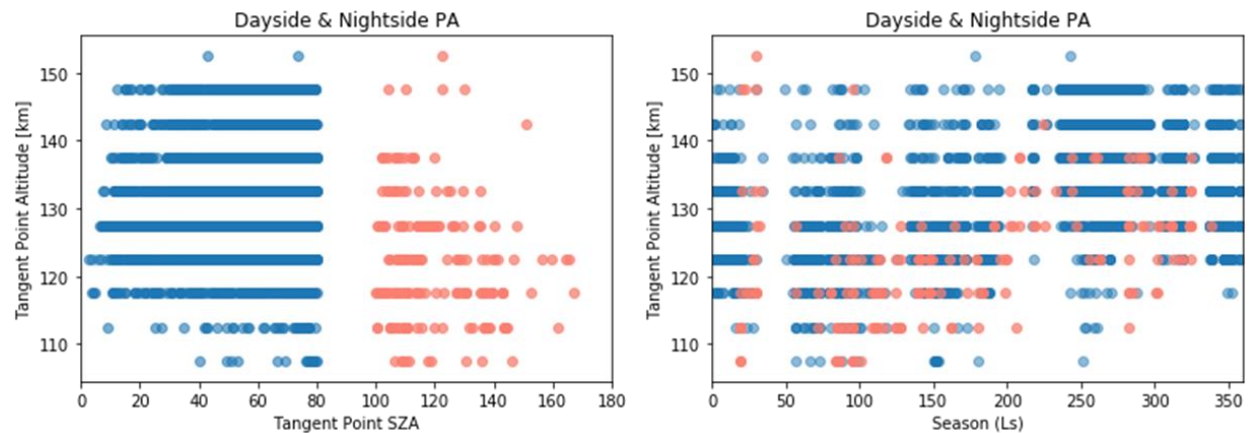




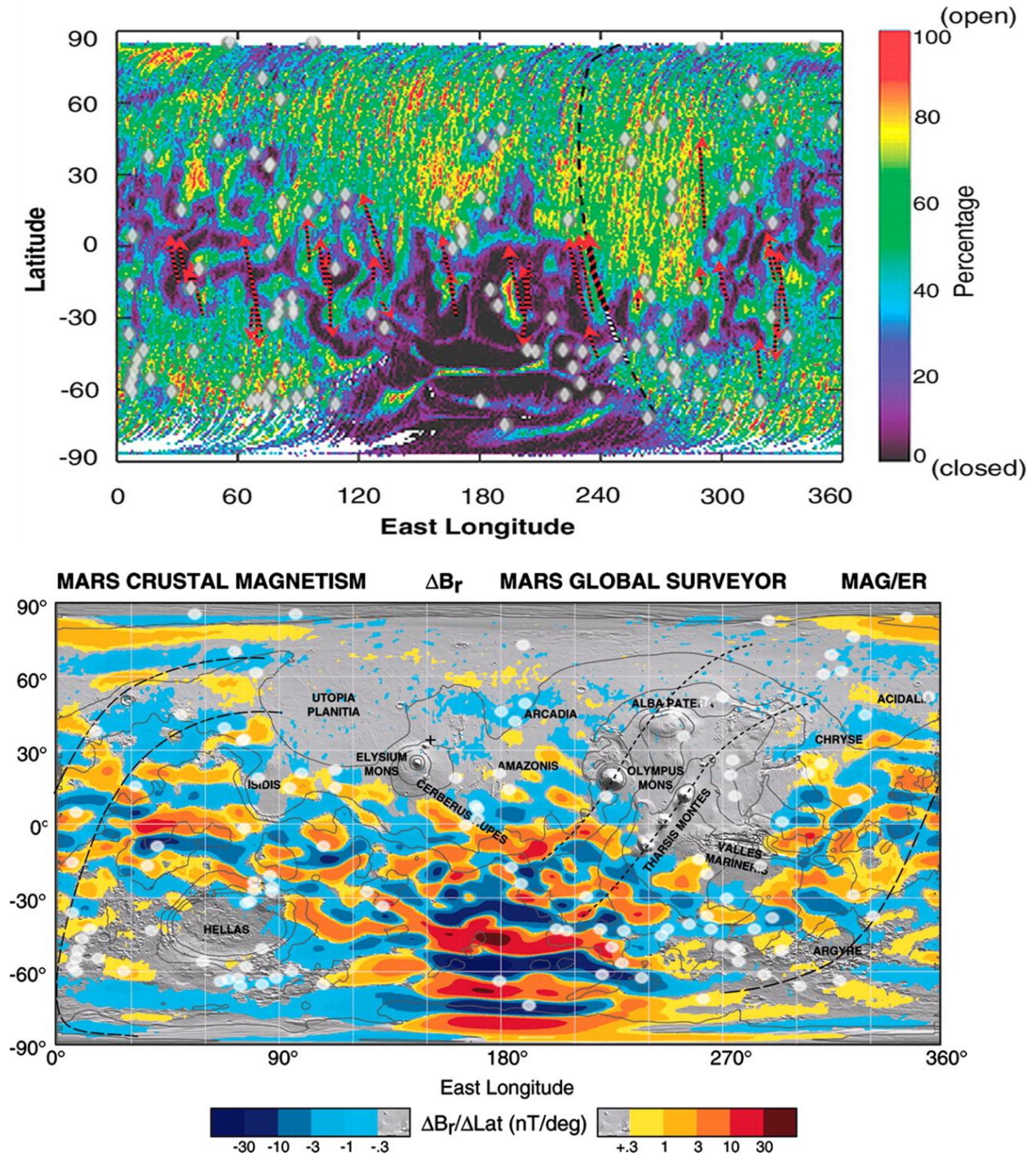
Supplementary Figure 4.5: Altitude-intensity profiles for the Ly- α and CO₂+UVD emissions for the three MAVEN orbits in Figure 4.2 (i.e., orbits 4294, 4223, and 4261).



Supplementary Figure 4.6: Ly- α altitude-intensity profiles overlain on top of a synthetic image format for the four MAVEN orbits from the Fowler et al. (2019) study with overlapping IUVS and SWIA observations that exhibit clear evidence of modulation in proton aurora observations.



Supplementary Figure 4.7: Comparison of dayside and nightside proton aurora peak altitudes relative to SZA (left) and season (right). The nightside proton aurora peak altitude appears to fall off with increasing SZA, and both types exhibit higher peak altitudes during the southern summer season (around $L_s \sim 270$).



Supplementary Figure 4.8: Locations of nightside proton aurora are shown in grey overlain on a map of (Top) open/closed field lines (map from Lundin et al., 2006) and (Bottom) remnant crustal field strengths and radial field orientations on shaded topography relief map (map from Connerney et al., 2005).

5. Evaluating Martian Proton Aurora through a Coordinated Multi-Model Comparison Campaign

For submission to *Journal of Geophysical Research: Space Physics*

Hughes, A., Chaffin, M., Mierkiewicz, E., Deighan, J., Schneider, N., Jain, S.,
Jolitz, R., Kallio, E., Gronoff, G., Shematovich, V., Bisikalo, D., Simon-Wedlund,
C., Gerard, J.C., Ritter, B., Halekas, J., and Girazian, Z., Hegyi, B.

Chapter 5 Key Points

- We undertake a multi-model comparison campaign to gain a better understanding of the physics and driving processes of Mars proton aurora
- The incident solar wind particle flux and velocity are found to be the two most influential parameters affecting the proton aurora profile
- All models in the study accurately represent the data, with minor discrepancies likely caused by model differences and input assumptions

Chapter 5 Abstract

Proton aurora are the most commonly occurring and yet the least studied type of aurora at Mars. In order to better understand the physics and driving processes of Martian proton aurora, we undertake a multi-model comparison campaign. Herein, we compare results from four different kinetic transport models with unique abilities to represent Martian proton aurora. This campaign is divided into two steps: an inter-model comparison step and a data-model comparison step. The first step entails modeling five different representative cases using similar constraints in order to better understand the capabilities and limitations of each of the models in the study. Through this step we find that the two primary variables affecting proton aurora are the incident solar wind particle flux and velocity. In the second step, we assess the robustness of each model based on their abilities to reproduce an example proton aurora event from the MAVEN/IUVS dataset. In so doing, we are able to better constrain the unique physical processes driving proton aurora that are incorporated in each model. The results of this comparative study provide a new understanding of the primary factors influencing variability in Martian proton aurora, as well as the dominant physics that need be incorporated in future models to accurately represent these events.

5.1 Introduction and Background

In this study, we undertake a comparative modeling campaign to better understand the physics and driving processes of Martian proton aurora. Proton aurora have been recently determined to be the most commonly observed type of aurora at Mars (Hughes *et al.*, 2019). This form of aurora is one of three types of Martian aurora, in addition to discrete (Bertaux *et al.*, 2005) and diffuse aurora (Schneider *et al.*, 2015). Further, proton aurora is the most recently discovered type of Martian aurora (Deighan *et al.*, 2018; Ritter *et al.*, 2018), and is thereby the least studied, and arguably the least understood type of Martian aurora. Many past efforts to model these phenomena have been unable to fully reproduce the observations (*e.g.*, Deighan *et al.*, 2018), suggesting a gap in our understanding and a need for further exploration of the underlying physics of these events through modeling.

In a previous statistical study, Hughes *et al.* (2019) used multiple Mars years of data from the Imaging UltraViolet Spectrograph (IUVS) (McClintock *et al.*, 2015) onboard the Mars Atmosphere and Volatile Evolution (MAVEN) spacecraft (Jakosky *et al.*, 2015) to assess the phenomenology of Martian proton aurora. Based on this study, Hughes *et al.* (2019) found that most “typical” Martian proton aurora events occur on the dayside of the planet (*i.e.*, at low solar zenith angles, SZAs) around the southern summer solstice (*i.e.*, solar longitude, Ls, ~270). This seasonal increase in proton aurora activity was found to be caused by an inflated Martian hydrogen (H) corona around southern summer solstice, which corresponds with higher H column densities and H escape rates due to dust activity and atmospheric temperatures reaching an annual maximum at this time (*e.g.*, Hughes *et al.*, 2019; Chaffin *et al.*, 2021; Chaffin *et al.*, 2014; Clarke *et al.*, 2014; Halekas, 2017). The seasonally increased abundance of H beyond the planet’s bow shock during this season allows a larger fraction of solar wind protons to be converted into H energetic neutral atoms (ENAs) (*i.e.*, through charge exchange and/or electron

stripping), which can then bypass the bow shock and magnetic pileup boundary to create more frequent proton aurora events with very large H Lyman-alpha ($\text{Ly-}\alpha$) emission enhancements during this time of year. We note that proton aurora can be identified in ultraviolet limb scan data as an enhancement in the $\text{Ly-}\alpha$ emission (121.6 nm) above the background coronal H brightness between an altitude of ~110-150 km; this enhancement is due to an additional contribution of H from the proton aurora-inducing H-ENAs as they de-excite and emit photons that can be detected by IUVS (see Figure 1 from Hughes *et al.* (2019) for more detail).

The purpose of this study is to gain a deeper understanding of Martian proton aurora. While previous studies of these unique aurora provided understandings of their phenomenology, frequency, and driving processes, much is still lacking in our understanding. Modeling proton aurora activity provides a unique opportunity to understand these events, as it allows us to constrain different input parameters and observe/predict the varying results. Moreover, by undertaking a comparative modeling campaign in which the results of multiple models are concurrently evaluated (with each model emphasizing different dominant physical processes and analytical solving techniques), we are able to simultaneously explore multiple possible outcomes for auroral events. We note, however, that the purpose of this campaign is *not* to determine which is the “best” proton/hydrogen precipitation model in the study, but rather to identify what each model *does best* in simulating proton/hydrogen precipitation at Mars. Through undertaking a rigorous assessment of Martian proton aurora using the results of multiple different simulations, we develop an understanding of the gaps in our knowledge and improve our abilities to more accurately model future proton aurora observations.

Being able to effectively model Martian proton aurora is necessary for both developing our understanding of observations of auroral events in the IUVS dataset, as well as the ability to

predict and understand future observations. We note that the statistical study by Hughes *et al.* (2019) incorporated data from only the first ~two Mars years of MAVEN orbits, taken during the declining and minimum portion of the solar cycle. While the Hughes *et al.* (2019) study encompassed many interesting proton aurora events, in this present study, we focus our efforts on modeling one particularly unique event from the dataset. The MAVEN mission continues to make new and exciting observations of Martian proton aurora, and new Mars missions with UV instrument capabilities are also beginning to make concurrent observations of these events. And as the current solar cycle continues to increase toward solar maximum (a period corresponding with larger and more frequent solar activity), we anticipate that the intensity and frequency of proton aurora events at Mars will also increase correspondingly (*e.g.*, Hughes *et al.*, 2019). Thus, it is imperative in our efforts to study proton aurora that we first develop a firm knowledge of the physics and driving processes through modeling these events; this understanding will then provide the necessary context for future efforts to accurately model new and unique auroral observations.

5.2 Modeling Campaign Description

5.2.1 Description of models/teams involved in study

In this study we incorporate four different proton/hydrogen precipitation models and a radiative transfer model. Detailed descriptions of each of the four proton/hydrogen precipitation models used in the study are provided in Appendix A. Here we briefly discuss the different modeling teams and types of models. A radiative transfer (RT) model is also used in this study to “forward model” the results of each step into observation space (*i.e.*, Steps 1B and 2B, respectively). This model, referred to herein as the Deighan Radiative Transfer model, is briefly described below (as written by J. Deighan).

5.2.1.1 Proton/Hydrogen Precipitation Models and Modeling Teams

We include four unique models/teams in this study: the Jolitz model (*i.e.*, “ASPEN”), the Kallio model, the Bisikalo/Shematovich *et al.* model, and the Gronoff *et al.* model (*i.e.*, “Aeroplanets”). The former three teams run Monte Carlo models (with the Jolitz and Kallio models being 3-D and the Bisikalo/Shematovich *et al.* model being 1-D). And the Gronoff *et al.* team uses a 1-D Kinetic model. As mentioned, detailed descriptions of these models can be found in Appendix A.

5.2.1.2 Radiative Transfer Model

To quantitatively compare the proton aurora modeling results and the IUVS limb observations it is necessary to perform a radiative transport calculation. While the H I 121.6 nm emission from thermal hydrogen is optically thick in the upper atmosphere of Mars (Anderson & Hord 1971), the emission associated with proton aurora can be considered optically thin due the large Doppler shifting caused by the high velocity of the ENAs. This both offsets the line center and broadens the width of the spectral line shape and ensures that few of the photons produced by proton aurora interact with the ambient thermal hydrogen population for most viewing geometries. This allows a simple line-of-sight integration to be employed, though CO₂ absorption must still be taken into account (Deighan *et al.* 2018, Gerard *et al.* 2019).

The procedure used to calculate a model brightness to compare with each measurement by IUVS is as follows: First, the model atmosphere is sampled at 1 km intervals starting from the reconstructed spacecraft position and extending out 3000 km along the line-of-sight vector. This ensures adequate sampling of the model VER, as the auroral emission typically has a scale height on the order of 10 km and a peak VER occurring 500-1700 km away from the spacecraft for IUVS periapse limb scans. The column of CO₂ between the spacecraft and each sample point in

the model is then integrated and an absorption optical depth is obtained using an absorption cross-section of $7.348 \times 10^{-20} \text{ cm}^2$ (Huestis & Berkowitz 2010). Beer's law is then applied to find the attenuation caused by CO_2 absorption for each sample point and the attenuated VER is integrated to obtain a column emission rate (CER). This is readily converted into the brightness unit of Rayleighs conventionally used for airglow and aurora (Hunten *et al.* 1956).

5.2.2 Campaign Outline/Steps

The purpose of this study is to gain a better understanding of the physics and driving processes of Martian proton aurora. This campaign is divided into two primary steps: an inter-model comparison step (Step 1) and a data-model comparison step (Step 2); each step is then subdivided to reflect the “native format” and “forward-modeled” results (*i.e.*, Steps 1-A and 1-B, as well as Steps 2-A and 2-B).

5.2.2.1 Step 1: Inter-model Comparison

We begin the campaign with an inter-model comparison in Step 1 using multiple different test cases of representative inputs to represent varying proton aurora conditions. The purpose of this step is to set a baseline for inter-model comparisons, and to compare the effects of varying input conditions on the results of each individual model.

Modelers were provided five different representative proton aurora conditions, each with varying solar wind velocity, H-ENA & proton fluxes at the top of the atmosphere, and CO_2 density profiles for high and low atmospheric temperature conditions. Using these inputs, modelers created Ly- α altitude vs. volume emission rate profiles with their respective models for each representative test case.

In Step 1A, we first compare the results in each modeler's "native format" (*e.g.*, volume emission rate). In Step 1B the results are "forward modeled" into observation space using the Deighan radiative transfer model.

5.2.2.2 Step 2: Data-model Comparison

In the second step, we assess the robustness of each of the models based on their abilities to reproduce a "typical" proton aurora detection from the MAVEN/IUVS dataset. In undertaking Step 2, different variables in the models were tuned to match proton aurora events in the MAVEN/IUVS dataset. Modelers were provided with relevant data inputs for a specific proton aurora event and challenged with accurately reproducing the event in their models. As in Step 1, the model results in Step 2A are provided in their native formats, and "forward modeled" into observation space in Step 2B using the Deighan radiative transfer model.

In the subsequent sections, we discuss the results of these steps. We also consider the inherent assumptions of each model (*e.g.*, altitude limits) and compare the differences in the model capabilities (*e.g.*, the physics represented in each model) that may impact the results.

5.3 Inputs and Results for Inter-model Comparison (Step 1)

5.3.1 Assumptions/Constraints for Step 1

To accurately compare the driving physics incorporated in each of the models, we utilize a number of constraints for each model in Step 1 (*i.e.*, the inter-model comparison step). The three primary constraints are 1) assuming the incident solar wind particle beam is monoenergetic; 2) assuming 1-D solar wind particle movement (*i.e.*, monodirectional) that is incident at the subsolar point (*i.e.*, $SZA = 0$); and 3) constraining the same cross section processes included in each model (yet allowing the use of different cross section values). We may empirically justify inclusion of the first two constraints based on previous observations of penetrating protons

showing a monoenergetic (*i.e.*, typically the same energy as the solar wind) population that is incident across the entire sunward-facing side of the planet (*e.g.*, Halekas *et al.*, 2015). For the third constraint, we specifically consider five cross section processes (for protons and/or H interacting with CO₂): elastic, charge exchange/electron capture, electron stripping, ionization, and Lyman- α . Although some models have the ability to incorporate additional processes, all have incorporated at least these five processes. Lastly, each modeling team incorporated their own Differential Scattering Cross Sections (DSCS) values.

5.3.2 *Representative inputs for Step 1*

In undertaking the inter-model comparison, we created five representative proton aurora events for each campaign team to model (Table 5.1). We selected baseline cases that resemble previous observations of Martian proton aurora (*e.g.*, Deighan *et al.*, 2018), and incrementally changed the input parameters in each subsequent case in order to quantify the effect of these parameters on the proton aurora profile. Specifically, we initially vary the type of incident particle at the top of the atmosphere (*i.e.*, 100% H-ENAs or 100% protons in Case 1 and Case 2, respectively), then the average incident particle beam flux (Case 3), the particle velocity (Case 4), and the neutral atmospheric temperature (Case 5). By changing the temperature in Case 5, we inherently also change the scale height, and thereby the CO₂ density profile. For simplicity and conciseness in this step, the representative inputs in Step 1 do not incorporate variations in solar zenith angle (SZA) or magnetic fields (*e.g.*, the models either ignored the effects of SZA altogether or assumed incidence at the subsolar point). We note that in this study we are exclusively interested in modeling the proton aurora profile under different input conditions; since proton aurora are almost entirely formed due to interactions between the incident particles and the neutral CO₂ atmosphere, the model results do not directly incorporate processes

occurring in the extended corona upstream of the bow shock (*e.g.*, charge exchange between solar wind protons and the H corona).

Table 5.1: Representative input for the five example cases in the inter-model comparison step (Step 1). These parameters were varied to assess their relative importance in each model.

	Case 1 (Baseline w/ H-ENAs)	Case 2 (Baseline w/ Protons)	Case 3 (Small Flux)	Case 4 (High Velocity)	Case 5 (High Temperature)
v [km/s]	400	400	400	800	400
$F_{\text{H-ENA}}$ [$\text{cm}^{-2}\text{s}^{-1}$]	10^7	0	10^6	10^7	10^7
F_{proton} [$\text{cm}^{-2}\text{s}^{-1}$]	0	10^7	0	0	0
CO ₂ Density Profile (varying Temp)	CO ₂ profile @ T=190K	CO ₂ profile @ T=190K	CO ₂ profile @ T=190K	CO ₂ profile @ T=190K	CO ₂ profile @ T=240K

In order to vary the neutral atmospheric temperature parameter (Case 5) modelers were provided with two different CO₂ density profiles, each containing altitude-binned (1 km bin) representative CO₂ number density values for the two respective temperature ranges of 190K (*i.e.*, baseline temperature) and 240K (*i.e.*, high temperature). These different CO₂ density values were created using the equation:

$$n(z) = n_{\text{ref}} * \exp((z_{\text{ref}} - z) / H). \quad (1)$$

where z is altitude, n_{ref} is the number density at a reference altitude, z_{ref} is the chosen reference altitude (in this case, 120 km), and H is the CO₂ scale height. Here we assume $n_{\text{ref}} = 1 \times 10^{11} \text{ cm}^{-3}$ at 120 km, and H is calculated for each temperature range using a values of $g = 3.46 \text{ m/s}^2$ (*i.e.*, g at the reference altitude of 120 km). The calculated H values for the low and high temperature cases were 10.4 km and 13.1 km, respectively.

5.3.3 Results of Step 1A

In Figure 5.1, it is evident that the results of the inter-model comparison show many similarities between the different modeled proton aurora volume emission rates (VERs), with the results of the Jolitz and Kallio models exhibiting the most similarities. There is a large range in the proton aurora peak altitudes between the models, where the Bisikalo/Schematovich *et al.* model consistently exhibits the lowest peak altitudes and the Gronoff *et al.* model exhibits the highest peak altitudes. Moreover, there are similar variabilities present within most of the models when evaluating the differences between each of the five representative cases. Almost all of the models show no difference in the proton aurora profile (*i.e.*, VER or altitude) based on varying the type of incident particle at the top of the atmosphere (*i.e.*, H-ENA or proton); the only exception is the Bisikalo/Schematovich *et al.* model, which exhibits a slight increase in the VER of the proton aurora profile for protons rather than H-ENAs as the incident particle. We note that a possible contributor to the similarities observed between the Jolitz and Kallio results could be the similar cross section values used between each of these two models.

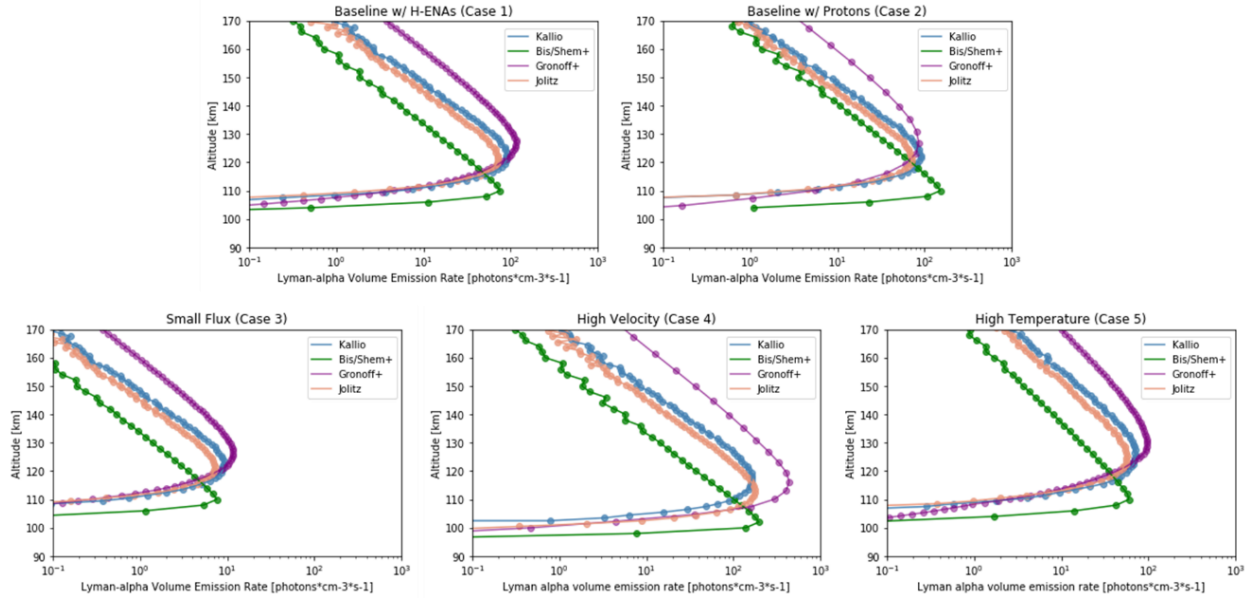


Figure 5.1: Simulation results of proton aurora altitude-VER profiles from each model for the five representative input cases in the inter-model comparison step of the campaign (Step 1-A). The two parameters that have the most significant effect on the results are the input solar wind flux and velocity.

5.3.4 Results of Step 1B

In Step 1-B we “forward model” the results of Step 1-A into observation space (*e.g.*, perform a “line-of-sight” integration comparison). In this step we consider the heuristic observations that would be made by MAVEN/IUVS under similar input conditions. In so doing, the model results are converted from Ly- α VER (in units of photons/cm³s) to Ly- α intensity (in units of kilorayleighs, kR), using the Deighan radiative transfer model. The results of this step provide a more reliable cross-model comparison.

As shown in Figure 5.2, the results of Step 1-B further reveal similarities in the model intensities and peak altitudes for each of the five cases. We find consistently in each model that the two major variables that affect the proton aurora profile are the penetrating particle flux and the particle velocity. Decreasing the flux by order of magnitude (Case 3) correspondingly decreases the Ly- α intensity by order of magnitude. Similarly, doubling the particle velocity (Case 4) noticeably increases the peak intensity in each model and decreases the peak altitude by

~5-10 km. In the final representative input case of increasing the atmospheric temperature (and thereby changing the neutral atmospheric scale height) (Case 5), all of the models show a slight corresponding decrease in the Ly- α intensity, and most models show an increase the peak altitude by ~5-10 km (with the exception of the Bisikalo/Schematovich *et al.* model, which does not exhibit a change in the peak altitude due to the changing temperature/scale height).

The consistency of these results confirms our understanding of the driving processes which have the most significant effect on the proton aurora profile. Particularly, we see in Cases 3 and 4 that the solar wind proton velocity and density (which also affect the particle energy and flux) are tremendously important in the formation of notable proton aurora events. Thus, we may predict from the results that high velocity and/or density solar events (*e.g.*, coronal mass ejections and solar energetic particle events) will correspondingly create significantly enhanced proton aurora events. And that major changes in the neutral atmospheric scale height (*e.g.*, local or global dust storms) can cause absorption by CO₂ on the bottom side of the proton aurora profile, leading to apparently less intense profiles exhibiting a higher peak altitudes.

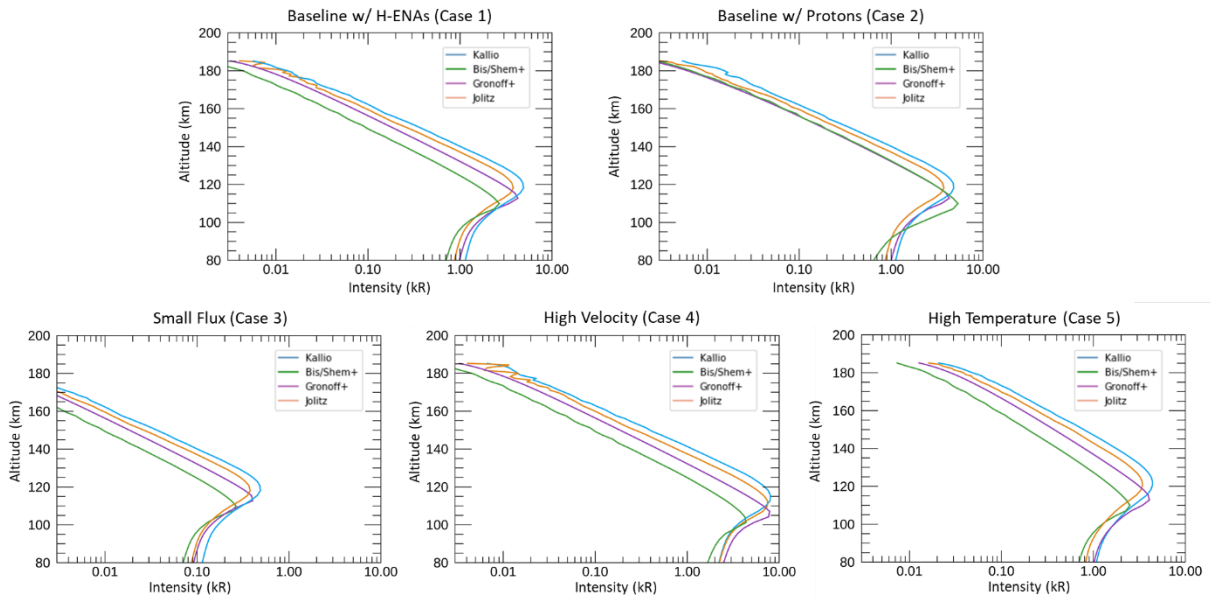


Figure 5.2: Simulation results from the inter-model comparison after running the results through the Deighan Radiative Transfer (RT) model (Step 1-B). Using the RT “forward-models” the results into observation space (e.g., perform a “line-of-sight” integration comparison). The model results more closely resemble each other after this step, but the dominant influencing factors identified in Step 1-A (Figure 5.1) are still present.

5.4 Inputs and Results for Data-Model comparison (Step 2)

5.4.1 Description of MAVEN/IUVS proton aurora observation and input data

For the data-model comparison stage of the campaign (Step 2), we selected a typical example of a proton aurora event from the MAVEN/IUVS dataset; specifically, we chose an event that occurred during MAVEN Orbit #4235. This particular proton aurora event occurs at low SZAs around southern summer solstice ($L_s \sim 270$), a period of time exhibiting frequent proton aurora activity and increased dust activity associated with the concurrent Martian dust storm season. Figure 5.3 shows the IUVS Ly- α intensity data for this orbit: the left-hand plot shows the altitude-intensity profile for each of the limb scans used in the study; and the right-hand plot is these profiles overlain on a synthetic image format of each of the IUVS limb scans from this orbit (horizontal) showing the Ly- α intensity for each of the 21 IUVS mirror integrations (vertical) and 7 spatial bins within each scan (e.g., similar to Figure 2 in Deighan *et*

al., 2018). There are eleven IUVS limb scans in this orbit, however, in order to only include the most robust data, we use only the middle nine IUVS scans in this study (yellow highlighted scans in Figure 5.3). Modeler's results were compared with IUVS Level 1C altitude-binned Ly- α intensity data from these nine scans in evaluating this step of the study.

There are minor peak altitude variations in IUVS Ly- α observations between scans throughout this orbit. These minor altitude variations correspond with similar altitude variations in the IUVS CO₂⁺UVD, suggesting the possible presence of waves and/or tides in the neutral atmosphere during this orbit (*e.g.*, *Lo et al.*, 2015; *England et al.*, 2016). The likely presence of waves/tides in this orbit is strengthened by similar observations in the MAVEN/NGIMS inbound CO₂ altitude-density profile. We note, however, that any minor variations in altitude should not have any significant influence on the modeled proton aurora profiles.

This particular proton aurora event exhibits an especially high orbit-mean peak enhancement (3.93 kR) as observed by IUVS. Also unique during this orbit is a particularly high penetrating proton flux ($2.73 \times 10^6 \text{ cm}^{-2}\text{s}^{-1}$) observed by MAVEN's Solar Wind Ion Analyzer (SWIA) instrument (*Halekas et al.*, 2013). SWIA observed a strong solar wind stream interaction during this orbit, resulting in this especially high penetrating proton flux. The MAVEN periapsis during this orbit is in the southern hemisphere on the dayside of the planet. Because the spacecraft periapsis does not occur near any remnant crustal fields, we do not expect a significant contribution (if any) from crustal fields during these observations. The average interplanetary magnetic field magnitude and angle during this orbit is $\sim 10 \text{ nT}$ and $\sim 45^\circ$, respectively.

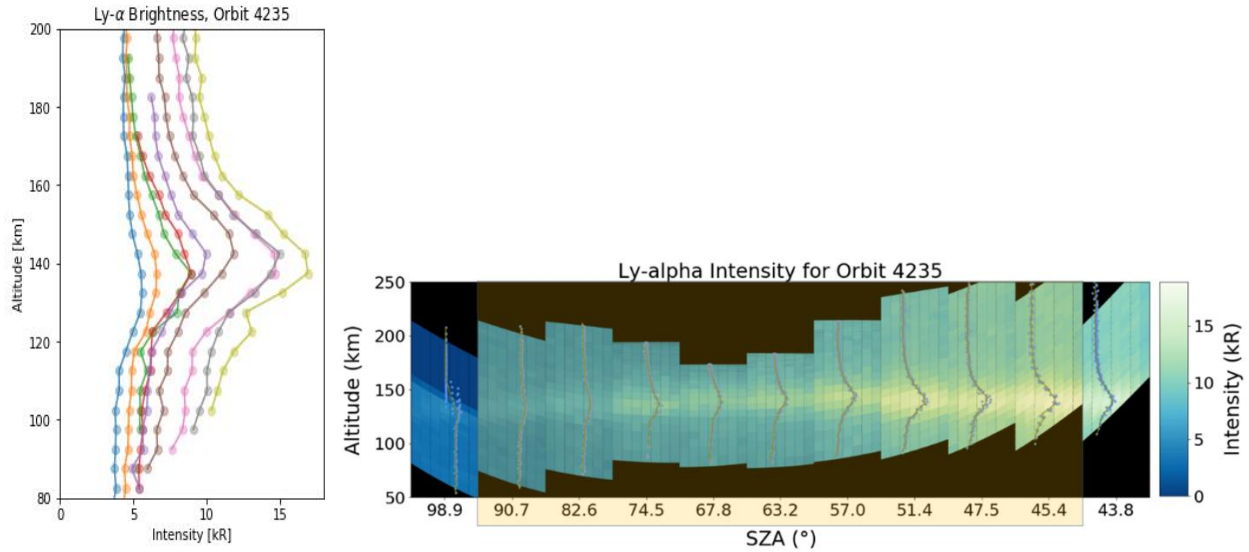


Figure 5.3: IUVS Ly- α intensity data of proton aurora observation used in the data-model portion of the campaign (Step 2). **Left:** IUVS altitude-intensity profiles for limb scans used in the study (MAVEN orbit 4235). **Right:** altitude-intensity profiles overlain on top of a synthetic image format of Ly- α intensities for each IUVS limb scan/mirror angle in this orbit (e.g., Figure 2 from Deighan et al. 2018). Note that only the central nine scans were used in this study (yellow highlighted scans), and that the given SZA values given correspond with the median SZA in each scan.

5.4.2 Assumptions/Constraints for Step 2

Modelers were provided with specific data instrument inputs for Step 2 (discussed more below). We apply many of the same constraints and assumptions as those applied in Step 1 (*i.e.*, assuming a monoenergetic incident particle beam, assuming monodirectional incident particle movement, and constraining the cross section processes used). One notable difference is that in Step 2 we incorporate the effects of differing SZA, in order to simulate the SZA ranges of the different IUVS scans during this orbit. And as in Step 1, we continue to exclude any possible effects due to electric or magnetic fields in this step.

In order to additionally simplify the inputs for this step, all models assume that the incident particle population is composed entirely of H-ENAs at the top of the atmosphere (*i.e.*, assuming a penetrating proton flux equal to zero). Based on our findings in Step 1, the proton aurora profile does not significantly change in most models when assuming 100% protons or 100% H-

ENA's. Thus, this assumption of particle composition should not significantly affect the final results. The H-ENA flux (F_{H-ENA}) was approximated using the equation:

$$F_{H-ENA} = F_{pp} * 13.5 \quad (2)$$

Where F_{pp} (the SWIA orbit mean penetrating proton flux) equals $2.73 \times 10^6 \text{ cm}^{-2}\text{s}^{-1}$ in this orbit, and 13.5 is the approximate percentage of the incoming beam of H-ENAs that is converted to protons. This conversion value was determined based on previous SWIA observations (*e.g.*, Halekas *et al.*, 2015; Halekas, 2017) by assuming that at the point when H-H⁺ equilibrium is reached in the collisional atmosphere the mix is ~92.5% ENAs and 7.5% protons (*i.e.*, the equilibrium fractionation for the relevant cross sections at 1 keV).

Another constraint carried over from Step 1 was that all models utilized the same representative CO₂ density (*i.e.*, a 1 km altitude-binned CO₂ number density profile). However, in Step 2, the theoretical profile CO₂ density line was created based on observed/derived neutral densities from two MAVEN instruments observing at different altitude ranges during this orbit: IUVS and the Neutral Gas and Ion Mass Spectrometer (NGIMS) (Mahaffy *et al.*, 2015). (We note that although NGIMS data are acquired during both the inbound and outbound portions of the orbit, we restrict this study to include only inbound data, due to instrument artifacts which have been found to artificially increase CO₂ densities in NGIMS outbound data.) The IUVS and NGIMS neutral densities are consistent with each other within the limited overlapping altitude range of the two instruments (*i.e.*, at a reference altitude of 170 km, the NGIMS CO₂ density is $\sim 1.48 \times 10^9 \text{ cm}^{-3}$, and the smallest derived CO₂ density from different IUVS limb scans is $\sim 1.74 \times 10^9 \text{ cm}^{-3}$).

Figure 5.4 shows the theoretical CO₂ profile for Step 2, which was created by fitting a best-fit exponential to the IUVS and inbound NGIMS data using equation (1). Where, in this

case, $n_{\text{ref}} = 1.1 \times 10^{11} \text{ cm}^{-3}$ (the average IUVS density at z_{ref}), $z_{\text{ref}} = 130 \text{ km}$ (the minimum altitude observed by IUVS during this orbit). The CO_2 scale height was estimated by varying the temperature value until an appropriate fit was achieved (using a value of $g = 3.41 \text{ m/s}^2$ at 130 km); a temperature of 180 K was used in calculating this best-fit line.

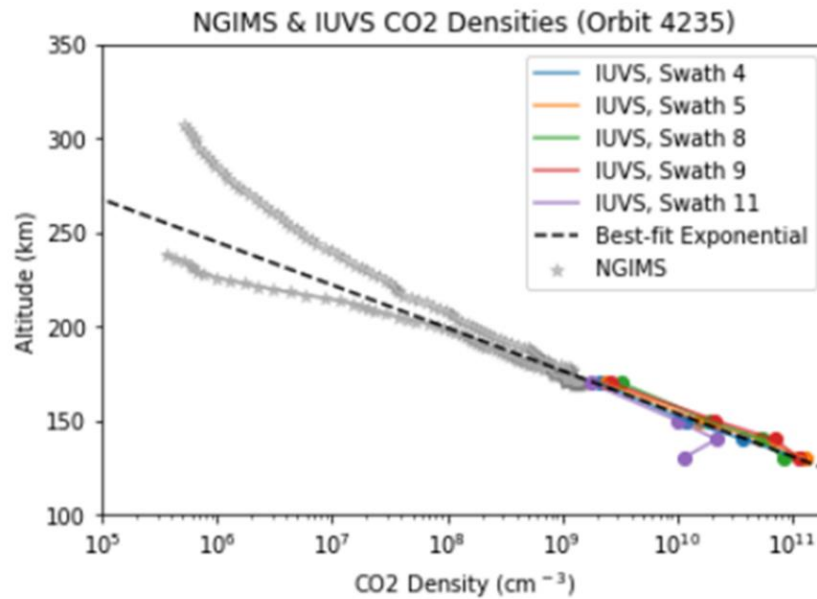


Figure 5.4: Empirically-derived theoretical CO_2 profile used in models for the data-model comparison step (Step 2). This profile was created by fitting a best-fit exponential to the derived IUVS and measured inbound NGIMS (lower NGIMS curve) data from this MAVEN orbit.

5.4.3 Results of Step 2A

The results of Step 2A show that all models are able to simulate the data to within an order of magnitude of the same VERs (Figure 5.5). As in Step 1, the results of Step 2A also show that the Jolitz and Kallio simulations are most similar to each other in terms of VERs & peak altitudes. Further, the Gronoff *et al.* model results exhibit relatively low VERs compared with other models, and the Bisikalo/Shematovich *et al.* model results exhibit relatively high VERs & low peak altitudes; however, we note that the peak altitudes in these model results display the most variability between SZAs, and that the highest SZA profiles could not be modeled due to model limitations.

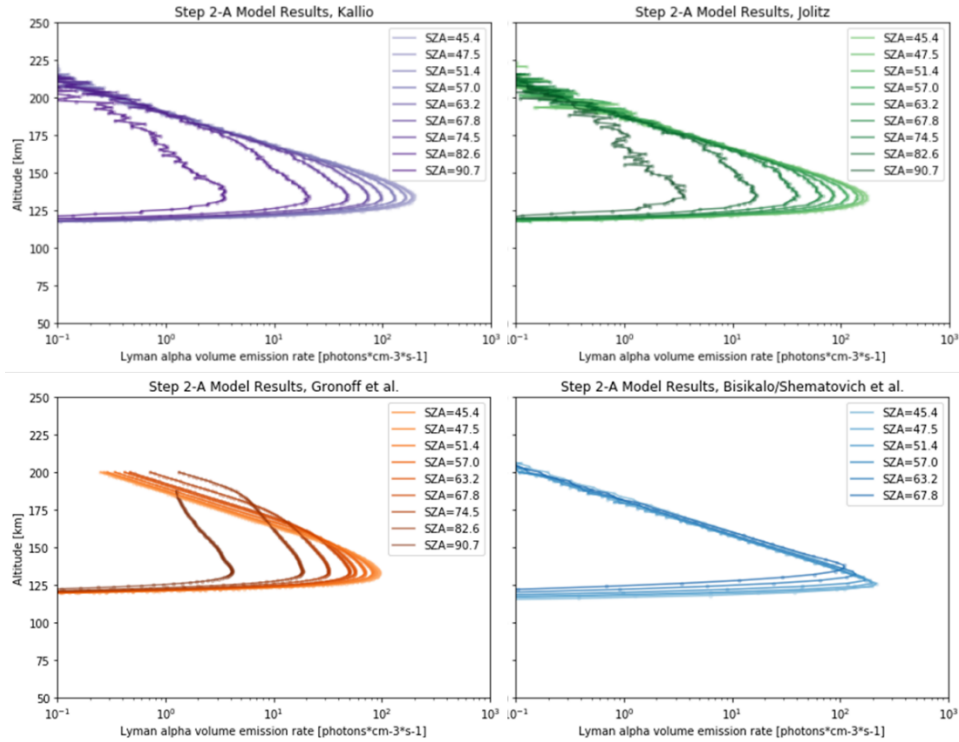


Figure 5.5: Simulation results from the data-model comparison step of the campaign (Step 2-A), showing proton aurora altitude-VER profiles from each model for the specified input parameters and SZAs. Most of the model results display similar peak altitudes and VERs (within an order of magnitude).

5.4.4 Results of Step 2B

Forward modeling the simulation results using the Deighan RT model allow an appropriate comparison between the model results and the IUVS data. In so doing, we determine through Step 2B that all of the models appear to underestimate the proton aurora brightness $\sim 5\text{-}10$ kR (Figure 5.6). It is also apparent that the peak altitudes of model results are $\sim 5\text{-}15$ km lower than the data peak altitudes.

It is important to note that the Ly- α brightness observed in the IUVS data is created by contributions from not only the non-thermal H producing proton aurora, but also from the thermalized background coronal H. Thus, by subtracting out the background coronal H from the IUVS proton aurora profiles, we are able to accurately compare the data with the model results. We perform this coronal H background subtraction by first estimating the background coronal H

during this time based on IUVS limb scan profiles from a nearby orbit that exhibit little/less evidence of enhancement due to proton aurora activity (created by fitting an arcsine function to the profiles from the nearby orbit). This estimated background Ly- α brightness due to the coronal H is then subtracted out from each corresponding IUVS limb scan from the orbit of interest (between the two scans observing at similar SZAs). The corrected intensities then reflect the H contribution only from proton aurora. In this orbit, the intensities are reduced significantly (by nearly 10 kR at low SZAs), but the shape of the profiles between ~110-150km (around the proton aurora profile peak) does not change. The profile peak altitudes typically also do not change as a result of this background subtraction routine (however, we note that in this case, the peak altitude of the lowest SZA profile has been shifted down by 5 km due to an altitude difference in the background subtracted profile).

Through implementing a background subtraction routine for the orbit of interest, we see that the model intensities appear to be much more closely correlated with those of the data for each limb scan profile (Figure 5.6, compare with far right plot). The observed background-subtracted data intensities at low SZA profiles lie between the Gronoff *et al.* and Bisikalo/Shematovich *et al.* results. However, at high SZAs, all three models for which results are available appear to model the data intensities rather accurately. The Kallio and Jolitz model intensities overestimate the data at low SZAs (*i.e.*, the largest intensity profiles) by a few kR, while the Gronoff *et al.* model intensities underestimate by a few kR. At low SZAs, the Bisikalo/Shematovich *et al.* model intensities closely correlate with the data intensities, but still slightly overestimate the data; however, comparison of the profiles at high SZAs is not possible due to the limitations which prevent creation of model simulations at higher SZAs. We note that

none of the model intensities exactly match with the data; possible reasons for these discrepancies are discussed in the following section.

In spite of the better agreement between data and model intensities after subtracting out the theoretical background Ly- α brightness, it also must be noted that significant peak altitude discrepancies between the models and the data are still present. This altitude discrepancy suggests that other processes/assumptions are not fully accounted for or understood in our evaluation of the results. In the following section, we examine numerous possible parameters that might be contributing to the observed discrepancies between the data and the models.

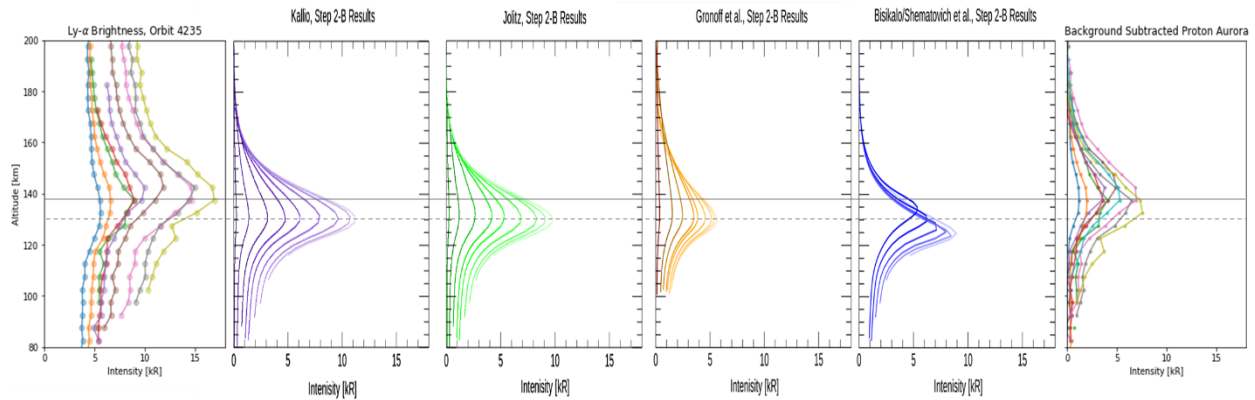


Figure 5.6: Simulation results for the data-model comparison after running the results through the Deighan Radiative Transfer (RT) model (Step 2-B). The uncorrected IUVS limb scan profiles for this orbit is shown on the far left plot, and the corrected background-subtracted limb scans (after subtracting out the theoretical “background” coronal H contribution) are shown on the far right plot. The Ly- α intensities of the model results much more closely correlate with those of the background-subtracted data. However, there is still a notable discrepancy between the average peak altitude of the data profiles (solid grey horizontal line) and the average peak altitude of the model profiles (dashed grey horizontal line). Note that the SZA of the observations is decreasing from left to right (i.e., moving toward the subsolar point), as shown in Figure 5.3.

5.5 Discussion of parameters affecting model differences and similarities

5.5.1 Monodirectional vs. Isotropic assumption

Another contribution to the data-model discrepancies in peak altitude is likely caused by the assumption of monodirectional particle movement of the incident solar wind. We include a terminology note here that in specifying “monodirectional” versus “isotropic” particle movement, we refer specifically to the bulk velocity (i.e., average speed and direction) of the protons in the incident solar wind beam. Thus, one might expect that if the assumption of

monodirectionality does indeed influence our results, the apparent data-model discrepancies should be improved (or at the very least, altered) by assuming isotropic particle movement/scatting. In order to test whether or not this assumption has a significant influence on the campaign results, two modeling teams (Kallio and Bisikalo/Shematovich *et al.* teams) carried out example simulations using similar input parameters but assuming isotropic particle movement/scatting. Figure 5.7 shows an example of this comparison using the Bisikalo/Shematovich *et al.* model. In these comparative simulations, as the incident particle population was made to resemble an isotropic beam, the VER of the proton aurora profile was decreased and the peak altitude was increased by ~5-20 km (with the largest altitude variability observed in the Kallio model). These variations (especially in altitude) could indeed contribute significantly to the observed data-model discrepancies. Further, in addition to these simulated differences in VER and peak altitude, the Bisikalo/Shematovich *et al.* model also predicted a much larger H flux in the upward direction in the isotropic case. This higher peak altitude in the proton aurora profile using the isotropic assumption in comparison with the monodirectional assumption is a direct result of H atoms being more efficiently backscattered due to collisions with CO₂ (*i.e.*, in the isotropic case, a fraction of precipitating H atoms are backscattered compared to no backscattering the monodirectional case). Because neither of these two extreme assumptions (*i.e.*, purely monodirectional or purely isotropic particle movement) is a probable physical occurrence, the actual particle precipitation pattern is likely somewhere between these two limiting cases. Thus, the variability observed in simulating these two different assumptions of particle movement provides relevant information regarding a possible range of peak altitudes in which the model results may exist. Moreover, we may also identify this assumption as a likely contributor to the observed discrepancies between the data and the models. However, a

lack of ability to quantify the fraction of monodirectional versus isotropic particle movement during this time prohibits any effort to quantify the effect of this assumption on the model results.

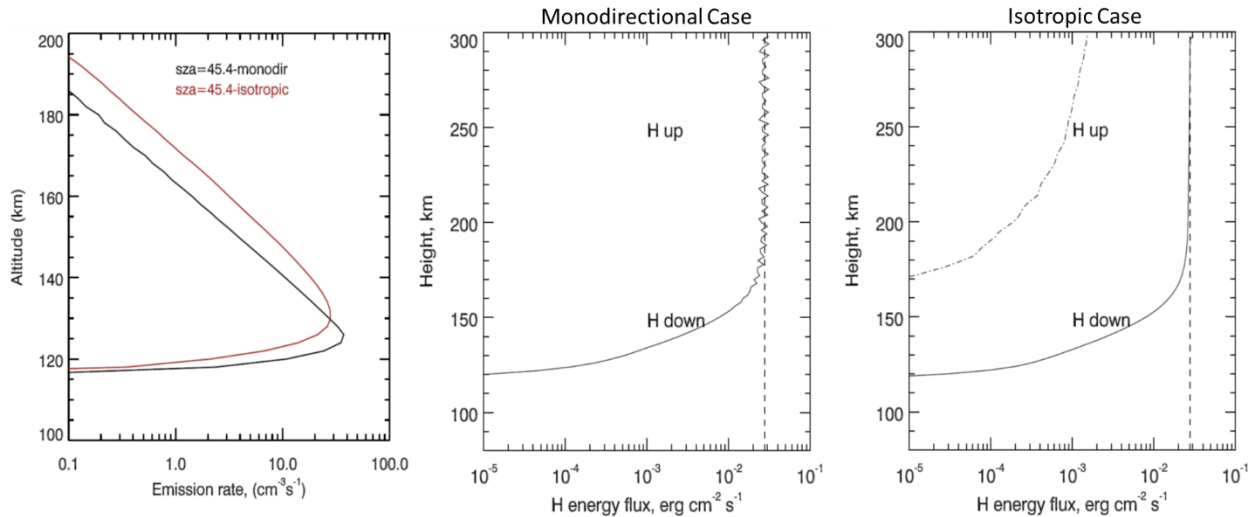


Figure 5.7: Example comparison of assuming purely monodirectional movement of the incident particle population versus purely isotropic (results from the Bisikalo/Shematovich et al. model). **Left:** Comparison proton aurora profiles using each assumption; **Middle:** Simulated H energy flux in the downward and upward directions using a monodirectional assumption; **Right:** Simulated H energy flux in the downward and upward directions using an isotropic assumption. The simulated proton aurora profile using the isotropic assumption has a higher peak altitude and smaller VER due to the larger upward (e.g., backscattered) H population. Although the models assume purely monodirectional movement in this study, the reality is likely somewhere between these extreme assumptions, which could in turn lead to some of the observed discrepancies between the data and the models in Step 2 of the campaign. (Figure credit: Bisikalo/Shematovich et al. team)

5.5.2 Cross Section Processes and Scattering Angle Distributions

While the models in this study constrain the cross section processes included in their simulations to the five processes that can be included in every model, most models do not use the same cross section values. These cross section values can indeed vary significantly with varying energy ranges. However, we note that the cross section values used in each model agree to within less than ~an order of magnitude of each other for the relevant energy range in this study (*i.e.*, between ~100eV – 2KeV). Therefore, while differences in cross section values may have minor effects in the model-model comparison, we do not expect these differing values to significantly affect the results of the data-model comparison.

5.5.3 *Other Assumptions*

There are a number of additional assumptions in this study that may have led to discrepancies between the models and the data. First, numerous data-driven assumptions were made in creating the theoretical CO₂ density profile for Step 2. Any of three variables could be altered that could in turn significantly affect the proton aurora profile: the energy of the incident particles, the density of the atmosphere at a reference altitude, or the neutral atmospheric scale height. All of these variables affect the peak altitude of the proton aurora profile, while changing the scale height and energy also affects the profile peak intensity (more specifically, changing the scale height can also affect how broad/narrow the profile shape becomes). In this study, we determined the atmospheric density at a reference altitude (130km) by using the average derived IUVS Level 2 CO₂ density at 130 km. Because the CO₂ density profile used by modelers in this study is theoretically derived, inaccuracies in the assumed quantities for reference density or scale height would lead to an inaccurate representation of the atmospheric density profile during this time. Thus, it is possible that the CO₂ density profile is not entirely accurate in representing the atmosphere at this time, possibly contributing to some of the discrepancies observed in the data-model comparison. However, observations by MAVEN/SWIA during this orbit provide confidence that the calculation of particle energy (based on average penetrating proton velocity) and the assumption of monoenergetic particle behavior are appropriate and accurate, and therefore do not significantly affect the results.

For simplicity in Step 2 we assume the precipitating particle population at the top of the atmosphere is entirely composed of H-ENA's. Although the incident particle population is indeed comprised of a fractionated portion of both ENAs and protons, this simplified assumption was preferred over a non-empirical assumption of an estimated fractionation ratio. Moreover, as

the results in Step 1 do not significantly change in most models based on the assumption of an entirely ENA- or proton-rich population, we would not expect the effects of this assumption on its own to have a significant impact on the final results. One potential exception may be the Bisikalo/Shematovich *et al.*, results in which the peak intensity somewhat increases if a particle population of entirely protons is assumed (as seen in Step 1-A and 1-B). Because the Bisikalo/Shematovich *et al.* results showed slight variability based on the assumed incident particle population, it is possible that the intensities in their model results might have been larger by changing this assumption (which may cause their simulated intensities to more closely resemble those of the Kallio and Jolitz models).

Lastly, the ENA flux used in Step 2 was calculated as an empirically derived fraction of the orbit-averaged SWIA penetrating proton flux. While this fraction is supported by previous observations by SWIA, the value can vary based on seasonal or spontaneous changes (*e.g.*, the solar wind proton flux, the neutral atmospheric scale height, or the location of the bow shock). As determined in Step 1, decreasing the flux by an order of magnitude will correspondingly decrease the proton aurora peak intensity by an order of magnitude. Thus, although the method used to calculate the ENA flux is believed to be an accurate approximation, we note that any major deviation from the statistical norm of local conditions during this orbit would cause discrepancies in accurately calculating the ENA flux. Moreover, independent of the statistical robustness of the empirically calculated ENA flux, because the actual penetrating particle population is composed of a combination of ENAs and protons (with the fraction of ENAs increasing with decreasing altitude) (*e.g.*, Halekas, 2017), the resulting model intensities for this step likely represent an upper limit for the simulated intensities (leading to the overestimation of profile intensities in most of the models). Thus, the combination of the assumption of a purely

ENA-rich particle population and the chosen method for calculating the ENA flux are most likely major contributors to the observed discrepancies between the data and model intensities.

5.5.4 Data Quality and Caveats

In addition to the possible sources of discrepancy in the model assumptions, we must also consider possible caveats associated with the data. Because IUVS is a remote sensing instrument its limb scan observations are created by integrating along the line of sight of the instrument. However, the SWIA penetrating proton fluxes are measured *in situ* during periapsis, and the orbit averaged value is used in this study. It must be considered that there may be spatial and/or temporal discrepancies between these observations, even though they are collected during the same orbit. Secondly, because IUVS Level 1C (L1C) data are processed and altitude-binned, we note that minor discrepancies may be introduced in the Ly- α intensities during the data reduction process. We also note that the MAVEN spacecraft potential at periapsis during this orbit was observed to be relatively large and negative; these are not ideal conditions for observing low energy charged particles, which limits our ability to compare the observations from most other MAVEN instruments during this orbit. The data used in this study does not incorporate low energy charged particles, and we are not aware of any potential caveats associated with the included datasets that could be influenced by the spacecraft potential.

5.6 Summary, Conclusions, and Future Work

The results of this modeling campaign provide a new understanding of the primary factors influencing variability in Martian proton aurora. We found the inter-model comparison step of the campaign that the two most influential variables affecting proton aurora are the incident solar wind flux and velocity. We also determined that most of the models in the study were able to simulate the representative inputs to within an order of magnitude, with the differences between

the models causing the observed inter-model variability. In the data-model comparison step of the campaign, we determined that all of the models were able to efficiently simulate the data, with most over-estimating and one under-estimating (*i.e.*, the Gronoff *et al.* model) the intensities. The discrepancies in intensities and peak altitudes between the data and models could be attributed to a number of possible assumptions in the campaign. And the differences between the model results in the data-model comparison step demonstrate the inherent capabilities, assumptions, and methodologies of each of the models.

By undertaking this comparative study, we are able to better constrain the driving processes of proton aurora as characterized by each contributing model, as well as the dominant physics that need be incorporated in future modeling studies to accurately represent these events. The results of this study are applicable not only for proton aurora at Mars, as similar auroral processes can occur on any planetary body that exhibits an induced magnetic field and a neutral H corona. Modeling studies such as this one are particularly important in efforts to study planetary bodies with minimal observations or where data are not available, whether in our solar system and beyond (*e.g.*, Venus, comets, and exoplanets).

In a future study, we aim to address the effects of magnetic and electric fields (*i.e.*, induced and/or crustal magnetic fields) on proton aurora. It will also be important to quantify the effect of the backscattered particle population on the proton aurora profile; because recent SWIA studies have shown that a significant portion of the incident particle population can be backscattered (Girazian and Halekas, 2021) this factor could thereby contribute to the observed data-model discrepancies. Additionally, we will aim to address the effects of CO₂ absorption on the proton aurora profile. Because absorption of Ly- α by CO₂ becomes significant below the peak of the proton aurora Ly- α emitting layer, it can have a non-trivial impact on proton aurora

modeling efforts. We note that this study depends strongly on consideration of the efficiency of charge exchange between protons in the undisturbed solar wind and H in the extended corona (as this is an upper boundary for calculations due to the precipitation of H-ENAs). Therefore, a possible next step for this campaign could be to consider the variations present in an energy spectrum of incident H atoms and protons (*i.e.*, an energy spectrum that is not monoenergetic). And finally, we will expand our analysis to include an “atypical” example of a proton aurora event in the data-modeling portion of the campaign (*e.g.*, spatially and/or temporally varying, nightside events, etc.).

6. Summary and Conclusions

6.1 Doctoral Dissertation Project Summary

In this final chapter I summarize the findings presented in this doctoral dissertation and discuss the significance in the Planetary Science field. As previously stated, the purpose of this project is to develop our understanding of the phenomenology, variability and driving processes of Martian proton aurora. In completing this dissertation project, I have directly addressed the primary research objectives highlighted at the beginning of this dissertation, which include:

- Creating a comprehensive database of Martian proton aurora and characterizing the phenomenology of these events, finding that proton aurora are uniquely constrained to the planet's dayside and occur almost continuously during the Martian southern summer season (Chapter 2).
- Evaluating the comparative variability between proton aurora and penetrating proton observations to identify the distinct effects of atmospheric dust activity and extreme solar events (Chapter 3).
- Constraining the geomagnetic locations of proton aurora occurrence at Mars to search for possible interaction with an upstream solar magnetic field, finding a possible preferential occurrence of proton aurora at specific cone/clock angles (Chapter 3).
- Identifying/characterizing unusual variability in "atypical" proton aurora observations (including nightside and "variable" proton aurora) to gain a deeper understanding of the trends and unique formation mechanisms of these uncommon events (Chapter 4).
- Developing the current understanding of proton aurora formation and variability through a coordinated multi-modeling comparison campaign, thereby helping to constrain the dominant physics/driving processes affecting proton aurora (Chapter 5).

6.2 Scientific Novelty and Press Coverage

As previously noted, this project is the first detailed study of Martian proton aurora to date. Thus, the scientific findings that resulted from this work are all novel developments in the field of Planetary Science. However, certain parts of this dissertation project gained particular attention/notoriety and were covered by numerous national and international press outlets, including a press release by the National Aeronautics and Space Administration (NASA). In this section, I briefly highlight these significant results. (Note that the NASA press release can be found here: <https://www.nasa.gov/press-release/goddard/2019/mars-proton-aurora-common>)

As discussed in Chapter 2, the results of our detailed statistical study found that proton aurora are primarily constrained to the dayside of the planet, occurring at low solar zenith angles (SZAs). Figure 6.1 shows a unique perspective of the spatially confined proton aurora on the sunward facing side of Mars. The locations of proton aurora on Mars are due to the *lack* of a global intrinsic magnetic field. Thus, this unique type of aurora on Mars provides new information about how the solar wind can interact with the upper atmospheres of planets to produce types of aurora that are not possible at Earth.

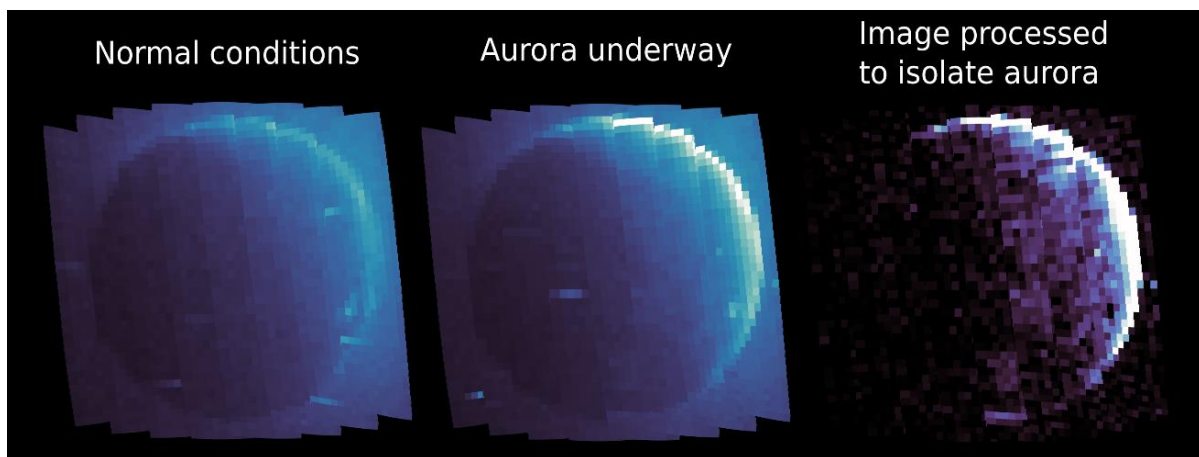


Figure 6.1: IUVS apoapsis observations of nominal conditional of the Martian hydrogen corona (left panel) and observations when proton aurora are underway (middle panel). By subtracting out the hydrogen coronal intensities we may see the spatial constraints proton aurora on the sunward facing side of the planet (right panel). (Image credit: NASA/LASP/Univ. of Colorado/ERAU)

Another unique finding from this study is the prominent seasonal variability and the nearly continuous occurrence of proton aurora around the Martian southern summer solstice. During this period Mars is relatively closer to the sun in comparisons with northern summer, causing higher atmospheric dust content and temperatures. This increased abundance of atmospheric dust leads to dust-induced hydrogen (H) escape, and thereby, an extended H corona beyond the bow shock (allowing for more charge exchange interactions between the solar wind and H in the Martian upper atmosphere). The result of this process is an annual maximum in proton aurora intensities, emission enhancements, and peak altitudes around southern summer, and an occurrence rate of nearly 100% on the dayside of the planet during this time. This variability is nicely demonstrated in the schematic in Figure 6.2.

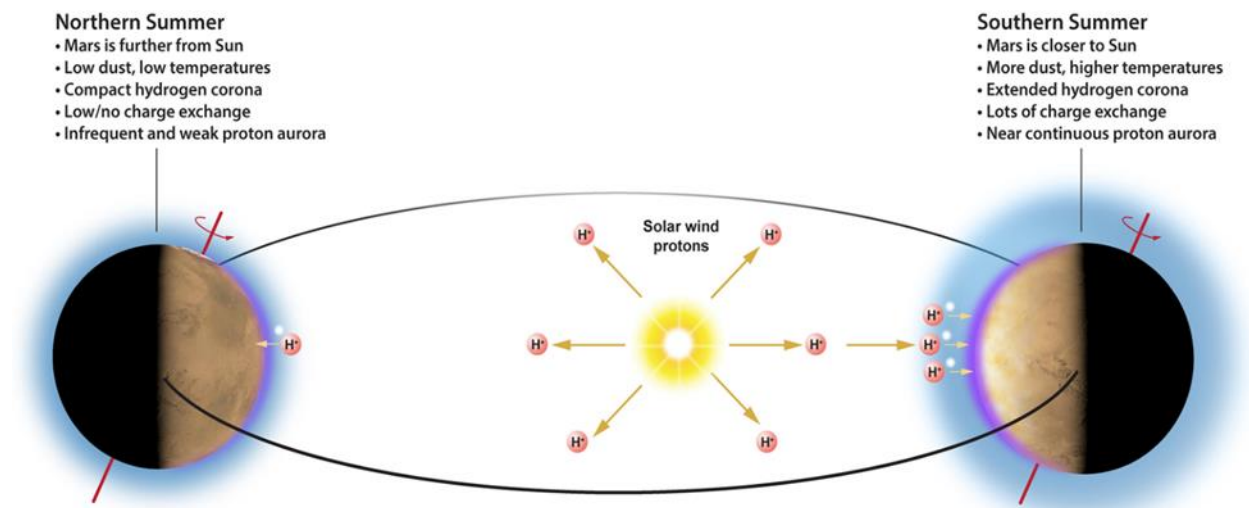


Figure 6.2: Martian proton aurora exhibit significant seasonal variation due to dust-driven lower-atmospheric forcing and hydrogen escape. The peak activity occurs during southern summer, when the Mars atmosphere experiences increased dust activity and higher temperatures. (Figure credit: NASA/LASP /Univ. of Colorado/ERAU)

Thus, another important discovery from this project is that proton aurora can actually be used as a proxy for evaluating Martian H escape and water loss to space! To summarize the intriguing significance of these results, I quote (myself) from the before-mentioned NASA press release: “Perhaps one day, when interplanetary travel becomes commonplace, travelers arriving

at Mars during southern summer will have front-row seats to observe Martian proton aurora majestically dancing across the dayside of the planet (while wearing ultraviolet-sensitive goggles, of course). These travelers will witness firsthand the final stages of Mars losing the remainder of its water to space.”

6.3 Conclusions

The results of this study inform our understanding of the unique characteristics, variability, and driving processes of Martian proton aurora, as well as the solar wind’s interaction with the upper atmosphere of Mars under varying conditions. These findings are relevant not only to Mars, but also to any planetary body that exhibits a hydrogen corona and lacks a global intrinsic magnetic field, both within our solar system and beyond (*e.g.*, Venus, comets, and exoplanets). The results of this project, in combination with other studies, will provide a more thorough understanding of the physical processes driving the evolution of the Martian atmosphere through time. This improved understanding of atmospheric processes and escape on Mars will pave the way for future robotic and human exploration missions to Mars and other planetary bodies in our solar system.

I look forward to continuing to work on the future projects that I have outlined in the previous chapters of this dissertation. I am delighted and honored to have been a part of the beginning stages of developing our understanding of Martian proton aurora - a unique/novel subject that is at the cutting edge of the Planetary Science field. And I am eager to see the exciting developments in this field in the years to come!

Bibliography

Chapter 1 References

- Akalin, F., D. Morgan, D. Gurnett, D. Kirchner, D. Brain, R. Modolo, M. Acuña, and J. Espley (2010), Dayside induced magnetic field in the ionosphere of Mars, *Icarus*, 206(1), 104–111.
- Bertaux, J.-L., Leblanc, F., Witasse, O., Quemerais, E., Lilensten, J., Stern, S. A., ... Korabiev, O., 2005. Discovery of an aurora on Mars. *Nature*, 435(7043), 790–794.
<https://doi.org/10.1038/nature03603>
- Bhattacharyya, D., J. T. Clarke, J. L. Bertaux, J. Y. Chaufray, and M. Mayyasi (2015), A strong seasonal dependence in the Martian hydrogen exosphere, *Geophysical Research Letters*, 42(20), 8678–8685.
- Chaffin, M. S., J.-Y. Chaufray, I. Stewart, F. Montmessin, N. M. Schneider, and J.-L. Bertaux (2014), Unexpected variability of Martian hydrogen escape, *Geophysical Research Letters*, 41(2), 314–320, doi:10.1002/2013gl058578.
- Clarke, J. T., J. L. Bertaux, J. Y. Chaufray, G. R. Gladstone, E. Quémerais, J. Wilson, and D. Bhattacharyya (2014), A rapid decrease of the hydrogen corona of Mars, *Geophysical Research Letters*, 41(22), 8013–8020.
- Deighan, J, S. K. Jain, M. S. Chaffin, X. Fang, J. S. Halekas, J. T. Clarke, N. M. Schneider, A. I. F. Stewart, J.-Y. Chaufray, J. S. Evans, M. H. Stevens, M. Mayyasi, A. Stiepen, M. Crismani, W. E. McClintock, G. M. Holsclaw, D. Y. Lo, F. Montmessin, F. Lefevre, B. M. Jakosky, 2018. Discovery of Proton Aurora at Mars. *Nature Astronomy*
- Eather, 1967. Auroral proton precipitation and hydrogen emissions. *Reviews of Geophysics and Space Physics*, 5(3), 207–285. <https://doi.org/>
- Halekas, J. S., E. R. Taylor, G. Dalton, G. Johnson, D. W. Curtis, J. P. McFadden, D. L. Mitchell, R. P. Lin, B. M. Jakosky 2013. The Solar Wind Ion Analyzer for MAVEN. *Space Science Rev.* Volume 195
- Halekas, J. S., R. J. Lillis, D. L. Mitchell, T. E. Cravens, C. Mazelle, J. E. P. Connerney, ... S. Ruhunusiri, 2015. MAVEN observations of solar wind hydrogen deposition in the atmosphere of Mars. *Geophys. Res. Lett.*, 42, 8901–8909.
<https://doi.org/10.1002/2015GL064693>
- Halekas, J. S., 2017. Seasonal variability of the hydrogen exosphere of Mars. *J. Geophys. Res.: Planets*, 122, 901–911. <https://doi.org/10.1002/2017JE005306>
- Jakosky, B. M. et al., 2015. The Mars Atmosphere and Volatile Evolution (MAVEN) mission. *Space Sci. Rev.* 195, 3–48.
- Kallio and Barabash, 2001. Atmospheric effects of precipitating energetic hydrogen atoms on the Martian atmosphere. *J. Geophys. Res.*, 106(A1), 165–177.
<https://doi.org/10.1029/2000JA002003>

- Mayyasi, M., Clarke, J., Bhattacharyya, D., Deighan, J., Jain, S., Chaffin, M., ... Jakosky, B. (2017), The Variability of Atmospheric Deuterium Brightness at Mars: Evidence for Seasonal Dependence. *J. Geophys. Res.: Space Physics*, 122, 10,811–10,823. doi: 10.1002/2017JA024666.
- McClintock, W. E., N. M. Schneider, G. M. Holsclaw, J. T. Clarke, A. C. Hoskins, I. Stewart, F. Montmessin, R. V. Yelle (2015), The Imaging Ultraviolet Spectrograph (IUVS) for the MAVEN Mission, *Space Sci. Rev.*, doi: 10.1007/s11214-014-0098-7.
- Ritter, B., J.-C. Gérard, B. Hubert, L. Rodriguez, and F. Montmessin, 2018. Observations of the proton aurora on Mars with SPICAM on board Mars Express. *Geophysical Research Letters*, 45. <https://doi.org/10.1002/2017GL076235>
- Schneider, N. M., J. I. Deighan, S. K. Jain, A. Stiepen, A. I. F. Stewart, D. Larson, D. L. Mitchell, C. Mazelle, C. O. Lee, and R. J. Lillis (2015), Discovery of diffuse aurora on Mars, *Science*, 350(6261), aad0313.
- Vegard, L. ,1939. Hydrogen showers in the auroral region. *Nature*, 144, 1089.

Chapter 2 References

- Akalin, F., D. Morgan, D. Gurnett, D. Kirchner, D. Brain, R. Modolo, M. Acuña, and J. Espley (2010), Dayside induced magnetic field in the ionosphere of Mars, *Icarus*, 206(1), 104-111.
- Bertaux, J.-L., Leblanc, F., Witasse, O., Quemerais, E., Lilensten, J., Stern, S. A., ... Korabiev, O. (2005), Discovery of an aurora on Mar, *Nature*, 435(7043), 790–794, doi: 10.1038/nature03603.
- Bougher, S. W., D. Pawlowski, J. M. Bell, S. Nelli, T. McDunn, J. R. Murphy, M. Chizek, and A. Ridley (2015), Mars Global Ionosphere-Thermosphere Model(MGITM): Solar cycle, seasonal, and diurnal variations of the Mars upper atmosphere, *J. Geophys. Res.: Planets*, 120, 311–342, doi:10.1002/2014JE004715.
- Bougher, Stephen W., Kali J. Roeten, Kirk Olsen, Paul R. Mahaffy, Mehdi Benna, Meredith Elrod, Sonal K. Jain et al. (2017), The structure and variability of Mars dayside thermosphere from MAVEN NGIMS and IUVS measurements: Seasonal and solar activity trends in scale heights and temperatures. *J. Geophys. Res.: Space Physics*, 122, 1296–1313, doi:10.1002/2016JA023454.
- Brain, D.A., Bagenal, F., Acuña, M.H., Connerney, J.E.P. (2003), Martian magnetic morphology: Contributions from the solar wind and crust. *J. Geophys. Res.*, 108 (A12), 1424. doi:10.1029/2002JA009482.
- Bhattacharyya, D., J. Clarke, J.-L. Bertaux, J.-Y. Chaufray, and M. Mayyasi (2017), Analysis and modeling of remote observations of the Martian hydrogen exosphere, *Icarus*, 281, 264-280.
- Bhattacharyya, D., J. T. Clarke, J. L. Bertaux, J. Y. Chaufray, and M. Mayyasi (2015), A strong seasonal dependence in the Martian hydrogen exosphere, *Geophysical Research Letters*, 42(20), 8678-8685.

- Chaffin, M., J.-Y. Chaufray, J. Deighan, N. Schneider, M. Mayyasi, J. Clarke, E. Thiemann, S. Jain, M. Crismani, and A. Stiepen (2018), Mars H Escape Rates Derived From MAVEN/IUVS Lyman Alpha Brightness Measurements and Their Dependence on Model Assumptions, *Journal of Geophysical Research: Planets*, 123(8), 2192-2210.
- Chaffin, M. S., J.-Y. Chaufray, I. Stewart, F. Montmessin, N. M. Schneider, and J.-L. Bertaux (2014), Unexpected variability of Martian hydrogen escape, *Geophysical Research Letters*, 41(2), 314-320, doi:10.1002/2013gl058578.
- Chaffin, M. S., J. Deighan, N. M. Schneider, and A. I. F. Stewart (2017), Elevated atmospheric escape of atomic hydrogen from Mars induced by high-altitude water, *Nature Geoscience*, 10(3), 174-178, doi:10.1038/ngeo2887.
- Chaufray, J.-Y., J.-L. Bertaux, F. Leblanc, and E. Quémerais (2008), Observation of the hydrogen corona with SPICAM on Mars Express, *Icarus*, 195(2), 598-613.
- Chaufray, J.-Y., F. Gonzalez-Galindo, F. Forget, M. A. Lopez-Valverde, F. Leblanc, R. Modolo, and S. Hess (2015), Variability of the hydrogen in the Martian upper atmosphere as simulated by a 3D atmosphere-exosphere coupling, *Icarus*, 245, 282-294.
- Clarke, J. T., J. L. Bertaux, J. Y. Chaufray, G. R. Gladstone, E. Quémerais, J. Wilson, and D. Bhattacharyya (2014), A rapid decrease of the hydrogen corona of Mars, *Geophysical Research Letters*, 41(22), 8013-8020.
- Crismani, M., J. Deighan, N. Schneider, J. Plane, P. Withers, J. Halekas, M. Chaffin, S. Jain, (2019), Localized Ionization Hypothesis for Transient Ionospheric Layers, *J. Geophys. Res.: Space Physics*, 124. doi: 10.1029/2018JA026251.
- Deighan, J, S. K. Jain, M. S. Chaffin, X. Fang, J. S. Halekas, J. T. Clarke, N. M. Schneider, A. I. F. Stewart, J.-Y. Chaufray, J. S. Evans, M. H. Stevens, M. Mayyasi, A. Stiepen, M. Crismani, W. E. McClintock, G. M. Holsclaw, D. Y. Lo, F. Montmessin, F. Lefevre, B. M. Jakosky (2018), Discovery of Proton Aurora at Mars, *Nature Astronomy*, 2(10), 802.
- Eather, (1967), Auroral proton precipitation and hydrogen emissions, *Reviews of Geophysics and Space Physics*, 5(3), 207-285.
- England, S. L., Liu, G., Withers, P., Yiğit, E., Lo, D., Jain, S., ... & Elrod, M., (2016), Simultaneous observations of atmospheric tides from combined in situ and remote observations at Mars from the MAVEN spacecraft. *J. Geophys. Res.: Planets*, Volume 121, Issue 4, pp. 594-607.
- X. Fang, M. W. Liemohn, J. U. Kozyra, S. C. Solomon (2004), Quantification of the spreading effect of auroral proton precipitation, *J. Geophys. Res.*, 109, A04309.
- Gerard, J. C., B. Hubert, B. Ritter, V. I. Shematovich, D. V. Bisikalo (2018), Lyman- α emission in the Martian proton aurora: Line profile and role of horizontal induced magnetic field, *Icarus*, 321, 266-271.
- Heavens, N. G., Kleinböhl, A., Chaffin, M. S., Halekas, J. S., Kass, D. M., Hayne, P. O., ... & Schofield, J. T. (2018), Hydrogen escape from Mars enhanced by deep convection in dust storms, *Nature Astronomy*, 2(2), 126.

- Halekas, J. S., E. R. Taylor, G. Dalton, G. Johnson, D. W. Curtis, J. P. McFadden, D. L. Mitchell, R. P. Lin, B. M. Jakosky (2013), The Solar Wind Ion Analyzer for MAVEN, *Space Science Rev.*, 195(1-4), 125-151.
- Halekas, J. S., Lillis, R. J., Mitchell, D. L., Cravens, T. E., Mazelle, C., Connerney, J. E. P., ... & Luhmann, J. G. (2015), MAVEN observations of solar wind hydrogen deposition in the atmosphere of Mars, *Geophys. Res. Lett.*, 42, 8901–8909, doi: 10.1002/2015GL064693.
- Halekas, J. S. (2017), Seasonal variability of the hydrogen exosphere of Mars, *J. Geophys. Res.: Planets*, 122, 901–911, doi: 10.1002/2017JE005306.
- Hall, B. E. S., Lester, M., Sánchez-Cano, B., Nichols, J. D., Andrews, D. J., Edberg, N. J., ... & Witasse, O. (2016), Annual variations in the Martian bow shock location as observed by the Mars Express mission, *J. Geophys. Res. Space Physics*, 121, doi:10.1002/2016JA023316.
- Jain, S. K., Stewart, A. I. F., Schneider, N. M., Deighan, J., Stiepen, A., Evans, J. S., ... & Clarke, J. T. (2015), The structure and variability of Mars upper atmosphere as seen in MAVEN/IUVS dayglow observations, *Geophys. Res. Lett.*, 42(21), 9023-9030. doi: 10.1002/2015GL065419
- Jain, S.; Deighan, J.; Schneider, N. M.; Stewart, I. F.; Crismani, M. M. J.; Stevens, M. H.; Evans, J. S.; Chaffin, M.; Gonzalez-Galindo, F.; Bougher, S. W. (2018), Effect of 2018 dust storm on Martian thermosphere as seen by MAVEN/IUVS limb scans, American Geophysical Union, Fall Meeting 2018, Abstract #P34A-05.
- Jakosky, B. M., Lin, R. P., Grebowsky, J. M., Luhmann, J. G., Mitchell, D. F., Beutelschies, G., ... & Baker, D. (2015), The Mars atmosphere and volatile evolution (MAVEN) mission, *Space Sci. Rev.*, 195(1-4), 3-48.
- Kallio, E. S., Luhmann, J. G. & Barabash, S. (1997), Charge exchange near Mars: the solar wind absorption and energetic neutral atom production, *J. Geophys. Res.*, 102, 22183–22197.
- Kallio, E., & Barabash, S. (2001), Atmospheric effects of precipitating energetic hydrogen atoms on the Martian atmosphere, *J. Geophys. Res.: Space Physics*, 106(A1), 165-177, doi: 10.1029/2000JA002003.
- Liu, G., England, S. L., Lillis, R. J., Withers, P., Mahaffy, P. R., Rowland, D. E., ... & Jakosky, B. (2018), Thermospheric expansion associated with dust increase in the lower atmosphere on Mars observed by MAVEN/NGIMS, *Geophys. Res. Lett.*, 45(7), 2901-2910.
- Lo, D. Y., Yelle, R. V., Schneider, N. M., Jain, S. K., Stewart, A. I. F., England, S. L., ... & Chaffin, M. S. (2015), Nonmigrating tides in the Martian atmosphere as observed by MAVEN IUVS, *Geophys. Res. Lett.*, 42(21), 9057-9063.
- Mayyasi, M., Bhattacharyya, D., Clarke, J., Catalano, A., Benna, M., Mahaffy, P., ... & Chaffin, M. (2018), Significant Space Weather Impact on the Escape of Hydrogen from Mars, *Geophys. Res. Lett.*, 45(17), 8844-8852.
- Mayyasi, M., Clarke, J., Bhattacharyya, D., Deighan, J., Jain, S., Chaffin, M., ... Jakosky, B. (2017), The Variability of Atmospheric Deuterium Brightness at Mars: Evidence for

- Seasonal Dependence. *J. Geophys. Res.: Space Physics*, 122, 10,811–10,823. doi: 10.1002/2017JA024666.
- McClintock, W. E., N. M. Schneider, G. M. Holsclaw, J. T. Clarke, A. C. Hoskins, I. Stewart, F. Montmessin, R. V. Yelle (2015), The Imaging Ultraviolet Spectrograph (IUVS) for the MAVEN Mission, *Space Sci. Rev.*, doi: 10.1007/s11214-014-0098-7.
- Nomura, R., Shiokawa, K., Omura, Y., Ebihara, Y., Miyoshi, Y., Sakaguchi, K., ... & Connors, M. (2016). Pulsating proton aurora caused by rising tone Pc1 waves. *J. Geophys. Res.: Space Physics*, 121(2), 1608-1618.
- Ozaki, M., Shiokawa, K., Miyoshi, Y., Kataoka, R., Yagitani, S., Inoue, T., ... & Otsuka, Y. (2016), Fast modulations of pulsating proton aurora related to subpacket structures of Pc1 geomagnetic pulsations at subauroral latitudes, *Geophys. Res. Lett.*, 43(15), 7859-7866.
- Rahmati, A., Larson, D. E., Cravens, T. E., Lillis, R. J., Halekas, J. S., McFadden, J. P., ... & DiBraccio, G. A. (2017), MAVEN measured oxygen and hydrogen pickup ions: Probing the Martian exosphere and neutral escape, *J. Geophys. Res.: Space Physics*, 122(3), 3689-3706.
- Ritter, B., J.-C. Gérard, B. Hubert, L. Rodriguez, and F. Montmessin (2018), Observations of the proton aurora on Mars with SPICAM on board Mars Express, *Geophys. Res. Lett.*, 45. doi: 10.1002/2017GL076235.
- Schneider, N. M., J. I. Deighan, S. K. Jain, A. Stiepen, A. I. F. Stewart, D. Larson, D. L. Mitchell, C. Mazelle, C. O. Lee, and R. J. Lillis (2015), Discovery of diffuse aurora on Mars, *Science*, 350(6261), aad0313.
- Vandaele, A. C., Korabiev, O., Daerden, F., Aoki, S., Thomas, I. R., Altieri, F., ... & Erwin, J. T. (2019). Martian dust storm impact on atmospheric H₂O and D/H observed by ExoMars Trace Gas Orbiter. *Nature*, 568(7753), 521.
- Vegard, L. (1939), Hydrogen showers in the auroral region, *Nature*, 144, 1089.

Chapter 3 References

- Chaffin, M. S., J.-Y. Chaufray, I. Stewart, F. Montmessin, N. M. Schneider, and J.-L. Bertaux (2014), Unexpected variability of Martian hydrogen escape, *Geophysical Research Letters*, 41(2), 314-320, doi:10.1002/2013gl058578.
- Chaffin, M., Kass, D., *et al.*, (2021), Regional Dust Storms on Mars Enhance Water Loss to Space, *Nature Astronomy*, (Accepted).
- Clarke, J. T., J. L. Bertaux, J. Y. Chaufray, G. R. Gladstone, E. Quémerais, J. Wilson, and D. Bhattacharyya (2014), A rapid decrease of the hydrogen corona of Mars, *Geophysical Research Letters*, 41(22), 8013-8020.
- Connerney, J.E.P., Espley, J., Lawton, P. et al. (2015), The MAVEN Magnetic Field Investigation. *Space Sci Rev* 195, 257–291. <https://doi.org/10.1007/s11214-015-0169-4>
- Deighan, J., S. K. Jain, M. S. Chaffin, X. Fang, J. S. Halekas, J. T. Clarke, N. M. Schneider, A. I. F. Stewart, J.-Y. Chaufray, J. S. Evans, M. H. Stevens, M. Mayyasi, A. Stiepen, M.

- Crismani, W. E. McClintock, G. M. Holsclaw, D. Y. Lo, F. Montmessin, F. Lefevre, B. M. Jakosky (2018), Discovery of Proton Aurora at Mars, *Nature Astronomy*, 2(10), 802.
- Forget, F., F. Hourdin *et al.* (1999). Improved general circulation models of the Martian atmosphere from the surface to above 80 km, *J. Geophys. Res.*, 104(E10), 24,155–24,175.
- Frey, H. U., S. B. Mend *et al.* (2001), The electron and proton aurora as seen by IMAGE-FUV and FAST. *Geophys. Res. Lett.*, 28, 6, 1135-1138.
- Gérard, J.-C., B. Hubert, *et al.* (2001), Observation of the proton aurora with IMAGE FUV imager and simultaneous ion flux *in situ* measurements, *J. Geophys. Res.*, 106, A12, 28939-28948.
- Gérard, J. C., B. Hubert, B. Ritter, V. I. Shematovich, D. V. Bisikalo (2018), Lyman- α emission in the Martian proton aurora: Line profile and role of horizontal induced magnetic field, *Icarus*, 321, 266-271.
- Halekas, J. S., E. R. Taylor, G. Dalton, G. Johnson, D. W. Curtis, J. P. McFadden, D. L. Mitchell, R. P. Lin, B. M. Jakosky (2013), The Solar Wind Ion Analyzer for MAVEN, *Space Science Rev.*, 195(1-4), 125-151.
- Halekas, J. S., Lillis, R. J., Mitchell, D. L., Cravens, T. E., Mazelle, C., Connerney, J. E. P., ... & Luhmann, J. G. (2015), MAVEN observations of solar wind hydrogen deposition in the atmosphere of Mars, *Geophys. Res. Lett.*, 42, 8901–8909, doi: 10.1002/2015GL064693.
- Halekas, J. S. (2017), Seasonal variability of the hydrogen exosphere of Mars, *J. Geophys. Res.: Planets*, 122, 901–911, doi: 10.1002/2017JE005306.
- Halekas, J. S., et al. (2016), Structure, dynamics, and seasonal variability of the Mars-solar wind interaction: MAVEN Solar Wind Ion Analyzer in-flight performance and science results, *J. Geophys. Res. Space Physics*, 121, doi:10.1002/2016JA023167.
- Hughes, A., Chaffin, M., Mierkiewicz, E., Deighan, J., Jain, S., Schneider, N., et al. (2019), Proton aurora on Mars: A dayside phenomenon pervasive in southern summer, *J. Geophys. Res.: Space Physics*, 124, 10,533–10,548, doi: 10.1029/2019JA027140.
- Jakosky, B. M., Lin, R. P., Grebowsky, J. M., Luhmann, J. G., Mitchell, D. F., Beutelschies, G., ... & Baker, D. (2015), The Mars atmosphere and volatile evolution (MAVEN) mission, *Space Sci. Rev.*, 195(1-4), 3-48.
- Larson, D.E., Lillis, R.J., Lee, C.O. et al. (2015), The MAVEN Solar Energetic Particle Investigation. *Space Sci Rev* 195, 153–172. <https://doi.org/10.1007/s11214-015-0218-z>
- Mayyasi, M., Bhattacharyya, D., Clarke, J., Catalano, A., Benna, M., Mahaffy, P., ... & Chaffin, M. (2018), Significant Space Weather Impact on the Escape of Hydrogen from Mars, *Geophys. Res. Lett.*, 45(17), 8844-8852.
- McClintock, W. E., N. M. Schneider, G. M. Holsclaw, J. T. Clarke, A. C. Hoskins, I. Stewart, F. Montmessin, R. V. Yelle (2015), The Imaging Ultraviolet Spectrograph (IUVS) for the MAVEN Mission, *Space Sci. Rev.*, doi: 10.1007/s11214-014-0098-7.
- Montabone, L., Forget, et al. (2015). Eight-year Climatology of Dust Optical Depth on Mars. *Icarus* 251, pp. 65-95. DOI: 10.1016/j.icarus.2014.12.034

Ritter, B., J.-C. Gérard, B. Hubert, L. Rodriguez, and F. Montmessin (2018), Observations of the proton aurora on Mars with SPICAM on board Mars Express, *Geophys. Res. Lett.*, 45. doi: 10.1002/2017GL076235

Chapter 4 References

- Bertaux, J.-L., Leblanc, F., Witasse, O., Quemerais, E., Lilensten, J., Stern, S. A., ... Korabiev, O., 2005. Discovery of an aurora on Mars. *Nature*, 435(7043), 790–794. <https://doi.org/10.1038/nature03603>
- Brinkfeldt, K., Gunell, H., Barabash, S., Frahm, R. A., Winningham, J. D., Kallio, E., ... & Dierker, C. (2006). First ENA observations at Mars: Solar-wind ENAs on the nightside. *Icarus*, 182(2), 439-447.
- Chaffin, M. S., J.-Y. Chaufray, I. Stewart, F. Montmessin, N. M. Schneider, and J.-L. Bertaux (2014), Unexpected variability of Martian hydrogen escape, *Geophysical Research Letters*, 41(2), 314-320, doi:10.1002/2013gl058578.
- Chaffin, M., Kass, D., *et al.*, (2021), Regional Dust Storms on Mars Enhance Water Loss to Space, *Nature Astronomy*, (Accepted).
- Clarke, J. T., J. L. Bertaux, J. Y. Chaufray, G. R. Gladstone, E. Quémerais, J. Wilson, and D. Bhattacharyya (2014), A rapid decrease of the hydrogen corona of Mars, *Geophysical Research Letters*, 41(22), 8013-8020.
- Connerney, J. E. P., M. H. Acuña, N. F. Ness, G. Kletetschka, D. L. Mitchell, R. P. Lin, H. Reme (2005). Tectonic implications of Mars crustal magnetism. *Proceedings of the National Academy of Sciences*, 102 (42) 14970-14975; DOI: 10.1073/pnas.0507469102
- Crismani, M., Deighan, J., Schneider, N., Plane, J., Withers, P., Halekas, J., *et al.* (2019). Localized ionization hypothesis for transient ionospheric layers. *Journal of Geophysical Research: Space Physics*, 124. DOI: 10.1029/2018JA026251
- Deighan, J, S. K. Jain, M. S. Chaffin, X. Fang, J. S. Halekas, J. T. Clarke, N. M. Schneider, A. I. F. Stewart, J.-Y. Chaufray, J. S. Evans, M. H. Stevens, M. Mayyasi, A. Stiepen, M. Crismani, W. E. McClintock, G. M. Holsclaw, D. Y. Lo, F. Montmessin, F. Lefevre, B. M. Jakosky (2018), Discovery of Proton Aurora at Mars, *Nature Astronomy*, 2(10), 802.
- England, S. L., Liu, G., Withers, P., *et al.* (2016). Simultaneous observations of atmospheric tides from combined in situ and remote observations at Mars from the MAVEN spacecraft. *J. Geophys. Res. Planets*, 121(4), 594–607. DOI: 10.1002/2016je004997
- Fowler, C. M., Halekas, J., Schwartz, S., Goodrich, K. A., Gruesbeck, J. R., & Benna, M. (2019). The modulation of solar wind hydrogen deposition in the Martian atmosphere by foreshock phenomena. *Journal of Geophysical Research: Space Physics*, 124(8), 7086-7097. <https://doi.org/10.1029/2019JA026938>
- Frey, H. U., S. B. Mende, T. J. Immel, S. A. Fuselier, E. S. Claflin, J.-C. Gérard, B. Hubert, 2002. Proton aurora in the cusp. *J. Geophys. Res.* 107, 1091. Halekas, J. S., E. R. Taylor, G. Dalton, G. Johnson, D. W. Curtis, J. P. McFadden, D. L. Mitchell, R. P. Lin, B. M.

- Jakosky (2013), The Solar Wind Ion Analyzer for MAVEN, *Space Science Rev.*, 195(1-4), 125-151.
- Girazian, Z., Mahaffy, P., Lee, Y., & Thiemann, E. M. B. (2019). Seasonal, solar zenith angle, and solar flux variations of O⁺ in the topside ionosphere of Mars. *Journal of Geophysical Research: Space Physics*, 124, 3125–3138. <https://doi.org/10.1029/2018JA026086>
- Guzewich, S. D., E. R. Talaat, and D. W. Waugh (2012). Observations of planetary waves and nonmigrating tides by the Mars Climate Sounder, *J. Geophys. Res.*, 117, E03010, DOI:10.1029/2011JE003924.
- Guzewich, S. D., Newman, *et al.* (2016). Atmospheric tides in Gale Crater, Mars. *Icarus* 268, pp. 37-49. DOI: 10.1016/j.icarus.2015.12.028.
- Halekas, J. S., Lillis, R. J., Mitchell, D. L., Cravens, T. E., Mazelle, C., Connerney, J. E. P., ... & Luhmann, J. G. (2015), MAVEN observations of solar wind hydrogen deposition in the atmosphere of Mars, *Geophys. Res. Lett.*, 42, 8901–8909, doi: 10.1002/2015GL064693.
- Halekas, J. S. (2017), Seasonal variability of the hydrogen exosphere of Mars, *J. Geophys. Res.: Planets*, 122, 901–911, doi: 10.1002/2017JE005306.
- Halekas, J. S., et al. (2016), Structure, dynamics, and seasonal variability of the Mars-solar wind interaction: MAVEN Solar Wind Ion Analyzer in-flight performance and science results, *J. Geophys. Res. Space Physics*, 121, doi:10.1002/2016JA023167.
- Hughes, A., Chaffin, M., Mierkiewicz, E., Deighan, J., Jain, S., Schneider, N., *et al.* (2019). Proton aurora on Mars: A dayside phenomenon pervasive in southern summer, *J. Geophys. Res.: Space Physics*, 124, 10,533–10,548, doi: 10.1029/2019JA027140.
- Hughes, A., Chaffin, M., Mierkiewicz, E., Schneider, N., Deighan, J., Jain, S., *et al.* (2021). A Combined Remote Sensing and In Situ assessment of Martian Proton Aurora. *J. Geophys. Res.: Space Physics*, (*In prep*).
- Jakosky, B. M., Lin, R. P., Grebowsky, J. M., Luhmann, J. G., Mitchell, D. F., Beutelschies, G., ... & Baker, D. (2015), The Mars atmosphere and volatile evolution (MAVEN) mission, *Space Sci. Rev.*, 195(1-4), 3-48.
- Larson, D.E., Lillis, R.J., Lee, C.O. et al. (2015), The MAVEN Solar Energetic Particle Investigation. *Space Sci Rev* 195, 153–172. <https://doi.org/10.1007/s11214-015-0218-z>
- Lo, D. Y., Yelle, R. V., Schneider, N. M., Jain, S. K., Stewart, A. I. F., England, S. L., *et al.* (2015). Nonmigrating tides in the Martian atmosphere as observed by MAVEN IUVS. *Geophysical Research Letters*, 42, 9057–9063. DOI: 10.1002/2015gl066268
- Lundin, R., D. Winningham, S. Barabash, R. Frahm, M. Holmström, J.-A. Sauvaud, A. Fedorov, K. Asamura, *et al.* (2006). Plasma Acceleration Above Martian Magnetic Anomalies, *Science*, 311, 5763, pp. 980-983, DOI: 10.1126/science.1122071.
- Mahaffy, P.R., Benna, M., King, T. *et al.* The Neutral Gas and Ion Mass Spectrometer on the Mars Atmosphere and Volatile Evolution Mission. *Space Sci Rev* **195**, 49–73 (2015). <https://doi.org/10.1007/s11214-014-0091-1>

- Mayyasi, M., Bhattacharyya, D., Clarke, J., Catalano, A., Benna, M., Mahaffy, P., ... & Chaffin, M. (2018), Significant Space Weather Impact on the Escape of Hydrogen from Mars, *Geophys. Res. Lett.*, 45(17), 8844-8852.
- McClintock, W. E., N. M. Schneider, G. M. Holsclaw, J. T. Clarke, A. C. Hoskins, I. Stewart, F. Montmessin, R. V. Yelle (2015), The Imaging Ultraviolet Spectrograph (IUVS) for the MAVEN Mission, *Space Sci. Rev.*, doi: 10.1007/s11214-014-0098-7.
- Nomura, R., Shiokawa, K., Omura, Y., Ebihara, Y., Miyoshi, Y., Sakaguchi, K., ... & Connors, M. (2016). Pulsating proton aurora caused by rising tone Pc1 waves. *J. Geophys. Res.: Space Physics*, 121(2), 1608-1618.
- Ozaki, M., Shiokawa, K., Miyoshi, Y., Kataoka, R., Yagitani, S., Inoue, T., ... & Otsuka, Y. (2016), Fast modulations of pulsating proton aurora related to subpacket structures of Pc1 geomagnetic pulsations at subauroral latitudes, *Geophys. Res. Lett.*, 43(15), 7859-7866.
- Palmroth, M., M. Grandin, M. Helin, P. Koski, A. Oksanen, M. A. Glad, R. Valonen, K. Saari, E. Bruus, J. Norberg, A. Viljanen, K. Kauristie, P. T. Verronen, 2020. Citizen Scientists Discover a New Auroral Form: Dunes Provide Insight Into the Upper Atmosphere, *AGU Advances*, 1, 1. doi.org/10.1029/2019AV000133.
- Ritter, B., J.-C. Gérard, B. Hubert, L. Rodriguez, and F. Montmessin 2018, Observations of the proton aurora on Mars with SPICAM on board Mars Express, *Geophys. Res. Lett.*, 45. doi: 10.1002/2017GL076235.
- Schneider, N. M., J. I. Deighan, S. K. Jain, A. Stiepen, A. I. F. Stewart, D. Larson, D. L. Mitchell, C. Mazelle, C. O. Lee, and R. J. Lillis (2015), Discovery of diffuse aurora on Mars, *Science*, 350(6261), aad0313.
- Wang, X.-D., Alho, M., Jarvinen, R., Kallio, E., Barabash, S., & Futaana, Y. (2018). Precipitation of hydrogen energetic neutral atoms at the upper atmosphere of Mars. *Journal of Geophysical Research: Space Physics*, 123, 8730–8748. <https://doi.org/10.1029/2018JA025188>
- Withers, P. (2009). A review of observed variability in the dayside ionosphere of Mars, *Advances in Space Research*, 44, 277–307. <https://doi.org/10.1016/j.asr.2009.04.027>
- Withers, P., S.W. Bougher, G.M. Keating, (2003). The effects of topographically-controlled thermal tides in the Martian upper atmosphere as seen by the MGS accelerometer, *Icarus*, 164, pp. 14-32.
- Yahnin, A. G., Yahnina, T. A., Frey, H. U., & Bösinger, T. (2010). Ionospheric Image of the Source Region of the IPDP Type Magnetic Pulsations. *Physics of Auroral Phenomena*, 32(1), 97-100.

Chapter 5 References

- Anderson, D. E., and Hord, C. W. (1971). Mariner 6 and 7 Ultraviolet Spectrometer Experiment: Analysis of hydrogen Lyman-alpha data, *J. Geophys. Res.*, 76(28), 6666– 6673, doi:10.1029/JA076i028p06666.

- Bertaux, J.-L., Leblanc, F., Witasse, O., Quemerais, E., Lilensten, J., Stern, S. A., ... Korabiev, O. (2005), Discovery of an aurora on Mar, *Nature*, 435(7043), 790–794, doi: 10.1038/nature03603.
- Chaffin, M. S., J.-Y. Chaufray, I. Stewart, F. Montmessin, N. M. Schneider, and J.-L. Bertaux (2014), Unexpected variability of Martian hydrogen escape, *Geophysical Research Letters*, 41(2), 314-320, doi:10.1002/2013gl058578.
- Chaffin, M., Kass, D., *et al.*, (2021), Regional Dust Storms on Mars Enhance Water Loss to Space, *Nature Astronomy*, (Accepted).
- Clarke, J. T., J. L. Bertaux, J. Y. Chaufray, G. R. Gladstone, E. Quémerais, J. Wilson, and D. Bhattacharyya (2014), A rapid decrease of the hydrogen corona of Mars, *Geophysical Research Letters*, 41(22), 8013-8020.
- Deighan, J, S. K. Jain, M. S. Chaffin, X. Fang, J. S. Halekas, J. T. Clarke, N. M. Schneider, A. I. F. Stewart, J.-Y. Chaufray, J. S. Evans, M. H. Stevens, M. Mayyasi, A. Stiepen, M. Crismani, W. E. McClintock, G. M. Holsclaw, D. Y. Lo, F. Montmessin, F. Lefevre, B. M. Jakosky (2018), Discovery of Proton Aurora at Mars, *Nature Astronomy*, 2(10), 802.
- England, S. L., Liu, G., Withers, P., Yiğit, E., Lo, D., Jain, S., ... & Elrod, M., (2016), Simultaneous observations of atmospheric tides from combined in situ and remote observations at Mars from the MAVEN spacecraft. *J. Geophys. Res.: Planets*, Volume 121, Issue 4, pp. 594-607.
- Gerard, J. C., B. Hubert, B. Ritter, V. I. Shematovich, D. V. Bisikalo (2018), Lyman- α emission in the Martian proton aurora: Line profile and role of horizontal induced magnetic field, *Icarus*, 321, 266-271.
- Girazian and Halekas (2021), Precipitating Solar Wind Hydrogen at Mars: Improved Calculations of the Backscatter and Albedo with MAVEN Observations, *J. Geophys. Res.: Planets*, Volume 126, Issue 2, doi: 10.1029/2020JE006666.
- Halekas, J. S., E. R. Taylor, G. Dalton, G. Johnson, D. W. Curtis, J. P. McFadden, D. L. Mitchell, R. P. Lin, B. M. Jakosky (2013), The Solar Wind Ion Analyzer for MAVEN, *Space Science Rev.*, 195(1-4), 125-151.
- Halekas, J. S., Lillis, R. J., Mitchell, D. L., Cravens, T. E., Mazelle, C., Connerney, J. E. P., ... & Luhmann, J. G. (2015), MAVEN observations of solar wind hydrogen deposition in the atmosphere of Mars, *Geophys. Res. Lett.*, 42, 8901–8909, doi: 10.1002/2015GL064693.
- Halekas, J. S. (2017), Seasonal variability of the hydrogen exosphere of Mars, *J. Geophys. Res.: Planets*, 122, 901–911, doi: 10.1002/2017JE005306.
- Huestis, D.L., and J. Berkowitz, (2010). Critical evaluation of the photoabsorption cross section of CO₂ from 0.125 to 201.6 nm at room temperature, *Advances in Geosciences Vol. 25: Planetary Science* 229-242
- Hughes, A., Chaffin, M., Mierkiewicz, E., Deighan, J., Jain, S., Schneider, N., et al. (2019), Proton aurora on Mars: A dayside phenomenon pervasive in southern summer, *J. Geophys. Res.: Space Physics*, 124, 10,533–10,548, doi: 10.1029/2019JA027140.

- Hunten, D.M., F.E. Roach, and J.W. Chamberlain, (1956). A photometric unit for the airglow and aurora, *Journal of Atmospheric and Terrestrial Physics*, Volume 8, Issue 6, Pages 345-346, [https://doi.org/10.1016/0021-9169\(56\)90111-8](https://doi.org/10.1016/0021-9169(56)90111-8).
- Jakosky, B. M., Lin, R. P., Grebowsky, J. M., Luhmann, J. G., Mitchell, D. F., Beutelschies, G., ... & Baker, D. (2015), The Mars atmosphere and volatile evolution (MAVEN) mission, *Space Sci. Rev.*, 195(1-4), 3-48.
- Kallio, E., & Barabash, S. (2001), Atmospheric effects of precipitating energetic hydrogen atoms on the Martian atmosphere, *J. Geophys. Res.: Space Physics*, 106(A1), 165-177, doi: 10.1029/2000JA002003.
- Lo, D. Y., Yelle, R. V., Schneider, N. M., Jain, S. K., Stewart, A. I. F., England, S. L., ... & Chaffin, M. S. (2015), Nonmigrating tides in the Martian atmosphere as observed by MAVEN IUVS, *Geophys. Res. Lett.*, 42(21), 9057-9063.
- Mahaffy, P.R., Benna, M., King, T. *et al.* The Neutral Gas and Ion Mass Spectrometer on the Mars Atmosphere and Volatile Evolution Mission. *Space Sci Rev* **195**, 49–73 (2015). <https://doi.org/10.1007/s11214-014-0091-1>
- McClintock, W. E., N. M. Schneider, G. M. Holsclaw, J. T. Clarke, A. C. Hoskins, I. Stewart, F. Montmessin, R. V. Yelle (2015), The Imaging Ultraviolet Spectrograph (IUVS) for the MAVEN Mission, *Space Sci. Rev.*, doi: 10.1007/s11214-014-0098-7.
- Ritter, B., J.-C. Gérard, B. Hubert, L. Rodriguez, and F. Montmessin (2018), Observations of the proton aurora on Mars with SPICAM on board Mars Express, *Geophys. Res. Lett.*, 45. doi: 10.1002/2017GL076235.
- Schneider, N. M., J. I. Deighan, S. K. Jain, A. Stiepen, A. I. F. Stewart, D. Larson, D. L. Mitchell, C. Mazelle, C. O. Lee, and R. J. Lillis (2015), Discovery of diffuse aurora on Mars, *Science*, 350 (6261), aad0313.

Appendix A: Proton/Hydrogen Precipitation

Model Descriptions

In this appendix we provide detailed descriptions of each of the four proton/hydrogen precipitation models used in our study. Descriptions are written by each modeling team and appropriate references are given at the end of each section.

I. Jolitz 3-D Monte Carlo Model (Model Name: “ASPEN”)

ASPEN (Atmospheric Scattering of Protons, Electrons, and Neutrals) is a 3D Monte Carlo test particle simulation. This model was initially developed to predict atmospheric ionization rates at Mars by solar energetic particles, which have higher energies than the ENAs studied in this paper [Jolitz et al. 2017], and has since been used to predict precipitating SEP electron fluxes at Mars [Jolitz et al. in-review]. The simulation solves the Lorentz force equations for energetic particle motion and uses a Monte Carlo approach to predict collisions and resulting energy loss in the atmosphere. Since magnetic fields were set to zero for this study, the transport equations reduced to ballistic motion.

The collisional energy degradation algorithm used in ASPEN was originally developed and described in Lillis et al. [2008] for an electron precipitation model. It is very similar to the Kallio model in approach. Stochastic collisions were modeled by inverting the relation between intensity, density, and absorption cross-section for a particle beam incident on a medium of scatterers (colloquially known as Beer’s law) to dynamically calculate a probability distribution function that is combined with a random number to predict variable distances between collisions. This probability distribution function is calculated for each individual particle and depends on the position, path, and energy through the planetary atmosphere. Similarly, whenever a collision

occurs, the type of collision is predicted probabilistically using the relative cross-section of each possible collisional process and the particle energy is decremented by the corresponding energy loss. As a particle loses energy, the relative cross-sections of each process change. For example, a 2 keV proton colliding with a carbon dioxide molecule has a roughly 70% likelihood of capturing an electron, but the likelihood for the same process when the proton is 20 eV is only 20%.

This model is highly dependent on the choice of cross-sections. For the application in this study, the selected cross-sections for hydrogen and proton impact on carbon dioxide are described in Jolitz et al. [2017], with one exception. The cross-sections for proton- and hydrogen-impact excitation was replaced with Lyman-alpha emission cross-sections. Unfortunately experimental measurements of the Lyman-alpha emission cross-section from proton and hydrogen atom impact on carbon dioxide is limited. As of the time of this paper's writing, only one set of measurements exist for 1-25 keV protons and hydrogen atoms [Birely and McNeal 1972]. The cross-section for emission by protons and hydrogen atoms below 1 keV is unknown. In order to approximate emission from particles at these energies, ASPEN uses a cross-section calculated by scaling the corresponding emission cross-sections from impact on molecular oxygen. ASPEN also accounts for the fact that proton-induced Lyman-alpha emission can only occur in addition to a charge exchange collision, since Lyman-alpha can only emitted by a hydrogen atom.

Since ASPEN is a 3D Monte Carlo simulation, predicting an accurate emission rate requires appropriate choice of initial conditions and a large volume of simulated particles. For Step 1, we simulated 10,000 particles incident on the subsolar point from an altitude of 600 km and calculated the emission rate by binning all Lyman-alpha emitting collisions as a function of

altitude and multiplying by the incident flux. For Step 2, we simulated 10,000 particles isotropically distributed in space on a plane perpendicular to the direction of solar wind flow. Each particle represents a fraction of the assumed incident flux. The emission rate was then calculated by weighing the total number of emissions binned by altitude, solar zenith angle, and the fraction of flux associated with each simulated particle.

References:

- Birely, J.H., and R.J. McNeal (1972), Lyman-alpha emission cross sections for collisions of 1-25 keV H⁺ and H with CO, CO₂, CH₄, and NH₃, *J.Chem Phys.*, 56 (5), 2189-94, doi:10.1063/1.1677518.
- Jolitz, R. D., C. F. Dong, C. O. Lee, R. J. Lillis, D. A. Brain, S. M. Curry, S. Bougher, C. D. Parkinson, and B. M. Jakosky (2017), A Monte Carlo model of crustal field influences on solar energetic particle precipitation into the Martian atmosphere, *J. Geophys. Res. Space Physics*, 122, 5653–5669, doi:10.1002/2016JA023781.
- Jolitz, R. D., C. F. Dong, A. Rahmati, D. A. Brain, C. O. Lee, R. J. Lillis, S. M. Curry, and B. M. Jakosky (in-review), Test particle model predictions of SEP electron transport and precipitation at Mars, *J. Geophys. Res. Space Physics*.
- Lillis, R. J., D. L. Mitchell, R. P. Lin, and M. H. Acuña (2008), Electron reflectometry in the Martian atmosphere, *Icarus*, 194(2) 544-61, doi:10.1016/j.icarus.2007.09.030.

II. Kallio 3-D Monte Carlo Model

The Kallio model is described in detail in *Kallio and Barabash*, 2000 and 2001.

(i) *General intro: nature of the model (DMSC/semi-analytical, 1D/3D), brief history of its development, general references*

The model is 3D Monte Carlo model where incident particle, either H⁺ or H, collides with neutral particles after with the velocity of the particle is changed. The model contains 6 elastic and 24 inelastic process but, in this study, only processes shown in Table X was used.

The model uses cartesian coordinate system both for the positions and velocities of the precipitating particles. In the coordinate system the x-axis points from the centre of Mars toward the Sun.

(ii) *Inputs, processes included, with relevant cross section references (in a separate table?), and outputs.*

The model inputs are neutral atom densities, energy dependent total cross sections (CS) the differential scattering cross sections (DSCS), the number of precipitating particles (N_H) and the initial positions ($\mathbf{r}_{\text{particle}(t=0)}$) and velocities ($\mathbf{v}_{\text{particle}(t=0)}$) of the precipitating particles, in the present case hydrogen atoms (H).

The total cross sections are given in *Kallio and Barabash, 2001* (Table 1 and Fig. 3) and the DSCS scattering angle distribution in *Kallio and Barabash, 2000* (Fig. 1, “nominal”) and 2001 (Fig. 2). Total cross sections give the probability that a collision occurs. Random numbers are used to model if a collision occurs and which collision process occurs. If a collision happens, then the DSCS determines the new velocity of the incident particle after collision. The value of the scattering angle is obtained by using a new random variable.

(iii) *Implementation and technical aspects: assumptions and constraints, domain of applicability and grid description, spatial resolution and timesteps, number of particles, overall performance?, etc.*

In the simulation, particles are injected into the upper atmosphere at the point $[x, y, z] = [260 \text{ km} + R_{\text{Mars}}, 0, 0]$, where the radius of the Mars, R_{Mars} , was in the simulation 3393 km. The velocity of the particles in the analysis presenting in this paper was a constant $\mathbf{v} = [v_x, v_y, v_z] = [-400, 0, 0]$ km/s, i.e. a beam of particles moved initially exactly toward the surface of the planet.

The model saves the position and the velocity of the particle if it has had a Ly- α collision process. The Ly- α volume production rate was derived from the saved positions of Ly- α processes by collecting the number of the Ly- α collision processes ($d\#_k^{\text{hf}}$) at a given altitude (h) ranges: $dh_k \equiv h_{k+1} - h_k$. Then the Ly- α volume of the emission was derived by using a 1D

approximation, i.e. assuming that the area of the emission perpendicular to the x-axis (dA_{hf}) is equal to the initial area in the solar wind (dA_{sw}) through which the precipitating particles initially came, $dA_{hf} = dA_{sw}$. Therefore, the volume (dV_k) from which the emission came within dh_k was assumed to be $dV_k = dh_k \times dA_{sw}$.

The altitude dependent Ly- α volume emission rate

$$q_k^{hf} = d\#_k^{hf} / (dt \times dV_k) = d\#_k^{hf} / (dt \times dh_k \times dA_{hf}) = d\#_k^{hf} / (dt \times dh_k \times dA_{sw}), \quad (1)$$

is finally obtained from the particle flux of the precipitating H particles (j_H), the number of the particles used in the MC simulation (N_H) and the time (dt) which takes N_H particles to go through the area dA_{sw} : $N_H = j_H dt \times dA_{sw}$. This gives $dt \times dA_{sw} = N_H / j_H$ and Eq (1) gets the form

$$q_k^{hf} = d\#_k^{hf} / (dt \times dV_k) = j_H [d\#_k^{hf} / (dh_k \times N_H)]. \quad (2)$$

In the analysed simulation N_H was 5000. As can be seen in Eq. (2) the particle flux j_H is just a scaling factor and in this paper, it was $10^7 \text{ cm}^{-3} \text{ s}^{-1}$. In the plots presented in this paper the Ly- α emission altitude profiles was derived in 1 km altitude bins, i.e., $dh_k = 1 \text{ km}$. This provided a relatively good compromise between modest statistical fluctuations and the accurate determination of the peak emission value and altitude.

(iv) possibly, strengths and applications most suited for the model

The largest uncertainty for the obtained Ly- α volume emission rate q_k^{hf} is related to the uncertainty of the used total cross sections and the differential scattering cross sections between H and H^+ particles and CO_2 molecules. In the simulation many of these H/ H^+ collisions with CO_2 are modelled with H/ H^+ collisions with O_2 and N_2 which was published in the literature (see *Kallio and Barabash, 2001, Table 1, for details*).

As described in *Kallio and Barabash, 2000 and 2001*, functional forms of the adopted DSCS are modelled following *Noël and Prölss (1993)*. The used DSCS (see *Kallio and*

Barabash, 2000, Fig. 1a, the “nominal” DCSC and *Kallio and Barabash*, 2001, Fig. 2) is a fit to the data of H – O₂ collisions from *Newmann et al.*, 1986, Table 4.

The inaccuracy caused by the 1D approximation, $dA_{hf} = dA_{sw}$, is small because the horizontal movement of the colliding particles in the atmosphere is small compared with the radius of the planet.

It is also worth to note that although the statistical fluctuations in the derived emission altitude profiles could be reduced by using a larger number of precipitating particles (now 5000) in the used 1 km altitude binning, the statistical fluctuations are relatively modest already for the used number of particles.

It is worth to note that the used MC model can be automatically used in the future more complicated situations than done in this paper. In this study the precipitating particles formed a monoenergetic beam and Ly- α emission was derived along the x-axis, i.e. at SZA = 0 deg. However, the velocity distribution function can be more complicated, for example Maxwellian velocity distribution function or the velocities can be read from a file. Moreover, the atmospheric density profile, $n(\mathbf{r})$ can be 2D, say $n(\mathbf{r}) = n(\text{SZA}, h)$. In such a case the MC model can be used to derive altitude profiles at a given SZA (see *Kallio and Barabash*, 2001, for details). The atmospheric density can also be 3D, i.e. $n(\mathbf{r}) = n(x, y, z)$, which would result in the 3D Ly- α emission rates. In the simulation the particle flux and their velocity distribution can also have latitude-longitude dependence (see *Kallio and Janhunen*, 2001, for details).

References:

- Kallio, E., and P. Janhunen, Atmospheric effects of proton precipitation in the Martian atmosphere and its connection to the Mars-solar wind interaction, *J. Geophys. Res.*, 106, 5617-5634, 2001.
- Kallio, E., and S. Barabash, Atmospheric effects of precipitating energetic hydrogen atoms on the Martian atmosphere, *J. Geophys. Res.*, 106, 165-178, 2001.

Kallio, E., and S. Barabash, On the elastic and inelastic collisions between precipitating energetic hydrogen atoms and Martian atmospheric neutrals *J. Geophys. Res.*, *105*, 24,973-24,996, 2000.

Noël, S. and G. W. Prölss, Heating and radiation production by neutralized ring current particles. *JGR, Volume 98, Issue A10, Pages 17317-17325*, 1993.

Newman, J. H., Y. S. Chen, K. A. Smith and R. F. Stebbings, Differential cross sections for scattering of 0.5-, 1.5-, and 5.0-keV hydrogen atoms by He, H₂, N₂, and O₂, *JGR, Volume 91, Issue A8, Pages 8947-8954*, 1986

III. Bisikalo/Shematovich et al. 1-D Monte Carlo Model

(a) Precipitating high-energy hydrogen atoms and protons lose their kinetic energy in the elastic and inelastic collisions, (b) ionization of target atmospheric molecules/atoms, and (c) charge transfer and electron capture collisions with the major atmospheric constituents – CO₂, N₂, and O included in the model. Secondary fast hydrogen atoms and protons carry enough kinetic energy to cycle through the collisional channels mentioned above and result in a growing set of translationally and internally excited atmospheric atoms and/or molecules.

To study the precipitation of high-energy H/H⁺ flux into the planetary atmosphere, we solve the kinetic Boltzmann equations (Shematovich et al., 2011) for H⁺ and H, including the collision term:

$$\mathbf{v} \frac{\partial}{\partial \mathbf{r}} f_{H/H^+} + \left(\mathbf{g} + \frac{e}{m_{H^+}} \mathbf{v} \times \mathbf{B} \right) \frac{\partial}{\partial \mathbf{v}} f_{H/H^+} = Q_{H/H^+}(\mathbf{v}) + \sum_{M=O, N_2, CO_2} J_{mt}(f_{H/H^+}, f_M). \quad (1)$$

Equation (1) is written in the standard form for the velocity distribution functions $f_{H/H^+}(r,v)$, and $f_M(r,v)$ for hydrogen atoms and protons (Gérard et al., 2000). The source term Q_{H/H^+} describes the production rate of secondary H/H^+ particles and the elastic and inelastic collisional terms J_{mt} for H/H^+ describe the energy and momentum transfer to the ambient atmospheric gas which is characterized by local Maxwellian velocity distribution functions. Our kinetic Monte Carlo model (Gérard et al., 2000; Shematovich et al., 2011) is used to solve kinetic equation (1). Model is 1D in geometric space and 3D in velocity space. Nevertheless, the 3D trajectories of H/H^+ are calculated in the code with final projection on radial direction. In the current version of the MC model (Shematovich et al., 2019) an arbitrary structure of the induced magnetic field of Mars; that is, all three components of the magnetic field $\mathbf{B} = \{B_x, B_y, B_z\}$, was taken into account. The details of the model implementation and statistics control with the variance below 10% can be found in (Shematovich et al., 2019). It should be pointed out that **a key aspect of this model is the probabilistic treatment of the scattering angle distribution**, which influences both the energy degradation rate and the angular redistribution of the precipitating protons and hydrogen atoms (Bisikalo et al., 2018; Shematovich et al., 2019). To do this, it is necessary to use both total and differential cross sections when calculating the post-collision velocities for high-energy precipitating H/H^+ and atmospheric particles.

The region under study is limited by the lower boundary, which is placed at 80 km, where H/H^+ particles are efficiently thermalized. The upper boundary is set at 500 km, where measurements or calculations of the precipitating fluxes of protons or hydrogen atoms are used as a boundary condition. Both table and/or analytic (Maxwellian and/or kappa-distribution) functions representing the energy spectra as well as the pitch-angle (monodirectional, isotropic, or limited by cone) distributions of precipitating particles could be used at the upper boundary. Detailed description of all model numerical aspects used for this kinetic MC model study could be found in recent papers (Bisikalo et al., 2018; Shematovich et al., 2019) and are shown in the scheme below.

References:

Gérard J.-C., Hubert B., Bisikalo D.V., and Shematovich V.I. Lyman-alpha emission in the proton aurora. *J. Geophys. Res.*, 2000, V. 105, No. A7, 15795.

Shematovich V. I., D. V. Bisikalo, C. Diéval, S. Barabash, G. Stenberg, H. Nilsson, Y. Futaana, M. Holmstrom, and J.-C. Gérard. Proton and hydrogen atom transport in the Martian upper atmosphere with an induced magnetic field. *J. Geophys. Res.*, 2011, V. 116, Issue A11, CiteID A11320.

Bisikalo D.V., Shematovich V.I., Gérard J.-C., Hubert B. Monte Carlo simulations of the interaction of fast proton and hydrogen atoms with the Martian atmosphere and comparison with in situ measurements. *Journal of Geophysical Research: Space Physics*, 2018, V. 123, Issue 7, pp. 5850-5861.

Shematovich V.I., Bisikalo D.V., Gérard J.-C., Hubert B. Kinetic Monte Carlo model of the precipitation of high-energy proton and hydrogen atoms into the Martian atmosphere with taking into account the measured magnetic field. *Astronomy Reports*, 2019, Vol. 63, No. 10, pp. 835–845.

IV. Gronoff et al. 1-D Kinetic Model (Model Name: “Aeroplanets”)

A. Introduction

The *Aeroplanets* model (G. Gronoff, Wedlund, Mertens, Barthélemy, et al. 2012; G. Gronoff, Wedlund, Mertens, and Lillis 2012a; Simon Wedlund et al. 2011) is a 1-D kinetic transport model computing the ionization and excitation of atmospheric species by photon, electron, proton, and cosmic rays impacts, including the effect of secondary particles (Fig. [fig:workflow_ion]). It is based on the Trans* model series, initially developed for the Earth (Lilensten et al. 1999; Lummerzheim and Lilensten 1994; C. Simon et al. 2007a), and subsequently adapted to Venus (Gronoff et al. 2007, 2008), Mars (Witasse et al. 2002, 2003; Simon et al. 2009; Nicholson et al. 2009), Titan (Gronoff, Lilensten, and Modolo 2009; Gronoff et al. 2009), etc., and including several other modules such as a fluid model. *Aeroplanets* constitutes an improvement in modularity and adaptability, with every separate module having the option of being turned off to study one specific aspect of particle precipitation in the atmosphere of planets.

The proton transport module is based on the work of (Galand et al. 1997, 1998), (Simon 2006) and (C. Simon et al. 2007b) for Earth, who solved semi-analytically the coupled proton-hydrogen dissipative kinetic transport equation for protons and hydrogen atoms charge-changing with neutral gas M:

$$H^+ + M \rightarrow H + M^+ \text{Electroncapture}, \sigma_{10} \quad H + M \rightarrow H^+ + M + e^- \text{Electronloss/} \\ \text{stripping}, \sigma_{01}.$$

It naturally includes angular redistributions due to magnetic mirror effects and to collisions.

B. Inputs and outputs

Inputs to the Aeroplanets model include cross sections, the vertical profile of atmosphere composition (i.e. composition at different altitudes), and the precipitating fluxes of particles such H and H⁺ at the top of the atmosphere (see Figure [\[fig:general_aeroplanets\]](#)). Outputs include the vertical profile of H and H⁺ differential energy fluxes, and the vertical profile of the production rate of excited and ionized species and electrons, including emissions. The produced photoelectrons can be plugged into the main Aeroplanets electron model as an external and additional source of ionization in the atmosphere.

Cross sections in Aeroplanets are taken from the latest version of the ATMOCIAD cross section and reaction rate database compiled and developed by (Simon Wedlund et al. 2011; Gronoff et al. 2012a Gronoff et al. 2021, in prep). In ATMOCIAD, experimental and theoretical cross sections as well as their uncertainties are collected. Many proton-hydrogen impact cross sections have been discussed in the seminal works of (Avakyan et al. 1998) and, in a lesser degree, of (Nakai et al. 1987); they contain a critical review of processes for photons, e⁻, H, H⁺ colliding with various gases of aeronomic interest and have been fully integrated into ATMOCIAD.

Specifically, the proton transport code uses the following energy-dependent cross sections process by process:

- **Elastic.** Parameterisations of (Kozelov and Ivanov 1992) originally valid for (H⁺, H) collisions with N₂, and assumed to be the same for CO₂ because of the lack of any recent measurements. The parameters are available in their Tables 1 and 2.
- **Ionisation.** For H⁺, (Rudd et al. 1983) for high energies, extended at $E < 5$ keV by (Avakyan et al. 1998). For H atoms, cross sections are based on (Basu et al. 1987) for N₂ and on (Avakyan et al. 1998) for the rescaling factor.
- **Electron capture (H⁺ → H).** (Kusakabe et al. 2000) for 0.2-4 keV protons, review by (Avakyan et al. 1998) based on all other available data for higher energies (Desesquelles, Do Cao, and Dufay 1966; Barnett and Gilbody 1968; Toburen, Nakai, and Langley 1968;

McNeal 1970; Rudd et al. 1983 for 5 – 150 keV). Note that recent sub-keV measurements have been made by (Werbowy and Pranszke 2016) for CO and CO₂, although these are not yet implemented in the ATMOCIAAD.

- **Electron loss ($\mathbf{H} \rightarrow \mathbf{H}^+$).** (Smith et al. 1976) between 0.25 – 5 keV, review by (Avakyan et al. 1998) using N₂ σ_{01} cross sections (Green and Peterson 1968) based on all other available data for higher energies.
- **Ly- α $\mathbf{H}(2p)$ and $\mathbf{H}(2s)$ states.** For both H⁺ and H collisions, exciting state H(2p) (Birely and McNeal 1972) corrected by factor 0.9 presumably because of observation angle as per recommendation of (Avakyan et al. 1998). For both impactors creating state H(2s), factor 1.35 on the measurements of (Birely and McNeal 1972) is applied.

Although ATMOCIAAD is an extensive collection of cross sections, there is still a rather poor characterization of cross sections at low energies (typically in the sub-keV range).

Regarding differential cross sections, Aeroplanets uses phase functions that are convolved with the energy-dependent cross sections above. For the particular cases computed for Step 1 of the present study, the following is used: For the two charge-transfer (10 and 01) and the elastic cross sections, the screened Rutherford function is used, equal to that of the electrons with a screening parameter equal to 10^{-3} (this is the same as in (Galand et al. 1997, 1998) and (Simon 2006; Simon et al. 2007) for Earth’s atmosphere):

$$\xi(\cos\vartheta) = \frac{4\epsilon(1 + \epsilon)}{(1 + 2\epsilon - \cos\vartheta)^2}$$

with $\vartheta = \mu\mu' + \sqrt{1 - \mu'^2}\sqrt{1 - \mu^2}\cos(\phi - \phi')$. μ and μ' are the cosine of the pitch angles before and after the collision, whereas ϕ and ϕ' are the azimuthal angles before and after the collision. For ionisation, a simple forward scattering is simply assumed, following (Galand et al. 1998) for the Earth case.

Because of the seamless implementation of ATMOCIAAD as input to Aeroplanets, other available sets of cross sections may be used. It is possible to estimate the uncertainties from the cross-sections using a Monte-Carlo approach as described in (Gronoff et al. 2012b; G. Gronoff, Wedlund, Mertens, and Lillis 2012b). The outputs of the proton-transport model are the ionization and dissociation rates (including excited states productions), the proton/H induced

electron flux (which can be used in the electron model), and the proton/H fluxes at the different altitudes.

C. Implementation

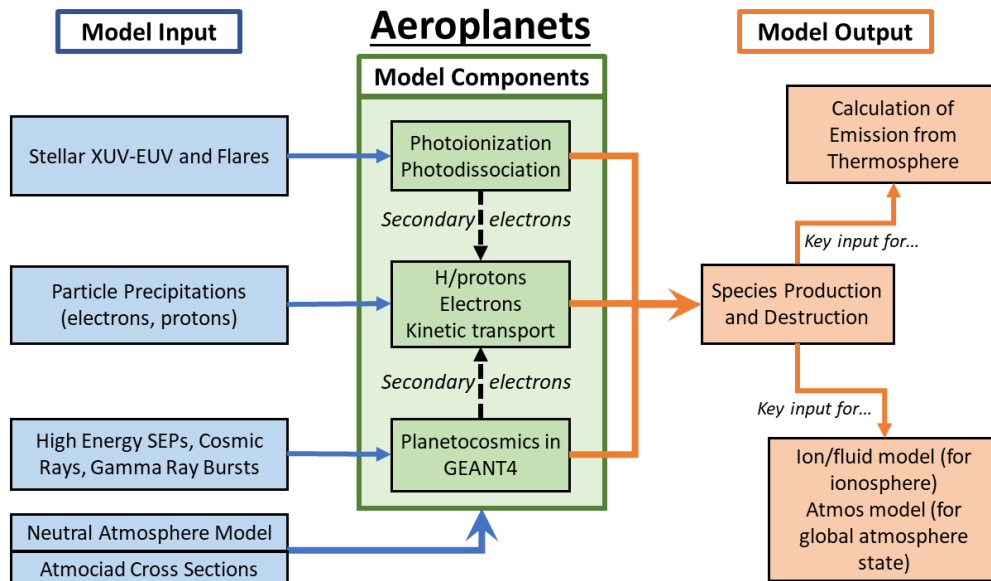
The solution of the dissipative coupled Boltzmann H/H⁺ equation is based on the seminal work of (Galand et al. 1997, 1998), later developed and adapted as a module into Aeroplanets following (C. Simon et al. 2007b). It is based on the original idea that dissipative forces responsible for angular redistributions (due to elastic scattering) can be introduced in the force term of the general Boltzmann equation (Galand et al. 1997). Rearranging the energy/angle terms of the (H,H⁺) coupled system of equations leads to a linear system of equations with large sparse square matrix A containing the energy degradation without angular redistributions of the incoming particle, for each altitude z so that:

$$\frac{\partial \Phi}{\partial z} = A\Phi + B$$

$\Phi = \begin{pmatrix} \phi_{H^+} \\ \phi_H \end{pmatrix}$ is the vector-flux of protons and hydrogen precipitating particles and B , the angular degradation term, is thus the term coupling downward and upward fluxes. Moreover, the mirror mode term can be switched on or off depending on the planet's configuration. The equation can be solved by calculating the exponential of matrix A for a typical grid of 100 energies and 10 angles; but which can be increased for better resolution. In order to achieve such a feat of simplification for a complex system of equations, the following assumptions are made in the case of the Mars code: (i) plane parallel geometry, with the atmosphere stratified horizontally, the pitch angle of the particles can be imposed, (ii) external forces neglected, (iii) steady-state fluxes, (iv) continuous slowing down approximation assumed because of the low energetic losses by the precipitating particles compared to the incident energy of the particles.

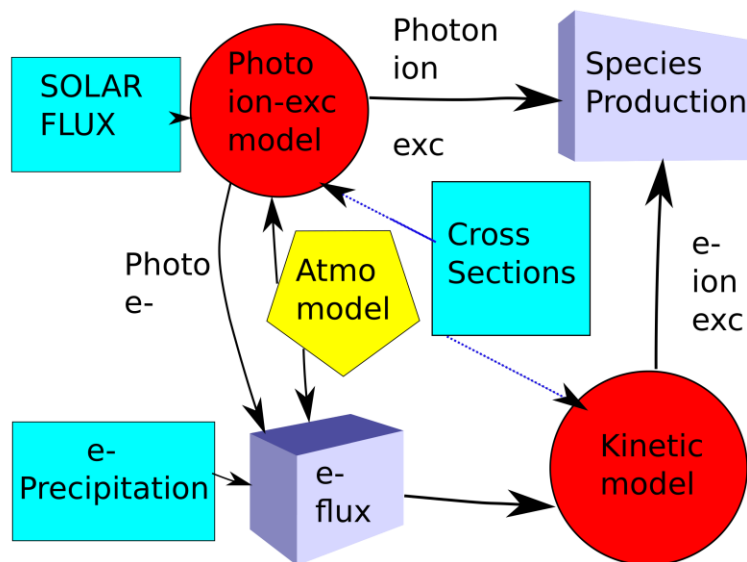
D. Strengths and applications

Aeroplanets is better qualified for the quick computation of the proton precipitation from a measured spectra near the planet, and for the quick computation of the whole effect of that precipitation thanks to its coupling with a secondary electron transport model. The analytic computation approach prevents the computation within very complex magnetic topologies (which are best handled by Monte-Carlo models) but is perfectly suited for handling large sets of initial angles and energies.



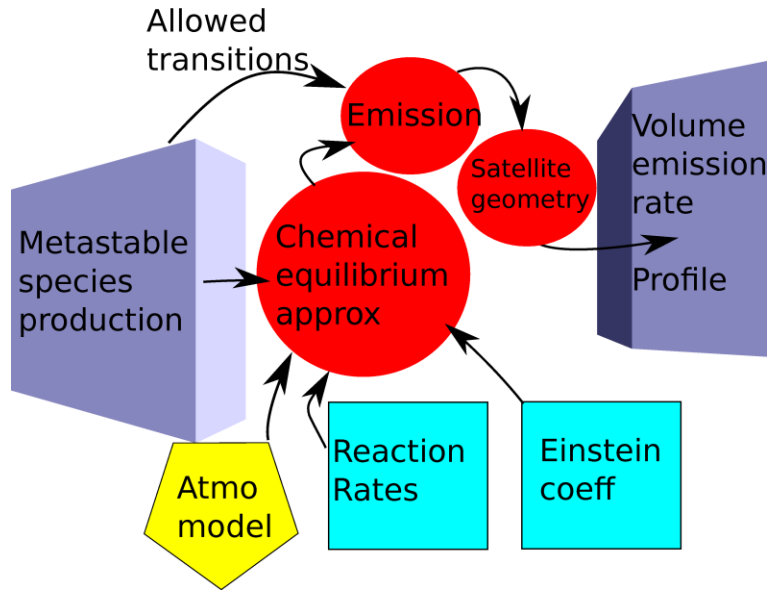
General computation performed in Aeroplanets

[fig:general_aeroplanets]



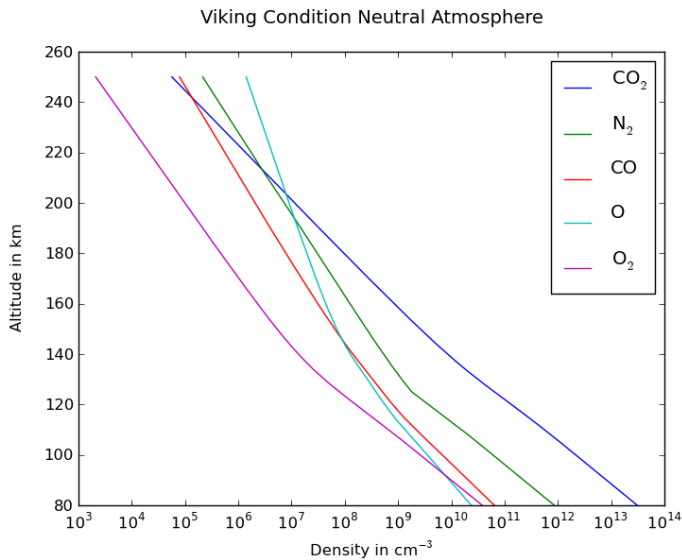
Workflow for the computation of the species production in Aeroplanets. The red circles emphasizes the model parts, the blue boxes the inputs, which can have strong influence on possible retrieval of the atmosphere. The Atmosphere model, which can either be an input for a simulation, or an output for the retrieval is described by a yellow hexagon. The outputs, which can be measured, or used for further computation are presented by the “3D” boxes. (Published in Gronoff et al., [2012a]).

[fig:workflow_ion]

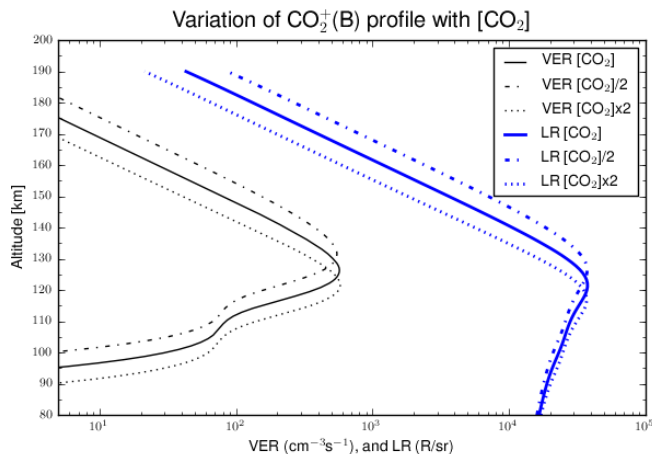


The workflow to model the emission as observed from a satellite from the modeling of the excited state species. (Published in Gronoff et al. [2012a])

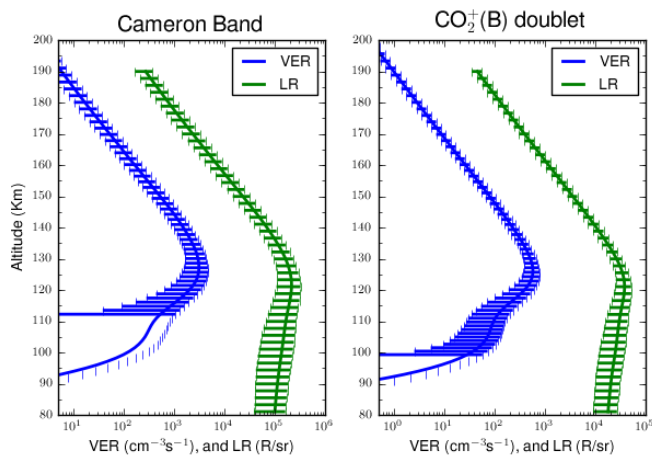
[fig:workflow_emit]



The neutral atmosphere computed by the MTGCM model for the Viking 1 landing conditions [Simon et al., 2009].



Sensitivity analysis of the $\text{CO}_2^+(B)$ doublet emission with the variation of the CO_2 density in the atmosphere of Mars.



Computation of the uncertainties with Aeroplanets. The large uncertainties below the peaks prevent an accurate determination of the density when the model is used for retrieval.

References:

- Avakyan, S.V., R.N. Ii'In, V.M. Lavrov, and G.N. Ogurtsov. 1998. Collision processes and excitation of UV emission from planetary atmospheric gases: a handbook of cross sections. Taylor & Francis, Amsterdam.
- Barnett, C. F., and H. B. Gilbody. 1968. "Measurements of Atomic Cross Sections in Static Gases." In Atomic Interactions Part a, edited by Benjamin Bederson and Wade L. Fite, 7:390.
- Basu, B., J. R. Jasperse, R. M. Robinson, R. R. Vondrak, and D. S. Evans. 1987. "Linear transport theory of auroral proton precipitation: A comparison with observations." J. Geophys. Res. 92 (A6): 5920–32. <https://doi.org/10.1029/JA092iA06p05920>.

- Birely, J. H., and R. J. McNeal. 1972. "Lyman-Alpha Emission Cross Sections for Collisions of 1-25 keV H^+ and H with CO , CO_2 , CH_4 , and NH_3 ." *J. Chem. Phys.* 56 (5): 2189–94. <https://doi.org/10.1063/1.1677518>.
- Desesquelles, J., G. Do Cao, and M. Dufay. 1966. "Etude de l'ionisation de quelques gaz par des ions accélérés H^+ et H_2^+ ." *C. R. Acad. Sci. Paris* 262 (B): 1329–32.
- Galand, M., J. Lilensten, W. Kofman, and D. Lummerzheim. 1998. "Proton Transport Model in the Ionosphere. 2. Influence of Magnetic Mirroring and Collisions on the Angular Redistribution in a Proton Beam." *Annales Geophysicae* 16 (October): 1308–21. <http://cdsads.u-strasbg.fr/abs/1998AnGeo..16.1308G>.
- Galand, M., J. Lilensten, W. Kofman, and D. Lummerzheim. 1998. "Proton transport model in the ionosphere. 2. Influence of magnetic mirroring and collisions on the angular redistribution in a proton beam." *Annales Geophysicae* 16 (October): 1308–21. <https://doi.org/10.1007/s00585-998-1308-y>.
- Galand, M., J. Lilensten, W. Kofman, and R. B. Sidje. 1997. "Proton Transport Model in the Ionosphere 1. Multistream Approach of the Transport Equations." *Journal of Geophysical Research* 102 (September): 22261–72. <http://cdsads.u-strasbg.fr/abs/1997JGR...10222261G>.
- Galand, M., J. Lilensten, W. Kofman, and R. B. Sidje. 1997. "Proton transport model in the ionosphere 1. Multistream approach of the transport equations." *Journal of Geophysics Research* 102 (September): 22261–72. <https://doi.org/10.1029/97JA01903>.
- Green, A. E. S., and L. R. Peterson. 1968. "Energy loss functions for electrons and protons in planetary gases." *J. Geophys. Res.* 73 (1): 233. <https://doi.org/10.1029/JA073i001p00233>.
- Gronoff, G., J. Lilensten, L. Desorgher, and E. Flückiger. 2009. "Ionization Processes in the Atmosphere of Titan. I. Ionization in the Whole Atmosphere." *Astronomy and Astrophysics* 506 (November): 955–64. <http://adsabs.harvard.edu/abs/2009A%26A...506..955G>.
- Gronoff, G., J. Lilensten, and R. Modolo. 2009. "Ionization Processes in the Atmosphere of Titan. II. Electron Precipitation Along Magnetic Field Lines." *Astronomy and Astrophysics* 506 (November): 965–70. <http://adsabs.harvard.edu/abs/2009A%26A...506..965G>.
- Gronoff, G., J. Lilensten, C. Simon, M. Barthélemy, F. Leblanc, and O. Dutuit. 2008. "Modelling the Venusian Airglow." *Astronomy and Astrophysics* 482 (May): 1015–29. <http://adsabs.harvard.edu/abs/2008A%26A...482.1015G>.
- Gronoff, G., J. Lilensten, C. Simon, O. Witasse, R. Thissen, O. Dutuit, and C. Alcaraz. 2007. "Modelling Dications in the Diurnal Ionosphere of Venus." *Astronomy and Astrophysics* 465 (April): 641–45. <http://adsabs.harvard.edu/abs/2007A%26A...465..641G>.
- Gronoff, G., C. Simon Wedlund, C. J. Mertens, and R. J. Lillis. 2012a. "Computing uncertainties in ionosphere-airglow models: I. Electron flux and species production uncertainties for Mars." *Journal of Geophysical Research (Space Physics)* 117 (April): 4306. <https://doi.org/10.1029/2011JA016930>.

- . 2012b. “Computing uncertainties in ionosphere-airglow models: I. Electron flux and species production uncertainties for Mars.” *Journal of Geophysical Research (Space Physics)* 117 (April): A04306. <https://doi.org/10.1029/2011JA016930>.
- Gronoff, Guillaume, Cyril Simon Wedlund, Christopher J. Mertens, Mathieu Barthélemy, Robert J. Lillis, and Olivier Witasse. 2012. “Computing Uncertainties in Ionosphere-Airglow Models: II. The Martian Airglow.” *J. Geophys. Res.* 117 (May): 17 PP. <https://doi.org/201210.1029/2011JA017308>.
- Gronoff, Guillaume, Cyril Simon Wedlund, Christopher J. Mertens, and Robert J. Lillis. 2012a. “Computing Uncertainties in Ionosphere-Airglow Models:I. Electron Flux and Species Production Uncertainties for Mars.” *J. Geophys. Res.* 117 (April): 18 PP. <https://doi.org/201210.1029/2011JA016930>.
- . 2012b. “Computing Uncertainties in Ionosphere-Airglow Models:I. Electron Flux and Species Production Uncertainties for Mars.” *J. Geophys. Res.* 117 (April): 18 PP. <https://doi.org/201210.1029/2011JA016930>.
- Kozelov, B. V., and V. E. Ivanov. 1992. “Monte Carlo calculation of proton-hydrogen atom transport in N₂.” *Plan. Space Sci.* 40 (11): 1503–11. [https://doi.org/10.1016/0032-0633\(92\)90047-R](https://doi.org/10.1016/0032-0633(92)90047-R).
- Kusakabe, Toshio, Kensuke Asahina, Jiang P. Gu, Gerhard Hirsch, Robert J. Buenker, Mineo Kimura, Hiroyuki Tawara, and Yohta Nakai. 2000. “Charge-transfer processes in collisions of H⁺ ions with H₂, D₂, CO, and CO₂ molecules in the energy range 0.2-4.0 keV.” *Phys. Rev. A* 62 (6): 062714. <https://doi.org/10.1103/PhysRevA.62.062714>.
- Lilensten, J., P. L. Blelly, W. Kofman, and D. Alcaydé. 1999. “Auroral Ionospheric Conductivities: A Comparison Between Experiment and Modeling, and Theoretical F10.7-Dependent Model for EISCAT and ESR.” *Ann. Geophys.* 14 (12): 1297–1304. <https://doi.org/10.1007/s00585-996-1297-7>.
- Lummerzheim, D., and J. Lilensten. 1994. “Electron Transport and Energy Degradation in the Ionosphere: Evaluation of the Numerical Solution, Comparison with Laboratory Experiments and Auroral Observations.” *Annales Geophysicae* 12 (November): 1039–51. <http://adsabs.harvard.edu/abs/1994AnGeo..12.1039L>.
- McNeal, R. J. 1970. “Production of Positive Ions and Electrons in Collisions of 1-25-keV Protons and Hydrogen Atoms with CO, CO₂, CH₄, and NH₃.” *J. Chem. Phys.* 53 (11): 4308–13. <https://doi.org/10.1063/1.1673938>.
- Nakai, Y., T. Shirai, T. Tabata, and R. Ito. 1987. “Cross Sections for Charge Transfer of Hydrogen Atoms and Ions Colliding with Gaseous Atoms and Molecules.” *Atomic Data and Nuclear Data Tables* 37 (January): 69. [https://doi.org/10.1016/0092-640X\(87\)90005-2](https://doi.org/10.1016/0092-640X(87)90005-2).
- Nicholson, William P., Guillaume Gronoff, Jean Lilensten, Alan D. Aylward, and Cyril Simon. 2009. “A Fast Computation of the Secondary Ion Production in the Ionosphere of Mars.” *Monthly Notices of the Royal Astronomical Society* 400 (November): 369–82. <http://adsabs.harvard.edu/abs/2009MNRAS.400..369N>.

- Rudd, M. E., T. V. Goffe, R. D. Dubois, L. H. Toburen, and C. A. Ratcliffe. 1983. “Cross sections for ionization of gases by 5-4000-keV protons and for electron capture by 5-150-keV protons.” *Phys. Rev. A* 28 (6): 3244–57. <https://doi.org/10.1103/PhysRevA.28.3244>.
- Simon, C., J. Lilensten, J. Moen, J. M. Holmes, Y. Ogawa, K. Oksavik, and W. F. Denig. 2007a. “TRANS4: A New Coupled Electron/Proton Transport Code - Comparison to Observations Above Svalbard Using ESR, DMSP and Optical Measurements.” *Annales Geophysicae* 25 (March): 661–73. <http://adsabs.harvard.edu/abs/2007AnGeo..25..661S>.
- . 2007b. “TRANS4: A New Coupled Electron/Proton Transport Code - Comparison to Observations Above Svalbard Using ESR, DMSP and Optical Measurements.” *Annales Geophysicae* 25 (March): 661–73. <http://adsabs.harvard.edu/abs/2007AnGeo..25..661S>.
- Simon, C., J. Lilensten, J. Moen, J. M. Holmes, Y. Ogawa, K. Oksavik, and W. F. Denig. 2007. “TRANS4: a new coupled electron/proton transport code - comparison to observations above Svalbard using ESR, DMSP and optical measurements.” *Annales Geophysicae* 25 (March): 661–73. <https://doi.org/10.5194/angeo-25-661-2007>.
- Simon, C., O. Witasse, F. Leblanc, G. Gronoff, and J.-L. Bertaux. 2009. “Dayglow on Mars: Kinetic Modelling with SPICAM UV Limb Data.” *Planetary and Space Science* 57 (July): 1008–21. <http://adsabs.harvard.edu/abs/2009P%26SS...57.1008S>.
- Simon, Cyril. 2006. “Contribution à L'étude Des Entrées d'énergie Solaire Dans L'ionosphère : Ions Doublement Chargés et Transport Cinétique Des Protons - Application à La Terre et à Titan.” PhD thesis, Université Joseph-Fourier - Grenoble I. <http://tel.archives-ouvertes.fr/tel-00109802>.
- Simon Wedlund, C., G. Gronoff, J. Lilensten, H. Ménager, and M. Barthélemy. 2011. “Comprehensive Calculation of the Energy Per Ion Pair or W Values for Five Major Planetary Upper Atmospheres.” *Annales Geophysicae* 29 (1): 187–95. <https://doi.org/10.5194/angeo-29-187-2011>.
- Simon Wedlund, C., G. Gronoff, J. Lilensten, H. Ménager, and M. Barthélemy. 2011. “Comprehensive calculation of the energy per ion pair or W values for five major planetary upper atmospheres.” *Annales Geophysicae* 29 (January): 187–95. <https://doi.org/10.5194/angeo-29-187-2011>.
- Smith, K. A., M. D. Duncan, M. W. Geis, and R. D. Rundel. 1976. “Measurement of electron loss cross sections for 0.25- to 5-keV hydrogen atoms in atmospheric gases.” *J. Geophys. Res.* 81 (13): 2231. <https://doi.org/10.1029/JA081i013p02231>.
- Toburen, L. H., M. Y. Nakai, and R. A. Langley. 1968. “Measurement of High-Energy Charge-Transfer Cross Sections for Incident Protons and Atomic Hydrogen in Various Gases.” *Physical Review* 171 (1): 114–22. <https://doi.org/10.1103/PhysRev.171.114>.
- Werbowy, S., and B. Pranszke. 2016. “Charge-exchange processes in collisions of H^+ , H_2^+ , H_3^+ , He^+ , and He_2^+ ions with CO and CO₂ molecules at energies below 1000 eV.” *Phys. Rev. A* 93 (2): 022713. <https://doi.org/10.1103/PhysRevA.93.022713>.
- Witasse, O., O. Dutuit, J. Lilensten, R. Thissen, J. Zabka, C. Alcaraz, P.-L. Blelly, et al. 2002. “Prediction of a CO₂+ Layer in the Atmosphere of Mars.” *Geophysical Research Letters* 29 (April): 104–1. <http://adsabs.harvard.edu/abs/2002GeoRL..29h.104W>.

- . 2003. “Correction to ‘Prediction of a CO₂+ Layer in the Atmosphere of Mars’.”
Geophysical Research Letters 30 (April): 12–11.
<http://adsabs.harvard.edu/abs/2003GeoRL..30g..12W>.